Universitat
de les Illes Balears

DOCTORAL THESIS
2016

INVERSE METHODS TO ESTIMATE SYNAPTIC CONDUCTANCES WITH EMPHASIS ON NON-SMOOTH DYNAMICAL SYSTEMS

Catalina Vich Llompart

Universitat
de les Illes Balears

DOCTORAL THESIS
2016

Doctoral Programme of Mathematics

INVERSE METHODS TO ESTIMATE SYNAPTIC CONDUCTANCES WITH EMPHASIS ON NON-SMOOTH DYNAMICAL SYSTEMS

Catalina Vich Llompart

Thesis Supervisors:
Antoni Guillamon
Universitat Politècnica de Catalunya, UPC
Rafel Prohens
Universitat de les Illes Balears, UIB

Doctor by the Universitat de les Illes Balears

Memòria presentada per a aspirar al grau de doctora en Matemàtiques
Departament de Ciències Matemàtiques i Informàtica
Universitat de les Illes Balears
Palma, Juliol de 2016

Catalina Vich Llompart

La present memòria ha estat co-dirigida pel Dr. Rafel J. Prohens Sastre, Professor Titular d'Universitat del Departament de Ciències Matemàtiques i Informàtica de la Universitat de les Illes Balears i pel Dr. Antoni Guillamon Grabolosa, Professor Titular de Matemàtica Aplicada del Departament de Matemàtiques de la Universitat Politècnica de Catalunya

Antoni Guillamon Grabolosa   Rafel J. Prohens Sastre

Abstract

Català   Aquesta tesi té com a finalitat contribuir en els àmbits científics de la *neurociència matemàtica i computacional* i del *sistemes dinàmics*. El principal problema que es vol tractar és el de l'estimació del curs temporal de les conductàncies sinàptiques a la qual una neurona està sotmesa, tot i que també tractem diferents qüestions sobre sistemes dinàmics i altres aspectes purament computacionals. Per tractar el problema de l'estimació, utilitzem models minimals que descriuen la dinàmica d'una sola neurona, els quals són estudiats emprant diferents tècniques sobre sistemes "slow-fast", equacions diferencials estocàstiques i models no diferenciables.

La quantitat d'informació que una sola neurona rep és rellevant a l'hora d'intentar determinar la connectivitat cerebral. No obstant això, el seu transcurs temporal no es pot extreure directament dels experiments, per la qual cosa es necessiten mètodes inversos per a estimar conductàncies a partir d'enregistraments factibles (com ara el potencial de membrana de la neurona). En la literatura, trobem diferents mètodes basats en processos d'inferència estocàstica i determinista. Tots els mètodes existents, tant experimentals com teòrics, presenten algunes deficiències importants: (a) suposicions errònies sobre relacions lineals entre el corrent d'entrada i el voltatge de sortida, les quals són sovint deduïdes després d'aplicar tècniques de filtratge que no poden eliminar completament els efectes no-lineals presents; i (b) la necessitat d'utilitzar més d'un enregistrament, fet que obliga a assumir la mateixa connectivitat funcional en dos experiments diferents. Aquests aspectes converteixen aquest tema en un desafiament no trivial per a la neurociència.

Sovint ignorar aquests obstacles pot portar-nos a grans errors en les estimacions, especialment, tal com s'ha vist en publicacions recents, en les regions de "spikes". En aquesta tesi veiem que els problemes derivats dels efectes no-lineals s'estenen també en les zones de no "spikes" quan es tracta amb traces de voltatges obtigudes sota la presència de corrents iònics actius en aquestes regions. En aquestes condicions, també proporcionem nous mètodes per a millorar les estimacions de les conductàncies sinàptiques. Els mètodes proposats, des dels punts de vista determinista i estocàstic, depenen de models que descriuen la dinàmica "subthreshold" i estan basats en no-linealitats. El mètode determinista aprofita la naturalesa "slow-fast" de l'activitat neuronal i proporciona excel·lents estimacions en experiments *in sillico*. Per tal de considerar el renou present en les dades experimentals, el mètode anterior s'ha estès a un mètode estocàstic, en el qual construïm un estimador *ad hoc* de màxima versemblança per al model no-lineal. Finalment, també proporcionem una prova de concepte d'un mètode d'estimació general determinista per a realitzar estimacions en la zona de "spikes"; en aquest cas, aprofitem tècniques dels sistemes lineals a trossos per a deduir relacions no-lineals d'entrada/sortida, que permeten l'estimació dels paràmetres sinàptics mitjançant la resolució d'equacions no-lineals.

Els resultats del nucli principal de la tesi es complementen amb dues immersions a dos aspectes més formatius en el marc científic que hem descrit anteriorment. D'una banda, un

estudi teòric/analític sobre sistemes diferencials lineals a trossos, de dinàmica "slow-fast" i n-dimensionals, on demostrem un teorema semblant al Teorema de Fenichel i l'existència i ubicació dels canards maximals. D'altra banda, també implementem una xarxa neuronal complexa que descriu l'alternança d'estats d'alta i baixa activitat observats en el còrtex visual, la qual utilitzem també com a punt de referència per a obtenir perfils de conductàncies sinàptiques *realistes*, en diferents neurones i per a diferents condicions de plasticitat en la xarxa. Aquestes traces de conductàncies poden ser emprades com a base de dades *in sillico* per a comprovar els nostres mètodes d'estimació.

English This thesis aims at contributing in the scientific fields of *mathematical and computational neuroscience* and *dynamical systems*. The main problem we address is the estimation of the time-course of synaptic conductances impinging on a neuron, but we also treat different related questions on dynamical systems and computational aspects. We tackle this estimation problem by using minimal models of single cell dynamics and studying them by means of different techniques for slow-fast dynamics, stochastic differential equations and non-smooth models.

The quantity of information that a single neuron is receiving is a relevant aspect when trying to unveil brain's connectivity. However, the time course of synaptic conductances cannot be extracted in a direct way from experiments and, therefore, inverse methods to estimate them from feasible recordings (like the neuron's membrane potential) become necessary. Both methods using stochastic and deterministic inference ideas have been proposed, but all the approaches provided in the literature, both experimental and theoretical, present some main shortcomings: (a) wrong assumptions of linear relationships between input current and output voltage, often inferred after filtering techniques that do not get completely rid of nonlinear effects; and, (b) the need of using more than one recording, thus forcing to assume the same functional connectivity in two different experiments. Thus, it becomes a non-trivial challenge for neuroscience.

Ignoring these obstacles sometimes leads to huge misestimations, specially in spiking regimes, as it has been shown in recent publications. In this thesis, we also describe the problems derived from nonlinear effects when dealing even with voltage traces obtained in the subthreshold regime, and we give new methods to improve the estimations of synaptic conductances when ionic currents are active in this regime. The methods proposed here, both deterministic and stochastic, rely on nonlinear basic models for subthreshold activity. The deterministic method takes advantage of the slow-fast nature of the activity and provides excellent estimations in *in sillico* experiments. To account for noise present in experimental data, we extend the method to a stochastic paradigm in which we build up an *ad hoc* maximum likelihood estimation for a nonlinear model. Finally, we also provide a proof-of-concept of a general deterministic approach to deal with estimations in spiking regimes; in this case, we take advantage of techniques from piecewise linear systems to derive nonlinear input/output relationships that allow the estimation of synaptic parameters by solving nonlinear equations.

The results of the main core of the thesis are complemented with two immersions on two formative aspects within the scientific framework described above. On one hand, a theoretical/analytical study of slow-fast n-dimensional piecewise linear differential systems, where we prove a Fenichel's like Theorem and the existence and location of maximal canards. On another hand, we also implement a complex neuronal network describing up/down states observed in the visual cortex, which we also use as a benchmark to obtain *realistic* synaptic conductance profiles for different cell types and diverse plasticity conditions in the network. These conductance traces can be used as *in sillico* datasets to test

our methods to estimate conductances.

Español   Esta tesis tiene como finalidad contribuir en los ámbito científicos de la *neuro-ciencia matemática y computacional* y de los *sistemas dinámicos*. El principal problema al cual queremos dirigirnos es el de la estimación del trasncurso temporal de las conductancias sinápticas a que una neurona está sometida. También queremos tractar diferentes cuestiones sobre sistemas dinámicos que modelan el comportamiento de las neuronas y sus aspectos computacionales. Para tratar dicho problema de estimación, utilizamos modelos minimales que describen la dinámica de una sola neurona, y los estudiamos utilizando diferentes técnicas de los sistemas "slow-fast", ecuaciones diferenciales estocásticas y modelos no-diferenciables.

La cantidad de información que una sola neurona recibe es relevante cuando se trata de dar a conocer la conectividad cerebral. No obstante, su transcurso temporal no puede ser extraido directamente de los experimentos, razón por la cual se necesitan métodos inversos de estimación de conductancias a partir de registros factibles (como ahora el potencial de membrana de la neurona). En la literatura encontramos diferentes métodos basados en procesos de inferencia estocástica y determinista. Todos estos métodos existentes, tanto experimentales como teóricos, presentan algunas deficiencias importantes: (a) suposiciones erróneas sobre relaciones lineales entre la corriente de entrada y la tensión de salida, las cuales son a menudo deducidas después de aplicar técnicas de filtrado que no pueden eliminar completamente los efectos no-lineales presentes; y (b) la necesidad de utilizar más de un registro, lo cual obliga a asumir la misma conectividad funcional en dos experimentos diferentes. Por lo tanto, dicho tema se convierte en un desafio no trivial para la neurociencia.

A menudo, ignorar estos obstaculos puede suponer grandes errores en las estimaciones, especialmente, tal y como se ha visto en publicaciones recientes, en regiones de "spikes". En esta tesis demostramos que los problemas derivados de los efectos no-lineales se extienden también a las zonas de no "spikes", cuando se trata con trazas de voltages obtenidas bajo la presencia de corrientes iónicas activas en estas regiones. En estas condiciones, también proporcionamos nuevos métodos para mejorar las estimaciones de conductancias sinápticas. Los métodos propuestos, desde el punto de vista determinista y estocástico, dependen de modelos que describen la dinámica "subthreshold" y estan basados en no-linealidades. El método determinista aprovecha la naturaleza "slow-fast" de la actividad neuronal proporcionando excelentes estimaciones en los experimentos *in sillico*. Para tener en cuenta el ruido presente en los datos experimentales, hemos extendido el método anterior a un método estocástico, en el cual construimos un estimador *ad hoc* de máxima semejanza para el modelo no-lineal. Finalmente, también proporcionamos una prueba de concepto de un método de estimación general determinista para realizar estimaciones en las zonas de "spikes". En tal caso, aprovechamos técnicas de los sistemes lineales a trozos, para deducir relaciones no-lineales de entrada/salida que permiten la estimación de los parámetros sinápticos mediante la resolución de ecuaciones no-lineales.

Los resultados del núcleo principal de la tesis se complementan con dos immersiones en dos aspectos más formativos en el marco científico descrito anteriormente. Por una parte, un estudio teórico/analítico sobre sistemas diferenciales lineales a trozos, de dinámica "slow-fast" y n-dimensionales, donde demostramos un teorema similar al Teorema de Fenichel y la existencia y ubicación de los canards maximales. Por otra parte, también implementamos una red neuronal compleja que describe los estados de alta y poca actividad observados en el córtex visual, la cual utilizaremos también como punto de referencia para obtener perfiles de conductancias sinápticas *realistas* desde diferentes tipus de neuronas

y para diferentes condiciones de plasticidad sobre la red neuronal. Dichas trazas de conductancias pueden ser utilizadas como base de datos *in sillico* para comprobar nuestros métodos de estimación.

Acknowledgements

After some years doing maths and learning about neuroscience, in these pages the real difficult work begins, that is, trying to write down everything I have done during this period of my live. Even though people say that all the difficult work is already done, sort the pile of papers that one has been recollecting during this time is something that can be even harder, and that it would have not been possible without some of the people around me.

So, first of all, I would like to thank my sister, for all the morning coffees and afternoon beers that I have had to pay for her to review some English sentences (including these ones). *És el que té anar-se'n 7 anys a viure a Londres i deixar-me a Mallorca!* And since I have already started with family, I am also grateful to my closest family, who has been around taking care of me, and cooking for me more than once these last months. *Així que sobretot padrina i mamà, gràcies!* Also to my group of friends, who even though they could not help me when technical things went wrong, they were right there together with my close family.

I cannot forget also the cafe-mates from Mallorca (Joan, Joan Carles i NN), who have had to listen to me when I was stressed (and not!), and with who these years have passed very fast so, *gràcies per ser allà i fer el possible perquè, cada dia que poguéssim, anéssim a fer el cafè i la xerradeta junts per distreure'ns.*

And speaking about cafe times, I am also grateful to the people from Copenhagen, who have been with me during my stay of research there, and with who four months have passed, as we say, *volant* (very fast), it felt like a week. From the Københavns universitet, I want to mention Prof. Rune Berg, thank you for providing me the experimental data and information about the experiments. Also, I would like to specially mention Prof. Susanne Ditlvesen, who accepted me there to work with her and who has been teaching me the basic knowledges about stochastic theory, which I did not have the opportunity to learn before. So, thanks for your patience and, now that I know that *søods* does not only mean fat from the milk, but also sweet depending on the context, then *tak, du var så sød at have mig der. Men jeg mangler stadig at høre dig danse Jazz.*

I cannot forget the people from the summer school in Poland, where I had the opportunity to learn more about computational neuroscience. Particularly, the group of students who were sharing information with me for our projects. Specially Prof. Paolo Massobrio, for accepting my proposal about neuronal networks and for helping me in this part of neuroscience that I did not know before. Also I want to thank you for not running away from me this last year when I had been busy trying to finish the other chapters of the thesis. So, *Grazie per essereci, e avermi insegnato molto sulle reti neurali. Ora possiamo andare a farci una grande birra per festeggiare e un caffè Illy davanti a qualche campanille.* And at this point, I can say thanks to Giacomo Cherubini to translate the italian and danish

previous statements (Susanne can judge your 3 years of danish classes).

Although my supervisors have been there to work with me, a lot, I am not going to mention them, yet. I thank first the Departament de Ciències Matemàtiques i Informàtica to accept me there as well as the dynamical systems and image processing research groups who have been close to me. Specially Ana Belen, with who I have been sharing teaching knowledges and with who I have grown up as a teacher. And Carmentxu who, even though she is not part of my research group, has been taking care of some paperwork about the course we are teaching together, while I have been using almost all my time writing all these pages. I also want to thank the Universitat Politècnica de Catalunya (UPC) that allowed Prof. Toni Guillamon be my advisor, even though the thesis is not developed at this university.

And last but not least, my advisors Toni Guillamon (from UPC), Rafel Prohens (from UIB), and although he is keeping saying he does not want to be one of my advisor, Antonio E. Teruel (from UIB). Without you, it could not have been possible to construct all this thesis, and to couple both neuroscience and dynamical systems. I got three academic fathers for the price of one. And, because I want to thank each of you one by one I have to decide who goes first, so I will do it as mathematicians do, by alphabetical order (with you, I am always the last one, luckily I can also publish to neuroscience journals and so my father's name shows up sometimes).

Toni, thanks a lot for accepting me as a student when you did not even know me. You accepted to be my master's thesis advisor and you have finished being my advisor in something bigger: my PhD, which could not have been possible without you. Because of you, I have learned all I know about neuroscience and also some English grammar (you have to share this last compliment with my sister, but both of you deserve it). You proposed me to work on the conductances' estimation problem, and now I can say I am happy of having accepted it. Moreover I am thankful because you wanted to keep working with me despite the distance and the extra work involved to him that my belonging to another university supposes. Before I met you, if someone had asked me about *Palíndroms*, I would have said that I had no idea about what it was. Now, I know that there is a kind of research group on this topic, in which, of course, you take part. Today, I can say that it is something difficult to come up with. But, for all the patience you have had with me, I also have had the patience to prepare one for you, hoping that it does not exist yet (since in this research world, however I know that it often happens that when you finally publish the paper, someone has already done it but you did not know it). So, to include on your webpage about Catalan palindromes, here it goes: *E! Toni G., Gin o tè?* (honestly, I know you prefer the first one).

Rafel, who has been there from the very beginning, from when I decided to go to Barcelona to do the master and learn about neuroscience. Thanks for proposing me, together with Tomeu Coll, to work with you on neuroscience; as I said to Toni, now I would not change the topic. I think we hit the nail on the head with the theme. I do really appreciate your effort working with me not only on the theoretical basis, in which you were more comfortable and expert, but also in the computational part. But let me tell you that doing always the easiest things, theoreticals, is falling into a monotonic "behaviour" (life), and we both know for sure that proving the monotonicity of periods can be challenging. Anyway, I have also fallen into monotonicity (what we call habits) of having lunch everyday, something you want me to change and make me have only an apple. However, I also have the proof of the contrary in some emails where you say: ≪*PD: Pensa a menjar. No t'amagreixis massa!*≫.

And, what to say to Antonio? *Tengo tantos pulpos "como animal de compañía" que ya no sé dónde meterlos. Tomo buena nota de la paella! y puedes acompañarla de una buena ración de pulpo a la gallega, que me han dicho por ahí que también tienes muchos...* Seriously, with your slow and my fast pace, we managed to find the appropriate rhythm of working with slow-fast piecewise linear systems and publish something on the topic, luckily for us, Rafel was around to take us to the equilibrium state. So, thanks for all the work you have done even though you have not wanted to be on the main page of the thesis. I would also like to thank you as well for all those time you have come to me with neuroscience questions which were challenging for me but at the same time I have learnt some valuable knowledge.

With the three of you, I have learned not only knowledge but also plenty of life experiences. Finally, thank you all for arranging all those courses, meetings, workshops, retreats, ... for me. I have made good use of the money.

Finalment, vull dedicar tota aquesta feina, a la família del Campet 1, Amargura 26 i Polígono 23 parcel·la 320. D'entre ells, especialment, al meu pare. A veure si et recuperes aviat que m'han dit que aquí no s'acaba la feina. Així que, amunt!

Contents

xii

Introduction

Along the last years, part of my professional training has been focused on the topics of mathematics, concretely in dynamical systems, and neuroscience. These two doctrines constitute the main core of this thesis, which combines them to give a step forward in one of the most challenging problems in neuroscience: *unveil brain's connectivity.*

Neurons are specific cells in the brain having the ability to transmit information between them as a consequence of sensory stimuli from the environment. Therefore, brain's connectivity may vary depending on the task being performed. Connections between neurons can be reinforced or debilitated according to emotions, thoughts, damages on the body, among others. The information is transmitted through electrical and chemical signals, which can amplify (excitation) or reduce (inhibition) the activity of the receiving neurons, and so the activity of the brain. This communication process is called synapse and changes on its strength are called the synaptic plasticity.

Depending on the animal species, its brain can be formed by thousands to billions of neurons, with a huge amount of total synaptic contacts (between 10^{14} and 10^{15}, for the human brain) thus increasing the complexity of the brain. In order to infer brain's connectivity and to understand the dynamics of information, processing methods are sought both from experimental and theoretical perspective.

A "local" simplified situation, despite of its global repercussion, is trying to find out which signal is receiving a single neuron subjected to a bombardment of synaptic inputs, that is input signals coming from other neurons, and then discern the temporal contributions of global excitation from those of global inhibition. This quantitative information is important for the integrative properties of cortical neurons which are believed to be altered under high-conductance states, see for instance Destexhe et al (2003). The relationship between the modulation of excitatory and inhibitory time courses is also important to get information about the wiring architecture of the cortex since it may help to distinguish between phase insensitive cortical coupling or spatial phase selective coupling, see McLaughlin et al (2000). On the other hand, this joint information is useful to study both the balance and the concurrence of excitation and inhibition, which are crucial features in many neuronal problems, see Wehr and Zador (2003) and Lombardi et al (2012) among others. Moreover, disruption of these features leads to severe disorders, so it is relevant to obtain precise estimations of the activity arriving to a specific cell.

Due to the multitude and the variety of synaptic contacts, obtaining direct measurements of the synaptic currents that the neuron is receiving at each moment in time is something unreachable. Therefore, inverse methods appear as an alternative to estimate the input (mainly, the conductances) from experimental measures. Experiments that provide membrane potential time courses from intracellular recordings of cortical cells are relevant in this regard, and have been carried out for different cell types in different brain areas,

see Hirsch et al (1998), Anderson et al (2000), Wehr and Zador (2003) and Monier et al (2008).

Broadly speaking, there are four main obstacles to overcome in order to provide effective solutions to this inverse problem. On one hand, one needs a mathematical model of the target neuron in which the synaptic conductances are well identified (generally, as parameters of the system). Aiming at giving methods as general as possible, the variety of neuron types does not advise to use very specific models, but rather minimal models that capture essential features of neuronal dynamics. This idea has been extensively used in the existing literature (see Borg-Graham et al (1998), Anderson et al (2000), Wehr and Zador (2003), Rudolph et al (2004), Pospischil et al (2009), Bédard et al (2011b), and Berg and Ditlevsen (2013), among others) assuming that data is following some underlying linear process.

Normally, the previous assumption involves a complementary treatment of the noise present in the data, which is the second main obstacle. Some experimental papers use strategies that consist of filtering the data before fitting them to the "minimal model" (Anderson et al (2000) and Borg-Graham et al (1998), among others). Other theoretical contributions have been mostly focused on the approach with Fokker-Planck equations to derive the mean and the variance of the whole temporal course for both the excitatory and the inhibitory inputs, see for instance Rudolph et al (2004). However, the main shortcoming, both of many experimental papers and the abovementioned theoretical methods, is the need for recording several membrane potential time courses assuming invariance of the conductances time courses across trials, which is the third main obstacle. However, to overcome such problems, the Fokker-Planck approach has been refined to avoid double recordings by using maximum likelihood estimators, see Pospischil et al (2009).

Recently, new efforts have been devoted to obtain direct estimations of the excitatory and inhibitory conductances: Bédard et al (2011b) takes advantage of oversampling the membrane potential with respect to the conductances time-scale, whereas other authors, see Kobayashi et al (2011), Paninski et al (2012), Berg and Ditlevsen (2013), Lankarany et al (2013a), Lankarany et al (2013b), Ditlevsen and Samson (2014) and Closas (2014), take advantage of statistical inference methods to extract on-line activity. In all these stochastic approaches, linear regression methods and maximum likelihood estimators are in order at some point of the procedure.

Despite of some excellent estimations obtained in particular circumstances, special in purely leaky subthreshold regimes, misestimations derived from the use of linear models have been reported (see Borg-Graham et al (1998) and Guillamon et al (2006)) in the spiking regime. Therefore, a fourth challenge, which is related to the type of minimal models to use, come into play. The problem is how to deal with the inverse estimation problem when the underlying model is no longer linear.

The basic reason for the misestimations in the spiking regime is that some nonlinear terms are active, and so even after filtering the membrane potential, the input-output relation is no longer linear. The problem could be spread also over non-spiking regimes as well, due to the eventual activity of subthreshold ionic channels, widely described from the eighties after seminal works as Hotson and Prince (1980). This nonlinear subthreshold activity cannot be discarded, even in the most careful experimental results on conductance estimation obtained up-to-date (see for instance Figure 6 in Rudolph et al (2004)). Of course, pharmacological blocks can reduce the activity of some targeted channels, but still it is actually difficult to completely reduce the neuron's activity to a pure passive filter.

Concerning mathematical approaches, models in dynamical systems, and specifically the

slow-fast ones, are useful to describe neuronal behaviours. The study of different aspects about these models (such as bifurcation diagrams, phase portraits, dynamics close to invariant manifolds, among others), can provide a more detailed knowledge about neuronal connections from where possible deterministic strategies can be extracted to estimate conductances. On the other hand, to tackle with possible noise from experimental recordings, the study of stochastic methods comes into play to reproduce, in a more realistic way, neuronal connections and so, new strategies can also be extracted by exploiting their resources.

Related to previous and open challenging problems, in this thesis, we basically aim to answer three main questions:

- *Are those misestimations on the spiking regime also presented in the subthreshold regime under the presence of subthreshold-activated ionic currents?*

- If misestimations in the subthreshold regime are relevant, *can we provide new strategies to overcome such problem having also into account, as much as possible, the rest of obstacles of the inverse methods?*

- *Can we also provide a first strategy to estimate conductances in those regimes where the target neuron presents an oscillatory behaviour?*

The answer to the three previous questions is mainly presented in Chapter 5, which is supported by chapters 3 and 4. These chapters are preceded by a background chapter (Chapter 1), devoted to introduce some basic concepts and tools that we are going to use in the three main chapters; and by a second chapter (the Chapter 2), which is dedicated to explain different mathematical models and data traces, used in this thesis to understand the behaviour of the brain and also to estimate conductances.

The three main chapters are entitled as *Slow-fast n-dimensional piecewise linear systems* (Chapter 3), *Effects of plasticity on synaptic conductances in a network with slow oscillations* (Chapter 4), and *Estimation of conductances in single point neurons* (Chapter 5), which is the nucleus of the current thesis, since it answers to the questions posed. Next we briefly explain each of them and the role they play in this thesis.

In Chapter 3 we deal with slow-fast dynamical piecewise linear differential systems, which are useful to reproduce neuronal behaviour. In the smooth context, the general frame to tackle the slow-fast behaviours is the geometric singular perturbation theory (GSPT), see Fenichel (1979) and Jones (1995). In the piecewise linear (PWL) framework, some elements of the GSPT can be explicitly obtained, which is an advantage. These elements give a more detailed knowledge not only of the model itself but also an insight on the smooth case. In this chapter, we analyse n-dimensional slow-fast systems in a piecewise linear framework. In particular, we prove a Fenichel's-like Theorem giving an explicit expression for the invariant slow manifold, that leads to the proof of existence and location of a special orbits, called maximal canards, which play an important role in defining thresholds, such as the spiking threshold (see Izhikevich (2007)). These results are already published in Prohens et al (2016).

Chapter 4 is intended to obtain information about synaptic conductances in a population of neurons. Here, we have been implemented a complex biophysical neuronal network, designed by Compte et al (2003), which describes the slow oscillations observed in the visual cortex and in which short-term plasticity has been added in order to see which are their effects in the synaptic conductances. Depression was already added by Benita et al

(2012) and we have incorporated a facilitation term. Part of the work done in this chapter has been developed in collaboration with Prof. Paolo Massobrio (DIBRIS at Università degli studi di Genova). Even though the work done in this chapter is just a numerical introduction to learn a little about conductances' changes in different short-term plasticity conditions, it opens new questions to be further investigated (see future work in Chapter 6).

Chapter 5 covers all procedures to estimate conductances that we have been developed along the thesis. Although they could be explained in different chapters, for their relevance in the thesis we decided to join them all inside a main chapter covering the core of the thesis. We split this chapter in two main sections: Section 5.1, which is dedicated to the estimation of conductances in the subthreshold regime; and Section 5.2, where the estimations of conductances are done in the oscillatory regime.

The first section of Chapter 5 is separated into two subsections. In Subsection 5.1.1, we study the influence of subthreshold activity in the estimation of synaptic conductances. We take advantage of conductance-based models to test this influence using several representative mechanisms to induce ionic subthreshold activity. In all the cases, we show that the currents activated during subthreshold activity can lead to significant errors when estimating synaptic conductances linearly. Thus, our results in this section add a new warning message when extracting conductance traces from intracellular recordings and the conclusions concerning neuronal activity that can be drawn from them. Additionally, we present an alternative method that takes into account the main nonlinear effects of specific ionic subthreshold currents. This method, based on a deterministic quadratization of the subthreshold dynamics, allows us to reduce the relative errors of the estimated conductances by more than one order of magnitude. This quadratization (see Rotstein (2015)) consists of a slow-fast system, and so we take advantage of its properties to proceed with the estimation procedure. Results in this chapter have been published in Vich and Guillamon (2015a).

The above deterministic approach accounts for the basic mechanisms but it does not pay special attention to the noise inherent to the experimental data. Next step was, then, to test the quadratization-based method in a stochastic environment. In Subsection 5.1.2, we extend the previous quadratic procedure to estimate synaptic conductances, based on a quadratization of a stochastic model that captures these nonlinearities in a more realistic framework, where noise is considered. In fact, we consider an stochastic version of the quadratic integrate-and-fire model, whose coefficients depend on the synaptic conductances. Then, the time course of the model coefficients is estimated by an approximate maximum likelihood procedure, which allows to estimate the time-varying excitatory and inhibitory conductances. A previous work in this subject is due to Berg and Ditlevsen (2013), whose authors have collaborated with us by providing experimental recordings and deep expertise about stochastic processes. This part of the chapter has been developed along my stay of research in the group of *Statistics and Probability Theory* at Københavns Universitet (Denmark, 2015/16), supervised and guided by Prof. Susanne Ditlevsen. A preprint of this work is already done to be submitted.

After providing some useful strategies to avoid conductances' misestimations in the subthreshold regime, in the second section of Chapter 5, we aim at giving a first proof-of-concept to address the estimation of synaptic conductances when a neuron is spiking. Our approach is based on a simplified model of neuronal activity, namely a piecewise linear version of the Fitzhugh-Nagumo model (see model Subsection 2.1.3.1). This simplified model allows an accurate knowledge of the nonlinear f-I curve by using standard techniques of nonsmooth dynamical systems. In the regular firing regime of the neuron's model, we ob-

tain an approximation of the period which, in addition, improves previous approximations given in the literature up-to-date. By knowing both this expression of the period and the current applied to the neuron, and then solving an inverse problem with a unique solution, we are able to estimate the steady synaptic conductance of the cell's oscillatory activity as well as to give good estimations when the synaptic conductance varies slowly in time. A preprint of this work is already done to be submitted.

General conclusions and future research proposals are provided in Chapter 6.

Figure 1 presents a conceptual diagram of the structure of this thesis and the relationship among chapters.
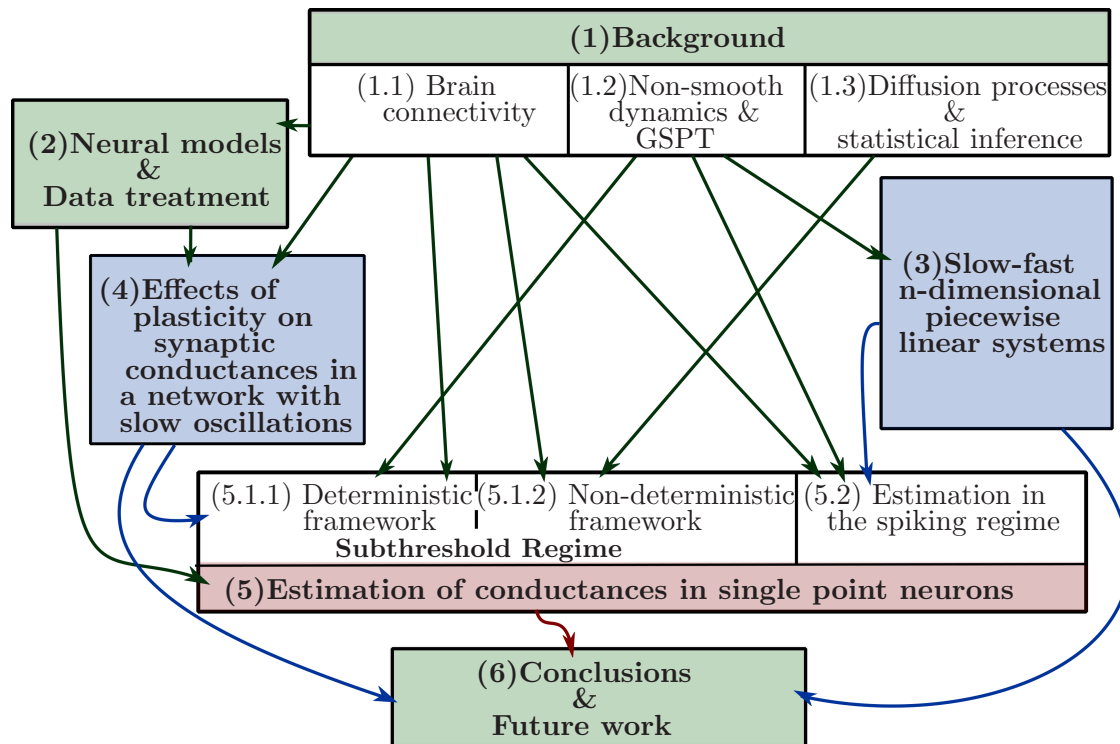

Figure 1: **Organization of the different chapters in the thesis**. Conceptual diagram explaining the relationship among the different chapters and how they are distributed. The numbers in the parentheses indicate the enumeration of chapters and sections. Green boxes represent introductory chapters whereas blue boxes depict the secondary chapters of results and the red box is the nucleus chapter of the thesis. The acronym GSPT stands for Geometric Singular Perturbation Theory.

Along the development of this thesis, I have also been attending the winter schools about dynamical systems called *Recent Trends in Nonlinear Sciences (RTNS)* from 2011 to 2013, held by the DANCE network, from who I received different grants to attend the all the schools; the summer school in computational neuroscience called *Advances Course in Computational Neuroscience (ACCN 2013)* at the Mathematical Research and Conference Centre (MRCC), Bedlewo (Poland), which has been supported by the Departament de Ciències Matemàtiques i Informàtica. And finally, from the stochastic point of view, I have also attended the summer school on *Foundations and Advances in Stochastic Filtering (FASF)* in 2015, which formation has been complemented with my stay of research in the Københavns Universitet, at the section of *Statistics and Probability Theory*. A stay of research has been done in the Università degli studi di Genova to work in the problem of computational neuronal networks.

All work presented in the thesis has been presented in some conferences and workshops. Results in Chapter 3, have been presented in the *10th AIMS Conference on Dynamical systems, Differential Equations and Applications (2014)*. At this conference, we have obtained the recognition of *outstanding student research paper quality and originality in the field of differential equations and dynamical systems* given by *The American Institute of Mathematical Sciences* (AIMS).

The preliminary results in Chapter 4 have been presented at the annual meeting *Computational Neuroscience (CNS 2014)*, held by the *OCNS organization* in Québec City. I received a grant from the organization of the congress to attend this meeting.

Results in Section 5.1.1 have been presented in some conferences and workshops. These meetings are, in a chronological order, *Barcelona Computational and Systems Neuroscience (BARCSYN 2013)*, in Barcelona; *Computational Neusociences (CNS 2013)*, in París at the Université Paris Descartes; the *10th AIMS Conference on Dynamical systems, Differential Equations and Applications (2014)*, in Madrid; *International Workshop on Neurodynamics (Ndy14)*, in Castro Urdiales at the Centro Internacional de Encuentros Matemáticos (CIEM); *BARCSYN 2014*, in Barcelona; and *CNS 2014*, in Québec city and held by the *OCNS organization*. I received a grant from the organization of the congress to attend this meeting.

Results in Section 5.1.2 have been accepted to be presented in Antibes-Juan Les Pins, France, at the *2nd International Conference on Mathematical NeuroScience (ICMNS 2016)*.

Results in Section 5.2 have been presented at the *CNS 2015*, in Praga; *BARCSYN 2015*, in Barcelona; and at the conference *Open problemes in nonsmooth dynamics*, in Barcelona, held by the Centre de Recerca Matemàtica (CRM).

Finally, I have been invited to present all work done in Chapter 5 in the *1st Workshop on Dynamical Systems in the Real Life (RDS 2016)* at Castelló, and it has also been accepted at the *10th European Conference on Mathematical and Theoretical Biology (ECMTB 2016)* held in Nottingham.

Chapter 1

Background

In this chapter, we introduce background concepts about neuroscience and mathematics. In particular, we explain basic facts regarding three different topics: connectivity in the brain, geometric singular perturbation theory and non-smooth dynamics, and, finally, stochastic processes and statistical inference. Once these topics are combined, they can explain relevant information about the behaviour of the brain and its working mechanisms. In our case, they also provide us with tools to elaborate inverse methods to make estimations about unknown parameters.

Despite the large amount of information available about these topics, we will focus on those concepts and theories directly involved with the aim and the development of our work. In the first section, we introduce some morphology about the neuron and we explain both the interaction between neurons, the synapse, and the functionality of a single neuron. An overview about changes on the strength of connection between neurons is also provided at the end to introduce the concept of plasticity. For a further detailed explanation on these topics we refer the reader to Rubin and Terman (2000), Dayan and Abbott (2005), Izhikevich (2007), and Ermentrout and Terman (2010) for an overview in modelling; and to Kandel et al (2013) for neurophysiology details.

Next section mainly focuses on two different types of systems that are often used to model the behaviour of the neurons: slow-fast systems and piecewise systems. The more relevant models for us are fully described in Chapter 2. In this chapter we only want to provide to the reader some important theorems, Fenichel's theorem and Llibre et al (2013) theorem; the concept of maximal canard orbits; and a brief explanation about piecewise systems providing the Filippov's convention to describe the flow on common boundaries. To learn more about these topics, we address the reader to Fenichel (1979), Filippov (1988), Jones (1995), Desroches et al (2012), Llibre and Teruel (2013), and Kuehn (2015).

Because the data obtained from experiments contains some noise, stochastic models are often used to elaborate more realistic neuronal models as well as to estimate parameters using statistical inference. In the last section of this chapter, we introduce the concept of stochastic process, given some examples of them; we explain the numerical tools we are using to solve stochastic differential equations (SDE); and finally the maximum likelihood estimator is described as a tool to estimate parameters in SDE. For further detailed see Wilkinson (2006), Ditlevsen and Samson (2013), and Berglund and Gentz (2008). In Chapter 3 of the last reference, N. Berglund and B. Gentz explain a comparison between stochastic and deterministic slow-fast theory, which we are not going to present here.

1.1   Brain connectivity

A human brain is formed, on average, by 84-100 billions of neurons. Neurons are important cells due to their ability to process and transmit information through electrical and chemical signals. These signals are called *action potentials* or, shortly, *spikes*, which are propagated over long distances and from one neuron to another.

In 1887, S. Ramón y Cajal proposed the *neuron doctrine* when, using the Golgi's method, he discovered the morphology and the connectivity between cells of the nerve system (called neurons by H.W.G Waldeyer in 1891). This method consists of using potassium dichromate and silver nitrate to randomly blemish few neurons that become dark black coloured, and so, visible for the microscope. In Figure 1.1 we can see a drawing by Ramón
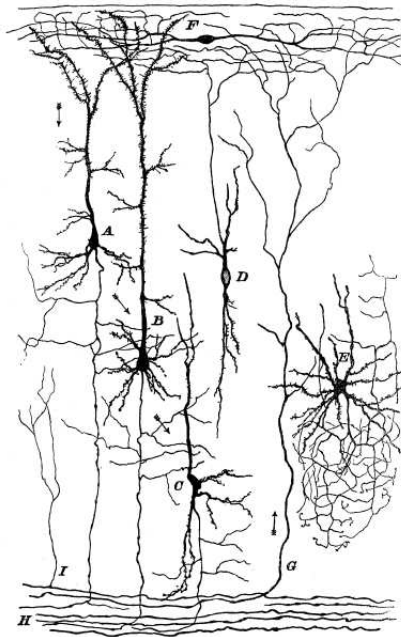

Figure 1.1: **The principal type of cells in the cerebral cortex of mammals.**. Drawing by Ramon y Cajal of different type of cells (each one enumerated by a different letter). Arrows represent the possible direction of the action potentials (also known as nerve impulses). Representation from Ramon y Cajal (1894)

y Cajal of the principal type of cells in the cerebral cortex of mammals. There, each neuron is labelled with a letter and the arrows represent a possible flow of the action potentials.

Even though there exists a large number of neurons in the brain and a multiple number of connections, a single neuron typically has three remarkable parts: the cell body, called *soma*, which contains the nucleus of the neuron; the *dendrites*, which are receptive input devices since they receive the information that comes from other cells; and the *axon*, which is the sending output device since from there the neuron sends information to the others.

Synapse

The transmission of information (activated by action potentials) from one cell to another receives the name of synapse (coined by C. Sherrington 1897) and it consists of an exchange of voltage between the transfer neuron, called *pre-synaptic neuron*, and the receiver neuron,

called *post-synaptic neuron.* There exist two different types of synapses: the chemical synapses, where neurotransmitters or other chemicals are released; and the electrical ones, where ions are transferred. The current that a neuron receives from the others is called *synaptic current.*

In the *chemical synapse*, the action potential comes from the terminal part of the axon of the pre-synaptic neuron to the dendrite (a part of it called spine) of the post-synaptic neuron. In this synapse, the two implicated neurons are not in touch; there exists a small gap between the axon of the pre-synaptic neuron and the dendrite of the post-synaptic where the synapse occurs, see Figure 1.2.

The terminal axon of a pre-synaptic neuron contains small vesicles that enclose different kinds of neurotransmitters inside such as Glutamate and GABA[1]. These neurotransmitters are released to the synaptic gap where they interact with receptors located in the spines of the dendrites of the post-synaptic neuron. These receptors allow the entrance of neurotransmitters inside the cell causing either an increase, decrease or non-response in voltage. There are different types of receptors and they only bind with a specific type of neurotransmitter. The receptor types for glutamate are called AMPA[2] and NMDA[3], whereas the receptors of GABA are called $GABA_A$[4] and $GABA_B$[5] receptors. In order to distinguish between the glutamate neurotransmitter that blinds to the AMPA or the NMDA receptor, we will call the neurotransmitter as the corresponding receptor that it joins. In Figure 1.2, we draw a representation of the chemical synaptic mechanism. For further details on chemical synapses and both neurotransmitters and receptors, see
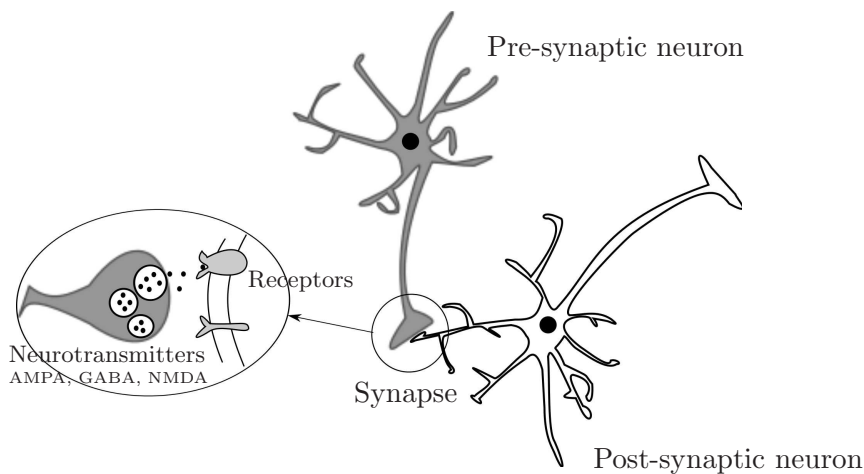

Figure 1.2: **A representation of the chemical synapse.** Drawing of a chemical synapse between two neurons. The grey neuron is considered to be the pre-synaptic neuron and the white one the post-synaptic neuron. The zoom in the synaptic gap shows the vesicles (while balls) inside the terminal axon (coloured in dark gray) of the pre-synaptic neuron containing the neurotransmitters (black dots), which are delivered to the synaptic gap and bound to the receptors (coloured in light gray) of the post-synaptic neuron.

Kandel et al (2013) Ch.12-15.

---

[1]GABA is the acronym of γ-aminobutyric acid. Both glutamate and GABA are the major excitatory and inhibitory transmitters, respectively, in the brain.

[2]AMPA is the acronym of α-amino-3-hydroxy-5-methyl-4-isoxazolepropionic acid, which is fast activating and deactivating.

[3]NMDA is the acronym of N-methyl-D-aspartate, which activates and deactivates slower than AMPA.

[4]$GABA_A$ produce a relatively fast Cl^- entrance.

[5]$GABA_B$ produce a slower and longer lasting K^+ entrance.

In the *electrical synapses*, the two involved neurons get extremely close and they get linked together by specific channels that connect the cytoplasm of the two cells. These channels, also called *gap junctions*, permit the flow of current directly from one neuron to the other. Most of the electrical synapses are bi-directional and they represent a minority of all the synapses. In Figure 1.3, we draw a representation of the electrical synaptic mechanism.
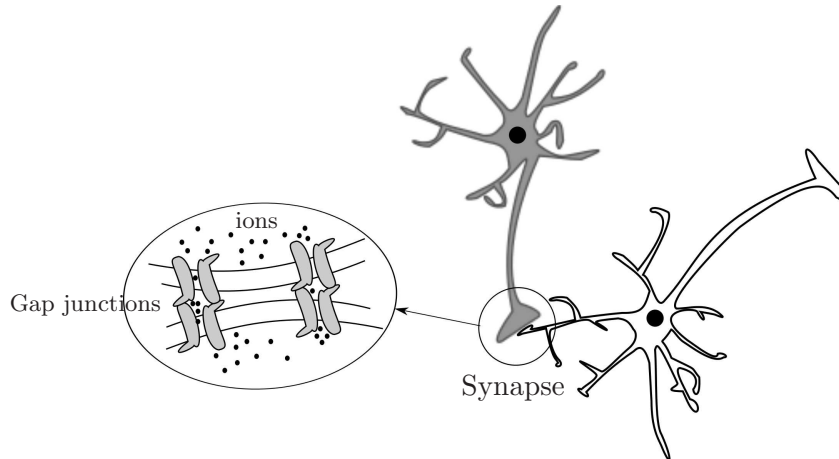

Figure 1.3: **A representation of the electrical synapse.** Drawing of an electrical synapse between two neurons. Since most of the times this synapse is bi-directional, we do not distinguish in the plot between pre-synaptic and post-synaptic neurons. The zoom in the synaptic gap shows the gap junctions (coloured in light gray), binding the two membranes, where ions (black dots) move forward or in both directions.

Ionic currents

Along the membrane, neurons contain different integral membrane proteins functioning as pores, called ion channels. These pores allow the flow of specific ions through the cell membrane, which can go inward or outward the cell, causing different responses to the neuron. The most predominant ions are sodium (Na^+), potassium (K^+), calcium (Ca^{2+}) and chloride (Cl^-).

Ion channels help to establish and control the small voltage gradient across the membrane of cells. They have a sensor acting as a gate that it is opened or closed in response to the external and internal voltage changes, regulating in that way the incoming and out-coming of ions. These gates are modelled by the so called *gating variables* and the total amount of current entering to the neuron through the ionic channels is called *ionic current*.

Depending on the processes involved on the ion channels, they can be open persistently or transiently. Channels that are persistently opened have only one activation mechanism (or gate) n to open and close the channel (see Figure 1.4A). When this gate opens, it is called *activation* and the closing of this gate is called *deactivation*. On the other hand, channels transiently opened are characterized to have a blocker mechanism to inactivate the entrance of ions; and so they have two different gates (or processes) with opposite voltage dependences: an opening mechanism m and a blocking mechanism h (see Figure 1.4B). The gate m works in a similar manner to the gate n, in the persistent case, whereas h (represented as a ball in Figure 1.4B) is inactivated or deinactivated by opposite voltage. That is, when voltage inside the neuron increases, gate m opens while gate h closes; and when the voltage decreases, m closes while h opens. As for the n gate, when m opens, it

is called activation and when it it closes is called deactivation; however, when h is opening it is called *deinactivation* while, when it is closing it is called *inactivation*, to distinguish between m and h.
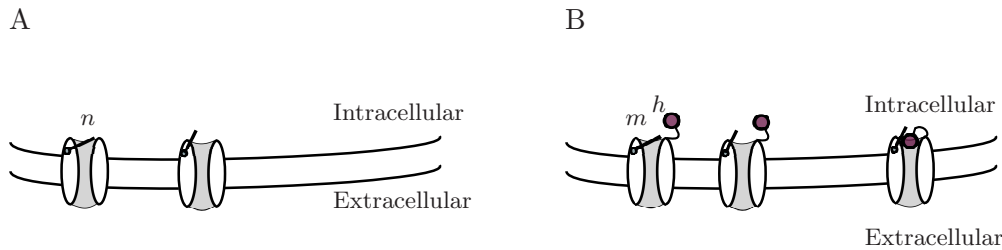

Figure 1.4: **A representation of different ion channels.** Drawing of different ion channels depending on the number of opening and closing mechanisms. Panel A represents a channel with one gating variable allowing the pass of current through the membrane (right channel) or not (left channel). Panel B represents a channel with two gating variables, an activation gate (line gate) and an inactivation gate (ball gate), allowing the pass of current through the membrane (central channel) or not (left and right channels).

Membrane potential changes

The difference of concentration of ions (voltage) between the interior of the cell and the exterior is called the *membrane potential*, which depends on time since the cell is continuously receiving information from other neurons or stimulated by external inputs (such as an image, a taste, a touch, ...).

When a neuron does not receive current neither from other cells nor from the surrounding bath, that is under resting conditions mentioned, neuron tends to maintain an equilibrium between the voltage that there exists inside the cell and the voltage outside. The driving source to maintain the equilibrium is called the *leak current* and, in this case, the membrane potential of a neuron tends to be approximately $-70\ mV$.

However, despite neurons may tend to an equilibrium state, their membrane potential varies depending on the type of ions and neurotransmitters that go inward or outward the cell. When the membrane potential increases is said *depolarization* and when it decreases is said *hyperpolarization*.

According to the ionic currents, the membrane potential is hyperpolarized when positively charged ions are flowing out the neuron (or negative ones flow in) and so the membrane potential becomes more negative; on the contrary, it is depolarized, when negatively charged ions leave the neuron (or positive ones enter) which produce the membrane potential to be more positive. Ion channels are the responsible for maintaining the membrane potential at the resting state of approximately $-70\ mV$; consequently, when other currents come from the environment or from others cells to alter the resting state of the neuron, ion channels open or close according to the value of the membrane potential and the type of ions that they allow to flow.

When the neuron is subjected to a synaptic current, and so to bombardments from other cells, the post-synaptic neuron can respond differently according to the type of the neurotransmitters. For the ones we are interested in, which are AMPA, GABA and NMDA, we have that both AMPA and NMDA cause an increment of the membrane potential (depolarization) of the post-synaptic neuron, that is, the neuron gets excited and so we have

an *excitatory post-synaptic response*. However, for the GABA neurotransmitter, the post-synaptic response leads to a decrement (hyperpolarization) of the membrane potential, where the neuron is inhibited and so we have an *inhibitory post-synaptic response*.

As a result of the post-synaptic response, we can split the synaptic current into two parts: the *excitatory synaptic current*, which is the current coming from an excitatory pool of neurons causing depolarizations of the membrane potential of the post-synaptic neuron; and the *inhibitory synaptic current*, which is the current coming from an inhibitory pool of neurons causing hyperpolarizations of the membrane potential of the post-synaptic neuron.

Sometimes it happens that a neuron is sufficiently depolarized, in such a way that the membrane potential reaches some threshold level causing a dramatic increment of the membrane potential, which becomes positive. Right after, a response mechanism is activated allowing the entrance of negatively charged ions to hyperpolarize the membrane potential in order to maintain the equilibrium mentioned before. In this case a spike (action potential) is generated spanning around 100 mV and lasting for approximately 1 ms.

Although an instantaneous pulse of current can generate a spike, the recent history of voltage changes is also involved in the generation of spikes. It is possible that a specific pulse of current is not able to cause any reaction to the neuron; however, after successive pulses of current, although the neuron tends to return to the resting state, the new pulses are added to the membrane potential causing possible spikes. Moreover, few milliseconds right after a spike has been generated, some currents that are incapable to initiate another spike can be still active under the threshold (that is, in the subthreshold). This interval of time, where ions remain active, is called the *absolute refractory period*. In this case, for a longer interval of time, lasting up to tenths of milliseconds after the spike, neuron is prevented from spiking again. This period is called the *relative refractory period*.

Membrane capacitance and reversal potentials

The cell membrane can be seen as an insulator of the membrane potential generated by the inflow of ions, neurotransmitters or other chemicals. The ability of the neuron to store charge of ions across the cell membrane is called *membrane capacitance*. In this work, we consider the membrane capacitance as a measure of the changes to membrane surface area, measured by $\mu A/cm^2$, unless otherwise is stated.

However, as we have seen, even though the membrane acts as a perfect electrical insulator, the cell membrane contains the ion channels allowing the flow of ions through the membrane. When the concentration of a specific ion is at the equilibrium state, that is when these ions are neither entering or leaving the neuron, the difference in concentration of these ions outside and inside the cell is called the Nerst potential or equilibrium potential. If the membrane potential is lower than this value, the specific gates are opened allowing the entrance of ions; but if the membrane potential is higher, then ions would flow out of the cell and so the direction of the flow is reversed. Then the Nerst potential is also called as *reversal potential*.

Conductances

Apart from the membrane capacitance, holding the membrane potential to a different level from the resting one requires a certain level of current, which is determined by the membrane resistance. The inverse of the membrane resistance is called the *conductance*. We consider three different types of conductances according to the type of current: the leak conductance, the ionic conductances and the synaptic conductances.

The *leak conductance* (g_L), also called passive conductance, is a value regulating the membrane resistance at the resting state to match the membrane resistance with the membrane capacitance. In general, we will take this value as constant.

The *ionic conductance* ($g_{ion}(t)$) relates to the amount of ions allowed to cross through a specific ion channel. Ionic conductances are voltage-dependent and they are modelled as

$$g_{ion}(t) = \bar{g}_{ion} P_{ion}(t),$$

where $P_{ion}(t)$ is the probability of activation or inactivation of the specific ion channel and $\bar{g}_{ion}$ is the maximal conductances allowed, which is considered to be constant. Unless otherwise is stated, along the thesis, in the case of ionic currents, we call ionic conductances to the maximal ones and we denote them by g_{ion} instead of $\bar{g}_{ion}$, in order to simplify notation.

Depending on the opening mechanism, as we have explained for the ion channels, this kind of conductances are also called persistent or transient ionic conductances. In the persistent ones only one gating variable n is considered at each channel and so $P_{ion}(t) = n^k(t)$, where k is the number of independent gating events and $n(t)$ describes the opening and closing of gate n. Similarly, in the transient case, since two processes with opposite voltage dependences are considered (an opening mechanism m and a non-blocking mechanism h), then $P_{ion}(t) = m^a(t)h^b(t)$, where a and b are the number of independent gating events, and both different from 0. Variables $m(t)$, $n(t)$ and $h(t)$ are considered to be probabilities such that 0 means that the are completely closed and 1 that they are completely open (see Section 2.1.2 for more details).

The *synaptic conductances* ($g_{syn}(t)$) describe the amount of information that the neuron is receiving from other neurons, providing an understanding of the connectivity in the brain. The estimation of these conductances is the main goal of this thesis.

Focusing only on the chemical synapses, we have seen that, when a synapse occurs, neuro-transmitters are released to the synaptic gap and they bind to the receptors. This binding leads to the opening of ion channels to modify the conductance of the post-synaptic neuron to complete the transmission of the action potential. Hence, the synaptic conductances can be modelled as the product of a maximal conductance ($\bar{g}_{syn}$) and the probability of the channel to be opened. The open probability depends on the pre- and post-synaptic neuron, and it can be split as the product of the probability of release (P_{rel}), which is the probability of a neurotransmitter to be liberated at the synaptic gap, times the synaptic strength variable (s), which is the probability of the post-synaptic neuron to open the channel. That is,

$$g_{syn}(t) = \bar{g}_{syn} s(t) P_{rel}(t).$$

Depending on the neurotransmitters and the receptors involved in the synapse, we have mentioned above that the change of current can be either excitatory or inhibitory, according to the post-synaptic response. Consequently, conductances can also be split into

excitatory conductances, when current comes from excitatory neurons causing an excitatory post-synaptic potential (EPSP), or *inhibitory conductances*, when current comes from inhibitory neurons causing an inhibitory post-synaptic potential (IPSP).

Plasticity

The term *plasticity* refers to the brain's ability to change throughout life, underlying memory and learning. Changes on the brain are related to changes on the synaptic strength. The effects of activity on the synaptic conductances can be given either for a short or a long term. Short-term plasticity (STP) refers to changes on the brain lasting from milliseconds to seconds or even a couple of minutes; on the other hand, the long term plasticity (LTP) refers to changes on the brain lasting for hours or even more. LTP is usually associated to the consolidation of the memory.

Depending on the effects on the strength of the synaptic conductances, plasticity can be either short (long) term depression, STD (LTD), or short (long) term facilitation, STF (LTF). *Depression* occurs due to a decrease in the readily releasable pool of vesicles (RRP) as a result of frequent stimulation, thus weakening the synapse. However, the *facilitation* is given by an increment of the probability of neurotransmitter release from the pre-synaptic membrane caused by the presence of residual Ca^{2+}, which strengthens the synapse (see the synaptic drive description in Section 2.1.4, for more details about STD, STF and how they are modelled).

Figure 1.5 shows the effects of the short-term depression (panel A) and short-term facilitation (panel B) on the voltage of an excitatory neuron when the full network has been depressed and facilitated respectively. Comparing these results (red lines) to the control voltage trace (black line) when neither depression nor facilitation has been added, one can see the effects of both plasticity mechanisms. Panel A shows that depression causes less
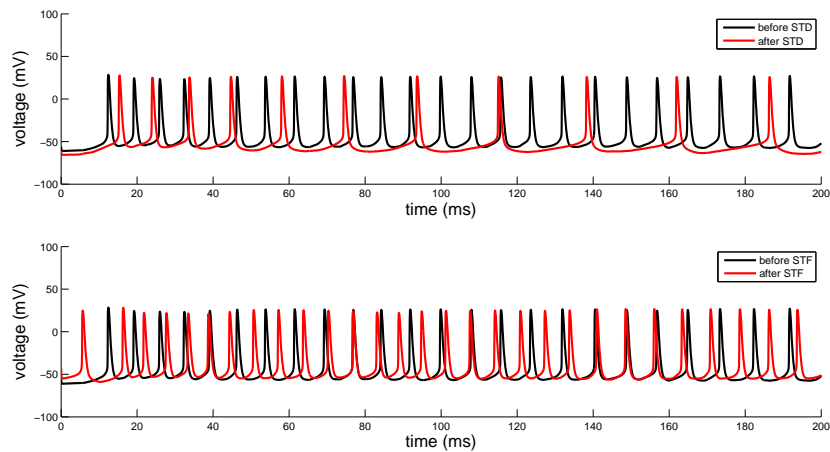
Figure 1.5: **A representation of the effects of the short-term plasticity.** Panel A depicts the effects of the short-term depression whereas panel B depicts the effects of the short-term facilitation. The traces represent the voltage of an excitatory neuron coming from the computational network described in Section 2.1.4. Black lines show the voltage of the neuron when network is neither depressed nor facilitated, and red lines show the voltage when depression (panel A) and facilitation (panel B) have been added.

spikes to the membrane potential presenting also a delay on the timing of the first spike

whereas, as it is shown in panel B, facilitation causes an increment of activity displaying an anticipation of the first spike.

Electrophysiological techniques

In electrophysiology, different techniques have been developed in order to obtain different measurements from neurons. These measurements involve voltage changes (the membrane potential) and electric currents through the ion channels.

Classical measurement techniques are based on the insertion of a pipette (whose diameter is less than one micrometer) into a single cell. This pipette has a hole at the contact corner with the neuron, which together with the cell membrane make a seal containing one or more ionic channels in its interior. The pipette also contains an electrode and when such electrode is in contact with the neuron, it leads the electric current to an amplifier. Moreover, the pipette is filled by a specific solution (or electrolyte) in accordance to the ionic composition of the extracellular or intracellular medium. Therefore, an electrode circuit is created to record the membrane potential or the ionic currents through the selected ion channels. Depending on the specific technique, different seals are done and different recordings are extracted. Other techniques, which are applied to the brain and commonly used in medicine, consist also on electrodes to make the recordings but without the necessity to insert the electrode inside the neuron such as the electroencephalography (EEG) or the electrocorticography (ECoG).

However, since we are interested in direct measurements from a single neuron, that is *intracellular recordings*, we need to insert the electrode inside the neuron. The patch can be done without damaging the cell membrane, as the cell-attached technique explained above, where only a seal is made; or by perforating the cell membrane. A first perforating variation is the *whole-cell patch*, where the cell membrane is broken under the seal allowing that the concentration on the pipette gets in contact to the cytoplasm solution, to finally replace it. With this kind of seal, the total current through all the ion channels can be recorded and not only the ones inside the pipette. Another variation is the *perforated-cell patch*, which is a version of the whole-cell patch where the hole in the membrane is done by a pharmacological agent. In this way, one can better control the intracellular medium to prevent, or at least minimise, possible losses of important components of the intracellular fluid.

Different techniques to do intracellular recordings are: the voltage clamp, the current clamp and the patch clamp.

Voltage clamp technique allows to record ionic currents through the membrane while the voltage is fixed to a certain value, which is chosen by the experimenter. Voltage can be fixed through the electrode injected to the neuron.

Current clamp technique allows to record the membrane potential by injecting a specific current into the neuron through the electrode inside the pipette. In this case, voltage is not fixed by the experimenter and so it is free to vary; and the amplifier records the membrane potential that the neuron generates on its own as a result of the injected current. Usually the injected current is considered to be a constant current or pulses of currents (see experimental recordings in Berg and Ditlevsen (2013)), but one can also fixed the conductance and compute the current we need to inject according to the output voltage; in this case, the technique receives the name of *dynamic clamp* (see experimental recordings in Bédard et al (2011b)).

Both voltage and current clamp techniques do not usually perforate the cell membrane.

Patch clamp technique can be applied in different ways: using the cell-attached configuration or either the whole-cell or preforated-cell configurations. In any case, the experimenter can maintain the voltage of the cell membrane to a constant value while changes on the currents are observed or, they can maintain the current while the membrane potential changes are observed. This technique allows to study the ionic channels at different levels: single ionic currents (with the cell-attached configuration) or the total ionic channels activity (with the whole-cell or perforated-cell configurations). Moreover, it also allows to easy manipulate the extracellular or intracellular fluid of the neuron during the realization, by changing the fluid of the pipette, since it has contact to the cytoplasm of the cell.

We refer to the reader to Molleman (2003) for more details on these electrophysiological techniques and, in particular, the patch clamp technique.

In order to record neural signals from a network of neurons, and not only from a single cell, some devices as the multielectrode arrays (MEAs) as been developed. In the MEAs case, multiple electrodes are inserted, at the same time, to different neurons and the individual membrane potential are recorded, which can then be compared to the information extracted from others cells directly connected or not.

A remarkable fact of all the existing techniques is that we can extract information about the time course of the membrane potential and the ionic currents. Moreover, these techniques allow us to obtain the relationship between the steady-state of the voltage for different applied currents; that is, the $V - I$ *curve*. Experimentally, to compute the $V - I$ curve, neurophysiologists usually consider the mean value of the recorded voltages in a time interval, in absence of synaptic inputs. On the other hand, when the neuron presents oscillations, the $f - I$ *curve* can also be extracted, where f refers to the frequency of oscillation.

However, as we have mentioned in the introduction, no electrophysiological techniques are known to record the synaptic conductances. Hence, inverse methods can be used to estimate them.

1.2 Non-smooth dynamics and Geometric Singular Perturbation theory

Dynamical systems applied to neuroscience allow to describe the behaviour of the neurons and how they interact. As we have seen in the previous section, neurons contain different gating variables that regulate the flow of ions, depending on the instantaneous membrane potential. Both, the gating variables and the membrane potential, depend on time and they can be modelled by differential equations describing their changes on time (see Chapter 2). The time scales on which these variables are expressed are, usually, very different. For instance, the gating variables evolve very slowly compared to the membrane potential evolution. This fact, among others, leads us to model the neurons by using slow-fast differential systems. We remark that this kind of systems are useful to describe behaviours combining variables with different time scales.

On the other hand, piecewise linear systems have been proven to be useful to describe realistic non-linear behaviours in more manageable way for computations (See Chapter 2).

Focusing on the membrane potential recordings, two main different behaviours are present: spiking regimes, where the neuron is constantly presenting action potential (that is, a firing state or tonic) and subthreshold regimes, where neuron does not exhibit any spike (that is, the silent state). These two different regimes are given in systems allowing, by changing a bifurcation parameter, the possibility to combine high and low oscillations. This parameter plays an important role in defining the neuron threshold (see Izhikevich (2007)).

Next we introduce the above mentioned differential systems (the slow-fast and the piece-wise differential systems) stating, in both cases, the useful properties that they provide us to develop our results. Moreover, we also introduce special orbits, called *maximal canard orbits*, that are involved in defining thresholds.

Geometric Singular Perturbation theory

Slow-fast systems are differential systems evolving on at least two different time scales. The standard form to present this kind of systems, when two time scales are considered, is

$$\dot{\mathbf{u}} = \frac{d\mathbf{u}}{dt} = \varepsilon \mathbf{g}(\mathbf{u}, \mathbf{v}, \varepsilon), \qquad \dot{\mathbf{v}} = \frac{d\mathbf{v}}{dt} = \mathbf{f}(\mathbf{u}, \mathbf{v}, \varepsilon), \tag{1.1}$$

where $\mathbf{u} \in \mathbb{R}^s$ is the slow variable, $\mathbf{v} \in \mathbb{R}^q$ is the fast variable, $\mathbf{f}$ and $\mathbf{g}$ are sufficiently smooth functions, and $0 < \varepsilon \ll 1$ is a small parameter representing the ratio of time scales. After reparametrizing the orbits by the slow time $\tau = t\varepsilon$, system (1.1) can be rewritten in the differentially equivalent form

$$\mathbf{u}' = \frac{d\mathbf{u}}{d\tau} = \mathbf{g}(\mathbf{u}, \mathbf{v}, \varepsilon), \qquad \varepsilon \mathbf{v}' = \varepsilon \frac{d\mathbf{v}}{d\tau} = \mathbf{f}(\mathbf{u}, \mathbf{v}, \varepsilon). \tag{1.2}$$

Geometric Singular Perturbation Theory (GSPT) is based on a geometric point of view to study slow-fast systems, focusing on normal forms for singularities, invariant manifolds, and the analysis of their unfoldings (see Fenichel (1979) and Jones (1995), among others). Fenichel (1979) paper was the pioneer to study the invariant manifolds using GSPT, reason why it is also called Fenichel's theory. That is, GSPT theory allows the analysis of the dynamics of system (1.1), when $\varepsilon \neq 0$, by combining the behaviour of the corresponding limiting problems given by $\varepsilon = 0$ in (1.1) and (1.2). In particular, under normal hyperbolicity conditions, this theory ensures the persistence of the *critical manifold* $\mathcal{S} = \{(\mathbf{u}, \mathbf{v}) \in \mathbb{R}^n : \mathbf{f}(\mathbf{u}, \mathbf{v}, 0) = \mathbf{0}\}$ of the *fast subsystem* (also called *layer problem*)

$$\dot{\mathbf{u}} = \mathbf{0}, \quad \dot{\mathbf{v}} = \mathbf{f}(\mathbf{u}, \mathbf{v}, 0), \tag{1.3}$$

as a manifold, $\mathcal{S}_\varepsilon$, locally invariant under the flow of system (1.1). Moreover, the stability properties of the manifold $\mathcal{S}_\varepsilon$ are inherited from those of the critical manifold $\mathcal{S}$, and the restriction of the flow of system (1.1) to $\mathcal{S}_\varepsilon$ is a regular perturbation of the *reduced flow*; that is, the flow of the *slow subsystem* (also called the *reduced problem*)

$$\mathbf{u}' = \mathbf{g}(\mathbf{u}, \mathbf{v}, 0), \quad \mathbf{0} = \mathbf{f}(\mathbf{u}, \mathbf{v}, 0), \tag{1.4}$$

which is an algebraic differential equation.

From previous considerations and since the time variable in the former system is the slow one, manifold $\mathcal{S}_\varepsilon$ is called *slow manifold*; that is, an invariant manifold such that, considering the fast scale, the speed of the orbits on this manifold tends to 0 as ε tends to 0.

The existence and the behaviour of the flow on and surrounding the slow manifold is stated in next result, the so called Fenichel's Theorem. The version we present here is extracted from Desroches et al (2012). See also Kuehn (2015).

Theorem 1.1 (Fenichel's Theorem, Fenichel (1979)). *Suppose $\hat{\mathcal{S}}$ is a compact normally hyperbolic submanifold (possibly with boundary) of the critical manifold $\mathcal{S}$ of system (1.1) and that f, $g \in \mathcal{C}^r$; $r < \infty$. Then for $\epsilon > 0$ sufficiently small, the following holds:*

a) *There exists a locally invariant manifold $\mathcal{S}_\epsilon$ diffeomorphic to $\hat{\mathcal{S}}$, where local invariance means that $\mathcal{S}_\varepsilon$ can have boundaries through which trajectories enter or leave.*

b) *$\mathcal{S}_\varepsilon$ has a Hausdorff distance of $O(\varepsilon)$ from $\hat{\mathcal{S}}$.*

c) *The flow on $\mathcal{S}_\varepsilon$ converges to the slow flow as ε tends to 0.*

d) *$\mathcal{S}_\varepsilon$ is $\mathcal{C}^r$-smooth.*

e) *$\mathcal{S}_\varepsilon$ is normally hyperbolic and it has the same stability properties with respect to the fast variables as $\hat{\mathcal{S}}$, i.e attracting, repelling or saddle type.*

f) *$\mathcal{S}_\varepsilon$ is usually not unique. In regions that remain at a fixed distance from the boundary of $\mathcal{S}_\varepsilon$, all manifolds satisfying (a)-(e) lie at a Hausdorff distance $O(e^{-K/\varepsilon})$ from each other for some $K > 0$ with $K = O(1)$.*

The normally hyperbolic manifold $\hat{\mathcal{S}}$ has associated local stable and unstable manifolds

$$W_{loc}^s(\hat{\mathcal{S}}) = \bigcup_{p \in \hat{\mathcal{S}}} W_{loc}^s(p) \quad \text{and} \quad W_{loc}^u(\hat{\mathcal{S}}) = \bigcup_{p \in \hat{\mathcal{S}}} W_{loc}^u(p)$$

where $W_{loc}^s(p)$ and $W_{loc}^u(p)$ are the local stable and unstable manifolds of p as a hyperbolic equilibrium of the layer equations, respectively. These manifolds also persist for $\varepsilon > 0$ sufficiently small: there exist local stable and unstable manifolds $W_{loc}^s(\hat{\mathcal{S}})$ and $W_{loc}^u(\hat{\mathcal{S}})$, respectively, for which conclusions (a)-(f) hold if we replace $\mathcal{S}_\varepsilon$ and $\hat{\mathcal{S}}$ by $W_{loc}^s(\mathcal{S}_\varepsilon)$ and $W_{loc}^s(\hat{\mathcal{S}})$ (or, similarly, $W_{loc}^u(\mathcal{S}_\varepsilon)$ and $W_{loc}^u(\hat{\mathcal{S}})$).

Then, $\mathcal{S}_\varepsilon$ is called a *Fenichel manifold* and, all the possible Fenichel manifolds represent a subclass of slow manifolds.

Canard orbits

When normal hyperbolicity fails, for instance on the fold manifold (i.e. points where $\mathcal{S}$ folds), the critical manifold can be formed by branches with different stability properties. Consequently, from Fenichel's Theorem, different stability branches for the slow manifold $\mathcal{S}_\varepsilon$ also appear. Therefore, under suitable conditions, there exist orbits closely following the attracting branch of the slow manifold, then passing close to the fold manifold, and finally moving close to the repelling branch of the slow manifold. These orbits are called *canard orbits* and they play a crucial role in explaining the complex slow-fast dynamics. See Desroches et al (2012) and references therein, for instance. When these orbits closely pass from the repelling branch to the attracting one, they receive the name of *faux canard orbits*.

In the planar case, canard orbits have been reported as periodic oscillations whose amplitude and period grow in a highly nonlinear manner; that is, for a control parameter,

these oscillations vary slowly except for an exponentially small range of values, where they suddenly grow extremely fast. This abrupt growth is called *canard explosion* and it can be observed near to the Hopf bifurcation, see Krupa and Szmolyan (2001) and Dumortier and Roussarie (1996).

Canard orbits were first reported in Benoît et al (1981), where authors studied the $2D$ *relaxation oscillations* by using non-standard analysis. We recall that a relaxation oscillation is a limit cycle characterized by two alternating processes on different time scales. After that, different points of view have been adopted to study the canard behaviour by using standard techniques such as: matched asymptotic expansions, see Eckhaus (1983), Benoît (1996) and Matzinger (2006) among others; invariant manifold theory and parameter blow-up, see Dumortier and Roussarie (1996), Krupa and Szmolyan (2001), and Szmolyan and Wechselberger (2001) among others. More recently, canard behaviour has been reported in piecewise-smooth dynamical systems, see Desroches et al (2013) and Fernández-García et al (2015), among others.

Special canard orbits are those lying in the intersection of the two branches of the slow manifold $\mathcal{S}_\varepsilon$ passing from the attracting to the repelling one or vice versa. Those orbits are referred as *maximal canards* and *faux maximal canards*, respectively. For a characterization of the existence and number of maximal canards see Desroches et al (2012). In the piecewise linear context, the existence of a maximal canard, for 3-dimensional systems, appears in Prohens and Teruel (2013). A complete characterization of maximal canards has been obtained in Desroches et al (2016a). In the n-dimensional case, some results on the characterization of maximal canards are presented in Chapter 3.

Non-smooth dynamics. Piecewise systems

Let us consider a family of m pairs, $m \in \mathbb{N}$, given by $\{f_i, G_i\}_{i=1}^m$, such that $G_i \subset \mathbb{R}^n$, $i = 1, \ldots, m$, are pairwise disjoint open sets, and where $f_i : \overline{G}_i \to \mathbb{R}^n$ is a vector valued smooth function on G_i, such that it is continuous on the closure of G_i, $\overline{G}_i$.

A piecewise differential system on $G = \cup_{i=1}^m G_i$ is defined as

$$\dot{\mathbf{x}} = \frac{d\mathbf{x}}{dt} = f(\mathbf{x}), \tag{1.5}$$

where $f(\mathbf{x}) = f_i(\mathbf{x})$, if $\mathbf{x}$ belongs to the region G_i.

When the boundaries of two previous regions intersect, that is when $I_{ij} = \partial G_i \cap \partial G_j \neq \emptyset$, we will assume that I_{ij} is a smooth hypersuface of $\mathbb{R}^n$. In this case, there exists a smooth function, g_{ij}, such that $I_{ij} = g_{ij}^{-1}(\{0\})$. By way of notation, we call *switching manifold* to each hypersurface I_{ij}.

The piecewise vector field given by system (1.5) is defined on the open region G. By using the Filippov convention (see Filippov (1988)), we extend the vector field to the switching manifolds. Before presenting this convention, let us introduce some previous notation. Given a pair (f_i, G_i) and a sufficiently smooth function $g : \overline{G}_i \to \mathbb{R}$, we consider the application of the vector field f_i to the function g, and denote it by $f_i g$, as the function $f_i g : \overline{G}_i \to \mathbb{R}$ given by $f_i g(\mathbf{x}) = \nabla g(\mathbf{x})^T f_i(\mathbf{x})$. Moreover, we denote by $f_i^2 g$ the application of the vector field f_i to the function $f_i g$.

Convention 1.1 (Filippov's convention)**.** *For each point* $\mathbf{x} \in \mathcal{F}_{ij}$, *we consider the vector* $\nabla g_{ij}(\mathbf{x})$. *Without lost of generality we can assume that* $\nabla g_{ij}(\mathbf{x})$ *points to the interior of the set* G_i.

a) *If $f_i g_{ij}(\mathbf{x}) f_j g_{ij}(\mathbf{x}) > 0$, then the vectors $f_i(\mathbf{x})$ and $f_j(\mathbf{x})$ are transversal, with the same direction, to the surface $\mathcal{F}_{ij}$ at the point $\mathbf{x}$. When $f_i g_{ij}(\mathbf{x}) > 0$, both vectors, $f_i(\mathbf{x})$ and $f_j(\mathbf{x})$, point to the interior of G_i and the vector field f at $\mathbf{x}$ is defined as $f(\mathbf{x}) = f_i(\mathbf{x})$. In this way, the orbit trough $\mathbf{x}$ can be understood a "passing" orbit from G_j to G_i, by crossing $\mathcal{F}_{ij}$. Otherwise, when $f_i g_{ij}(\mathbf{x}) < 0$, the vector field at $\mathbf{x}$ is defined as $f(\mathbf{x}) = f_j(\mathbf{x})$ and, in this case, the orbit is considered to pass from G_i to G_j. These orbits are often called crossing orbits of system (1.5) (see Figure 1.6A) and the subset of $\mathcal{F}_{ij}$ containing the points where crossing orbits pass through is called the sewing region.*

b) *Let us assume that $f_i g_{ij}(\mathbf{x}) f_j g_{ij}(\mathbf{x}) < 0$. Then, the vector field f at $\mathbf{x}$ is defined as*

$$f(\mathbf{x}) = (1 - \lambda^*) f_i(\mathbf{x}) + \lambda^* f_j(\mathbf{x}),$$

where

$$\lambda^* = \frac{f_i g_{ij}(\mathbf{x})}{f_i g_{ij}(\mathbf{x}) - f_j g_{ij}(\mathbf{x})}$$

In this case, the extended vector field f turns out to be parallel to the switching manifold. Hence the orbit trough $\mathbf{x}$ remains in $\mathcal{F}_{ij}$ and it is called a "sliding" orbit. We observe that some authors restrict the sliding region to the subset of the switching manifold where $f_i g_{ij}(\mathbf{x}) < 0$, while the subset at where $f_i g_{ij}(\mathbf{x}) > 0$ is called escaping region.

c) *Let us now consider that $f_i g_{ij}(\mathbf{x}) f_j g_{ij}(\mathbf{x}) = 0$. When $f_i(\mathbf{x}) = \mathbf{0}$ or $f_j(\mathbf{x}) = \mathbf{0}$, the point $\mathbf{x}$ is an equilibrium point of the vector field f_i or of the vector field f_j. In this case, f is defined at $\mathbf{x}$ as $f(\mathbf{x}) = \mathbf{0}$. Consider now that $f_i(\mathbf{x}) \neq \mathbf{0}$ and $f_j(\mathbf{x}) \neq \mathbf{0}$. When $f_i g_{ij}(\mathbf{x}) \neq 0$ (respectively, $f_j g_{ij}(\mathbf{x}) \neq 0$), the vector $f_j(\mathbf{x})$ (respectively, $f_i(\mathbf{x})$) is tangent to the switching manifold at $\mathbf{x}$. Then, f is defined at $\mathbf{x}$ as $f(\mathbf{x}) = f_j(\mathbf{x})$ (respectively, $f(\mathbf{x}) = f_i(\mathbf{x})$) and the point $\mathbf{x}$ is called a fold point.*

Finally, when $f_i g_{ij}(\mathbf{x}) = 0$ and $f_j g_{ij}(\mathbf{x}) = 0$, that is when both $f_i(\mathbf{x})$ and $f_j(\mathbf{x})$ are tangent to the switching manifold, the vector field f at $\mathbf{x}$ is defined as $f(\mathbf{x}) = \mathbf{0}$. In this case $\mathbf{x}$ is called a two-fold point and they are classified as: visible-visible, when $f_i^2 g_{ij}(\mathbf{x}) > 0$ and $f_j^2 g_{ij}(\mathbf{x}) < 0$; invisible-invisible, when $f_i^2 g_{ij}(\mathbf{x}) < 0$ and $f_j^2 g_{ij}(\mathbf{x}) > 0$; visible-invisible, when $f_i^2 g_{ij}(\mathbf{x}) > 0$ and $f_j^2 g_{ij}(\mathbf{x}) > 0$; and invisible-visible, when $f_i^2 g_{ij}(\mathbf{x}) < 0$ and $f_j^2 g_{ij}(\mathbf{x}) < 0$.

When no confusion arises, we call piecewise vector field f to the extended one by using Filippov's convention. The piecewise vector field, f, to each point $\mathbf{x}$ on the switching manifold $\mathcal{F}_{ij}$, results to be continuous at $\mathbf{x}$ when $f_i(\mathbf{x}) = f_j(\mathbf{x})$.

Piecewise linear differential systems

Piecewise linear differential (PWL) systems are piecewise systems, $\{f_i, G_i\}_{i=1}^m$, where the local vector field f_i is given by the linear function $f_i(\mathbf{x}) = A_i \mathbf{x} + \mathbf{b}_i$, such that A_i is an $n \times n$ matrix, $\mathbf{b}_i$ is an n-dimensional vector and G_i is an open region. In other words, a PWL differential is given by

$$\dot{\mathbf{x}} = f(\mathbf{x}), \tag{1.6}$$

where $f(\mathbf{x}) = A_i \mathbf{x} + \mathbf{b}_i$ when $\mathbf{x} \in G_i$. When system (1.6) is continuous, that is when $A_i \mathbf{x} + \mathbf{b}_i = A_j \mathbf{x} + \mathbf{b}_j$, for all $\mathbf{x}$ lying on the common boundary, $I_{i,j}$, of G_i and G_j, the switching manifold results to be a linear manifold (see Llibre and Teruel (2013)).
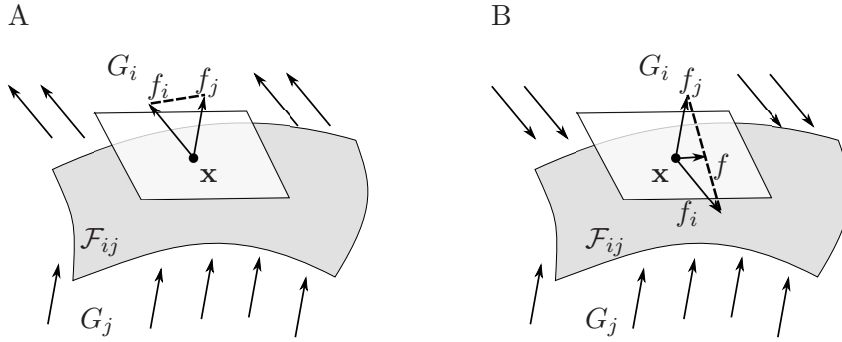
Figure 1.6: **Filippov's convention.** Figure depicting the extension of the vector field (1.5), to the switching manifold, by using Filippov's convention. Panel A shows the case when the vectors $f_i(\mathbf{x})$ and $f_j(\mathbf{x})$ point to the same open region separated by the switching manifold. In this case the orbit crosses the switching manifold, that is the crossing motion, and $f(x) = f_i(x)$. Panel B shows the case when the vectors $f_i(\mathbf{x})$ and $f_j(\mathbf{x})$ point to different open regions separated by the switching manifold. In this case the orbit slides along the switching manifold, that is the sliding motion.

PWL systems are characterized to reproduce complex behaviour exhibited by nonlinear smooth systems, but in a framework which is more friendly for computation, see Di Bernardo (2008), Llibre and Teruel (2013), and references therein. In this way, these systems have been long time used to understand the intricate behaviour taking place around a folded singularity in a slow-fast system, such as in Komuro and Saito (1991), Arima et al (1997), Doi and Kumagai (2004), Desroches et al (2013), Prohens and Teruel (2013), Prohens et al (2016), and Desroches et al (2016b). Moreover, they have been widely used to modelize real phenomena, in particular neuronal behaviour, see for instance Coombes (2001), Tonnelier and Gerstner (2003), Tonnelier (2003), Coombes (2008), and Fernández-García et al (2015).

In this work we consider continuous PWL differential systems defined all over $\mathbb{R}^n$, i.e. such that $\cup_{i=1}^m \overline{G}_i = \mathbb{R}^n$.

We observe that the continuous PWL system (1.6) is globally Lipschitz with Lipschitz constant $L = \max_j\{||A_j||\}$. In fact, given two points $\mathbf{x}_i$ and $\mathbf{x}_j$ lying in G_i and G_j, respectively, and considering $\mathbf{x}_0 \in I_{i,j}$ such that $\mathbf{x}_i$, $\mathbf{x}_0$ and $\mathbf{x}_j$ are collinear points, then

$$
\begin{aligned}
||(A_i\mathbf{x}_i + \mathbf{b}_i) &- (A_j\mathbf{x}_j + \mathbf{b}_j)|| \\
&= ||(A_i\mathbf{x}_i + \mathbf{b}_i) - (A_i\mathbf{x}_0 + \mathbf{b}_i) + (A_j\mathbf{x}_0 + \mathbf{b}_j) - (A_j\mathbf{x}_j + \mathbf{b}_j)|| \\
&\leq ||A_i(\mathbf{x}_i - \mathbf{x}_0) + A_j(\mathbf{x}_0 - \mathbf{x}_j)|| \\
&\leq ||A_i||\,||(\mathbf{x}_i - \mathbf{x}_0)|| + ||A_j||\,||(\mathbf{x}_0 - \mathbf{x}_j)|| \\
&\leq \max_i ||A_i||(||\mathbf{x}_i - \mathbf{x}_0|| + ||\mathbf{x}_0 - \mathbf{x}_j||) \\
&= \max_i ||A_i||(||\mathbf{x}_i - \mathbf{x}_j||).
\end{aligned}
$$

Therefore, the existence and uniqueness of solution is guaranteed for every initial condition $\mathbf{x}$, and their maximal definition interval is whole $\mathbb{R}$. Locally, the expression of this solution is explicitly given by

$$
\phi(t, \mathbf{x}) = e^{tA_i}\mathbf{x} + \int_0^t e^{(t-s)A_i}\mathbf{b}_i\, ds\,, \quad \mathbf{x} \in G_i. \tag{1.7}
$$

An equilibrium point $\mathbf{e} \in \overline{G}_i$ of the PWL system (1.6) satisfies that $A_i\mathbf{e} + \mathbf{b}_i = \mathbf{0}$. The converse implication is not always true. In fact, a zero of $A_i\mathbf{x} + \mathbf{b}_i$ is an equilibrium point

of PWL system (1.6) if this zero belongs to $\overline{G}_i$. Otherwise, this zero is called a *virtual equilibrium*.

Despite to have local expressions for each solution, it is not possible to obtain their global explicit expression. In fact, expression (1.7) is highly nonlinear in t, which implies, in general, the difficulty of obtaining an explicit expression for the flight time of the orbit to go from a point $\mathbf{x}_1$ to a point $\mathbf{x}_2$. Nevertheless, when $\mathbf{x}_1$ and $\mathbf{x}_2$ are in the same region G_i, and the piece of the orbit connecting them, γ, is also contained in G_i, we can use an alternative procedure to compute this flight time, which is explained below.

Let $\mathbf{v}$ be an eigenvector of the matrix A_i corresponding with the real eigenvalue λ, $<\mathbf{v}>$ be the span of $\mathbf{v}$, and $\mathbf{v}^\perp$ be the vector space ortogonal to $\mathbf{v}$. Since $\mathbb{R}^n = <\mathbf{v}> \bigoplus \mathbf{v}^\perp$, let $\hat{\mathbf{x}}_1$ and $\hat{\mathbf{x}}_2$ be the projections onto $<\mathbf{v}>$ of $\mathbf{x}_1$ and $\mathbf{x}_2$, respectively. As the system is locally linear, the flight time to go from $\mathbf{x}_1$ to $\mathbf{x}_2$ is the same than the time to go from $\hat{\mathbf{x}}_1$ to $\hat{\mathbf{x}}_2$, which satisfies $\hat{\mathbf{x}}_2 - \mathbf{e} = e^{\lambda t}(\hat{\mathbf{x}}_1 - \mathbf{e})$. Therefore,

$$t = \ln\left(\frac{\|\hat{\mathbf{x}}_1 - \mathbf{e}\|}{\|\hat{\mathbf{x}}_2 - \mathbf{e}\|}\right). \tag{1.8}$$

In Section 5.2, we take advantage of this fact to compute, in a different way, the flight times between points contained in the same region.

Planar continuous PWL differential differential systems with three regions of linearity, i.e. $\{A_i\mathbf{x} + \mathbf{b}, G_i\}_{i=1}^3$ with $A_1 = A_3$, $\mathbf{b}_1 = -\mathbf{b}_3$ and $\mathbf{b}_2 = \mathbf{0}$ are completely studied, from the qualitative point of view, in Llibre and Teruel (2013). In the case $\mathbf{b}_2 \neq \mathbf{0}$, that is under nonsymmetry assumptions, a characterization of the existence and uniqueness of limit cycles has been done by Llibre et al (2013). In the case of three different regions, when the system exhibits only one equilibrium point of node or focus type lying in the central region then, this system can be written in the Liénard form

$$\begin{cases} \dot{x} = F(x) - y, \\ \dot{y} = g(x) - \delta, \end{cases} \tag{1.9}$$

where

$$F(x) = \begin{cases} t_L(x+1) - t_c & \text{if } x \leq -1, \\ t_M x & \text{if } |x| \leq 1, \\ t_R(x-1) + t_c & \text{if } x \geq 1, \end{cases} \qquad g(x) = \begin{cases} d_L(x+1) - d_c & \text{if } x \leq -1, \\ d_M x & \text{if } |x| \leq 1, \\ d_R(x-1) + d_c & \text{if } x \geq 1, \end{cases}$$

$x, y \in \mathbb{R}$; L, M and R stand for the left, middle and right regions; and t_k and d_k are the trace and the determinant of A_k, where $k \in \{L, M, R\}$. Then the following theorem characterizes under which conditions this kind of systems exhibit a limit cycle, which is, in fact, unique.

Theorem 1.2 (Llibre et al (2013)). *Consider the differential system* (1.9) *with only one equilibrium point in the central zone, i.e. $d_M > 0$, $-d_M < \delta < d_M$, and d_L, $d_R \geq 0$. If the external traces satisfy t_L, $t_R < 0$, while the central trace is positive, that is $t_M > 0$, then the equilibrium point is surrounded by a limit cycle which is unique and stable.*

1.3   Diffusion processes and statistical inference

As we mentioned above, recording from neurons is a noisy process and so stochastic differential systems can be taken into account to describe and treat real data. For this

reason, in this section, we also introduce some basics about stochastic processes and we depict some examples that are related to neuroscience. The information we explain is mostly obtained from Ditlevsen and Samson (2013).

In order to extract the membrane potential from stochastic neuronal models, numerical tools may be necessary if the model is not analytically solvable, as the model we use in Section 5.1.2. In this section, we only give specifications about the numerical methods that we use in this thesis. However, adapting the most common numerical tools for solving deterministic differential systems to the stochastic framework is not trivial. We refer the reader to Iacus (2008) for further references.

Since stochastic models are also important in other fields such as physics and economics, a large number of different statistical inference techniques have been developed to estimate parameters in stochastic models. Some of these techniques are maximum likelihood estimators, Markov Chain Monte Carlo, Kalman filters, particle filters,... (see Chen (2003), for instance). Here, we focus on the maximum likelihood estimator, which will be used in Chapter 5.

Stochastic processes

A *stochastic process* is a random variable which depends on the time, t, and on the result, w, of an experiment. We denote a stochastic process by $X(t, w)$; the values it takes are called *states*. Hereinafter, we denote a stochastic process $X(t, w)$ by $X(t)$, when no confusion arise. Any stochastic process can be considered as a discrete-time process if the states are separate, isolated points; or as a continuous-time process if the states are connected.

For a fixed result of the experiment w, the process can be seen as a function in time, usually denoted by $X_w(t)$. This function is called a *realization*, a *simple path* or a *trajectory* of the process $X(t, w)$.

A particular case of an stochastic process is the *Markov process*, named in honor of Andrey Markov. This process has the property to present events that do not depend on the past ones, and so one can imagine these processes as memoryless processes: knowing the present state of the process, one can not get information about the past to be used to predict future states. Hence, predictions on the future are only based on the present. Mathematically written, only the value of $X(t)$ matters for predicting $X(t + 1)$, and so the conditional probabilities satisfies

$$P(future \mid past, \ present) = P(future \mid present).$$

A Markov process with continuous states evolving continuously in time is called *diffusion process*.

Another stochastic process is the *martingale*, where the future movements are unpredictable. That is, given all the past observations, the conditional expected value, $\mathbb{E}$, of the next one is equal to the last observation. Then, for all $n = 1, 2, \ldots, X(t_n)$ is a martingale if

- $\mathbb{E}[|X(t_n)|] < \infty$,

- $\mathbb{E}[X(t_{n+1})|X(t_1), \ldots X(t_n)] = X(t_n)$.

A process is considered to behave like a martingale if its trajectories display no discernible trends or periodicities.

A *Wiener process*, named in honor of Norbert Wiener, and also called as standard Brownian motion, in honor to Robert Brown, is a diffusion process where the random variable only changes continuously. Sometimes Wiener and Brownian processes are distinguished by considering that the Brownian process has a normal distribution whereas no assumption on the distribution of the Wiener process is made, and so it is assumed to be a martingale. Here, we consider a Wiener process $W(t)$ such that

- $W(0) = 0$,

- $W(t)$ has independent increments; that is, for $0 \leq s < t < u < v$, $W(t) - W(s)$ and $W(v) - W(u)$ are independent random variables.

- For all $0 \leq s < t$, $W(t) - W(s) \sim \sqrt{t-s}\,\mathcal{N}(0,1)$

And so, a Wiener process satisfies that changes on the variables, for a short time period dt, follow a normal distribution function with mean 0 and variance dt (as the Brownian process).

The realizations of a Wiener process is, as we prove above, nowhere differentiable since it is everywhere of unbounded variation, because $W(t+dt) - W(t)$ is of order $\sqrt{dt}$ instead of order dt. In general, the total variation of a real-valued function f on an interval $[a,b] \subset \mathbb{R}$ is defined as

$$V_a^b(f) = \sup \sum_{k=1}^n |f(t_k) - f(t_{k-1})|,$$

where the supreme is taken over all $n \in \mathbb{N}$ and over all choices of $\{t_k\}_{k=1}^n + 1$ such that $a = x_1 < \ldots < x_{n+1} = b$. When $V_a^b(f) < \infty$ and f is right-continuous, then we say that f is of bounded variation on $[a,b]$ (see Ditlevsen and Samson (2013)). However,

$$
\begin{aligned}
V_s^t(W) \;&= \sup \sum_{k=1}^n |W(t_k) - W(t_{k-1})| \\
&\geq \lim_{n\to\infty} \sum_{k=1}^n \left| W\left(s + \frac{k}{n}(t-s)\right) - W\left(s + \frac{k-1}{n}(t-s)\right) \right| \\
&\simeq \lim_{n\to\infty} \sum_{k=1}^n \sqrt{\frac{1}{n}(t-s)} = \infty.
\end{aligned}
$$

Stochastic differential equations

A *stochastic differential equation* (SDE) is given by a deterministic ordinary differential equation where a noise term is added to the driving equation; that is

$$dX(t) = \mu(X(t),t)dt + \sigma(X(t),t)dW(t) \tag{1.10}$$

where $X(t)$ is an stochastic process and $W(t)$ is a Wiener process, where the differential $dW(t)$ means $dW(t) = \xi(t)dt$ and $\xi(t)$ is a *white noise process*; that is, a stochastic process normally distributed for any fixed time t and uncorrelated, such that $\mathbb{E}[\xi(t)] = 0$ and $\mathbb{E}[\xi(t)\xi(s)] = 0$ if $s \neq t$. Function μ is called the *drift coefficient* or *deterministic component*, and σ is called the *diffusion coefficient* or the *stochastic component*.

Integrating equation (1.10), we obtain that

$$X(t) = X(t_0) + \int_{t_0}^{t} \mu(X(s), s)ds + \int_{t_0}^{t} \sigma(X(s), s)dW(s),$$

where the first integral is an ordinary integral, coming from the deterministic coefficient of the SDE. Since the Wiener process is non-differentiable, the second integral needs to be defined.

Let us consider an arbitrary function $f(t)$. Then the integral $\int_{t_0}^{t} f(s)dW(s)$ is defined as:

- If $f(t)$ is a constant function, i.e. $f(t) = \sigma$, then, since the increments of a Wiener process have expectation 0, we would also expect a random variable with expectation 0, and so

$$\int_{t_0}^{t} f(s)dW(s) = \sigma(W(t) - W(t_0)).$$

- If $f(t)$ is a non-random step function such that $f(s) = \sigma_j$ on $t_j \leq s \leq t_{j+1}$ for $j = 1, \ldots, n$, $t_1 = t_0$ and $t_{n+1} = t$, then

$$\int_{t_0}^{t} f(s)dW(s) = \sum_{j=1}^{n} \sigma_j(W(t_{j+1}) - W(t_j)).$$

- If $f(t)$ is a random and measurable function with respect to the σ-algebra generated by the random variables $\{W(s)\}_{s \leq t}$; that is, the values of $f(t)$ are determined by the values of $W(s)$, for $s \leq t$ and $\mathbb{E}[\int_{t_0}^{t} f(s)^2 ds] < \infty$, then

$$\int_{t_0}^{t} f(s)dW(s) = \lim_{|\Pi_n| \to 0} \sum_{j=1}^{n} f(t_j^*)(W(t_{j+1}) - W(t_j))$$

where Π_n is a partition $\{t\}_{j=1}^{n+1}$ of the interval $[t_0, t]$; $|\Pi_n|$ is the norm of the partition, i.e. $|\Pi_n| = \max\{|t_{j+1} - t_j|\}_{j=1}^{n}$ and $f(t)$ is approximated by $f(t_j^*)$ for $t_j \leq t < t_{j+1}$ and $t_j^* \in [t_j, t_{j+1}]$ (see Ditlevsen and Samson (2013) for more details).

The way how the t_j^* are chosen leads to differences in the solution of the integral. For instance, considering $f(t) = W(t)$, if we choose $t_j^* = t_j$ (the left end point) then, since the Wiener process has independent increments with mean 0, the expectation

$$\mathbb{E}\left[\sum_{j=1}^{n} W(t_j)(W(t_{j+1}) - W(t_j)) \right] = 0.$$

However, if we choose $t_j^* = t_{j+1}$ (the right end point), since the Wiener process has mean 0 and so the variance is $\mathbb{E}[W^2]$, then the expectation

$$\mathbb{E}\left[\sum_{j=1}^{n} W(t_{j+1})(W(t_{j+1}) - W(t_j)) \right] = t - t_0.$$

Depending on the choice of t_j^*, two different integrals are useful and common: the called Itô integral, when t_j^* is considered to be the end left point, that is $t_j^* = t_j$; and the Stratonovich integral, when t_j^* is considered to be the middle point, that is $t_j^* = (t_j + t_{j+1})/2$.

Solving the SDE by the Itô integral we obtain the so called *Itô diffusion* if both the drift and the diffusion coefficients do not depend upon time or *Itô process* if they do.

Some examples of Itô diffusion used in biology are:

1. The Wiener process given by

$$dX(t) = \mu dt + \sigma dW(t)$$

which is used, for instance, to describe a particle suspended in water that is bombarded by water molecules. It has been also proposed as a simplification model for the membrane potential evolution in a neuron (see Ditlevsen and Samson (2013))

2. The Geometric Brownian motion given by

$$dX(t) = \mu X(t)dt + \sigma X(t)dW(t)$$

which is used, for instance, to describe the enzymatic process to breakdown the effects of a drug supplied as a bolus to the blood.

3. The Ornstein-Uhlenbeck (OU) process given by

$$dX(t) = -\frac{1}{\tau}(X(t) - \alpha)dt + \sigma dW(t).$$

This process is attracted to some constant level α but is continuously perturbed by noise; having an stationary solution that follows a normal distribution with mean α and variance $\sigma^2\tau/2$.

That is the case of the membrane potential of a neuron. In fact, the membrane potential is constantly bombarded by chemical or electrical pulses coming from other neurons or from the surrounding environment. However, at the same time, it is attracted to a resting state (see subsection *Membrane potential changes* in Section 1.1). This process is often used to generate synaptic conductances, as we use in Section 2.2.2.

4. The Cox-Ingersoll-Ross process given by

$$dX(t) = -\frac{1}{\tau}(X(t) - \alpha)dt + \sigma\sqrt{X(t)}dW(t),$$

where α and $X(t)$ remains positive. This process also admits a stationary solution and an application of it is given in neuroscience to describe the hyperpolarization of the membrane potential caused by the inhibitory reversal potential.

When the diffusion term does not depend on the state variable $X(t)$, such as (1) and (3), we say that the process has *additive noise*. Otherwise, like processes in (2) and (4), we say that the process has *multiplicative noise*.

Monte Carlo Simulations

All the examples of the Itô diffusion above described can be explicitly solved. However, this is something that usually does not happen. When no explicit solution can be analytically given, numerical methods need to be used. Hence, we can approximate different characteristics of the process by simulations. Different methods, such as the Euler method

(also called Euler-Maruyama method), the Milstein method, and the Shoji-Ozaki method, among others, can be used to simulate such processes. Since in this thesis we only use the Euler method, we are going to describe it. However, we refer the reader to Iacus (2008) for mode details about the different methods, some codes in R, and a comparison (advantages and disadvantages) along them.

Euler method. Assume we want to approximate a state $X(t)$ being the solution of the stochastic differential equation (1.10) in some interval $[0, t]$. Therefore, let the time discretization given by $0 = t_0 < t_1 < \ldots < t_N = t$ and $\Delta_j = t_{j+1} - t_j$ be the time steps, which can be either equidistant or not. Moreover, consider $\Delta W_j = W(t_{j+1}) - W(t_j)$ be the increments of the Wiener process such that $\Delta W_j \sim \mathcal{N}(0, \Delta_j)$. Therefore,

$$X_{j+1} = X_j + \mu(X_j, t)\Delta_j + \sigma(X_j, t)\Delta W_j, \quad \text{and} \quad X_0 = X(t_0);$$

such that $X_{j+1} = X(t_{j+1})$, discretized, and $\Delta W_j = \sqrt{\Delta_j}\xi_j$, with ξ_j being a normal distribution with mean 0 and variance 1, for all j. In this case, $\{X_j\}_{j=0}^N$ weakly converges with order 1, see Iacus (2008).

The Milstein method is a version of the Euler method consisting of to add a term on the discretization which depends on the derivative of the noise. This method strongly converges with order 1, see Iacus (2008). However, when $\sigma(X(t), t)$ does not depend on $X(t)$, both methods coincide.

Statistical Inference

Descriptive statistics is solely concerned about properties of the data such as finding the expectation value, the variance and so on. However, it does not assume that the data can come from a larger population, as the case of estimating parameters in the connectivity of the brain, where the population is larger than the observed data set.

Different estimators have been proposed to estimate parameters based on the knowledge of the transition densities (as the maximum likelihood estimator, which is explained below) or other such as Monte Carlo methods, the moments' method, Kalman filter, martingale estimating functions, Bayesian methods, and so on (see Ditlevsen and Samson (2013) and Baron (2013) among others). We focus on the maximum likelihood estimator, which will be used in Chapter 5.

Maximum likelihood estimator. A statistical inference method we will use to estimate parameters is the *maximum likelihood estimator* (MLE) based on the knowledge of the transition densities to explicitly formulate the likelihood function.

Let $X_0, \ldots, X_N$ be discrete observations at times $0 = t_0 < t_1 < \ldots t_N = t$, respectively, of an Itô process $X(t)$, satisfying the SDE

$$dX_t = \mu(t, X(t); \theta)dt + \sigma(t, X(t); \theta)dW(t),$$

where θ refers to a vector of unknown parameters. Then, the *likelihood function* of θ, $\mathcal{L}(\theta)$, is given by the product of the transition densities; that is,

$$\mathcal{L}(\theta) = \mathcal{L}(\theta, (X_0, \ldots, X_N)) = p(X_0; \theta) \prod_{j=1}^N p(X_j | X_{j-1}; \theta)$$

where $p(X_0; \theta)$ is the density of the initial value X_0, which is considered equal to 1, and $p(X(t)|X(s); \theta)$ for $0 \leq s < t$ is the transition density of $X(t)$.

To avoid the product of the transition densities, we consider the log-likelihood given by

$$\log \mathcal{L}(\theta) = \sum_{j=1}^{N} \log p(X_j | X_{j-1}; \theta).$$

Hence, the score function to compute the maximum of the likelihood is the vector of partial derivatives with respect to the θ components such as

$$U(\theta) = \sum_{j=1}^{N} \frac{\partial}{\partial \theta} \log p(X_j | X_{j-1}; \theta).$$

Since the likelihood depends on the transition density function $p(\cdot)$, when it is unknown, it needs to be approximated. A first approach to the likelihood function is approximating $p(\cdot)$ by a Gaussian density using the correct expectation and variation. That is,

$$p(X_j | X_{j-1}; \theta) \approx \frac{1}{\sqrt{2\pi\phi(\delta_j, X_j; \theta)}} \exp\left\{ -\frac{(X_{j-1} - F(\delta_j, X_j; \theta))^2}{2\phi(\delta_j, X_j; \theta)} \right\}$$

where $\delta_j = t_{j+1} - t_j$, $F(\delta_j, X_j; \theta) = \mathbb{E}_\theta[X_{\delta_j} | X_0 = X_j]$, and $\phi(\delta_j, X_j; \theta) = \text{Var}_\theta(X_{\delta_j} | X_0 = X_j)$. A second approach can be obtained by computing an approximation of $p(\cdot)$ based on the Euler-Maruyama method, which is the one we will use, or the Milstein method, by replacing $p(\cdot)$ by the Gaussian density of the Euler-Maruyama (see Appendix B) or the Milstein method. Another approach can be given introducing a set of auxiliary data points between each observations to finally approximate the likelihood via numerical integration. And finally, an alternative is to generate trajectories using Brownian bridges (that is, a continuous-time stochastic process $B(t)$ such that it is defined as $B(t) := (W(t)|W(1) = 0)$ for $t \in [0,1]$, and so its probability distribution is considered to be the conditional probability distribution of a Wiener process $W(t)$ with $B(1) = 0$. For more details see Ditlevsen and Samson (2013).

Chapter 2

Neural models and data treatment

In this chapter we present an evolution of different existing neural models. Although we focus on the neural models which are of interest to the results of this thesis, we also briefly explain the origin of them to provide a good reading flow for the reader (see Dayan and Abbott (2005) and Izhikevich (2007), among other). Moreover, we also present the synaptic inputs we have considered to generate *in sillico* data from computational models.

In the estimation procedures based on stochastic models (see Section 5.1.2), we also use data that comes from intracellular recordings, in fact *in vivo* data from a motorneuron provided by Prof. R. Berg (University of Copenhagen). Hence, at the end of this chapter we also explain how this data has been recorded in Berg's lab and the features which are relevant in this thesis.

In order to facilitate a straightforward reading, specific methods only used in particular chapters are introduced at the corresponding chapter.

2.1 Mathematical models of neuronal dynamics

In this section, we aim to present different models describing neuron dynamics at different levels of accuracy. Neural models have been basically developed to describe changes in the membrane potential of a single neuron, which might or might not interact with other neurons in the brain. The first models we can find in the literature describe the subthreshold intrinsic activity of an isolated single neuron. However, these models have been improved to obtain more realistic descriptions not only of the subthreshold activity, but also of the suprathreshold activity of the neuron and the interactions between different neurons.

We first describe some of these single neural models, emphasizing the ones we are using in Chapter 5 to estimate conductances. After that, we also present a neural network with a plasticity mechanism, which we are using in Chapter 4 to study the effects of the plasticity on the conductances. For a more detailed explanation of the basic neural models we refer the reader to Izhikevich (2007).

2.1.1 Integrate-and-Fire (IF) models

One of the earliest models to describe the behaviour of a neuron was first proposed by Louis Lapicque in 1907 in its paper *From frogs to integrate-and-fire* (see Brunel and van Rossum (2007)). In this case, the changes on the membrane potential of a neuron, $dV(t)/dt$, are formulated to be directly proportional to the input current, $I(t)$. That is, the membrane potential obeys the ordinary differential equation

$$C\frac{dV(t)}{dt} = I(t),$$

where C is the capacitance of the membrane.

This model includes a reset mechanism in such a way that, when the membrane potential, $V(t)$, reaches a certain threshold value, V_{th}, where a spike is assumed to occur, then $V(t)$ is reset to the resting membrane potential, $V_{rest} < V_{th}$, after which the differential equation applies again. For this reason this neural model is called Integrate-and-Fire (hereinafter referred to as IF) model.

One of the problems of this model is that it has no time-dependent memory. That is, if the model receives a pulse of external input current at a specific time, which does not immediately provoke a spike, then this pulse remains until the neuron fires again, where a reset on the membrane potential is done. However, this is not a real effect in neurons, whose membrane potential tends to an equilibrium value, and so mechanisms are activated in response to this current. Moreover, it also presents the inconvenient that the initialization shape of the spike is not accurate. In order to solve these two problems, the IF model has been improved in several ways.

A first improvement was to add a leak term to the membrane potential in order to reflect the in- and out-come of ions through the membrane, until the interior of the cell reaches a specific equilibrium value, V_L. This model is called the Leaky integrate-and-fire (LIF) model, which is still a linear model, and it is modelled as

$$C\frac{dV}{dt} = -g_L(V(t) - V_L) + I(t).$$

However, this model does not yet capture the dynamics of the membrane potential close to or during the spikes. Therefore, to describe the activity of the subthreshold regime in a more accurate way, a quadratic version of the IF model, based in the ideas of the θ-model presented in Ermentrout and Kopell (1986), was developed. This model is referred to as the Quadratic integrate-and-fire (QIF) model and it captures the $f - I$ curve accurately for a broad range of input currents (see Fourcaud-Trocmé et al (2003)), but it still presents problems capturing the initialization shape of the spike. Consequently, some other adaptations have been done using an exponential version to better capture the spike generation such as the Exponential integrate-and-fire (EIF) model (see Fourcaud-Trocmé et al (2003)) or the adaptive Exponential integrate-and-fire (aEIF) model (see Brette and Gerstner (2005)). Finally, other generalizations have been recently developed to also consider the tonic firing and the bursting behaviours (see Coombes et al (2012), Jimenez et al (2013), and references therein).

Next, we describe in more detail a version of the QIF model, where a noise term has been added. This model is used in Section 5.1.2 to estimate conductances in the subthreshold regime under the presence of noise.

2.1.1.1 Quadratic Integrate-and-Fire (QIF) model

As we have mentioned above, the quadratic integrate-and-fire (QIF) model allows to accurately describe the subthreshold dynamics of the neurons, even under the presence of activated subthreshold ionic currents; see for instance Ermentrout and Kopell (1986) and Fourcaud-Trocmé et al (2003). This model is a second order approximation of nonlinear models.

In our simulations we consider a version of the QIF model, including an external current and a stochastic term to describe possible noise. This noise can come externally from the measurements of the data or intrinsically from the neuron. This stochastic version of the QIF model is given by

$$C\frac{dV}{dt} = \alpha \left(V(t) - V_T\right)^2 - I_T + I(t) + \eta(t), \tag{2.1}$$

where $V(t)$ stands for the membrane potential; C is the capacitance; I_T is the largest input current at which the neuron does not spike in the absence of both synaptic input, applied current and noise, V_T denotes the corresponding voltage of the $V - I$ curve at I_T, and $\alpha = g_L/(2\Delta_T)$, where g_L is the leak conductance and Δ_T is the spike slope factor at I_T, which corresponds to the inverse of the curvature of the $V - I$ curve at (I_T, V_T). Finally, $\eta(t)$ is a noise process, with zero mean and σ variance, modelling the random arrivals of synaptic input.

2.1.2 Hodgkin-Huxley type neural models

In 1952, Hodgkin and Huxley proposed a neural model, referred to as the Hodgkin-Huxley model (hereinafter as HH model), describing the generation of an action potential in a squid giant axon. The model explained recent results concerning the gating variables of ion channels, see Hodgkin and Huxley (1952). In this model, they describe the ionic mechanisms involved in both the initialization and the propagation of an action potential, for what, in 1963, they received the Nobel Prize in Physiology or Medicine. This kind of models take into account how easily the gating variables allow the ions flow through the membrane, that is, they consider the conductances, as we next explain. We want to remark that models with this property are referred to as *conductance-based models*. In the Hodgkin-Huxley model, the ionic currents are supposed to be sensitive to a single type of ions.

The HH model is described by the electric circuit in Figure 2.1, which in particular represents the membrane potential, $V(t)$, of the neuron. The parameter C in the circuit stands for the capacitance of the neuron's membrane, whereas g_{ion} is the conductance of a specific ionic channel (where $ion \in \{K, Na\}$ such that K stands for the potassium and Na for sodium), I_{ion} is the current through the specific ion channel and V_{ion} is its reversal potential. Moreover, g_L and V_L are considered to be the leak conductance and the reversal potential, respectively. On the other hand, I_L is the leak current, which is the intrinsic current of the neuron such that, in absence of other ionic currents, it causes that the membrane potential reaches an equilibrium state between the inside and outside potentials (see Section 1.1).

From Ohm's law and Kirchhoff's laws, the dynamics of the membrane potential is described by the differential equation

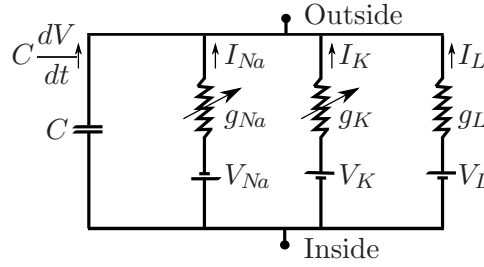$$C\frac{dV}{dt} = -I_{Na} - I_K - I_L.$$

Figure 2.1: **The equivalent electric circuit of the Hodgkin-Huxley model.** Representation of the electric circuit describing the membrane potential, $V(t)$, of a single neuron with the ionic channels considered in the Hodgkin-Huxley model.

By using a series of voltage clamp recordings, a technique to record the total amount of current of the cell by clamping the voltage (see Section 1.1, *Electrophysiological techniques*), for a different extracellular concentrations of sodium and potassium ions, Hodgkin and Huxley characterized the ionic currents as

$$I_{ion} = g_{ion}(t)(V(t) - V_{ion}).$$

However, they also realised that the channels are not always opened. The channels are activated or inactivated depending on the concentration of the corresponding ion inside and outside the cell. More concretely, Hodgkin and Huxley considered the ionic conductances $g_{ion}(t)$ as $g_{ion}(t) = \bar{g}_{ion}P_{ion}(t)$, where $\bar{g}_{ion}$ is the maximal conductance of the ion channel and $P_{ion}(t)$ is the portion of open channels in a large population (see Section 1.1). The portion of open channels in a large population was described, in a sketchy way, as

$$P_{ion}(t) = m^a h^b,$$

where m and h are the ratio of activating and inactivating channels, respectively, and a and b stand for the number of activation or inactivation gates, respectively. Notice that, in the case that $b = 0$, then the corresponding current in persistent; otherwise it is transient (see Section 1.1).

If the channel is completely open we will have that $m = 1$, whereas $m = 0$ if it is completely closed. However, the channels can also be partially activated having $0 < m < 1$. Same results happen with h but in an inverse order. Therefore, the dynamics of these gating variables were modelled by Hodgkin and Huxley as

$$\frac{dw}{dt} = \phi_w \left(\alpha_w(V)(1 - w) - \beta_w(V)w \right) = \phi_w dfrac{w_\infty(V) - w}{\tau_w(V)}, \qquad (2.2)$$

where ϕ_w is a non-dimensional temperature factor, which is different for each w, and w represents any of the gating variables; in general,

$$w_\infty(W) = \frac{\alpha_w(V)}{\alpha_w(V) + \beta_w(V)}, \qquad \tau_w(V) = \frac{1}{\alpha_w(V) + \beta_w(V)}, \qquad (2.3)$$

for a given functions $\alpha_w(V)$ and $\beta_w(V)$ which vary depending on the ionic channel.

The classical model of Hodgkin and Huxley was developed considering, as ionic currents, only sodium and potassium ionic currents, such that $I_{Na} = g_{Na}m^3h(v - V_{Na})$ and $I_K = g_K n^4(v - V_K)$. The activation gating variable for I_K is referred to as n instead of m, since it is the usual notation for this specific gating variable in the literature. However, this model can be modified according to different anatomical and physiological conditions that different animals and different types of neurons exhibit.

Next, we present two different variations of the HH model describing different kinds of cells and considering different types of activated ionic currents. The first model we present is a *pyramidal cell model* having a simple spiking mechanism and also some ionic currents active in the subthreshold regime. The second model is a reduced model for *medial entorhinal cortex stellate cell* displaying subthreshold oscillations. A reduction of the stellate model without the spiking mechanism, is also described.

2.1.2.1 Pyramidal cell model

One of the HH-like models we are going to use next is the one given in Wang (1998). This model describes the behaviour of a pyramidal neuron that has two compartments, the dendrite and the soma plus the axonal initial segment. However, in our study we only consider the somatic compartment and we add a low-threshold Ca^{2+} current, called I_{LTS}, obtained from Destexhe et al (1993). These modifications are done to obtain a model with minimal complexity endowed with a spiking mechanism and two different current sources for subthreshold activity. The spiking mechanism is provided by sodium and potassium currents, I_{Na}, I_K. The sources for subthreshold activity are a calcium-activated afterhyperpolarising potassium current, I_{AHP}, and the low-threshold Ca^{2+} current, I_{LTS}. These two currents are chosen to display different ways to induce ionic activity in subthreshold regimes. On one side, the AHP current is generated by slow currents that turn on right after the spike; on the other hand, low-threshold currents are usually activated at voltage values above resting potential but not high enough to evoke spikes.

Following the Hodgkin-Huxley arguments, the dynamics of the membrane potential for our *modified pyramidal model* is given by

$$C\frac{dV}{dt} = -I_L(t) - I_{Na}(t) - I_K(t) - I_{Ca}(t) - I_{AHP}(t) - I_{LTS}(t) + I(t),$$

where C is the capacitance, $I(t)$ is the external current, and $I_L(t)$ and $I_{ion}(t)$ are the leak and the respective ion currents which are described by equations

$$
\begin{aligned}
I_L(t) &= g_L(V - V_L), \\
I_{Na}(t) &= g_{Na}m_\infty^3(V)h(V - V_{Na}), \\
I_K(t) &= g_K n^4(V - V_K), \\
I_{Ca}(t) &= g_{Ca}ml_\infty(V)(V - V_{Ca}), \\
I_{AHP}(t) &= g_{AHP}\frac{c}{c+K_D}(V - V_K), \\
I_{LTS}(t) &= g_{LTS}m_{LTS,\infty}^3(V)h_{LTS}(V - V_{Ca}),
\end{aligned}
$$

where $V = V(t)$; V_{ion} and g_{ion} represent the specific ion reversal potentials and maximal conductances, respectively, $c = c(t)$ is the intracellular calcium concentration $[Ca^{2+}]$ and K_D represents a growth factor of the $I_{AHP}(t)$ current. The variables $h = h(t)$, $n = n(t)$, and $h_{LTS} = h_{LTS}(t)$ are gating variables governed by first-order kinetics of type (2.2 -2.3).

The m-type variables are considered to be at the steady-state, $ml = ml_\infty(V)$, $m = m_\infty(V)$ and $m_{LTS} = m_{LTS,\infty}(V)$, because they are assumed to have a faster dynamics than the membrane potential and the rest of variables. More precisely, the functions describing the

gating dynamics are given by:

$$\alpha_h(V) = 0.07 \exp(-(V+50)/10),$$
$$\beta_h(V) = 1/(1+\exp(-0.1(V+20))),$$
$$\alpha_n(V) = -0.01(V+34)/(\exp(-0.1(V+34))-1),$$
$$\beta_n(V) = 0.125 \exp(-(V+44)/25),$$
$$\alpha_m(V) = -0.1(V+33)/(\exp(-0.1(V+33))-1),$$
$$\beta_m(V) = 4 \exp(-(V+58)/12),$$
$$ml_\infty(V) = 1/(1+\exp(-(V+20)/5)),$$
$$m_{LTS,\infty}(V) = 1/(1+\exp(-(V+65)/7.8)),$$
$$h_{LTS,\infty}(V) = 1/(1+\exp((V+81)/11)),$$
$$\tau_{LTS}(V) = h_{LTS,\infty}(V)\exp((V+162.3)/17.8).$$

Notice that the function h_{LTS} is a sigmoidal function with a low inflection point that induces the desired low-threshold activation.

The intracellular calcium concentration $c = [Ca^{2+}]$ is assumed to be governed by a leaky-integrator

$$dc/dt = -\alpha I_{Ca} - c/\tau_{Ca}, \qquad (2.4)$$

where τ_{Ca} is the time constant and α is proportional to the membrane area divided by the volume below the membrane.

The biophysical parameters considered in this model are:

Conductances (mS/cm^2) : $g_L = 0.1$, $g_{Na} = 45$, $g_K = 18$, $g_{Ca} = 1.0$, $g_{AHP} = 5.0$, $g_{LTS} = 0.5$;

Reversal potentials (mV) : $V_L = -65$, $V_{Na} = 55$, $V_K = -80$, $V_{Ca} = 120.0$,

Capacitance $(\mu F/cm^2)$: $C = 1$;

$Non-dimensional$ constants : $\phi_n = \phi_h = 4$, $\phi_{LTS} = 2$;

Other constants : $\alpha = 0.002\,\mu M(ms\,\mu A)^{-1}cm^2$, $\tau_{Ca} = 80\,ms$, $K_D = 30.0\,\mu M$.

2.1.2.2 Stellate cell model

The second model we are going to consider in our simulations is a HH-like model, describing a medial entorhinal cortex stellate cell (see Rotstein et al (2006)). This model is used in its complete form and also in its reduced version, which is given in Rotstein (2015). We first present the full version of the model.

Complete stellate cell model. The stellate cell model is a seven dimensional model consisting of four different currents, the sodium (Na) and the potassium (K) currents, which cause spiking regimes; and the persistent sodium (NaP) current and the h-current, whose interaction induces subthreshold oscillations independently of the spiking mechanism (see Rotstein (2015)).

Following the Hodgkin-Huxley formalism, the dynamics of the membrane potential for the stellate cell model is given by

$$C\frac{dV}{dt} = -I_L(t) - I_{Na}(t) - I_K(t) - I_{NaP}(t) - I_h(t) + I(t), \qquad (2.5)$$

where C is the capacitance, $I(t)$ is the external current, and I_L and I_{ion} the leak and the respective ion currents. The h-current has two components, a fast one, r_f, and a slow one, r_s.

The different currents of the model are described by equations

$$I_L = g_L(V - V_L),$$
$$I_{Na} = g_{Na}m^3h(V - V_{Na}),$$
$$I_K = g_K n^4(V - V_K),$$
$$I_{NaP} = g_p p(V - V_{Na}),$$
$$I_h = g_h(0.65r_f + 0.35r_s)(V - V_h),$$

where V_{ion} and g_{ion} represent the specific ion reversal potentials and maximal conductances, respectively.

All the gating variables w, which can be either m, h, n, p, r_f or r_s, follow the type of kinetics given in (2.2-2.3), with:

$$\alpha_m(V) = -0.1\,(V + 23)/(\exp(-0.1(V + 23)) - 1),$$
$$\beta_m(V) = 4\,\exp(-(V + 48)/18),$$
$$\alpha_h(V) = 0.07\,\exp(-(V + 37)/20),$$
$$\beta_h(V) = 1/(1 + \exp(-0.1(V + 7))),$$
$$\alpha_n(V) = -0.01\,(V + 27)/(\exp(-0.1(V + 27)) - 1),$$
$$\beta_n(V) = 0.125\,\exp(-(V + 37)/80),$$
$$\alpha_p(V) = 1/(0.15(1 + \exp(-(V + 38)/6.5))),$$
$$\beta_p(V) = \exp(-(V + 38)/6.5)/(0.15(1 + \exp(-(V + 38)/6.5))),$$
$$r_{f,\infty}(V) = 1/(1 + \exp((V + 79.2)/9.78)),$$
$$\tau_{r_f}(V) = 0.51/(\exp(V - 1.7)/10 + \exp(-(V + 340)/52)) + 1,$$
$$r_{s,\infty}(V) = 1/(1 + \exp((V + 2.83)/15.9))^{58},$$
$$\tau_{r_s}(V) = 5.6/(\exp(V - 1.7)/14 + \exp(-(V + 260)/43)) + 1.$$

The biophysical parameters are:

Conductances $(mS/cm^2):\ g_L = 0.1,\ g_{Na} = 52,\ g_K = 11,\ g_p = 0.5,\ g_h = 1.5;$
Reversal potentials $(mV):\ V_L = -65,\ V_{Na} = 55,\ V_K = -90,\ V_h = .20,$
Capacitance $(\mu F/cm^2):\ C = 1,$
$Non-dimensional\ constants: \phi_m = \phi_h = \phi_n = \phi_p = \phi_{r_f} = \phi_{r_s} = 1.$

Reduced stellate cell model - Quadratization of the model.   In order to avoid possible contamination of the spiking regimes during the estimation procedures, in Chapter 5 we consider a reduction of the stellate model by ignoring the spiking mechanism. That is, we only take into account the persistent sodium current, I_{NaP}, and the fast component of the h-current, I_h, to be active. Both currents are involved in rhythmic subthreshold oscillations (see Dickson et al (2000), for instance).

Under the presence of both I_{NaP} and I_h currents, since I_h is a resonant current[6] and I_{NaP} an amplifying[7] one, the interaction between them often induces nonlinearities of quadratic

---

[6]A resonant current is a current causing oscillations on the membrane potential
[7]An amplifying current is a current that increases the membrane potential

type in the voltage response (see Rotstein (2015)). Since these nonlinear effects cannot be captured by a linearization of the model, a quadratization has been proposed by Rotstein (2015) to capture the parabolic shape of the voltage nullcline. The general quadratization is given by

$$\frac{dV}{dt} = aV^2 - w + I(t),$$

$$\frac{dw}{dt} = \varepsilon(\alpha V - \lambda - w),$$

(2.6)

where w is defined attempting to capture the effect of the gating variables. Parameters a, α, ε and λ are taken as constants, and are defined in terms of the biophysical parameters of the original model (2.5) mimicking the geometry of the phase-plane. In this sense, a controls the curvature of the v-nullcline, α controls the slope of the w-nullcline, ε stands for the time scale separation between V and w, which tends to be small, and λ controls the relative displacement between the two nullclines.

For the biophysical parameters considered in our model, the constant parameters of the quadratization turn out to be $a = 0.1$, $\alpha = 0.4$, $\varepsilon = 0.01$ and $\lambda = -0.2$ (see Rotstein (2015)).

2.1.3 FitzHugh-Nagumo model

In 1961, FitzHugh-Nagumo (FHN) model (see FitzHugh (1961) and Nagumo et al (1962)) was derived as a two dimensional simplification of the Hodgkin-Huxley model of a spike generation in squid giant axon. The model is based on a separation of time scales and exploits similarities and correlations between the currents. This model was also called *Bonhoeffer-van der Pol (BVP) model*.

As we said in Section 2.1.2, the initial HH model only considers the leak, the sodium and the potassium currents, such that $I_{Na}(t)$ is modulated by an activating gating variable, $m(t)$, and an inactivating one, $h(t)$, whereas $I_K(t)$ is only modulated by one activating gating variable, $n(t)$. Based on the dynamics of the gating variables, a first simplification that FitzHugh did was to suppose the gating variable $m(t)$ to be on its steady state, that is $m(t) = m_\infty(V(t))$, since $m(t)$ shows a faster dynamics than the other variables. On the other hand, regarding $n(t)$ and $h(t)$, these two gating variables present a similar dynamics, which are related according to $1 - h(t) = an(t)$.

Considering a new variable $w(t) = 1 - h(t)$, which exploits the similarities in the dynamics between $h(t)$ and $n(t)$, the 4-dimensional HH model was reduced to the 2-dimensional model

$$C\frac{dV}{dt} = -g_{Na}m_\infty^3(V)(1-w)(V-V_{Na}) - g_K\left(\frac{w}{a},\right)^4(V-V_K) - g_L(V-V_L) + I(t),$$

$$\frac{dw}{dt} = \frac{w_\infty(V) - w}{\tau_w(V)},$$

more commonly written as

$$C\frac{dV}{dt} = F(V,w) + I(t), \qquad \frac{dw}{dt} = G(V,w),$$

where $F(V,w) = 0$ defines a N-shape curve in the phase plane and it describes the membrane potential dynamics, whereas $G(V,w) = 0$ defines a S-shape curve in the phase plane

and it describes the mutually related dynamics of the h and n gating variables. In order to mimic the dynamical behaviour of this system, FitzHugh and Nagume introduce a cubic polynomial system. This system can be written in general as

$$C\frac{dV}{dt} = f(V) - w + I(t),$$

$$\frac{dw}{dt} = aV - w + b,$$

where $f(V)$ is a cubic polynomial.

Although this model is a reduction of the HH model, it describes the mathematical principle of an action potential generation and also the subthreshold behaviour. Depending on a constant value of injected current I, this model can present either different equilibrium points or a periodic orbit. Then, both a resting state or a repetitive firing state can be described. In fact, varying I, the model typically presents a Hopf bifurcation point, where at some finite frequency, the equilibrium point loses the stability (see FitzHugh (1961)).

In this thesis we will also consider a further simplification of the FitzHugh-Nagumo model consisting of using piecewise linear functions instead of $f(V, w)$ and $g(V, w)$. This system, called the *McKean model*, preserves the shape of the membrane potential $V(t)$ and it allows an exact knowledge of the nonlinear $f - I$ curve by means of standard techniques of non-smooth dynamical systems (see Coombes (2001)). We use it in Section 5.2, to estimate conductances in the spiking regime.

2.1.3.1   McKean model

In Section 5.2, we use the McKean model given by the piecewise linear differential system

$$\begin{cases} C\dot{V} = f(V) - w - w_0 + I(t), \\ \dot{w} = V - \gamma w - V_0, \end{cases}$$

where $I(t)$ is the external current and $f(V)$ is a piecewise linear caricature of the cubic FitzHugh-Nagumo function given by

$$f(V) = \begin{cases} -V & V < a/2, \\ V - a & a/2 \leq V \leq (1+a)/2, \\ 1 - V & V > (1+a)/2. \end{cases}$$

Biologically, the variables of the model are considered to be the membrane potential, $V(t)$, and the component of the membrane current, $w(t)$. The parameters a, w_0, V_0, and $\gamma > 0$ may be considered as conductance properties and combinations of membrane reversal potentials. Function $f(V)$ determines the outward membrane current at $V(t)$. Finally, C corresponds to the cell membrane capacitance which is assumed to be small and bounded $0 < C \ll 0.1$. See McKean (1970) for more details. The existence of this small parameter C makes the system to present a slow-fast dynamics, where V is the fast variable and w is the slow one.

2.1.4   Neuronal network model with short-term plasticity

Even though this thesis is focused on the estimation of conductances, it is also interesting to see the effects that the plasticity has on the conductances. For instance, how they change

when the network is depressed or facilitated. For this reason, we have implemented a complex biophysical network model describing slow oscillations observed in a small part of the visual cortex (see Compte et al (2003)), where short-term plasticity has been added according to Dayan and Abbott (2005). The short-term depression (STD) was already added in Benita et al (2012) reproducing the synaptic depression observed experimentally by Reig et al (2006), and showing the impact of STD on the network's behaviour.

The network consists of a population of 320 Hodgkin-Huxley type neurons, where the 80% of them are excitatory pyramidal cells and the 20% are inhibitory interneurons. All the neurons are equidistantly distributed on a line segment and interconnected through biologically plausible synaptic dynamics, with 20 random out-coming connections per neuron that are normally distributed by a Gaussian distribution $\mathcal{N}(0, \sigma^2)$; that is, neurons that are closer among them have more probability to be connected than the ones that are located further. For the excitatory neurons we use $\sigma = 250 \ \mu m$ whereas for the inhibitory neurons we use $\sigma = 125 \ \mu m$ (see Compte et al (2003), and references therein). Moreover, we consider the total length of the network of 5 mm. Figure 2.2) represents the connectivity matrix between the neurons, where the white points mean that they are connected.
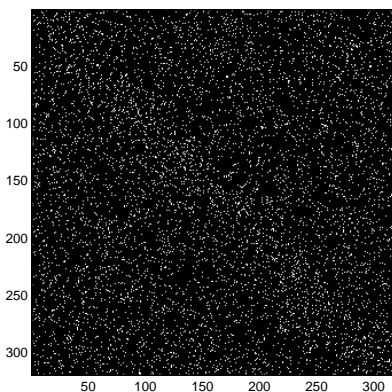

Figure 2.2: **Connectivity matrix of the population.** This plot shows whether two neurons are connected or not. Each row represents an enumerated pre-synaptic neuron whereas each column refers to the post-synaptic one. White points mean that the two corresponding neurons are connected whereas black dots mean that they do not.

Pyramidal neurons (excitatory neurons). The pyramidal neurons are considered to be two-compartment neurons, the soma and a dendrite. The somatic compartment is modelled by the spiking currents I_K and I_{Na}, the leak current I_L, and also a fast A-type K^+ current, I_A, a non-inactivating slow K^+ current, I_{KS}, and a Na^+-dependent K^+ current, I_{KNa}. The dendrite contains a high-threshold Ca^{2+} current, I_{Ca}, a Ca^{2+}-dependent K^+ current, a non-inactivating (persistent) Na^+ current, I_{NaP}, and finally an inward rectifier (activated by hyperpolarization) non-inactivating K^+ current, I_{AR}. The two compartments are coupled by the parameter g_{sd}.

The membrane potential in the soma and in the dendrite of each cell are given by

$$CA_s \frac{dV_s}{dt} = -A_s(I_L + I_{Na} + I_K + I_A + I_{KS} + I_{KNa}) - I_{syn,s} - g_{sd}(V_s - V_d),$$

$$CA_d \frac{dV_d}{dt} = -A_s(I_{Ca} + I_{KCa} + I_{NaP} + I_{AR}) - I_{syn,d} - g_{sd}(V_d - V_s),$$

where C is the membrane capacitance; V_s and V_d stand for the membrane potential at the soma and at the dendrite, respectively; parameters A_s and A_d refer to the area of the soma and the dendrite, respectively; $I_{syn,s}$ is the synaptic current impinging on the soma and $I_{syn,d}$ is the synaptic current impinging on the dendrite.

The ionic currents for the excitatory cells follow a Hodgkin-Huxley formalism governed by the first-order kinetics equation (2.2 -2.3). Hence, the currents and the respective gating variables are given by

$I_{Na} = g_{Na}m_\infty^3 h(V - V_{Na})$, where
$\quad m_\infty = \alpha_m/(\alpha_m + \beta_m);$ $\qquad\qquad\qquad h_\infty = \alpha_h/(\alpha_h + \beta_h);$
$\quad \alpha_m = 0.1(V + 33)/(1 - \exp(-(V + 33)/10));$ $\quad \alpha_h = 0.07\exp(-(V + 50)/10);$
$\quad \beta_m = 4\exp(-(V + 53.7)/12);$ $\qquad\qquad \beta_h = 1/(1 + \exp(-(V + 20)/10));$

$I_K = g_K n^4(V - V_K);$ where
$\quad n_\infty = \alpha_n/(\alpha_n + \beta_n);$
$\quad \alpha_n = 0.1(-v + 34)/(1 - \exp(-(V + 34)/10));$
$\quad \beta_n = 0.125\exp(-(V + 44)/25);$

$I_L = g_L(V - V_L);$

$I_A = g_A m_{A,\infty}^3 h_A(V - V_K)$, where
$\quad m_{A,\infty} = 1/(1 + \exp(-(V + 50)/20)); \quad h_{A,\infty} = 1/(1 + \exp(V + 80)/6);$
$\quad \tau_{h_A} = 15\ ms;$

$I_{KS} = g_{KS}m_{KS}(V - V_K)$, where
$\quad m_{KS,\infty} = 1/(1 + \exp(-(V + 34)/6.5));$
$\quad \tau_{KS} = 8/(\exp(-(v + 55)/30) + \exp((V + 55)/30));$

$I_{NaP} = g_{NaP}m_{NaP,infty}^3(V - V_{Na})$, where
$\quad m_{NaP,\infty} = 1/(1 + \exp(-(V + 55.7)/7.7));$

$I_{AR} = g_{AR}h_{AR,infty}(V - V_K)$, where
$\quad h_{AR,\infty} = 1/(1 + \exp((V + 75)/4));$

$I_{Ca} = g_{Ca}m_{Ca,infty}^2(V - V_{Ca})$, where
$\quad m_{Ca,\infty} = 1/(1 + \exp(-(V + 20)/9)); \quad d[Ca^{2+}]/dt = -\alpha_{Ca}A_d I_{Ca} - [Ca^{2+}]/\tau_{Ca};$
$\quad \alpha_{Ca} = 0.005\ \mu M/(nA \cdot ms); \qquad \tau_{Ca} = 150\ ms;$

$I_{KCa} = g_{KCa}[Ca^{2+}]/([Ca^{2+} + K_D])(V - V_K);$

$I_{KNa} = g_{KNa}\omega_\infty([Na^+])(V - V_K)$, where
$\quad \omega_\infty = 0.37/(1 + (38.7/[Na^+])^{3.5});$
$\quad d[Na^+]/dt = -\alpha_{Na}(A_s I_{Na} + A_d I_{NaP})$
$\qquad\qquad -R_{pump}\left\{[Na^+]^3/([Na^+] + 15^3) - [Na^+]_{eq}^3/([Na^+]_{eq}^3 + 15^3)\right\}.$

The ionic conductances are $g_{Na} = 50\ mS/cm^2$, $g_K = 10.5\ mS/cm^2$, $g_L = 0.0667 \pm 0.0667\ mS/cm^2$, $g_A = 1\ mS/cm^2$, $g_{KS} = 0.576\ mS/cm^2$, $g_{NaP} = 0.0686\ mS/cm^2$, $g_{AR} =$

$0.0257\ mS/cm^2$, $g_{Ca} = 0.43\ mS/cm^2$, $g_{KCa} = 0.57\ mS/cm^2$, and $g_{KNa} = 1.33\ mS/cm^2$. The ionic reversal potentials are $V_{Na} = 55\ mV$, $V_K = -100\ mV$, $V_L = -60.95 \pm 0.3\ mV$, and $V_{Ca} = 120\ mV$. The rest of constant values are $C = 1\ \mu F/cm^2$, $\phi = 1$, $A_s = 0.015\ mm^2$, $A_d = 0.35\ mm^2$, $g_{sd} = 1.75 \pm 0.1\ \mu S$, $K_D = 30\ \mu M$, $R_{pump} = 0.018\ mM/ms$, and $[Na^+]_{eq} = 9.5\ mM$. The standard deviation for the connection probability is $\sigma = 250\ \mu m$.

Interneurons (inhibitory neurons). The interneurons are considered as point neurons which only one compartment, the soma, which is driven by the leak, sodium and potassium currents following Wang and Buzsáki (1996).

The membrane potential of each neuron is given by

$$CA\frac{dV}{dt} = -A(I_L + I_{Na} + I_K) - I_{syn},$$

where V stands for the membrane potential, A is the total neuronal surface area and I_{syn} is the synaptic current impinging on the interneuron.

The ionic currents are given by

$I_{Na} = g_{Na}m_\infty^3 h(V - V_{Na})$, where
     $m_\infty = \alpha_m/(\alpha_m + \beta_m)$; $h_\infty = \alpha_h/(\alpha_h + \beta_h)$;
     $\alpha_m = 0.5(V + 35)/(1 + \exp(-(V + 35)/10))$; $\alpha_h = 0.35\exp(-(V + 58)/20)$;
     $\beta_m = 20\exp(-(V + 60)/18)$; $\beta_h = 5/(1 + \exp(-(V + 28)/10))$;

$I_K = g_K n^4(V - V_K)$; where
     $n_\infty = \alpha_n/(\alpha_n + \beta_n)$;
     $\alpha_n = 0.05(V + 34)/(1 - \exp(-(V + 34)/10))$;
     $\beta_n = 0.625\exp(-(V + 44)/80)$.

$I_L = g_L(V - V_L)$.

The ionic conductances for the interneurons are $g_{Na} = 35\ mS/cm^2$, $g_K = 9\ mS/cm^2$, and $g_L = 0.1025 \pm 0.0025\ mS/cm^2$. The ionic reversal potentials are $V_{Na} = 55\ mV$, $V_K = -90\ mV$, and $V_L = -63.8 \pm 0.15\ mV$. The rest of constant values are $C = 1\ \mu F/cm^2$ and $A = 0.02\ mm^2$. The standard deviation for the connection probability is $\sigma = 125\ \mu m$.

Notice that, both for the inhibitory and the excitatory neurons, the only sources of noise in the network come from the random connectivity between neurons and the randomly distributed parameters g_L, V_L and g_{sd}.

As commented above, these models will be used to simulate a network and study the outcoming synaptic conductances. We next describe the synaptic rules we impose to achieve the network dynamics.

Synaptic dynamics. When the j-th presynaptic neuron performs a spike, a group of neurotransmitters is released causing an activation of the strength of the synapse, $s_j(t)$, and an activation of the synaptic plasticity, that is, the probability of release $P_{rel,j}(t)$. Therefore, these neurotransmitters bind to the corresponding receptors of the postsynaptic

neuron causing an inflow of current that is modelled as

$$I_{syn} = \sum_{i \in \mathcal{P}} g_{syn,i} s_i(t) P_{rel,i}(t)(V - V_{syn})$$

where V is the voltage of a postsynaptic neuron, $\mathcal{P}$ is the set of all presynaptic neurons and V_{syn} is the synaptic reversal potential. Note that, indeed, $s_i(t)$ depends on both the pre-synaptic and the post-synaptic neuron. In this model, we assume that it only depends on the pre-synaptic cell.

The most common neurotransmitters that mediate the synapse are AMPA, NMDA or GABA. The first two neurotransmitters cause excitatory synapses whereas the last one inhibitory synapse, see Section 1.1, *Synapse*.

The synaptic strengths for the AMPA and GABA follow the differential equation

$$\frac{ds_i}{dt} = \alpha f(V_{pre,i}) - \frac{s_i}{\tau}; \qquad f(V_{pre,i}) = 1/(1 + \exp(-(V_{pre,i} - 20)/2)),$$

whereas the synaptic strength for the NMDA follows a second order differential equation written, in a first order differential system, as

$$\frac{ds_i}{dt} = \alpha x(1 - s_i) - \frac{s_i}{\tau}; \quad \text{and} \quad \frac{dx}{dt} = \alpha_x f(V_{pre,i}) - \frac{s_i}{\tau_x},$$

where $V_{pre,i}$ stands for the presynaptic voltage.

The parameters involved for the AMPA neurotransmitter are $\alpha = 3.48$, $\tau = 2\ ms$, and $V_{syn,AMPA} = 0\ mV$; for the NMDA neurotransmitter, they are $\alpha = 0.5$, $\tau = 100\ ms$, $\alpha_x = 3.48$, $\tau_x = 2\ ms$, and $V_{syn,NMDA} = 0\ mV$; and finally, for the GABA neurotransmitter, they are $\alpha = 1$, $\tau = 10\ ms$, and $V_{syn,GABA} = -70\ mV$. Note that, since each type of neurotransmitters has different a value of τ, their dynamics evolve differently, being AMPA and GABA faster than NMDA.

The probability of release $P_{rel}(t)$ follows the differential equation

$$\frac{dP_{rel}}{dt} = (P_0 - P_{rel})/\tau_{rel},$$

where P_0 is the probability of release at the steady state and τ_{rel} is the time to go back to the steady state when a deviation from P_0 occurs. In our simulations, we consider $P_0 = 1$ for the depression and $P_0 = 0.1$ for the facilitation.

When a synapse occurs, the probability of release of each neurotransmitter by the pre-synaptic neuron, changes according to a depression or a facilitation factor, f_D and f_F respectively (see Dayan and Abbott (2005)). Namely,

$P_{rel} \leftarrow f_D P_{rel}$, when short-term depression is considered; and,

$P_{rel} \leftarrow P_{rel} + f_F(1 - P_{rel})$, when short-term facilitation is considered.

If the pre-synaptic neuron is excitatory, then only the P_{rel} of the NMDA and AMPA neurotransmitters is affected, whereas if the pre-synaptic neuron is inhibitory, then the P_{rel} of GABA is changed. Parameters f_D and f_F take values between 0 and 1.

To describe the connectivity among different pools of neurons (excitatory and inhibitory), some rules have been considered in Compte et al (2003) and Benita et al (2012) causing

that, the final inhibitory (I_I) and excitatory (I_E) currents for each neuron j are given, respectively, by

$$I_{I,j}(t) = g_{GABA,j}(t)(V - V_{syn,GABA});$$
$$I_{E,j}(t) = g_{AMPA,j}(t)(V - V_{syn,AMPA}) + g_{NMDA,j}(t)(V - V_{syn,NMDA})$$

such that the conductances g_{GABA}, g_{AMPA} and g_{NMDA} are given by, being the i and j the pre- and post-synaptic neuron respectively,

$$g_{GABA,j}(t) = \begin{cases} g_{IE} \ s_{GABA,j}(t) \ P_{rel_{GABA,j}}(t), & \text{if } i \text{ is inhibitory and } j \text{ is excitatory;} \\ g_{II} \ s_{GABA,j}(t) \ P_{rel_{GABA,j}}(t), & \text{if } i \text{ and } j \text{ are inhibitory;} \end{cases}$$

$$g_{AMPA,j}(t) = \begin{cases} g_{EE}^{AMPA} \ s_{AMPA,j}(t) \ P_{rel_{AMPA,j}}(t), & \text{if } i \text{ and } j \text{ are excitatory;} \\ g_{EI}^{AMPA} \ s_{AMPA,j}(t) \ P_{rel_{AMPA,j}}(t), & \text{if } i \text{ is excitatory and } j \text{ is inhibitory;} \end{cases}$$

$$g_{NMDA,j}(t) = \begin{cases} g_{EE}^{NMDA} \ s_{NMDA,j}(t) \ P_{rel_{NMDA,j}}(t), & \text{if } i \text{ and } j \text{ are excitatory;} \\ g_{EI}^{NMDA} \ s_{NMDA,j}(t) \ P_{rel_{NMDA,j}}(t), & \text{if } i \text{ is excitatory and } j \text{ is inhibitory,} \end{cases}$$

where $g_{IE} = 4.15 \ nS$, $g_{II} = 0.165 \ nS$, $g_{EE}^{AMPA} = 5.4 \ nS$, $g_{EI}^{AMPA} = 2.25 \ nS$, $g_{EE}^{NMDA} = 0.9 \ nS$, and $g_{EI}^{NMDA} = 0.5 \ nS$.

All synapses are supposed to be chemical, neglecting possible electrical coupling.

This network was initially designed for a population of 1280 neurons by Compte et al (2003). Even though in our work we only use a network of 320 neurons (in order to reduce the computational time), no significant differences have been noticed in preliminary runs with 1280 and 320 neurons, respectively.

For more details on the network see Compte et al (2003) and Benita et al (2012).

2.2   Synaptic drive

The membrane potential traces we use come from the computational models described previously in this chapter and also from *in vivo* experiments. In this section we explain the synaptic current we use in the computational models to generate *in sillico* data. In Section 2.2.1 we model the synaptic current and in Section 2.2.2 we depict the synaptic input we use.

2.2.1   Modelling chemical synapses

In general the external current, $I(t)$, is split into two relevant currents: the applied current, I_{app}, which is often used as a control parameter, and the synaptic current, I_{syn}, which is the current that the neuron is receiving from other neurons; that is, $I(t) = I_{app} - I_{syn}$, formulation that we are going to consider in the single cell models described in Section 2.1.

Since the pre-synaptic neuron can be either excitatory or inhibitory, depending on the type of neurotransmitters that the neuron has (see Section 1.1), the synaptic current can also be split taking into account the amount of excitatory and inhibitory current that the neuron is receiving. Then, the synaptic current can be given by

$$I_{syn} = g_E(t)(V(t) - V_E) + g_I(t)(V(t) - V_I),$$

where $g_E(t)$ and $g_I(t)$ are the excitatory and the inhibitory conductances, respectively, and V_E and V_I are the excitatory and the inhibitory reversal potentials, respectively.

In all neuronal models we use in Chapter 5, except the McKean model, the synaptic current is split into the excitatory and the inhibitory parts, being the reversal potentials given by $V_E = 0\ mV$, $V_I = -80\ mV$. For the pyramidal model, described in Section 2.1.2.1 with external current given in Section 2.2.1, we take $I_{app} \in [-1, 1]\ \mu A/cm^2$ (see Appendix B in Guillamon et al (2006) for a justification of this choice), unless otherwise is stated. For the stellate model, described in Section 2.1.2.2 with external current given in Section 2.2.1, we will usually take $I_{app} \in [-4, -3]\ \mu A/cm^2$, unless otherwise is stated. The applied current in the QIF model, described in Section 2.1.1.1 with external current in Section 2.2.1, is chosen to avoid the neuron from firing, and it depends on the model we would like to approximate (see Section 5.1.2.1).

In the McKean model, described in Section 2.1.3.1 with external current given in Section 2.2.1, since we are only interested in the synaptic current, we do not split it and we consider V_{syn}, which is considered to lie between the boundaries, $a/2$ and $(1+a)/2$, to be biologically plausible. In our simulations, we took V_{syn} as the central value of this interval; that is, $V_{syn} = 1/4 + 1/2a$.

2.2.2   Synaptic inputs

In the simulations of the models, we consider different traces of conductances that come from three different sources: toy traces obtained as sinusoidal functions that combine different frequencies and amplitudes; traces that follow an Ornstein-Uhlenbeck (OU) process, see Section 1.3, with an added sinusoidal behaviour; and finally traces that are obtained from a computational network that models layer4 Cα of primary visual cortex. Next, we explain each of them in a more detailed way.

2.2.2.1   Conductances generated with deterministic sinusoidal shapes

To see the efficiency of the estimation procedure described in Section 5.2, and to compare whether it is related to the frequency and amplitude of the conductances, we create some synaptic conductance traces with different frequencies and amplitudes. These traces are going to be used to simulate membrane potential traces in the McKean model. Since in this model we do not discern between excitatory and inhibitory conductances, only the total synaptic conductance is created.

In Figure 2.3 the different synaptic conductance traces that have been generated are depicted. In Panel A, the conductance trace has only high amplitude oscillations, such that $g_{syn}(t) = 0.2\sin(2\pi t/10) + 0.2)$. The second conductance trace, Panel B, combines small with big oscillations and it is given by $g_{syn}(t) = 0.2\sin(2\pi t/30) + 0.2/5\sin(2\pi t/5) + 0.2$. Finally, in the last trace we consider, Panel C, both frequency and amplitude of the small oscillations have been changed with respect to the one in Panel B to create a faster conductance trace that abruptly changes in time. The equation of this conductance trace is given by $g_{syn}(t) = 0.1\sin(2\pi t/20) + 0.2\sin(2\pi t/2) + 0.4$.
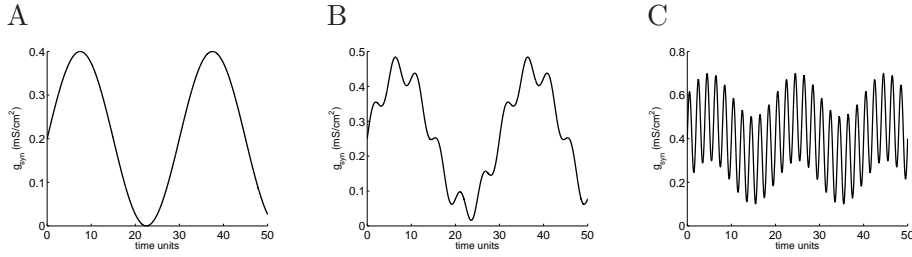
Figure 2.3: **Toy conductance traces.** Complete $50\,ms$ time courses of the total synaptic conductances $(g_{syn}(t))$ used to drive the activity of the target neuron. The traces have been generated as: $g_{syn}(t) = 0.2\sin(2\pi t/10) + 0.2$, in Panel A; $g_{syn}(t) = 0.2\sin(2\pi t/30) + 0.2/5\sin(2\pi t/5) + 0.2$, in Panel B; and $g_{syn}(t) = 0.1\sin(2\pi t/20) + 2\cdot 0.1\sin(2\pi t/2) + 0.4$, in Panel C; in order to obtain different kinds of oscillations.

2.2.2.2 Conductances following an OU-process

To computationally test the stochastic estimation procedure given in Section 5.1.2, we consider a trace of conductances that follows an Ornstein-Uhlenbeck (OU) process, where a sinusoidal behaviour has been added. That is, the conductances follow the stochastic differential equation

$$dg_x(t) = \frac{1}{\tau_x}\left(x_0 + \mu_x\cos(w_x t) - g_x(t)\right)dt + \sigma_x dW(t), \qquad (2.7)$$

where x denotes either the excitatory (E) or the inhibitory (I) conductances. In the simulations, we set the constant values $\tau_E = 10\,ms$, $\tau_I = 5\,ms$, $g_{E_0} = 1\,mS/cm^2$, $g_{I_0} = 0.7\,mS/cm^2$, $\mu_E = 0.0321\,mS/cm^2$, $\mu_I = 0.0867\,mS/cm^2$, $w_E = w_I = 2\pi/1000\ m^{-1}$, $\sigma_E = 0.00064\ mS/(cm^2\sqrt{ms})$, and $\sigma_I = 0.00065\ mS/(cm^2\sqrt{ms})$, where the subscripts E and I stand for the excitatory and the inhibitory conductances, respectively. These values have been chosen with the aim of collecting data with amplitude and frequency similar to the estimated conductance traces in the experimental data in Berg and Ditlevsen (2013).

In Figure 2.4 the time course of excitatory and the inhibitory conductances obtained in this case is represented.

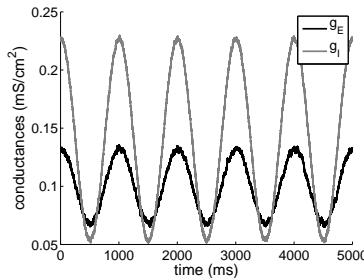Figure 2.4: **Conductance trace following an OU-process combined with a sinusoidal function.** Complete $(5\,s)$ time courses of the excitatory $(g_E(t)$, black trace) and inhibitory $(g_I(t)$, grey trace) conductances used to drive the activity of the target neuron. The conductance traces have been generated as an OU-process where a sinusoidal function has been added to obtain an oscillatory behaviour.

2.2.2.3   Conductances extracted from an *in sillico* network

As test conductance courses, we will also use conductance traces (with a $1\,ms$ resolution) obtained from a computational network that models layer $4C\alpha$ of primary visual cortex, see McLaughlin et al (2000) and Tao et al (2004). The complete conductance traces fed into the pyramidal cell model are shown in Figure 2.5. In the stellate cell model, we have rescaled these data by a factor of 3 in order to adjust to the amplitude of the input used in Rotstein (2015).
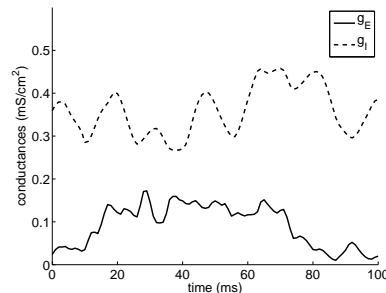

Figure 2.5: **Conductance traces obtained *in sillico* from layer $4C\alpha$ of primary visual cortex .** Complete $(1\,ms)$ time courses of the excitatory ($g_E(t)$, solid trace) and inhibitory ($g_I(t)$, dashed trace) conductances used to drive the activity of the target neuron. The conductance traces have been obtained from a computational network that models layer $4C\alpha$ of primary visual cortex (see McLaughlin et al (2000) and Tao et al (2004)).

For the McKean model, we use a $50\,ms$ total synaptic conductance trace, which is obtained as the sum of the excitatory and the inhibitory conductances and rescaled as in the stellate model (by a factor of 3). The time course of the total synaptic conductance is plotted in Figure2.6.
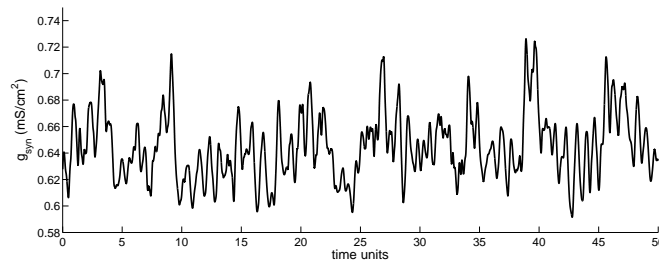
Figure 2.6: **Total synaptic conductance trace obtained *in sillico* from layer $4C\alpha$ of primary visual cortex.** Complete $(50\,ms)$ time courses of the synaptic conductances used to drive the activity of the target neuron in the McKean model. The conductance trace has been obtained from a computational network that models layer $4C\alpha$ of primary visual cortex (see McLaughlin et al (2000) and Tao et al (2004)).

2.3   Experimental data

In Chapter 5, we use membrane potential traces obtained also by *in vivo* experiments as examples to test the methods of estimation of conductances that we derive. This experimental data has been obtained by Prof. Rune Berg using the current clamp technique, see Chapter 1, *Electrophysiological techniques.*

In the *in vivo* experiments, we use real data where traces of 25 *s* of the membrane potential of a motoneuron were measured during different current injections under the same mechanical stimulation. The trace we use to estimate *in vivo* conductances is given in Figure 2.7.
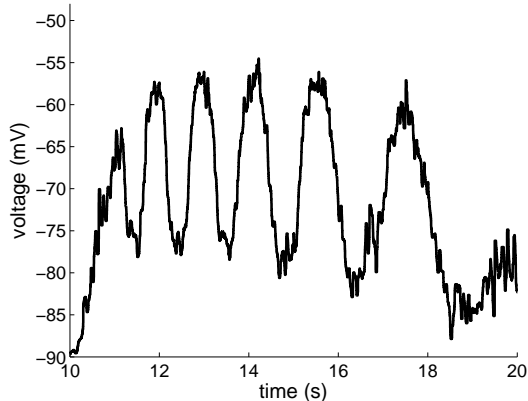

Figure 2.7: **Intracellular recording of spinal motorneuron of read-eared turtles**. Complete (20 *s*) time course of the membrane potential extracted in current-clamp mode of spinal motorneuron of red-eared turtles.

Briefly, the experiments were performed in an integrated spinal cord-carapace preparation from an adult red-eared turtle (*Trachemys scripta elegans*) as in Petersen et al (2014) and Ves (2015). In the integrated preparation, the spinal cord remains in the spinal canal with the tactile sensory nerves from the carapace intact. The motor nerves are carefully transected to avoid muscle movements and dissected out for electroneurogram recordings. A scratch reflex was activated by mechanical somato-sensory stimulation of selected regions on the carapace, which induced motor network activity of ∼20 s duration. Intracellular recordings in current-clamp mode were obtained from a motoneuron in segment D10. Data were sampled at 20 kHz, i.e. the time step between observations as $\Delta = 0.05$ms.

In Figure 2.8, we depict the $V - I$ relationship (red dots) obtained by injecting different levels of current into the neuron in absence of synaptic activity. To compute this curve, once we have obtained the time course of $V(t)$, we have averaged, for each value of injected current I, the membrane potential over time. In this Figure we also made a linear fit (grey line) and a quadratic fit (black line) of the $V - I$ points. The quadratic fit is clearly chosen above the linear fit using either AIC[8] or BIC[9] criteria, since differences are both larger than 10 (ΔAIC = 14.54, ΔBIC = 13.45). This is the value suggested in Burnham and Anderson (2002) as the critical value for the less plausible model to have essentially no support in the data compared with the better model.

The quadratic approximation is given by $V(I_{app}) = -1.94I_{app}^2 + 13.09I_{app} - 72.14$. Since the last input current for which the neuron did not spike was 0.55 $\mu A/cm^2$, we set $I_T = -0.55 \ \mu A/cm^2$, which corresponds to $V_T = -79.926 \ mV$ from the $V - I$ curve. The remaining neuron parameters have been computed as $V_L = -77 \ mV$, $V_I = -79 \ mV$, $V_E = 0 \ mV$, $g_L = 0.026 \ mS/cm^2$, $I_{app} = -1.24 \ \mu A/cm^2$, and $C = 1 \ \mu F/cm^2$; these values

---

[8]AIC is the acronym of *Akaike information criterion*. It is a statistical measure to estimates the quality of each mode. It is given as $AIC = 2k - 2\ln(\hat{\mathcal{L}})$, where k is the number of parameters to be estimated and $\hat{\mathcal{L}}$ the maximum value of the likelihood function

[9]BIC is the acronym of *Bayesian information criterion*. It is given as $BIC = k\ln(n) - 2\ln(\hat{\mathcal{L}})$, where k is the number of parameters to be estimated, n is the length of the trace (number of observations), and $\hat{\mathcal{L}}$ the maximum value of the likelihood function
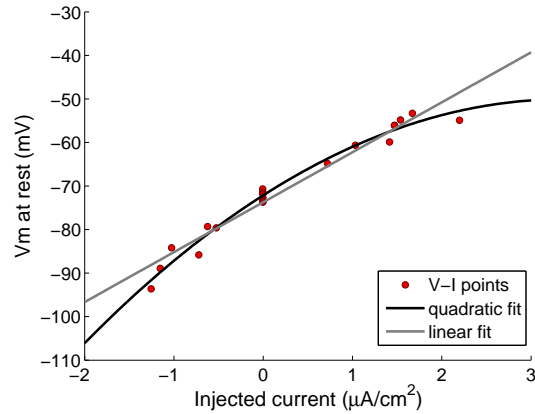
Figure 2.8: **V-I curve of the measured motoneuron**. The red dots are the $V - I$ relations obtained by applying different current levels to the motoneuron. The black line shows the quadratic fit to these points, the grey line depicts the linear fit.

have been obtained from the actual data by using the R. Berg code at Berg (2013) (see also Petersen et al (2014)).

2.4 Numerical methods

Along the thesis we use different numerical methods, mainly to solve ordinary differential systems but also implicit equations and to treat the data we are obtaining. Depending on the model we are using and the procedures we follow, in Chapter 4 and also in the different sections of Chapter 5 we use different mathematical tools, all of them implemented in Matlab®.

2.4.1 Numerical methods for the neuronal network

The systems of differential equations of the neuronal network in Chapter 4 were integrated by using the Runge-Kutta 4-5 method with a fixed time step of 0.05 ms, which is the smallest time step usually used in experimental recordings.

In order to represent the dynamics of the neuron, because of the large amount of neurons it has, we use two different neural coding schemes, which are the instantaneous firing rate (IFR) and the raster plot. Following, we explain both of them.

2.4.1.1 Instantaneous firing rate description

To code the activity of the neurons in the network we use the *instantaneous firing rate* (IFR) coding. The IFR for each neuron is computed by binning the spike train (we use a bin width of 100 ms) and dividing the number of spikes detected within the bin. That is, for each window of 100 ms, we average the number of spikes over time. To obtain a smoother IFR function, the average number of spikes computed within the bin are convoluted with a Gaussian function with mean $\mu = 25\ ms$ and standard deviation $\sigma = 5\ ms$.

The analysis has been performed by adapting the tool SPYCODE developed in Matlab by Bologna et al (2010).

By averaging the IFR over all the excitatory neurons we obtain what we call the *excitatory IFR*, which corresponds to all the excitatory population. In the same way, if we consider all inhibitory neurons, then we obtain what we call the *inhibitory IFR*, see lower subpanels in Figure 4.1.

2.4.1.2   Coloured raster plot description

Using the IFR coding scheme, we do not have information about the onset time of the action potentials. To visualize this information we use coloured raster plots where colours indicate the IFR (the warmer the colour, the highest the IFR) and the axes represent time and neurons' position, see upper subpanels in Figure 4.1. Therefore, for each neuron we distinguish the firing onset when the colour in the corresponding horizontal line changes from the darkest blue to other color. As a result, we can also visualize the synchrony of the onset in the entire population.

2.4.2   Numerical methods for the deterministic conductances' estimation

The systems of differential equations, of both models used in Section 5.1.1, were integrated using the Runge-Kutta 4-5 method with a fixed time step of $0.05\,ms$. First, we tested that voltage traces did not change when using lower time steps and higher order variable step methods, but the fact of needing equispaced values for the filtering process was a key point for the method's choice in this case (see Vich (2012)). Moreover, to solve the integral in Subsection 5.1.1.3, paragraph *Quadratization alternative*, we have used the trapezoidal rule with the same time step than for the integration method, $0.05\,ms$. The Matlab code of the quadratic approach to estimate conductances given in Subsection 5.1.1.2, *Quadratization approach*, is available at Vich and Guillamon (2015b).

2.4.3   Numerical methods for the non-deterministic conductances' estimation

In Section 5.1.2, the stochastic differential equations, both for the synaptic drive and the neuron models, have been solved using the Euler-Maruyama method with a step size of $\Delta = 0.01\,ms$. Then, data has been subsampled every 5-th observation to reduce discretization errors. In this case, we get samples with time step $0.05\,ms$, which is like our experimental data.

2.4.4   Numerical methods for the conductances' estimation in the spiking regime

In Section 5.2, to contrast the goodness of the approximated period expression $\hat{T}$, the numerical periodic considered as the real one has been computed using both Newton-Raphson method and bisection method with a tolerance $TOL = 1e - 11$ (see Appendix C.1 for more details of the routine). Same methods have been used to estimate the synaptic conductance g_{syn} with tolerance $TOL = C^2$.

Moreover, to integrate the differential piecewise linear system we have used the Runge-Kutta 7-8 method with tolerance $TOL = 1e - 8$ and a maximal step size $h_{max} = 1e - 1$. We have used the `edo78` function of Matlab®.

Finally, a cubic spline interpolation has been used to estimate the time-course of the synaptic conductances. We have used the `spline` function of Matlab®.

50

Chapter 3

Slow-fast n-dimensional piecewise linear systems

3.1 Introduction and main results

Slow-fast systems are differential systems evolving on two different time scales, described in Section 1.2, systems (1.1) and (1.2). We will follow the terminology introduced there.

Slow-fast systems are widely used to model complex oscillatory behaviours exhibited by real systems. In neuroscience, the burst waveform or the mixed-mode oscillations (MMO) are two examples of such a complex behaviour.

The burst waveform consists of voltage patterns of a neuron characterized by periods of electrical spikes followed by periods of quiescence during which the neuron is repolarized. This phenomena involves a physiological slow variable that eventually changes the behaviour of the fast subsystem, for instance, going from an oscillatory to an equilibrium regime, and so forth. An extensive list of slow-fast mechanisms for bursting patterns appears in Izhikevich (2007), see also the references therein.

On the other hand, the MMO is a periodic behaviour which presents an evident oscillatory structure within each period alternating groups of small and large-amplitude oscillations. MMOs can be observed in several application areas such that chemical reaction dynamics (see references in Desroches et al (2010) and Desroches et al (2012)), in neuroscience (see, for instance, Krupa et al (2008), Wechselberger and Weckesser (2009a), and Wechselberger and Weckesser (2009b)), in mathematical biology (see Akman et al (2005)), and in population dynamics (see Brøns et al (2013)). Mechanisms for the creation of small oscillations in slow-fast systems are related to the intricate geometry of multiple-time-scale dynamical systems. For a recent account on MMO and slow-fast dynamics, we refer the reader to the interesting survey of Desroches et al (2012).

Under normal hyperbolicity conditions, Fenichel's geometric theory (Fenichel (1979) and Jones (1995)), which is also recollected in Theorem 1.1, ensures the persistence of the critical manifold $\mathcal{S} = \{(\mathbf{u}, \mathbf{v}) \in \mathbb{R}^n : \mathbf{f}(\mathbf{u}, \mathbf{v}, 0) = \mathbf{0}\}$ of the fast subsystem (1.3) as the slow manifold, $\mathcal{S}_\varepsilon$, which is locally invariant under the flow of system (1.1). Moreover, the stability properties of the manifold $\mathcal{S}_\varepsilon$ are inherited from those of the critical manifold $\mathcal{S}$, and the restriction of the flow of system (1.1) to $\mathcal{S}_\varepsilon$ is a regular perturbation of the reduced flow (1.4).

When normal hyperbolicity fails, for instance on the fold manifold (i.e. points where $\mathcal{S}$ folds), under suitable conditions, the slow-fast systems present canard orbits. Experimental observations of canard orbits were early reported (see Itoh and Tomiyasu (1990)) and slow-fast systems with piecewise linear vector field were considered to prove the existence of canard orbits (see Komuro and Saito (1991) and Arima et al (1997)). An increasing interest about slow-fast piecewise linear vector fields can be noticed in the number of recent publications as, for instance, Llibre et al (2002), Nakano et al (2005), Desroches and Jeffrey (2011), Rotstein et al (2012), and Desroches et al (2013). This interest is also extended to more general contexts like continuous piecewise smooth vector fields (see Pokrovskii et al (2011)) or discontinuous piecewise smooth vector fields (see Buzzi et al (2012)).

This chapter is mainly concerned with maximal canard orbits occurring in n-dimensional piecewise linear slow-fast systems. More precisely, conditions for the existence of maximal canard orbits and/or faux maximal canard orbits are established in Theorem 3.2. In Theorem 3.3 we show that these maximal canards perturb from singular orbits (singular canards) whose order of contact with the fold manifold is greater than or equal to two.

We remark that, in the smooth case, the standard way to study maximal canards is by analysing the reduced flow around the folded singularities (singular points of the slow subsystem lying in the fold manifold and appearing after regularization), see Wechselberger (2012). In our framework, to tackle the study of maximal canards we are following the approach in Prohens and Teruel (2013); there, the attracting and repelling branches of the slow manifold, and also their intersection, are explicitly obtained as a consequence of a Fenichel's-like Theorem for PWL systems. In the current work we extend this result to the n-dimensional case as Theorem 3.1. For a version of Fenichel's Theorem in the smooth case, see Theorem 1.1, or Desroches et al (2012) and Wechselberger (2012).

Slow manifolds play an important role for singularly perturbed problems and expressions of them can be obtained, as power series expansion in the singular perturbation parameter, for singularly perturbed linear systems, see Kokotović et al (1999, Chapter 2) and Khorasani (1986, 1989). Even when these results are well known, as far as we know, the problem of studying the intersections between the attracting and the repelling branches of the slow manifold, in order to obtain maximal canards, has not been addressed yet in the study of n-dimensional singularly perturbed piecewise linear systems. In this chapter we are tackling with this study.

Throughout this chapter, we are considering the n-dimensional singularly perturbed differential system (1.1) with $n \geq 2$, $s = n - 1$ slow variables $\mathbf{u} = (u_1, \ldots, u_s)$, $q = 1$ fast variable v, given by

$$\mathbf{g}(\mathbf{u}, v, \varepsilon) = A\mathbf{u} + \mathbf{a}v + \mathbf{b} \quad \text{and} \quad f(\mathbf{u}, v, \varepsilon) = u_1 + |v|,$$

where $A = (a_{ij})_{1 \leq i,j \leq s}$ is an $s \times s$ real matrix and, $\mathbf{a} = (a_1, a_2, \ldots, a_s)^T$ and $\mathbf{b} = (b_1, b_2, \ldots, b_s)^T$ are vectors in $\mathbb{R}^s$. In Theorem 3.2, the case $n = 2$ is treated as an exception (see Remark 3.1). From now on the superscript T stands for the transposed object.

Summing up, we are considering the singularly perturbed differential system

$$\begin{cases} \dot{\mathbf{u}} = \varepsilon(A\mathbf{u} + \mathbf{a}v + \mathbf{b}), \\ \dot{v} = u_1 + |v|, \end{cases} \tag{3.1}$$

together with its associated non-perturbed systems, the fast subsystem

$$\begin{cases} \dot{\mathbf{u}} = \mathbf{0}, \\ \dot{v} = u_1 + |v|, \end{cases} \tag{3.2}$$

and the slow subsystem

$$\begin{cases} \mathbf{u}' = A\mathbf{u} + \mathbf{a}v + \mathbf{b}, \\ 0 = u_1 + |v|. \end{cases} \tag{3.3}$$

We want to point out that the slow subsystem (3.3) is a linear differential equation defined on the critical manifold $\mathcal{S} = \{(\mathbf{u}, v) \in \mathbb{R}^n : u_1 + |v| = 0\}$ which splits into the two normally hyperbolic parts $\mathcal{S}^+ = \mathcal{S} \cap \{v > 0\}$ and $\mathcal{S}^- = \mathcal{S} \cap \{v < 0\}$, and the manifold $\mathcal{F} = \mathcal{S} \cap \{v = 0\}$. As we claim in Lemma 3.1, the vector field defined on each of these open half-hyperplanes is linear, but it is not defined on $\mathcal{F}$. To overcome this problem, we consider the Filippov's convention, described in Convention 1.1 (see also Filippov (1988)). Then, the reduced flow associated with the slow-fast system (3.1) is generated by the discontinuous piecewise linear system (3.11) in Section 3.2.

The vector field given by system (3.1) is continuous and nonlinear, since the function $f(\mathbf{u}, v, \varepsilon)$ is piecewise linear. Therefore, the behaviour of the flow is set by coupling the flow of the two linear systems given by f, each one defined on one of the half-spaces which are splitted by the hyperplane $\{v = 0\}$, so called the switching manifold.

Before to state our main results, we introduce the superscript notation $+$ and $-$ referring the object to the half-space $\{v \geq 0\}$ and $\{v \leq 0\}$, respectively, in which this object is restricted. Therefore, system (3.1) writes as

$$\begin{pmatrix} \dot{\mathbf{u}} \\ \dot{v} \end{pmatrix} = \begin{cases} B_\varepsilon^+ \begin{pmatrix} \mathbf{u} \\ v \end{pmatrix} + \mathbf{c}_\varepsilon & \text{if } v \geq 0, \\[2ex] B_\varepsilon^- \begin{pmatrix} \mathbf{u} \\ v \end{pmatrix} + \mathbf{c}_\varepsilon & \text{if } v \leq 0, \end{cases} \tag{3.4}$$

where

$$B_\varepsilon^+ = \begin{pmatrix} \varepsilon A & \varepsilon \mathbf{a} \\ \mathbf{e}_1^T & 1 \end{pmatrix}, \qquad B_\varepsilon^- = \begin{pmatrix} \varepsilon A & \varepsilon \mathbf{a} \\ \mathbf{e}_1^T & -1 \end{pmatrix}, \qquad \mathbf{c}_\varepsilon = \begin{pmatrix} \varepsilon \mathbf{b} \\ 0 \end{pmatrix}, \tag{3.5}$$

and $\mathbf{e}_1$ is the first element of the canonical base of $\mathbb{R}^s$.

Given a point $\mathbf{q} \in \mathbb{R}^n$, we denote the orbit of system (3.4) through $\mathbf{q}$ by $\gamma_\mathbf{q}$. As long as the orbit $\gamma_\mathbf{q}$ remains in $\{v \geq 0\}$, $\gamma_\mathbf{q}$ is part of the flow of the linear system $\dot{\mathbf{x}} = B_\varepsilon^+ \mathbf{x} + \mathbf{c}_\varepsilon$. Therefore, its behaviour is determined by the eigenvalues of the matrix B_ε^+. As we see in Section 3.3, the spectrum of the matrix B_ε^+ decomposes into two parts, one formed by s eigenvalues (taking into account the multiplicity) of $O(\varepsilon)$ and the other one which is a real eigenvalue of $O(1)$. We denote them by

$$\lambda_k^+ = \beta_k^+ \varepsilon + O(\varepsilon^2) \text{ for } k = 1, \dots, s \quad \text{and} \quad \lambda_n^+ = 1 + O(\varepsilon).$$

The first s eigenvalues are responsible for the slow dynamics whereas the last one is responsible for the fast dynamics in $\{v \geq 0\}$. Consequently, for ε small enough, the slow dynamics is restricted to a half-hyperplane defined by the generalized eigenvectors associated to the eigenvalues $\{\lambda_k^+\}_{k=1}^s$. As it is shown in Section 3.3, this half-hyperplane is the slow manifold in $\{v \geq 0\}$ and, it is given by

$$\mathcal{S}_\varepsilon^+ = \left\{ (\mathbf{u}, v) \in \mathbb{R}^n : v \geq 0, \ -\mathbf{e}_1^T (\varepsilon A - \lambda_n^+ I)^{-1} \mathbf{u} + v = \frac{\varepsilon}{\lambda_n^+} \mathbf{e}_1^T (\varepsilon A - \lambda_n^+ I)^{-1} \mathbf{b} \right\}.$$

Similar arguments can be applied as long as the orbit $\gamma_\mathbf{q}$ lies in $\{v \leq 0\}$. In this case, the spectrum of the matrix B_ε^- decomposes into

$$\lambda_k^- = \beta_k^- \varepsilon + O(\varepsilon^2) \text{ for } k = 1, \dots, s, \quad \text{and} \quad \lambda_n^- = -1 + O(\varepsilon),$$

and the slow dynamics takes place on the half-hyperplane (slow manifold in $\{v \leq 0\}$) given by

$$\mathcal{S}_\varepsilon^- = \left\{ (\mathbf{u}, v) \in \mathbb{R}^n : \ v \leq 0, \ -\mathbf{e}_1^T (\varepsilon A - \lambda_n^- I)^{-1} \mathbf{u} + v = \frac{\varepsilon}{\lambda_n^-} \mathbf{e}_1^T (\varepsilon A - \lambda_n^- I)^{-1} \mathbf{b} \right\}.$$

Since $\mathcal{S}_\varepsilon^+$ and $\mathcal{S}_\varepsilon^-$ are slow manifolds, the set $\mathcal{S}_\varepsilon = \mathcal{S}_\varepsilon^+ \cup \mathcal{S}_\varepsilon^-$ is also a slow manifold. In fact, $\mathcal{S}_\varepsilon$ results to be a Fenichel's manifold as we show in the following Fenichel's-like Theorem.

Theorem 3.1. *For a sufficiently small and $\varepsilon > 0$, the manifold $\mathcal{S}_\varepsilon = \mathcal{S}_\varepsilon^+ \cup \mathcal{S}_\varepsilon^-$ satisfies the following statements.*

a) *$\mathcal{S}_\varepsilon$ is locally invariant under the flow of system* (3.1).

b) *The restriction on $\mathcal{S}_\varepsilon$ of the flow of system* (3.1) *is a regular perturbation of the reduced flow defined by the slow subsystem* (3.3) *on the critical manifold $\mathcal{S}$.*

c) *$\mathcal{S}_\varepsilon^+$ is the repelling branch of S_ε and $\mathcal{S}_\varepsilon^-$ is the attracting branch of S_ε.*

d) *Given a compact subset $\hat{S}$ of the critical manifold $\mathcal{S}$, there exists a compact subset $\hat{S}_\varepsilon$ of the slow manifold $\mathcal{S}_\varepsilon$ which is diffeomorphic to $\hat{S}$ and such that $d_H(\hat{S}_\varepsilon, \hat{S}) = O(\varepsilon)$, where d_H denotes the Hausdorff distance.*

A point $\mathbf{p}_\varepsilon$ in $\mathcal{S}_\varepsilon^+ \cap \mathcal{S}_\varepsilon^-$, it is said to be a maximal canard (resp. faux maximal canard) point if the orbit, $\gamma_{\mathbf{p}_\varepsilon}$, through $\mathbf{p}_\varepsilon$ is a maximal canard (resp. faux maximal canard) orbit. From Theorem 3.1, since $\mathcal{S}_\varepsilon^+$ (resp. $\mathcal{S}_\varepsilon^-$) is the repelling (resp. attracting) branch of the slow manifold, the direction of the flow at every point $\mathbf{p}_\varepsilon$ in $\mathcal{S}_\varepsilon^+ \cap \mathcal{S}_\varepsilon^- \subset \{v = 0\}$ gives us a criterion to distinguish between maximal canard points (when the flow goes in the $\mathbf{e}_n$ direction) and faux maximal canard points (when the flow goes in the $-\mathbf{e}_n$ direction). Here and hereinafter, $\mathbf{e}_n$ stands for the n-th element in the canonical base of $\mathbb{R}^n$. Pay attention on the fact that $\mathbf{e}_1$ has been formerly defined as the first element of the canonical base of $\mathbb{R}^s$.

The direction of the flow of system (3.1) at a point $\mathbf{p}_\varepsilon$ belonging to the switching manifold $\{v = 0\}$, is given by the order of contact of the flow with $\{v = 0\}$ at $\mathbf{p}_\varepsilon$. In terms of the vector field written as in equation (3.4), this order of contact is k (with $k \in \mathbb{N}$) when

$$\mathbf{e}_n^T (B_\varepsilon^+ \mathbf{p}_\varepsilon + \mathbf{c}_\varepsilon) = \mathbf{e}_n^T (B_\varepsilon^- \mathbf{p}_\varepsilon + \mathbf{c}_\varepsilon) \neq 0, \qquad\qquad\qquad \text{if } \ k = 1,$$

$$\begin{cases} \mathbf{e}_n^T (B_\varepsilon^+)^r (B_\varepsilon^+ \mathbf{p}_\varepsilon + \mathbf{c}_\varepsilon) = \mathbf{e}_n^T (B_\varepsilon^-)^r (B_\varepsilon^- \mathbf{p}_\varepsilon + \mathbf{c}_\varepsilon) = 0 \quad \text{for} \quad r = 0, \ldots, k-2, \\ \\ \mathbf{e}_n^T (B_\varepsilon^+)^{k-1} (B_\varepsilon^+ \mathbf{p}_\varepsilon + \mathbf{c}_\varepsilon) = \mathbf{e}_n^T (B_\varepsilon^-)^{k-1} (B_\varepsilon^- \mathbf{p}_\varepsilon + \mathbf{c}_\varepsilon) \neq 0. \end{cases} \quad \text{if } \ k \geq 2,$$

$$\tag{3.6}$$

When the order of contact is even, the orbit $\gamma_{\mathbf{p}_\varepsilon}$ does not cross the switching manifold, and it is locally contained in the half-space $\{v \geq 0\}$ (when $\mathbf{e}_n^T (B_\varepsilon^+)^{k-1} (B_\varepsilon^+ \mathbf{p}_\varepsilon + \mathbf{c}_\varepsilon) > 0$) or in $\{v \leq 0\}$ (when $\mathbf{e}_n^T (B_\varepsilon^+)^{k-1} (B_\varepsilon^+ \mathbf{p}_\varepsilon + \mathbf{c}_\varepsilon) < 0$). Otherwise, when the order of contact is odd, the orbit $\gamma_{\mathbf{p}_\varepsilon}$ crosses the switching manifold either transversally (if $k = 1$) or tangentially (if $k > 1$); in both cases, the orbit crosses in the direction of $\mathbf{e}_n$ if $\mathbf{e}_n^T (B_\varepsilon^+)^{k-1} (B_\varepsilon^+ \mathbf{p}_\varepsilon + \mathbf{c}_\varepsilon) > 0$ or in the direction of $-\mathbf{e}_n$, when $\mathbf{e}_n^T (B_\varepsilon^+)^{k-1} (B_\varepsilon^+ \mathbf{p}_\varepsilon + \mathbf{c}_\varepsilon) < 0$, see Llibre and Teruel (2004).

Following this approach, in the next theorem we obtain conditions on the coefficients of system (3.1) to ensure the existence of maximal canard points and, in this case, we provide the expression of these points.

Theorem 3.2. *For $\varepsilon > 0$ small enough, let us consider system (3.1) where $A = (a_{ij})_{1 \le i,j, \le s}$, $\mathbf{a} = (a_i)_{1 \le i \le s}^T$, and $\mathbf{b} = (b_i)_{1 \le i \le s}^T$.*

a) *Suppose $s \ge 2$. If $a_{1j} \ne 0$ for some $j \in \{2, \dots, s\}$ then, $\mathcal{S}_\varepsilon^+ \cap \mathcal{S}_\varepsilon^-$ is a linear manifold of dimension $n - 3$ such that each point $\mathbf{p}_\varepsilon$ in $\mathcal{S}_\varepsilon^+ \cap \mathcal{S}_\varepsilon^-$ satisfies that $\mathbf{p}_\varepsilon = (u_1, u_2, \dots, u_s, 0)^T$ where*

$$
u_1 = -\frac{\varepsilon^2}{\lambda_n^+ \lambda_n^-} \frac{1}{a_{1j}} \left(\sum_{k=2}^s (a_{1k} a_{kj} b_1 - a_{1k} a_{1j} b_k) + \sum_{\substack{k=2 \\ k \ne j}}^s \sum_{l=2}^s (a_{1k} a_{1l} a_{lj} - a_{1j} a_{1l} a_{lk}) u_k \right)
$$
$$
+ O(\varepsilon^3),
$$

$$
u_j = -\frac{1}{a_{1j}} \left(b_1 + \sum_{\substack{k=2 \\ k \ne j}}^s a_{1k} u_k \right) + O(\varepsilon).
$$

Moreover,

a.1) *If $u_1 > 0$, then $\mathbf{p}_\varepsilon$ is a maximal canard point with order of contact one;*

a.2) *If $u_1 < 0$, then $\mathbf{p}_\varepsilon$ is a faux maximal canard point with order of contact one;*

a.3) *If $u_1 = 0$, then $\mathbf{p}_\varepsilon$ is a contact point with order of contact greater than or equal to two.*

b) *Suppose that $s = 1$, or $s \ge 2$ and $a_{1j} = 0$ for all $j \in \{2, \dots, s\}$.*

b.1) *If $b_1 = 0$, then $\mathcal{S}_\varepsilon^+ \cap \mathcal{S}_\varepsilon^-$ is a linear manifold of dimension $n - 2$. Furthermore, $\mathcal{S}_\varepsilon^+ \cap \mathcal{S}_\varepsilon^-$ is invariant under the flow of system (3.1) and so, neither maximal nor faux maximal canard orbits exist.*

b.2) *If $b_1 \ne 0$, then $\mathcal{S}_\varepsilon^+ \cap \mathcal{S}_\varepsilon^-$ is empty and so, neither maximal nor faux maximal canard orbits exist.*

Remark 3.1. *In the case $n = 2$, that is when $s = 1$, only statements (b.1) and (b.2) of Theorem 3.2 can be applied. Hence, neither maximal nor faux maximal canard orbits exist.*

Remark 3.2. *We relate the results obtained in Theorem 3.2 with those in the smooth context through the paper of Wechselberger (2012). In order to do that, let us consider system*

$$
\begin{cases}
\dot{u}_1 = \frac{1}{2} \mu u_2 - (1 + \mu) v, \\
\dot{u}_2 = 1 + a_{21} u_1 + a_{22} u_2 + a_2 v, \\
\dot{u}_j = b_j + \sum_{k=1}^s a_{jk} u_k, \quad j = 3, \dots, s \\
\varepsilon \dot{v} = u_1 + |v|,
\end{cases}
\tag{3.7}
$$

which is obtained by keeping the linear terms of the canonical form (20) in Wechselberger (2012) and by replacing the quadratic term in the fast equation by an absolute value.

When $\mu \ne 0$, from Theorem 3.2(a) applied to (3.7) and since $s = n - 1$, there exists an $(s - 2)$-dimensional manifold composed by maximal or faux maximal canard points depending on the sign of

$$
u_1 = \frac{\varepsilon^2}{\lambda_n^+ \lambda_n^-} \frac{\mu}{2} + O(\varepsilon^3).
$$

In the folded saddle case, i.e. when $\mu < 0$, since $u_1 > 0$, every point in the $(s-2)$-dimensional manifold is a maximal canard. In this case, both the dimension of the manifold and the character of its points agree with the smooth case stated in Wechselberger (2012, Theorem 4.1). On the other hand, in the folded node case, i.e. when $\mu > 0$, every point in the referred manifold is a faux maximal canard. In this case, the dimension of the manifold also agrees with the stated in Wechselberger (2012, Theorem 4.2), meanwhile the character of the orbits through this manifold is not.

Maximal canard orbits can be obtained as a perturbation of singular orbits passing through folded singularities, see Brøns et al (2006) and Wechselberger (2012). These orbits are the so called singular canards. From Theorem 3.2(a.1) and (a.2), since the expression of $\mathbf{p}_\varepsilon$ is known, by tending ε to zero, we are able to obtain the singular canards which are the source of the maximal canard orbits having order of contact equal to one with the switching manifold.

As we claim in the next result, these singular canards flow through contact points - of order greater than or equal to 2 - of the reduced flow with the hyperplane $\mathcal{F}$. According to the Filippov's convention (Filippov (1988)), given in Convention 1.1, only escaping and sliding open regions can be distinguished on $\mathcal{F}$, see Remark 3.3. Furthermore, tangency points result to be contact points of order greater than or equal to 2. Usually, contact points of order 2 are referred as two-fold singularities (two-fold, for short). We use this terminology for every contact point of even order of contact. Depending on the behaviour of the surrounding reduced flow, two-folds are classified as visible, invisible or visible/invisible, see Jeffrey and Colombo (2009) and Jacquemard et al (2013). In Figure 3.1 we depict a visible two-fold in panel (a) and an invisible two-fold in panel (b), for a 3-dimensional reduced flow. The visible/invisible case can be generally obtained by taking half picture of panel (a) and combining it with the other half of panel (b). This case is not considered in Figure 3.1 because, as we mention in Remark 3.3, visible/invisible two-fold singularities cannot take place in our framework.

Singular canards in the visible two-fold are the orbits flowing through the contact point, meanwhile the singular canard in the invisible two-fold reduces to the contact point. The way in which maximal and faux maximal canards perturb from these singular canards are illustrated through two examples in Section 3.4, the first in a four dimensional framework and the other in a three dimensional one.

Theorem 3.3. *Consider system (3.1). For $\varepsilon > 0$ small enough next statements hold.*

    a) Each point $\mathbf{p}_\varepsilon$ in $\mathcal{S}_\varepsilon^+ \cap \mathcal{S}_\varepsilon^-$ lies in the unfolding of a contact point of order greater than or equal to 2 of the slow subsystem (3.3) with the hyperplane $\mathcal{F}$.

    b) If $n = 3$, then each maximal canard point (resp. faux maximal canard point) of order 1 lies in the unfolding of a visible (resp. invisible) two-fold of the slow subsystem (3.3).

The rest of this chapter is organized into four sections. In Section 3.2 we describe the unperturbed dynamics associated to the fast subsystem (3.2) and to the slow one (3.3). In Section 3.3 we analyze the perturbed dynamics given by system (3.1) and we provide the proofs of the main results. Concretely, the expression of the locally invariant slow manifold $\mathcal{S}_\varepsilon$ and the proof of the Theorem 3.1 is presented in Subsection 3.3.1. The proofs of theorems 3.2 and 3.3 are shown in Subsection 3.3.2. In Section 3.4, we present two examples to visualize our results. Conclusions are presented in Section 3.5. In the Appendix A, some matrix properties used in this chapter are given.
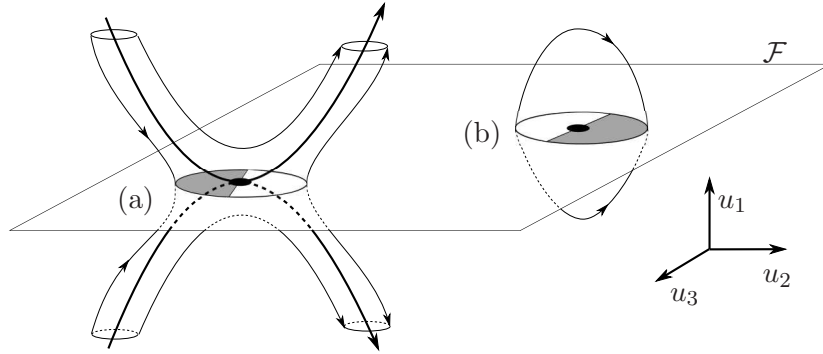
Figure 3.1: Representation of a 3-dimensional reduced flow surrounding a two-fold on the manifold $\mathcal{F}$: (a) visible two-fold, (b) invisible two-fold. The grey areas in the neighbourhood of the contact point correspond to the sliding regions while the white areas correspond to the escaping regions. The 2-dimensional case can be easily derived by removing the u_3-dimension.

3.2   Unperturbed dynamics

In this section we discuss the dynamics of the two unperturbed problems associated to the slow-fast system (3.1); namely, the fast subsystem (3.2), also called the stratified problem, and the slow subsystem (3.3) also called the reduced problem.

Concerning the dynamical behaviour of system (3.2), given a solution of this system, its s-first components are constant whereas the last one is changing in time. As a consequence, each orbit lies in a straight line.

The critical manifold, which is composed by the singular points of the stratified problem, is defined by the zeros of the second equation in (3.2), that is $\mathcal{S} = \{u_1 + |v| = 0\}$. The Jacobian matrix of the vector field at every point on $\mathcal{S}$ with $v \neq 0$ is

$$\begin{pmatrix} 0 & \ldots & 0 & \\ \vdots & \ddots & \vdots & \mathbf{0} \\ 0 & \ldots & 0 & \\ & \mathbf{e}_1^T & & \pm 1 \end{pmatrix}$$

where ± 1 stands for $+1$ if $v > 0$ and -1 if $v < 0$. In both cases the Jacobian matrix has exactly $s = n - 1$ null eigenvalues plus one non-zero. Hence, each point in $\mathcal{S}$ with $v \neq 0$ is a normally hyperbolic singular point. Moreover, since the non-zero eigenvalue has the same sign as v, we conclude that $\mathcal{S}^+ = \{u_1 + v = 0; \ v > 0\}$ is the repelling branch of the critical manifold $\mathcal{S}$, while $\mathcal{S}^- = \{u_1 - v = 0; \ v < 0\}$ is the attracting branch of $\mathcal{S}$. On the other hand, since the vector field is not differentiable at $v = 0$, the Jacobian matrix evaluated at points in $\mathcal{F} = \{u_1 = 0, \ v = 0\}$ is not defined.

Concerning the slow subsystem (3.3), its dynamics takes place on the s-dimensional manifold $\mathcal{S}$. Since equation (3.3) is a differential-algebraic equation, a usual way to analyze its dynamics is by considering a locally conjugate system. In our case we consider system

$$\tilde{\mathbf{u}}' = \begin{cases} P(A - \mathbf{a}\mathbf{e}_1^T)P\tilde{\mathbf{u}} + P\mathbf{b} & \text{if } \mathbf{e}_1^T\tilde{\mathbf{u}} > 0, \\ (A + \mathbf{a}\mathbf{e}_1^T)\tilde{\mathbf{u}} + \mathbf{b} & \text{if } \mathbf{e}_1^T\tilde{\mathbf{u}} < 0 \end{cases} \tag{3.8}$$

defined on $\mathbb{R}^s \setminus \{\mathbf{e}_1^T\tilde{\mathbf{u}} = 0\}$, where $P = I - 2\mathbf{e}_1\mathbf{e}_1^T$ and $\tilde{\mathbf{u}} = (v, u_2, \ldots, u_s)$. From now on, by way of notation, we will refer $\tilde{\mathbf{u}}$ by $\mathbf{u}$ when the slow subsystem is considered. In the

next result we prove that system (3.8) is locally conjugate to the slow subsystem (3.3). When no confusion arise, we also call slow subsystem to system (3.8).

Lemma 3.1. *Slow subsystem (3.3) restricted on $\mathcal{S} \setminus \mathcal{F}$ is differentially conjugate to the discontinuous piecewise linear differential system (3.8) defined on $\mathbb{R}^s \setminus \{\mathbf{e}_1^T \mathbf{u} = 0\}$.*

Proof. Deriving the algebraic equation in (3.3) with respect to τ when $v \neq 0$, we obtain the n-dimensional piecewise linear system

$$\begin{cases} \mathbf{u}' = A\mathbf{u} + \mathbf{a}v + \mathbf{b}, \\ v' = -\dfrac{|v|}{v} u_1', \end{cases} \tag{3.9}$$

which is defined in $\mathbb{R}^n \setminus \{v = 0\}$ and coincides with (3.3) in $\mathcal{S} \setminus \mathcal{F}$.

Consider the projection $\pi : \mathbb{R}^n \to \mathbb{R}^s$ given by $\pi(\mathbf{u}, v) = \mathbf{u} + (v - u_1)\mathbf{e}_1$. Note that $\pi(\mathbf{u}, v) = (v, u_2, \ldots, u_s)^T$. Since each point of $\mathcal{S}$ satisfies the expression $|v| = -\mathbf{e}_1^T \mathbf{u}$, the restriction of the projection π on $\mathcal{S}$ can be written as the piecewise function

$$\tilde{\mathbf{u}} = \pi|_{\mathcal{S}}(\mathbf{u}, v) = \begin{cases} P\mathbf{u} & \text{if } v \geq 0, \\ \mathbf{u} & \text{if } v < 0, \end{cases}$$

where P is the $s \times s$ involutory matrix $I - 2\mathbf{e}_1\mathbf{e}_1^T$. To simplify notation, from now on we use π to denote $\pi|_{\mathcal{S}}$. Since $P\mathbf{u} = \mathbf{u}$ when $(\mathbf{u}, v) \in \mathcal{F}$, the restricted function π is a homeomorphism with inverse function given by

$$\pi^{-1}(\tilde{\mathbf{u}}) = \begin{cases} (P\tilde{\mathbf{u}}, \ \mathbf{e}_1^T \tilde{\mathbf{u}}) & \text{if } \mathbf{e}_1^T \tilde{\mathbf{u}} \geq 0, \\ (\tilde{\mathbf{u}}, \ \mathbf{e}_1^T \tilde{\mathbf{u}}) & \text{if } \mathbf{e}_1^T \tilde{\mathbf{u}} < 0. \end{cases}$$

In fact, π is differentiable in $\mathcal{S} \setminus \mathcal{F}$ with Jacobian matrix

$$D\pi|_{(\mathbf{u}, v)} = \begin{cases} (P|\mathbf{0}) & \text{if } v > 0, \\ (I|\mathbf{0}) & \text{if } v < 0, \end{cases}$$

where $(P|\mathbf{0})$ and $(I|\mathbf{0})$ stand for the augmented matrices by appending a last null column to the matrices P and I respectively. Therefore, π is a diffeomorphism defined on $\mathcal{S} \setminus \mathcal{F}$ inducing the differential equation on $\mathbb{R}^s \setminus \{\mathbf{e}_1^T \tilde{\mathbf{u}} = 0\}$ given by

$$\tilde{\mathbf{u}}' = \begin{cases} P(A - \mathbf{a}\mathbf{e}_1^T)P\tilde{\mathbf{u}} + P\mathbf{b} & \text{if } \mathbf{e}_1^T \tilde{\mathbf{u}} > 0, \\ (A + \mathbf{a}\mathbf{e}_1^T)\tilde{\mathbf{u}} + \mathbf{b} & \text{if } \mathbf{e}_1^T \tilde{\mathbf{u}} < 0, \end{cases}$$

which is differentially conjugate to (3.9) on $\mathcal{S} \setminus \mathcal{F}$ and, hence, to the slow subsystem (3.3) on $\mathcal{S} \setminus \mathcal{F}$. $\qquad\square$

Since the slow subsystem (3.8) is linear on the half-spaces $\{\mathbf{e}_1^T \mathbf{u} > 0\}$ and $\{\mathbf{e}_1^T \mathbf{u} < 0\}$, the reduced flow is determined by the eigenvalues of the matrices $P(A - \mathbf{a}\mathbf{e}_1^T)P$ and $A + \mathbf{a}\mathbf{e}_1^T$, respectively. On the manifold $\{\mathbf{e}_1^T \mathbf{u} = 0\}$, the direction of the reduced flow depends on the order of the contact points. In next lemma, we analyze this order of contact.

Lemma 3.2. *Let $\mathbf{u}$ be a contact point of the reduced flow defined by the slow subsystem (3.8) with the hyperplane $\{\mathbf{e}_1^T \mathbf{u} = 0\}$. The order of contact of $\mathbf{u}$ is one if and only if $\mathbf{e}_1^T(A\mathbf{u} + \mathbf{b}) \neq 0$ and, the order of contact is $k \geq 2$, if and only if $\mathbf{e}_1^T A^r(A\mathbf{u} + \mathbf{b}) = 0$ when $r = 0, 1, \ldots, k-2$ and $\mathbf{e}_1^T A^{k-1}(A\mathbf{u} + \mathbf{b}) \neq 0$.*

Proof. Since $P = I - \mathbf{e}_1\mathbf{e}_1^T$, it is satisfied that $P = P^{-1}$ and $\mathbf{e}_1^T P = -\mathbf{e}_1^T$. Moreover, when $\mathbf{e}_1^T \mathbf{u} = 0$, it is also held that $P\mathbf{u} = \mathbf{u}$,

$$
\begin{aligned}
\mathbf{e}_1^T \left(P \left(A - \mathbf{a}\mathbf{e}_1^T \right) P \right)^r \left(P(A - \mathbf{a}\mathbf{e}_1^T)P\mathbf{u} + P\mathbf{b} \right) &= - \mathbf{e}_1^T \left(A - \mathbf{a}\mathbf{e}_1^T \right)^r (A\mathbf{u} + \mathbf{b}), \\
\mathbf{e}_1^T \left(A + \mathbf{a}\mathbf{e}_1^T \right)^r \left(\left(A + \mathbf{a}\mathbf{e}_1^T \right) \mathbf{u} + \mathbf{b} \right) &= \mathbf{e}_1^T \left(A + \mathbf{a}\mathbf{e}_1^T \right)^r (A\mathbf{u} + \mathbf{b}),
\end{aligned}
\tag{3.10}
$$

for $r \geq 0$.

The case $k = 1$ follows by taking $r = 0$ in expressions (3.10). If $k \geq 2$, under the assumption $\mathbf{e}_1^T A^r (A\mathbf{u} + \mathbf{b}) = 0$ for $r = 0, 1, \ldots, k-2$ and $\mathbf{e}_1^T A^{k-1}(A\mathbf{u} + \mathbf{b}) \neq 0$, it follows from expressions (3.10) that $\mathbf{e}_1^T \left(A - \mathbf{a}\mathbf{e}_1^T \right)^r (A\mathbf{u}+\mathbf{b}) = \mathbf{e}_1^T \left(A + \mathbf{a}\mathbf{e}_1^T \right)^r (A\mathbf{u}+\mathbf{b}) = \mathbf{e}_1^T A^r (A\mathbf{u}+\mathbf{b}) = 0$ for $r = 0, 1, \ldots, k-2$ and $\mathbf{e}_1^T \left(A - \mathbf{a}\mathbf{e}_1^T \right)^{k-1} (A\mathbf{u} + \mathbf{b}) = \mathbf{e}_1^T \left(A + \mathbf{a}\mathbf{e}_1^T \right)^{k-1} (A\mathbf{u} + \mathbf{b}) = \mathbf{e}_1^T A^{k-1}(A\mathbf{u} + \mathbf{b}) \neq 0$. Therefore, in terms of the vector field of subsystem (3.8), it means that $\mathbf{u}$ is a contact point of order k. The reverse implication is obtained by assuming $\mathbf{e}_1^T \left(A - \mathbf{a}\mathbf{e}_1^T \right)^r (A\mathbf{u} + \mathbf{b}) = 0$ for $r = 0, 1, \ldots, k-2$, $\mathbf{e}_1^T \left(A - \mathbf{a}\mathbf{e}_1^T \right)^{k-1} (A\mathbf{u} + \mathbf{b}) \neq 0$ and, by applying an induction on r. □

The slow subsystem (3.8) can be extended, by adopting Filippov's convention (see Convention 1.1 or Filippov (1988)), to the hyperplane $\{\mathbf{e}_1^T\mathbf{u} = 0\}$ as

$$
\mathbf{u}' = \begin{cases}
P(A - \mathbf{a}\mathbf{e}_1^T)P\mathbf{u} + P\mathbf{b} & \mathbf{e}_1^T\mathbf{u} > 0, \\
\dfrac{1}{2}(P + I)(A\mathbf{u} + \mathbf{b}) & \mathbf{e}_1^T\mathbf{u} = 0, \\
(A + \mathbf{a}\mathbf{e}_1^T)\mathbf{u} + \mathbf{b} & \mathbf{e}_1^T\mathbf{u} < 0.
\end{cases}
\tag{3.11}
$$

Remark 3.3. *Since $\mathbf{e}_1^T P = -\mathbf{e}_1^T$, the vector field on $\{\mathbf{e}_1^T\mathbf{u} = 0\}$ satisfies $\mathbf{e}_1^T(P + I)(A\mathbf{u} + \mathbf{b}) = 0$, so sewing regions do not exist. Moreover, for contact points $\mathbf{u}_0$ of order two i.e. when $r = 1$ in equalities (3.10), these expressions write as $-\mathbf{e}_1^T A(A\mathbf{u}_0 + \mathbf{b}) \neq 0$ and $\mathbf{e}_1^T A(A\mathbf{u}_0 + \mathbf{b}) \neq 0$, since $\mathbf{e}_1^T(A\mathbf{u}_0 + \mathbf{b}) = 0$. Hence, visible/invisible two-fold singularities cannot be.*

3.3   Perturbed dynamics

3.3.1   Dynamics around the slow manifold

In this subsection we analyze the dynamics of the perturbed differential system (3.1), written as system (3.4), through different lemmas which lead us to prove Theorem 3.1. We present a self-contained proof including: an explicit relation between the eigenvalues of both the unperturbed and the singularly perturbed systems, and an explicit expression for the slow manifold.

Since system (3.1) is piecewise linear, first we deal with the spectrum of the associated matrices B_ε^+ and B_ε^-. After that, by using the generalized eigenvectors associated to the slow eigenvalues, we give explicit expressions of two locally invariant half-hyperplanes $\mathcal{S}_\varepsilon^+$ and $\mathcal{S}_\varepsilon^-$. Finally we prove that $\mathcal{S}_\varepsilon^+ \cup \mathcal{S}_\varepsilon^-$ is a Fenichel's slow manifold. That is, $\mathcal{S}_\varepsilon = \mathcal{S}_\varepsilon^+ \cup \mathcal{S}_\varepsilon^-$.

Lemma 3.3. *Let us consider system (3.1) written as system (3.4).*

  a) *The spectrum of the matrix B_ε^+ is composed by s eigenvalues of $O(\varepsilon)$ plus one eigenvalue of $O(1)$. To be precise, the eigenvalues are*

$$
\lambda_k^+ = \beta_k^+ \varepsilon + O(\varepsilon^2) \text{ for } k = 1, \ldots, s \text{ and } \lambda_n^+ = 1 + \mathbf{e}_1^T\mathbf{a}\,\varepsilon + O(\varepsilon^2)
$$

where each β_k^+ is an eigenvalue of the associated matrix $P(A - \mathbf{a}\mathbf{e}_1^T)P$ of the slow subsystem (3.8) defined on $\{\mathbf{e}_1^T\mathbf{u} > 0\}$.

b) *The spectrum of the matrix B_ε^- is composed by*

$$\lambda_k^- = \beta_k^- \varepsilon + O(\varepsilon^2) \ \text{for} \ k = 1, \ldots, s \ \text{and} \ \lambda_n^- = -1 - \mathbf{e}_1^T\mathbf{a}\,\varepsilon + O(\varepsilon^2)$$

where each β_k^- is an eigenvalue of the associated matrix $A + \mathbf{a}\mathbf{e}_1^T$ of the slow subsystem (3.8) defined on $\{\mathbf{e}_1^T\mathbf{u} < 0\}$.

Proof. Let us consider system (3.4). Let B_0^+ and B_0^- be the limits when ε tends to zero of the matrices B_ε^+ and B_ε^-, respectively. From equation (3.5), it is easy to check that B_0^+ (respectively, B_0^-) has one eigenvalue equal to 0 with multiplicity s and one eigenvalue equal to 1 (respectively, equal to -1). Therefore, in system (3.4), the eigenvalues of B_ε^+ and B_ε^- are obtained by adding terms of order 1 and higher in ε to the eigenvalues of B_0^+ and B_0^-, respectively.

The remainder of the proof is devoted to compute the coefficient of ε in the development of λ_k^+. Similar arguments can be applied to compute the corresponding coefficient of λ_k^-.

Given k such that $1 \le k \le s$, consider the eigenvalue λ_k^+ of B_ε^+. Then, it is satisfied that

$$0 \ = \det\left(B_\varepsilon^+ - \lambda_k^+ I\right) = \det\begin{pmatrix} \varepsilon A - \lambda_k^+ I & \varepsilon\mathbf{a} \\ \mathbf{e}_1^T & 1 - \lambda_k^+ \end{pmatrix}$$

$$= \varepsilon^s \det\begin{pmatrix} A - (\beta_k^+ + O(\varepsilon))I & \mathbf{a} \\ \mathbf{e}_1^T & 1 - \beta_k^+\varepsilon + O(\varepsilon^2) \end{pmatrix}.$$

The matrix in the last determinant can be expressed as the sum of one non ε-depending matrix and another one containing only terms on ε. Therefore, applying Lemma A.2(a) given in Appendix A, the last expression writes as

$$0 = \det\begin{pmatrix} A - \beta_k^+ I & \mathbf{a} \\ \mathbf{e}_1^T & 1 \end{pmatrix} + O(\varepsilon),$$

which, by using Lemma A.1 in Appendix A, can be simplified as $\det\left(A - \mathbf{a}\mathbf{e}_1^T - \beta_k^+ I\right) + O(\varepsilon) = 0$. Since this equation is satisfied for every ε small enough, we conclude that $\det\left(A - \mathbf{a}\mathbf{e}_1^T - \beta_k^+ I\right) = 0$ and so β_k^+ is an eigenvalue of the matrix $A - \mathbf{a}\mathbf{e}_1^T$. On the other hand, since P is an involutory matrix, the matrices $A - \mathbf{a}\mathbf{e}_1^T$ and $P(A - \mathbf{a}\mathbf{e}_1^T)P$ have the same eigenvalues. This proves the lemma for the eigenvalues λ_k^+ with $1 \le k \le s$.

Consider now the eigenvalue λ_n^+. A direct consequence of Lemma A.2(b) given in Appendix A is that

$$0 = \det(B_\varepsilon^+ - \lambda_n^+ I) = \det\begin{pmatrix} \varepsilon A - \lambda_n^+ I & \varepsilon\mathbf{a} \\ \mathbf{e}_1^T & 1 - \lambda_n^+ \end{pmatrix} = \det\begin{pmatrix} -\lambda_n^+ I & \varepsilon\mathbf{a} \\ \mathbf{e}_1^T & 1 - \lambda_n^+ \end{pmatrix} + O(\varepsilon^2).$$

The determinant in the last member can be developed in terms of ε, by using the coffactor expansion along the last row. Hence, the previous equation is written as

$$0 = (-\lambda_n^+)^{s-1}\left((\lambda_n^+)^2 - \lambda_n^+ - \varepsilon\,\mathbf{e}_1^T\mathbf{a}\right) + O(\varepsilon^2).$$

Therefore, replacing λ_n^+ by $1 + \alpha\varepsilon + O(\varepsilon^2)$ in the previous equation and taking into account that this equation is satisfied for all $\varepsilon > 0$ small enough, we conclude that $\alpha = \mathbf{e}_1^T\mathbf{a}$. □

From the expression of the eigenvalues of the matrices B_ε^+ and B_ε^- provided in Lemma 3.3, we conclude that λ_n^+ and λ_n^- are responsible for the fast dynamics (we call them the fast eigenvalues) whereas, also considering Lemma 3.1, the remaining eigenvalues $\{\lambda_k^+\}_{k=1}^s$ and $\{\lambda_k^-\}_{k=1}^s$ are responsible for the slow dynamics (we call them the slow eigenvalues). We also want to remark the relation between the slow eigenvalues and the eigenvalues of the slow subsystem (3.8), since the second ones appear as the first coefficient in the development in ε of the first ones. Hence, the slow dynamics takes place on the hyperplanes generated by the generalized eigenvectors associated with the slow eigenvalues.

Let $\mathbf{w}^+$ and $\mathbf{w}^-$ be eigenvectors associated with the eigenvalues λ_n^+ and λ_n^- of the transposed matrices $(B_\varepsilon^+)^T$ and $(B_\varepsilon^-)^T$, respectively. That is

$$(\mathbf{w}^+)^T B_\varepsilon^+ = \lambda_n^+ (\mathbf{w}^+)^T \ \text{ and } \ (\mathbf{w}^-)^T B_\varepsilon^- = \lambda_n^- (\mathbf{w}^-)^T.$$

Since λ_n^+ is different from λ_k^+, $k = 1, \ldots, s$ (see Lemma 3.3), the eigenvector $\mathbf{w}^+$ is orthogonal to the generalized eigenvectors associated to the slow eigenvalues. Analogous arguments apply to the $\mathbf{w}^-$ eigenvector. Consequently, we define the half-hyperplanes

$$S_\varepsilon^+ = \left\{ \mathbf{p} = (\mathbf{u}, v)^T \in \mathbb{R}^n : v \geq 0, \ (\mathbf{w}^+)^T \mathbf{p} = \frac{-(\mathbf{w}^+)^T \mathbf{c}_\varepsilon}{\lambda_n^+} \right\},$$

$$(3.12)$$

$$S_\varepsilon^- = \left\{ \mathbf{p} = (\mathbf{u}, v)^T \in \mathbb{R}^n : v \leq 0, \ (\mathbf{w}^-)^T \mathbf{p} = \frac{-(\mathbf{w}^-)^T \mathbf{c}_\varepsilon}{\lambda_n^-} \right\}.$$

Lemma 3.4. *The manifold $\mathcal{S}_\varepsilon^+ \cup \mathcal{S}_\varepsilon^-$ is locally invariant under the flow of system* (3.1) *written, in its matrix form, as system (3.4).*

Proof. Let $\mathbf{p} = (\mathbf{u}, v)^T \in \mathcal{S}_\varepsilon^+$. Since $v \geq 0$ and

$$(\mathbf{w}^+)^T \left(B_\varepsilon^+ \mathbf{p} + \mathbf{c}_\varepsilon \right) = \lambda_n^+ (\mathbf{w}^+)^T \mathbf{p} + (\mathbf{w}^+)^T \mathbf{c}_\varepsilon = 0,$$

the vector field defined by system (3.4) at $\mathbf{p}$ is tangent to the half-hyperplane $\mathcal{S}_\varepsilon^+$ at this point. We conclude that $\mathcal{S}_\varepsilon^+$ is locally invariant ($\mathcal{S}_\varepsilon^+$ has a boundary at $v = 0$) under the flow. The lemma follows by applying similar arguments to $\mathcal{S}_\varepsilon^-$. $\square$

By computing expressions of the eigenvectors $\mathbf{w}^+$ and $\mathbf{w}^-$, in the next result we obtain explicit expressions of the half-hyperplanes $\mathcal{S}_\varepsilon^+$ and $\mathcal{S}_\varepsilon^-$.

Lemma 3.5. *Let us consider system* (3.1) *written in its matrix form as system (3.4). For ε sufficiently small it follows that*

$$\mathcal{S}_\varepsilon^+ = \left\{ (\mathbf{u}, v) \in \mathbb{R}^n : \ v \geq 0, \ -\mathbf{e}_1^T (\varepsilon A - \lambda_n^+ I)^{-1} \mathbf{u} + v = \frac{\varepsilon}{\lambda_n^+} \mathbf{e}_1^T (\varepsilon A - \lambda_n^+ I)^{-1} \mathbf{b} \right\}$$

and

$$\mathcal{S}_\varepsilon^- = \left\{ (\mathbf{u}, v) \in \mathbb{R}^n : \ v \leq 0, \ -\mathbf{e}_1^T (\varepsilon A - \lambda_n^- I)^{-1} \mathbf{u} + v = \frac{\varepsilon}{\lambda_n^-} \mathbf{e}_1^T (\varepsilon A - \lambda_n^- I)^{-1} \mathbf{b} \right\}.$$

Proof. Consider an eigenvector $\mathbf{w}^+$ written as $\mathbf{w}^+ = (\mathbf{w}_1^+, \mathrm{w}_n^+)^T$. Since $(\mathbf{w}^+)^T B_\varepsilon^+ = \lambda_n^+ (\mathbf{w}^+)^T$, from the expression of B_ε^+ in equation (3.5), it is satisfied that

$$(\mathbf{w}_1^+)^T (\varepsilon A - \lambda_n^+ I) + \mathrm{w}_n^+ \mathbf{e}_1^T = 0,$$
$$(\mathbf{w}_1^+)^T \varepsilon \mathbf{a} + \mathrm{w}_n^+ (1 - \lambda_n^+) = 0.$$

$$(3.13)$$

By Lemma A.3(b) given in Appendix A, since ε is small enough, the matrix $\varepsilon A - \lambda_n^+ I$ is regular. Then, from the first equation in (3.13), $\mathbf{w}_1^+$ can be written as a function of $\mathbf{w}_n^+$. By fixing $\mathbf{w}_n^+ = 1$, we obtain $\mathbf{w}^+ = \left(-\mathbf{e}_1^T(\varepsilon A - \lambda_n^+ I)^{-1}, 1\right)^T$. Hence, the expression of $\mathcal{S}_\varepsilon^+$ is derived from equation (3.12).

The lemma is finally proved by following the same procedure to compute $\mathbf{w}^-$ and $\mathcal{S}_\varepsilon^-$. $\square$

Lemma 3.6. *Let us consider system* (3.1) *written in its matrix form as system (3.4). For $\varepsilon > 0$ small enough, $\mathcal{S}_\varepsilon^+$ is a repellor manifold and $\mathcal{S}_\varepsilon^-$ is an attractor one.*

Proof. Let $\mathbf{v}_n^+$ be an eigenvector of the matrix B_ε^+ associated to the eigenvalue λ_n^+, $\mathbf{p}$ be a point in $\mathcal{S}_\varepsilon^+$, and $\mathbf{q} = \mathbf{p} + \delta \mathbf{v}_n^+$ be a point outside the invariant manifold $\mathcal{S}_\varepsilon^+$. Consider $\mathbf{x_p}(t)$ and $\mathbf{x_q}(t)$ be the solutions of system (3.4) with initial conditions $\mathbf{p}$ and $\mathbf{q}$, respectively. Since the considered system is locally linear, for $|t|$ small enough, $\mathbf{x_q}(t) = e^{B_\varepsilon^+ t}\mathbf{q} + \int_0^t e^{B_\varepsilon^+ (t-s)}\mathbf{c}_\varepsilon\, ds = \mathbf{x_p}(t) + e^{\lambda_n^+ t}\delta\mathbf{v}_n^+$. In view of $\mathcal{S}_\varepsilon^+$ is locally invariant and $\lambda_n^+ > 0$, for ε sufficiently small, the solution $\mathbf{x_q}(t)$ moves away from the manifold $\mathcal{S}_\varepsilon^+$ with the exponential ratio $e^{\lambda_n^+ t}$, implying that $\mathcal{S}_\varepsilon^+$ is a repellor manifold.

Similar arguments can be applied to analyze the stability of $\mathcal{S}_\varepsilon^-$, finishing the proof of the lemma. $\square$

In Lemma 3.6, we have described the flow of the perturbed system (3.1) surrounding the manifold $\mathcal{S}_\varepsilon^+ \cup \mathcal{S}_\varepsilon^-$. In the next result, since $\mathcal{S}_\varepsilon^+ \cup \mathcal{S}_\varepsilon^-$ is locally invariant, we prove that $\mathcal{S}_\varepsilon^+ \cup \mathcal{S}_\varepsilon^-$ is the slow manifold $\mathcal{S}_\varepsilon$ of system (3.1) and, we also discuss the behaviour of the flow on this manifold.

Lemma 3.7. *The flow of system (3.4) restricted to the invariant manifold $\mathcal{S}_\varepsilon^+ \cup \mathcal{S}_\varepsilon^- \cap \{v \neq 0\}$ is a regular perturbation of the reduced flow defined by (3.3) and restricted to $\mathcal{S} \setminus \mathcal{F}$.*

Proof. To prove the lemma, we are going to show that the projection by $\pi(\mathbf{u}, v) = \mathbf{u} + (v - u_1)\mathbf{e}_1$ of the vector field (3.4) defined on $(\mathcal{S}_\varepsilon^+ \cup \mathcal{S}_\varepsilon^-) \cap \{v \neq 0\}$ is a regular perturbation of the vector field given by system (3.8).

Let $(\mathbf{u}, v) \in \mathcal{S}_\varepsilon^+ \cap \{v \neq 0\}$. By definition of $\mathcal{S}_\varepsilon^+$, see Lemma 3.5, the variable v can be expressed as a function of the variable $\mathbf{u}$. The component u_1 can be also expressed as a function of variable v and the rest of components of $\mathbf{u}$. Similar arguments can be applied when $(\mathbf{u}, v) \in \mathcal{S}_\varepsilon^- \cap \{v \neq 0\}$. Hence, we obtain

$$
v = \begin{cases} \mathbf{e}_1^T(\varepsilon A - \lambda_n^+ I)^{-1}\left(\dfrac{\varepsilon}{\lambda_n^+}\mathbf{b} + \mathbf{u}\right) & \text{if } (\mathbf{u}, v) \in \mathcal{S}_\varepsilon^+, \\[2ex] \mathbf{e}_1^T(\varepsilon A - \lambda_n^- I)^{-1}\left(\dfrac{\varepsilon}{\lambda_n^-}\mathbf{b} + \mathbf{u}\right) & \text{if } (\mathbf{u}, v) \in \mathcal{S}_\varepsilon^- \end{cases}
$$

and

$$
u_1 = U_1(\hat{\mathbf{u}}, v) = \begin{cases} \dfrac{1}{\mathbf{e}_1^T(\varepsilon A - \lambda_n^+ I)^{-1}\mathbf{e}_1}\left(v - \mathbf{e}_1^T(\varepsilon A - \lambda_n^+ I)^{-1}\left(\dfrac{\varepsilon}{\lambda_n^+}\mathbf{b} + \hat{\mathbf{u}}\right)\right) & \text{if } v > 0, \\[3ex] \dfrac{1}{\mathbf{e}_1^T(\varepsilon A - \lambda_n^- I)^{-1}\mathbf{e}_1}\left(v - \mathbf{e}_1^T(\varepsilon A - \lambda_n^- I)^{-1}\left(\dfrac{\varepsilon}{\lambda_n^-}\mathbf{b} + \hat{\mathbf{u}}\right)\right) & \text{if } v < 0, \end{cases}
$$

where $\hat{\mathbf{u}} = (0, u_2, \ldots, u_s)^T$. Then, the projection π restricted to $(\mathcal{S}_\varepsilon^+ \cup \mathcal{S}_\varepsilon^-) \cap \{v \neq 0\}$ satisfies

$$\tilde{\mathbf{u}} = \pi(\mathbf{u}, v) = \begin{cases} \mathbf{u} + \left(\mathbf{e}_1^T(\varepsilon A - \lambda_n^+ I)^{-1} \left(\dfrac{\varepsilon}{\lambda_n^+} \mathbf{b} + \mathbf{u} \right) - u_1 \right) \mathbf{e}_1 & \text{if } (\mathbf{u}, v) \in \mathcal{S}_\varepsilon^+, \\[3mm] \mathbf{u} + \left(\mathbf{e}_1^T(\varepsilon A - \lambda_n^- I)^{-1} \left(\dfrac{\varepsilon}{\lambda_n^-} \mathbf{b} + \mathbf{u} \right) - u_1 \right) \mathbf{e}_1 & \text{if } (\mathbf{u}, v) \in \mathcal{S}_\varepsilon^- \end{cases}$$

with inverse given by $\pi^{-1}(\tilde{\mathbf{u}}) = (U_1(\tilde{\mathbf{u}} - \tilde{u}_1 \mathbf{e}_1, \tilde{u}_1), \tilde{u}_2, \ldots, \tilde{u}_s, \tilde{u}_1)^T$.

Since the Jacobian matrix of π is

$$D\pi(\mathbf{u}, v) = \begin{cases} \left(I + \mathbf{e}_1 \mathbf{e}_1^T \left((\varepsilon A - \lambda_n^+ I)^{-1} - I \right) \big| \mathbf{0} \right) & \text{if } v > 0, \\ \left(I + \mathbf{e}_1 \mathbf{e}_1^T \left((\varepsilon A - \lambda_n^- I)^{-1} - I \right) \big| \mathbf{0} \right) & \text{if } v < 0, \end{cases}$$

the induced vector field on $\mathbb{R}^s \setminus \{\tilde{u}_1 = 0\}$ is given by

$$\dot{\tilde{\mathbf{u}}} = \begin{cases} D\pi \left(\pi^{-1}(\tilde{\mathbf{u}}) \right) \left(B_\varepsilon^+ \pi^{-1}(\tilde{\mathbf{u}}) + \mathbf{c}_\varepsilon \right) & \text{if } \mathbf{e}_1^T \tilde{\mathbf{u}} > 0, \\ D\pi \left(\pi^{-1}(\tilde{\mathbf{u}}) \right) \left(B_\varepsilon^- \pi^{-1}(\tilde{\mathbf{u}}) + \mathbf{c}_\varepsilon \right) & \text{if } \mathbf{e}_1^T \tilde{\mathbf{u}} < 0. \end{cases} \tag{3.14}$$

By parametrizing the time ($\tau = t\varepsilon$) and taking into account the expressions of the vector $\mathbf{c}_\varepsilon$ and the matrices B_ε^+ and B_ε^-, see equation (3.5), the vector field (3.14) is written as

$$\tilde{\mathbf{u}}' = \begin{cases} \left(I + \mathbf{e}_1 \mathbf{e}_1^T \left((\varepsilon A - \lambda_n^+ I)^{-1} - I \right) \right) \left((A|\mathbf{a}) \pi^{-1}(\tilde{\mathbf{u}}) - \dfrac{\varepsilon}{\lambda_n^+} \dfrac{\mathbf{e}_1^T(\varepsilon A - \lambda_n^+ I)^{-1} \mathbf{b}}{\mathbf{e}_1^T(\varepsilon A - \lambda_n^+ I)^{-1} \mathbf{e}_1} A\mathbf{e}_1 + \mathbf{b} \right) \\ \hfill \text{if } \mathbf{e}_1^T \tilde{\mathbf{u}} > 0, \\[6mm] \left(I + \mathbf{e}_1 \mathbf{e}_1^T \left((\varepsilon A - \lambda_n^- I)^{-1} - I \right) \right) \left((A|\mathbf{a}) \pi^{-1}(\tilde{\mathbf{u}}) - \dfrac{\varepsilon}{\lambda_n^-} \dfrac{\mathbf{e}_1^T(\varepsilon A - \lambda_n^- I)^{-1} \mathbf{b}}{\mathbf{e}_1^T(\varepsilon A - \lambda_n^- I)^{-1} \mathbf{e}_1} A\mathbf{e}_1 + \mathbf{b} \right) \\ \hfill \text{if } \mathbf{e}_1^T \tilde{\mathbf{u}} < 0. \end{cases}$$
$$\tag{3.15}$$

Considering the fact that

$$\lim_{\varepsilon \to 0} \left(I + \mathbf{e}_1 \mathbf{e}_1^T \left((\varepsilon A - \lambda_n^+ I)^{-1} - I \right) \right) = P, \quad \lim_{\varepsilon \to 0} \left(I + \mathbf{e}_1 \mathbf{e}_1^T \left((\varepsilon A - \lambda_n^- I)^{-1} - I \right) \right) = I$$

and

$$\lim_{\varepsilon \to 0} U_1(\tilde{\mathbf{u}} - \tilde{u}_1 \mathbf{e}_1, \tilde{u}_1) = \begin{cases} -\tilde{u}_1 & \text{if } \mathbf{e}_1^T \tilde{\mathbf{u}} > 0, \\ \tilde{u}_1 & \text{if } \mathbf{e}_1^T \tilde{\mathbf{u}} < 0, \end{cases}$$

then the limit

$$\lim_{\varepsilon \to 0} \pi^{-1}(\tilde{\mathbf{u}}) = \begin{cases} P\tilde{\mathbf{u}} & \text{if } \mathbf{e}_1^T \tilde{\mathbf{u}} > 0, \\ \tilde{\mathbf{u}} & \text{if } \mathbf{e}_1^T \tilde{\mathbf{u}} < 0 \end{cases}$$

is derived. Finally, using that $\mathbf{e}_1^T P \tilde{\mathbf{u}} = -\mathbf{e}_1^T \tilde{\mathbf{u}}$, we conclude that system (3.15) tends to the differential system (3.8) as ε tends to zero. $\qquad \square$

Proof of Theorem 3.1. Statements (a), (b) and (c) are straightforward consequences of Lemmas 3.4, 3.7 and 3.6, respectively.

To prove statement (d), we proceed as follows. Given a compact subset $\hat{\mathcal{S}}$ of the critical manifold $\mathcal{S}$, we split it into the two compact subsets $\hat{\mathcal{S}}^+ = \hat{\mathcal{S}} \cap \{v \geq 0\}$ and $\hat{\mathcal{S}}^- = \hat{\mathcal{S}} \cap \{v \leq 0\}$ and, we want to prove the existence of two compact subsets, $\hat{\mathcal{S}}_\varepsilon^+$ and $\hat{\mathcal{S}}_\varepsilon^-$, such that $d_H(\hat{\mathcal{S}}_\varepsilon^+, \hat{\mathcal{S}}^+) = O(\varepsilon)$ and $d_H(\hat{\mathcal{S}}_\varepsilon^-, \hat{\mathcal{S}}^-) = O(\varepsilon)$. The proof will finish by setting $\hat{\mathcal{S}}_\varepsilon = \hat{\mathcal{S}}_\varepsilon^+ \cup \hat{\mathcal{S}}_\varepsilon^-$.

Consider ε small enough. Due to the fact that the matrix $\varepsilon A - \lambda_n^+$ is invertible (see Lemma A.3(b) given in Appendix A), by isolating v and by adding u_1 at both sides of the expression of $\mathcal{S}_\varepsilon^+$ in Lemma 3.5, we obtain

$$
\mathcal{S}_\varepsilon^+ = \left\{ (\mathbf{u}, v) \in \mathbb{R}^n : \ v \geq 0, \ u_1 + v = \frac{\varepsilon}{\lambda_n^+} \mathbf{e}_1^T (\varepsilon A - \lambda_n^+ I)^{-1} \mathbf{b} + \mathbf{e}_1^T \left((\varepsilon A - \lambda_n^+)^{-1} + I \right) \mathbf{u} \right\}.
$$

Let K be the compact set obtained by projecting $\hat{\mathcal{S}}^+$ on its first s components. By way of notation we call $\mathrm{proj}_{\mathbb{R}^s}$ to this map, i.e. $K = \mathrm{proj}_{\mathbb{R}^s}(\hat{\mathcal{S}}^+)$. Therefore, taking $\hat{\mathcal{S}}_\varepsilon^+ = \mathrm{proj}_{\mathbb{R}^s}^{-1}(K) \cap \mathcal{S}_\varepsilon^+$, we are going to see that $d_H(\hat{\mathcal{S}}_\varepsilon^+, \hat{\mathcal{S}}^+) = O(\varepsilon)$.

Using the expansion of $(\varepsilon A - \lambda_n^+ I)^{-1}$ provided in Lemma A.3(b) and the fact that $\lambda_n^+ = 1 + O(\varepsilon)$ (see Lemma 3.3), we obtain $(\varepsilon A - \lambda_n^+ I)^{-1} = -I + O(\varepsilon)$. Whence, $\hat{\mathcal{S}}_\varepsilon^+ = \{ (\mathbf{u}, v) \in \mathbb{R}^n : \ v \geq 0, \ u_1 + v = O(\varepsilon) \}$, since $\mathbf{u} \in K$. Hence $d_H(\hat{\mathcal{S}}_\varepsilon^+, \hat{\mathcal{S}}^+) = O(\varepsilon)$, because $\hat{\mathcal{S}}^+ = \{ (\mathbf{u}, v) \in \mathbb{R}^n : \ v \geq 0, \ u_1 + v = 0 \}$. In a similar way, by taking $\hat{\mathcal{S}}_\varepsilon^- = \mathrm{proj}_{\mathbb{R}^s}^{-1}(K) \cap \mathcal{S}_\varepsilon^-$, we obtain $d_H(\hat{\mathcal{S}}_\varepsilon^-, \hat{\mathcal{S}}^-) = O(\varepsilon)$.

<div align="right">□</div>

3.3.2   Existence of maximal canard and faux maximal canard orbits

In this subsection, given the local linear manifolds $\mathcal{S}_\varepsilon^+$ and $\mathcal{S}_\varepsilon^-$, we first present conditions on the coefficients of system (3.1) to obtain maximal and faux maximal canard points. Second, since these points are located in the intersection $\mathcal{S}_\varepsilon^+ \cap \mathcal{S}_\varepsilon^-$, we use their order of contact with the flow to discuss the existence of solution points of the linear system defined by this intersection. Finally, as a consequence, we provide the proofs of theorems 3.2 and 3.3.

From Lemma 3.5, a point $\mathbf{p}_\varepsilon = (\mathbf{u}, v)$ belongs to the intersection $\mathcal{S}_\varepsilon^+ \cap \mathcal{S}_\varepsilon^-$ if and only if the coordinate v is zero and the vector $\mathbf{u} = (u_1, u_2, \ldots, u_s)^T$ satisfies the following two-dimensional linear system with $s = n - 1$ variables

$$
\begin{cases}
z_{11}^+ u_1 + z_{12}^+ u_2 + \ldots + z_{1s}^+ u_s = -\dfrac{\varepsilon}{\lambda_n^+} \displaystyle\sum_{k=1}^{s} z_{1k}^+ b_k, \\[4mm]
z_{11}^- u_1 + z_{12}^- u_2 + \ldots + z_{1s}^- u_s = -\dfrac{\varepsilon}{\lambda_n^-} \displaystyle\sum_{k=1}^{s} z_{1k}^- b_k,
\end{cases}
\tag{3.16}
$$

where z_{ij}^+ and z_{ij}^- are the (i,j)-th elements of the matrices $(\varepsilon A - \lambda_n^+ I)^{-1}$ and $(\varepsilon A - \lambda_n^- I)^{-1}$, respectively. Next lemma provides conditions on the coefficients of system (3.1) to ensure the existence of solutions in system (3.16).

Lemma 3.8. *Let us consider system* (3.1) *with $\varepsilon > 0$ small enough.*

    a) Suppose $s \geq 2$. If $a_{1j} \neq 0$ for some $j \in \{2, \ldots, s\}$ then, $\mathcal{S}_\varepsilon^+ \cap \mathcal{S}_\varepsilon^-$ is a linear manifold

of dimension $n-3$ and every $\mathbf{p}_\varepsilon = (u_1, u_2, \ldots, u_s, 0)^T \in \mathcal{S}_\varepsilon^+ \cap \mathcal{S}_\varepsilon^-$ *satisfies*

$$u_1 = -\frac{\varepsilon^2}{\lambda_n^+ \lambda_n^-} \frac{1}{a_{1j}} \left(\sum_{k=2}^{s} (a_{1k}a_{kj}b_1 - a_{1k}a_{1j}b_k) + \sum_{\substack{k=2 \\ k \neq j}}^{s} \sum_{l=2}^{s} (a_{1k}a_{1l}a_{lj} - a_{1j}a_{1l}a_{lk})u_k \right)$$
$$+ O(\varepsilon^3),$$

$$u_j = -\frac{1}{a_{1j}} \left(b_1 + \sum_{\substack{k=2 \\ k \neq j}}^{s} a_{1k}u_k \right) + O(\varepsilon).$$

b) *Suppose that* $s = 1$, *or* $s \geq 2$ *and* $a_{1j} = 0$ *for all* $j \in \{2, \ldots, s\}$.

   b.1) *If* $b_1 = 0$, *then* $\mathcal{S}_\varepsilon^+ \cap \mathcal{S}_\varepsilon^-$ *is a linear manifold of dimension* $n-2$. *Furthermore,* $S_\varepsilon^+ \cap S_\varepsilon^-$ *is invariant under the flow of system (3.1) and so, neither maximal nor faux maximal canard orbits exist.*

   b.2) *If* $b_1 \neq 0$, *then* $\mathcal{S}_\varepsilon^+ \cap \mathcal{S}_\varepsilon^-$ *is empty and neither maximal nor faux maximal canard orbits exist.*

Proof. Under the assumption of statement (a), let $j_0 \in \{2, \ldots, s\}$ be a subscript such that $a_{1j_0} \neq 0$ and consider the squared submatrix formed by the first and the j_0-th columns of the coefficient matrix in system (3.16). For simplicity we call it M. The determinant of M is computed, by Lemma A.3(b.1), as

$$\det M = z_{11}^+ z_{1j_0}^- - z_{1j_0}^+ z_{11}^- = \frac{\lambda_n^+ - \lambda_n^-}{(\lambda_n^+ \lambda_n^-)^2} \left(\varepsilon a_{1j_0} + \varepsilon^2 \frac{\lambda_n^+ + \lambda_n^-}{\lambda_n^- \lambda_n^+} \sum_{k=1}^{s} a_{1k}a_{kj_0} + O(\varepsilon^3) \right) \neq 0.$$

Consequently, the dimension of the linear manifold $\mathcal{S}_\varepsilon^+ \cap \mathcal{S}_\varepsilon^-$ is $n-3$ and, the components u_1 and u_{j0} can be expressed as a function of the rest of components as

$$\begin{pmatrix} u_1 \\ u_{j0} \end{pmatrix} = M^{-1} \begin{pmatrix} -\dfrac{\varepsilon}{\lambda_n^+} \sum\limits_{k=1}^{s} z_{1k}^+ b_k - \sum\limits_{\substack{k=2 \\ k \neq j_0}}^{s} z_{1k}^+ u_k \\[4mm] -\dfrac{\varepsilon}{\lambda_n^-} \sum\limits_{k=1}^{s} z_{1k}^- b_k - \sum\limits_{\substack{k=2 \\ k \neq j_0}}^{s} z_{1k}^- u_k \end{pmatrix}.$$

Statement (a) of this lemma follows straightforward by using the expansion in power series in ε of $z_{i,j}^+$ and $z_{i,j}^-$ given in Lemma A.3(b.1) of Appendix A.

Suppose now that $a_{1j} = 0$ for all $j \in \{2, \ldots, s\}$. From Lemma A.3(b.2) in Appendix A, it follows that $z_{1j}^+ = 0$, $z_{1j}^- = 0$ for $j \in \{2, \ldots, s\}$,

$$z_{11}^+ = -\frac{1}{\lambda_n^+} \left(1 + \sum_{k=1}^{\infty} \left(\frac{\varepsilon a_{11}}{\lambda_n^+} \right)^k \right) \neq 0, \quad z_{11}^- = -\frac{1}{\lambda_n^-} \left(1 + \sum_{k=1}^{\infty} \left(\frac{\varepsilon a_{11}}{\lambda_n^-} \right)^k \right) \neq 0.$$

Therefore, system (3.16) can be recast as $u_1 = -\frac{\varepsilon}{\lambda_n^+} b_1$ and $u_1 = -\frac{\varepsilon}{\lambda_n^-} b_1$. Since $\lambda_n^+ \lambda_n^- < 0$, we conclude that this system is compatible only if $b_1 = 0$. In this case, the linear manifold

$\mathcal{S}_\varepsilon^+ \cap \mathcal{S}_\varepsilon^-$ has dimension $n-2$. Since, $a_{1j} = 0$ for all $j \in \{2, \ldots, s\}$, $b_1 = 0$ and $u_1 = 0$, by one hand, and $v = 0$ on $\mathcal{S}_\varepsilon^+ \cap \mathcal{S}_\varepsilon^-$, on the other; then, $\mathcal{S}_\varepsilon^+ \cap \mathcal{S}_\varepsilon^-$ is invariant under the flow of system (3.1). A direct consequence of this invariance is the fact that neither maximal nor faux maximal canards orbits can exist. This proves statement (b). Assuming that $b_1 \neq 0$, we have that system (3.16) is incompatible and, hence, statement (c) follows. $\quad\square$

The analysis of the direction of the vector field of system (3.1) at the intersection points $\mathbf{p}_\varepsilon \in \mathcal{S}_\varepsilon^+ \cap \mathcal{S}_\varepsilon^-$, shown in Lemma 3.8(a), allows us to characterize them as maximal or faux maximal canard points. We approach this analysis, concerning the order of contact, in next lemma.

Lemma 3.9. *Let k be the order of contact of the flow of system* (3.1) *with the switching manifold $\{v = 0\}$ at a contact point $\mathbf{p} = (\mathbf{u}, 0)^T \in \mathbb{R}^n$.*

a) *$k = 1$ if and only if $\mathbf{e}_1^T \mathbf{u} \neq 0$. Moreover, if $\mathbf{e}_1^T \mathbf{u} > 0$ (resp. $\mathbf{e}_1^T \mathbf{u} < 0$) the orbit $\gamma_\mathbf{p}$ through $\mathbf{p}$ crosses $\{v = 0\}$ in the direction (resp. opposite direction) of the vector $\mathbf{e}_n$.*

b) *$k = 2$ if and only if $\mathbf{e}_1^T \mathbf{u} = 0$ and $\mathbf{e}_1^T(A\mathbf{u} + \mathbf{b}) \neq 0$.*

c) *$k \geq 3$ if and only if $\mathbf{e}_1^T \mathbf{u} = 0$, $\mathbf{e}_1^T A^r (A\mathbf{u} + \mathbf{b}) = 0$ with $r = 0, 1, \ldots, k-3$ and $\mathbf{e}_1^T A^{k-2}(A\mathbf{u} + \mathbf{b}) \neq 0$.*

Proof. Consider the system (3.1) written in its matrix form (3.4). To prove statement (a), by straightforward computations, we obtain

$$\mathbf{e}_n^T \left(B_\varepsilon^+ \mathbf{p} + \mathbf{c}_\varepsilon\right) = \mathbf{e}_n^T \left(B_\varepsilon^- \mathbf{p} + \mathbf{c}_\varepsilon\right) = \mathbf{e}_1^T \mathbf{u}. \tag{3.17}$$

Therefore, from the previous equalities and expressions (3.6), we obtain that the order of contact at $\mathbf{p}$ is $k = 1$ if and only if $\mathbf{e}_1^T \mathbf{u} \neq 0$. Moreover, since the vector $(B_\varepsilon^+ \mathbf{p} + \mathbf{c}_\varepsilon) = (B_\varepsilon^- \mathbf{p} + \mathbf{c}_\varepsilon)$ is tangent to the flow at the point $\mathbf{p}$, we conclude statement (a).

To prove statement (b), let us consider Lemma A.4 of Appendix A where the matrix B is either B_ε^+ or B_ε^- and the vector $\mathbf{c}$ is $\mathbf{c}_\varepsilon$, as they are given in expressions (3.5). In this case, since $\mathbf{e}_1^T \mathbf{u} = 0$, by considering the equality of Lemma A.4(a) and multiplying both sides for the last element of the canonical base of $\mathbb{R}^n$, we obtain

$$\mathbf{e}_n^T B_\varepsilon^+ \left(B_\varepsilon^+ \mathbf{p} + \mathbf{c}_\varepsilon\right) = \mathbf{e}_n^T B_\varepsilon^- \left(B_\varepsilon^- \mathbf{p} + \mathbf{c}_\varepsilon\right) = \varepsilon \, \mathbf{e}_1^T (A\mathbf{u} + \mathbf{b}). \tag{3.18}$$

Then, the proof of statement (b) follows from expressions (3.6), (3.17) and (3.18).

Finally, to prove statement (c), let us assume that $k \geq 3$, $\mathbf{e}_1^T \mathbf{u} = 0$ and $\mathbf{e}_1^T A^l (A\mathbf{u} + \mathbf{b}) = 0$ for all $l = 0, \ldots, k-3$. Therefore, by Lemma A.4(b) and following the same procedure than before,

$$\mathbf{e}_n^T \left(B_\varepsilon^+\right)^{k-1} \left(B_\varepsilon^+ \mathbf{p} + \mathbf{c}_\varepsilon\right) = \mathbf{e}_n^T \left(B_\varepsilon^-\right)^{k-1} \left(B_\varepsilon^- \mathbf{p} + \mathbf{c}_\varepsilon\right) = \varepsilon^{k-1} \mathbf{e}_1^T A^{k-2}(A\mathbf{u} + \mathbf{b}). \tag{3.19}$$

Hence, statement (c) is a consequence of expressions (3.6), (3.17), (3.18) and (3.19). $\quad\square$

Proof of Theorem 3.2. Statement (a) follows from Lemma 3.8(a), where we have characterized the points $\mathbf{p}_\varepsilon = (\mathbf{u}_\varepsilon, 0)^T$ in the intersection $\mathcal{S}_\varepsilon^+ \cap \mathcal{S}_\varepsilon^-$.

In order to distinguish whether $\mathbf{p}_\varepsilon$ is a maximal canard or a faux maximal canard point and so, to end the proof of statement (a), we recall that in Lemma 3.9(a) we analyze the

sign of the non-zero equation in (3.6). Therefore, when $\mathbf{e}_1^T \mathbf{u}_\varepsilon > 0$, the order of contact of $\mathbf{p}_\varepsilon$ is $k = 1$, and the orbit $\gamma_{\mathbf{p}_\varepsilon}$ crosses the switching manifold from $\mathcal{S}_\varepsilon^-$ to $\mathcal{S}_\varepsilon^+$ implying that $\mathbf{p}_\varepsilon$ is a maximal canard point. This proves statement (a.1). Similarly, if $\mathbf{e}_1^T \mathbf{u}_\varepsilon < 0$, the order of contact of $\mathbf{p}_\varepsilon$ is also $k = 1$, the orbit $\gamma_{\mathbf{p}_\varepsilon}$ crosses the switching manifold from $\mathcal{S}_\varepsilon^+$ to $\mathcal{S}_\varepsilon^-$, and so $\mathbf{p}_\varepsilon$ is a faux maximal canard point. This proves (a.2).

Otherwise, when $\mathbf{e}_1^T \mathbf{u}_\varepsilon = 0$, the order of contact k is greater than one, proving (a.3). We note that, in this case, the maximal canard points are those satisfying that k is odd and $\mathbf{e}_1^T A^{k-1}(A\mathbf{u}_\varepsilon + \mathbf{b}) > 0$ (see Lemma 3.9(c)) and the faux maximal canard points are those satisfying that k is also odd but $\mathbf{e}_1^T A^{k-1}(A\mathbf{u}_\varepsilon + \mathbf{b}) < 0$.

Finally, statements (b.1) and (b.2) follow from Lemma 3.8(b.1) and (b.2), respectively. $\qquad\square$

Proof of Theorem 3.3. Let $\mathbf{p}_\varepsilon = (\mathbf{u}_\varepsilon, 0)^T$ be a point in $\mathcal{S}_\varepsilon^+ \cap \mathcal{S}_\varepsilon^-$ and $\mathbf{p}_0 = (\mathbf{u}_0, 0)^T$ be the limit of $\mathbf{p}_\varepsilon$ when ε tends to zero. To prove statement (a) we are going to see that $\mathbf{e}_1^T \mathbf{u}_0 = 0$ and $\mathbf{e}_1^T (A\mathbf{u}_0 + \mathbf{b}) = 0$, i.e. that $\mathbf{p}_0$ is a contact point of order greater than or equal to two of the slow subsystem with the hyperplane $\mathcal{F}$ (see Lemma 3.2).

From the expressions of the manifolds $\mathcal{S}_\varepsilon^+$ and $\mathcal{S}_\varepsilon^-$ in Lemma 3.5, $\mathbf{p}_\varepsilon$ satisfies that

$$\mathbf{e}_1^T (\varepsilon A - \lambda_n^+ I)^{-1} \left(\mathbf{u}_\varepsilon + \frac{\varepsilon}{\lambda_n^+} \mathbf{b} \right) = 0 \quad \text{and} \quad \mathbf{e}_1^T (\varepsilon A - \lambda_n^- I)^{-1} \left(\mathbf{u}_\varepsilon + \frac{\varepsilon}{\lambda_n^-} \mathbf{b} \right) = 0.$$

Moreover, from the development of the matrices $(\varepsilon A - \lambda_n^+ I)^{-1}$ and $(\varepsilon A - \lambda_n^- I)^{-1}$ in power series of ε (see Lemma A.3(b) in Appendix A), these equalities can be rewritten as

$$\mathbf{e}_1^T \mathbf{u}_\varepsilon + \sum_{k=1}^{\infty} \left(\frac{\varepsilon}{\lambda_n^+} \right)^k \mathbf{e}_1^T A^{k-1}(A\mathbf{u}_\varepsilon + \mathbf{b}) = 0,$$

$$\tag{3.20}$$

$$\mathbf{e}_1^T \mathbf{u}_\varepsilon + \sum_{k=1}^{\infty} \left(\frac{\varepsilon}{\lambda_n^-} \right)^k \mathbf{e}_1^T A^{k-1}(A\mathbf{u}_\varepsilon + \mathbf{b}) = 0.$$

Therefore, considering the limit when ε tends to zero in each one of the above equations, we conclude that $\mathbf{e}_1^T \mathbf{u}_0 = \lim_{\varepsilon \searrow 0} \mathbf{e}_1^T \mathbf{u}_\varepsilon = 0$. On the other hand, by subtracting the second equation in (3.20) to the first one, and removing the common factor ε, we obtain

$$\left(\frac{1}{\lambda_n^+} - \frac{1}{\lambda_n^-} \right) \mathbf{e}_1^T (A\mathbf{u}_\varepsilon + \mathbf{b}) + \sum_{k=1}^{\infty} \varepsilon^k \left(\frac{1}{\left(\lambda_n^+ \right)^{k+1}} - \frac{1}{\left(\lambda_n^- \right)^{k+1}} \right) \mathbf{e}_1^T A^k(A\mathbf{u}_\varepsilon + \mathbf{b}) = 0. \tag{3.21}$$

Since λ_n^+ and λ_n^- are different numbers, taking the limit when ε tends to zero in (3.21), it follows that $\mathbf{e}_1^T (A\mathbf{u}_0 + \mathbf{b}) = \lim_{\varepsilon \searrow 0} \mathbf{e}_1^T (A\mathbf{u}_\varepsilon + \mathbf{b}) = 0$, which ends the proof of statement (a).

In the particular case of $n = 3$, that is when $s = 2$, taking $\mathbf{p}_\varepsilon = (u_1, u_2, 0)^T$ be the unique maximal canard or faux maximal canard point, from Theorem 1.2 in Prohens and Teruel (2013) it follows that $a_{12} \neq 0$, $u_1 = -\frac{d_3}{\lambda_n^+ \lambda_n^-} \varepsilon^2$ with $d_3 = b_1 a_{22} - b_2 a_{12}$ and $\mathbf{u}_0 = (0, -b_1/a_{12})^T$. Since $\mathbf{p}_\varepsilon$ is a contact point of order one, from Lemma 3.9(a) we obtain that $u_1 \neq 0$ and direct computations give $\mathbf{e}_1^T A(A\mathbf{u}_0 + \mathbf{b}) = -d_3 \neq 0$. Therefore, $\mathbf{u}_0$ is a contact point of order two of the reduced flow with $\mathcal{F}$ (see Lemma 3.2), which proves statement (b). $\qquad\square$

3.4   Examples

In this section, we illustrate through two examples our results. A 4-dimensional example allows us to see the coexistence of maximal and faux maximal canards. However, in order to fully appreciate how a faux maximal canard bifurcates from the perturbation of an invisible two-fold, we also consider an example in $\mathbb{R}^3$.

3.4.1   A 4-dimensional piecewise linear example

Let us consider the following 4-dimensional piecewise linear version of the canonical form in the expression (20) in the work of Wechselberger (2012),

$$
\begin{cases}
\dot{u}_1 = \frac{1}{2}\mu u_2 - (1+\mu)v, \\
\dot{u}_2 = a_{23}u_3 + 1, \\
\dot{u}_3 = u_3, \\
\varepsilon\dot{v} = u_1 + |v|,
\end{cases}
\tag{3.22}
$$

where μ and $a_{23} \geq 0$ are fixed real parameters. The parameter a_{23} has been added so that the example exhibits the most complete structure of orbits connecting the two branches of the slow manifold.

The linear systems, defined by system (3.22) at each side of the switching manifold $\{v = 0\}$, have eigenvalues given by

$$
\lambda_1^+ = \lambda_1^- = 0, \qquad\qquad \lambda_2^+ = \lambda_2^- = \varepsilon,
$$
$$
\lambda_3^+ = -\lambda_3^- = \tfrac{1-\sqrt{1-4\varepsilon(1+\mu)}}{2}, \qquad \lambda_4^+ = -\lambda_4^- = \tfrac{1+\sqrt{1-4\varepsilon(1+\mu)}}{2},
$$

where the fast ones are λ_4^+ and λ_4^-. From Theorem 3.1, the slow manifold $\mathcal{S}_\varepsilon$ is given by the union of the repelling branch

$$
S_\varepsilon^+ = \left\{ (\mathbf{u}, v) \in \mathbb{R}^4 : \ v \geq 0, \quad u_1 + \frac{\varepsilon\mu}{2\lambda_4^+}u_2 - \frac{\varepsilon^2\mu a_{23}}{2\lambda_4^+(\varepsilon - \lambda_4^+)}u_3 + \lambda_4^+ v = -\frac{\varepsilon^2\mu}{2(\lambda_4^+)^2} \right\}
$$

and the attracting one

$$
S_\varepsilon^- = \left\{ (\mathbf{u}, v) \in \mathbb{R}^4 : \ v \leq 0, \quad u_1 + \frac{\varepsilon\mu}{2\lambda_4^-}u_2 - \frac{\varepsilon^2\mu a_{23}}{2\lambda_4^-(\varepsilon - \lambda_4^-)}u_3 + \lambda_4^- v = -\frac{\varepsilon^2\mu}{2(\lambda_4^-)^2} \right\}.
$$

If $\mu = 0$, the intersection of these half-hyperplanes is the plane $\mathcal{S}_\varepsilon^+ \cap \mathcal{S}_\varepsilon^- = \{u_1 = 0, \ v = 0\}$, which is invariant under the flow of system (3.22). Therefore, neither maximal nor faux maximal canards exist. This statement agrees with Theorem 3.2(b.1). Otherwise, if $\mu \neq 0$, the intersection $\mathcal{S}_\varepsilon^+ \cap \mathcal{S}_\varepsilon^-$ yields to the locus of either maximal or faux maximal canard points, and it corresponds to the straight line

$$
\mathcal{S}_\varepsilon^+ \cap \mathcal{S}_\varepsilon^- = \left\{ \left(\frac{\varepsilon^2\mu}{2}\left(\frac{a_{23}}{\varepsilon^2 - (\lambda_4^+)^2}u_3 - \frac{1}{(\lambda_4^+)^2} \right), \ \frac{\varepsilon^2 a_{23}}{\varepsilon^2 - (\lambda_4^+)^2}u_3, \ u_3, \ 0 \right)^T : u_3 \in \mathbb{R} \right\}.
$$

Depending on the sign of the first coordinate of each point $\mathbf{p}_\varepsilon \in \mathcal{S}_\varepsilon^+ \cap \mathcal{S}_\varepsilon^-$, from the last equation in (3.22), $\mathbf{p}_\varepsilon$ is a maximal or faux maximal canard point. This declaration agrees with Theorem 3.2(a). Next we discuss about the coexistence of both maximal and faux maximal canard orbits, depending on the parameters a_{23} and μ.

When $a_{23} = 0$, the sign of the first coordenate of $\mathbf{p}_\varepsilon$ does not change along $\mathcal{S}_\varepsilon^+ \cap \mathcal{S}_\varepsilon^-$. Therefore, maximal and faux maximal canard points do not coexist on this straight line. Specifically, only maximal canard points exist when $\mu < 0$ and only faux maximal canard points exist when $\mu > 0$. Note that this case corresponds to the 4-dimensional piecewise linear system discussed in Remark 3.2.

On the other hand, if $a_{23} > 0$, the first coordinate vanishes when $u_3^* = \frac{1}{a_{23}}\left(\left(\frac{\varepsilon}{\lambda_4^+}\right)^2 - 1\right)$, that is at the point

$$\mathbf{p}_\varepsilon^* = \left(0,\ \left(\frac{\varepsilon}{\lambda_4^+}\right)^2,\ \frac{1}{a_{23}}\left(\left(\frac{\varepsilon}{\lambda_4^+}\right)^2 - 1\right),\ 0\right)^T.$$

Since expression (3.6) holds for $k = 2$, i. e.

$$\mathbf{e}_4^T(B_\varepsilon^+ \mathbf{p}_\varepsilon^* + \mathbf{c}_\varepsilon) = \mathbf{e}_4^T(B_\varepsilon^- \mathbf{p}_\varepsilon^* + \mathbf{c}_\varepsilon) = 0$$

$$\mathbf{e}_4^T B_\varepsilon^+(B_\varepsilon^+ \mathbf{p}_\varepsilon^* + \mathbf{c}_\varepsilon) = \mathbf{e}_4^T B_\varepsilon^-(B_\varepsilon^- \mathbf{p}_\varepsilon^* + \mathbf{c}_\varepsilon) = \frac{\varepsilon^3 \mu}{2\left(\lambda_4^+\right)^2} \neq 0,$$

the flow has second order contact with the switching manifold at point $\mathbf{p}_\varepsilon^*$. Then, the orbit through $\mathbf{p}_\varepsilon^*$ does not cross the switching manifold; this fact means that the orbit remains confined in one of the half-hyperplanes, depending on the sign of μ. Therefore, this point is neither a maximal nor a faux maximal canard point. Nevertheless, $\mathbf{p}_\varepsilon^*$ is a relevant point since it separates the half-line formed by the maximal canard points ($u_3 < u_3^*$ if $\mu > 0$ or $u_3 > u_3^*$ if $\mu < 0$) from that formed by the faux maximal canard points ($u_3 > u_3^*$ if $\mu > 0$ or $u_3 < u_3^*$ if $\mu < 0$).

To see the source of maximal and faux maximal canards, take the limiting case when ε tends to zero of the straight line $\mathcal{S}_\varepsilon^+ \cap \mathcal{S}_\varepsilon^-$ and $\mathbf{p}_\varepsilon^*$; that is

$$\mathcal{S}_0^+ \cap \mathcal{S}_0^- = \{(0, 0, u_3, 0) : u_3 \in \mathbb{R}\} \quad \text{and} \quad \mathbf{p}_0^* = \left(0, 0, -\frac{1}{a_{23}}, 0\right),$$

and consider, from system (3.8), the reduced flow given by

$$\begin{cases} v' = \mathrm{sgn}(v)\left((1+\mu)v - \frac{1}{2}\mu u_2\right), \\ u_2' = a_{23}u_3 + 1, \\ u_3' = u_3. \end{cases}$$

Straightforward computations show that each point in the straight line $\mathcal{S}_0^+ \cap \mathcal{S}_0^-$ is a contact point of order two, except the $\mathbf{p}_0^*$ point which is a contact point of order three. This result agrees with Theorem 3.3(a). Moreover, note that $\mathbf{p}_0^*$ separates visible from invisible two-folds in the way depicted in Figure 3.2. We conclude that maximal canard points and faux maximal canard points bifurcate from visible and invisible two-fold singularities, respectively. This fact might indicate that Theorem 3.3(b) is also true for $n > 3$.

3.4.2   A 3-dimensional piecewise linear example

In order to illustrate how a faux maximal canard orbit bifurcates from the perturbation of an invisible two-fold singularity, which results to be a singular faux canard, let us consider the following 3-dimensional piecewise linear system

$$\begin{cases} \dot{u}_1 = \frac{1}{2}\mu u_2 - (1+\mu)v, \\ \dot{u}_2 = 1, \\ \varepsilon\dot{v} = u_1 + |v|, \end{cases} \tag{3.23}$$
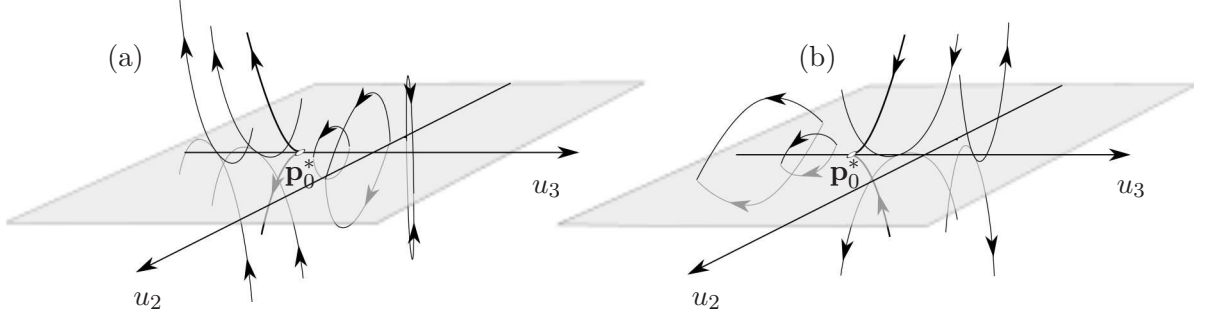
Figure 3.2: Reduced flow defined by the piecewise linear system (3.22) on the fold manifold $\{v = 0\}$ (grey areas). The upper half-space corresponds to the repelling branch of the critical manifold and the bottom half-space corresponds to the attracting one. Each point in the u_3-axis is a two-fold singularity except the point $\mathbf{p}_0^*$ which has order of contact equal to three. Therefore, $\mathbf{p}_0^*$ separates visible two-folds from invisible two-folds: (a) when $\mu > 0$ and (b) when $\mu < 0$.

where $\mu > 0$. This system is a piecewise linear version of the canonical form given by the expression (20) in the work of Wechselberger (2012).

As in previous example, at each side of the switching manifold $\{v = 0\}$, system (3.23) has eigenvalues given by

$$\lambda_1^+ = \lambda_1^- = 0, \quad \lambda_2^+ = -\lambda_2^- = \frac{1-\sqrt{1-4\varepsilon(1+\mu)}}{2}, \quad \lambda_3^+ = -\lambda_3^- = \frac{1+\sqrt{1-4\varepsilon(1+\mu)}}{2},$$

where the fast ones are λ_3^+ and λ_3^-.

The repelling and attracting branches are respectively

$$\mathcal{S}_\varepsilon^+ = \{(u_1, u_2, v) \in \mathbb{R}^3 : v \geq 0, \ 2(\lambda_3^+)^2 u_1 + \lambda_3^+ \varepsilon \mu u_2 + 2(\lambda_3^+)^3 v = -\varepsilon^2 \mu\},$$
$$\mathcal{S}_\varepsilon^- = \{(u_1, u_2, v) \in \mathbb{R}^3 : v \geq 0, \ 2(\lambda_3^-)^2 u_1 + \lambda_3^- \varepsilon \mu u_2 + 2(\lambda_3^-)^3 v = -\varepsilon^2 \mu\}.$$

Their intersection takes place at the point

$$\mathbf{p}_\varepsilon^* = \left(\frac{-\varepsilon^2 \mu}{2(\lambda_3^+)^2}, 0, 0\right),$$

and the intersection of $\mathcal{S}_\varepsilon^+$ and $\mathcal{S}_\varepsilon^-$ with the u_2-axis takes place at the points $\mathbf{p}^+ = (0, -\varepsilon/\lambda_3^+, 0)^T$ and $\mathbf{p}^- = (0, -\varepsilon/\lambda_3^-, 0)^T$, respectively.

By Theorem 3.2, since the first component of $\mathbf{p}_\varepsilon^*$ is negative, a faux maximal canard through this point exists. Moreover, according to expression (3.6), $\mathbf{p}^+$ and $\mathbf{p}^-$ are contact points of order two, where the non-zero conditions are given by $-(\varepsilon^2 \mu)/(2\lambda_3^+) < 0$ and $-(\varepsilon^2 \mu)/(2\lambda_3^-) > 0$, respectively. Therefore, the orbit through $\mathbf{p}^+$ is locally contained in $\{v \leq 0\}$ and the orbit through $\mathbf{p}^-$ is locally contained in $\{v \geq 0\}$, see Figure 3.3, left bottom panel.

To see the singular orbit from which the faux maximal canard bifurcates, we consider the limiting case when ε tends to zero. The critical manifold is $\mathcal{S} = \{(u_1, u_2, v) \in \mathbb{R}^3 : u_1 + |v| = 0\}$ and, from expression (3.8), the reduced flow is given by

$$\begin{cases} v' = \text{sgn}(v)\left((1+\mu)v - \frac{1}{2}\mu u_2\right), \\ u_2' = 1. \end{cases}$$

We observe that, the points $\mathbf{p}_\varepsilon^*$, $\mathbf{p}^+$ and $\mathbf{p}^-$ tend to the origin $\mathbf{p}_0^* = (0, 0, 0)^T$ as ε goes to zero. Straightforward computations show that $\mathbf{p}_0^*$ is an invisible two-fold singularity, which agrees with Lemma 3.2. See Figure 3.3, left upper panel for a three dimensional representation of the reduced flow.
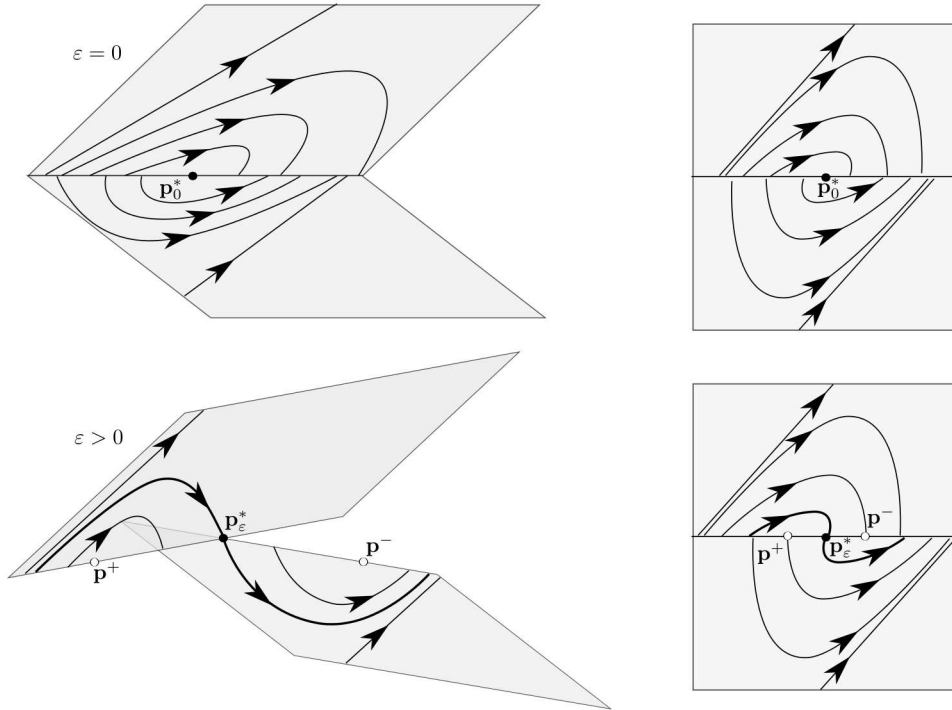

Figure 3.3: Representation of the 2-dimensional reduced flow of system (3.23). Upper panel shows the unperturbed case surrounding the invisible two-fold $\mathbf{p}_0^*$. Bottom panel shows the perturbed flow where the black point $\mathbf{p}_\varepsilon^*$ stands for the faux maximal canard point, while the white points $\mathbf{p}^+$ and $\mathbf{p}^-$ are the breaking points of $\mathbf{p}_0^*$. These white points are invisible two-fold singularities for $\mathcal{S}_\varepsilon^+$ and $\mathcal{S}_\varepsilon^-$, respectively. In right panels we depict the projection, on $\{v = 0\}$, of the reduced flow represented in left panels.

Therefore, the point $\mathbf{p}_0^*$ is the singular faux canard since the faux maximal canard through $\mathbf{p}_\varepsilon^*$ bifurcates from $\mathbf{p}_0^*$ after perturbing the system.

3.5 Discussion

In this chapter we have done a next step towards a systematic study of slow-fast dynamics in a piecewise linear setting. An explicit expression for the slow manifold have been derived. This expression allows to find maximal canard orbits just by intersecting the attracting and repelling branches of the slow manifold. By continuation of these intersection points, as ε tends to zero, we obtain the points from where maximal canard orbits perturb. These points are contact points of order greater than or equal to two of the reduced flow with the fold manifold.

In the smooth case, former points are the folded singularities, and the analysis of maximal canards are done by perturbing them. We remark that in our piecewise linear framework this analysis goes exactly on the opposite direction; that is by obtaining the maximal

canard points from the intersection of the slow manifolds and then looking for the singular canards as the limiting case.

Comparing the theory of canards in the smooth case with our results in the non-smooth setting, in Remark 3.2 we conclude that in both situations the dimension of the locus in the switching manifold, corresponding to maximal or faux maximal canard orbits, coincide. However, regarding the character of canard orbits, whereas in the folded saddle case they agree, in the folded node case they do not. This disagreement could be triggered by the fact that, in our context, normal hyperbolicity is not lost as in the smooth case, it is simply non-defined. To overcome this situation, other piecewise linear structures, having the possibility to lose normal hyperbolicity, could be proposed. On this way, we mention the work in progress of Desroches et al (2016b).

Note that the fast equation in system (3.1) is rather general since each system (3.1) with the fast equation $\dot{v} = \mathbf{d}^T \mathbf{u} + |v|$, where $\mathbf{d} \neq \mathbf{0}$, can be transformed into system (3.1) by the linear change of variables $\mathbf{u} \to \left(\mathbf{d}^T \mathbf{u}, u_2, \ldots, u_n \right)^T$.

We want to observe that the matrix approach used in this paper may be used to analyze the slow-fast dynamics in a more general context, for instance, by considering the number of fast variables greater than one.

Chapter 4

Effects of plasticity on synaptic conductances in a network with slow oscillations

Neurons in the brain are continuously bombarded by thousands of highly fluctuating inputs which generate irregular and variable spike trains. The richness of cognitive skills and adaptive properties of the human brain are matched by the great complexity of its anatomy and physiology at all levels, from synapses to sensory maps and systems. This is also reflected in the heterogeneity of temporal dynamics associated to those levels, spanning more than ten orders of magnitude, from microseconds to years. The structural features of cortical networks are clearly linked to aspects of brain function and dynamics, playing a crucial role in determining which functional patterns (and thus, brain states) can and cannot occur. Network connectivity contributes to promote highly complex neural activations, to maximize information transmission and processing, and to drive the network towards dynamic states characterized by synchronous/asynchronous features (see Diesmann et al (1999), Parga and Abbott (2007) and Renart et al (2010)). Network dynamics originated by the interactions of neuronal assemblies has been extensively studied and characterized in different ways both in vivo and in vitro during resting conditions or spontaneous activity (see Buzsáki and Draguhn (2004), van Pelt et al (2004) and Eytan and Marom (2006)), as well as when external stimuli are delivered to the system (see Massobrio et al (2007), Wagenaar et al (2005), and Marguet and Harris (2011)).

An important aspect of the brain's connectivity is the plasticity, changes in the brain connections that can last from milliseconds to years, where the synaptic efficacy changes over time, reflecting the history of the presynaptic activity. When changes take place in a short period of time, this phenomenon is called the short-term plasticity (STP); and two types of STP have been experimentally observed: the short-term depression (STD) and the short-term facilitation (STF) (see Section 1.1). Depending on the cortical areas, plasticity can be either STD-domatinated, STF-dominated, or presenting both mechanisms at the same time (see Stevens and Wang (1995), Abbott and Regehr (2004), Zucker and Regehr (2002), among others). STD has a large impact on network computations. Experimental results suggest that this kind of plasticity is modulated by cortical activity, increasing during the silent states and decreasing during activity states of the neuron. On the other hand, STF is present at synaptic level depicting a longer time scale than STD. The simultaneous presence of such two plasticity mechanisms is responsible of the genesis of particular spiking patterns like bursts, network bursts, up/down states, among others.

Although in the last years advancements in the technology helped to unravel hidden mechanisms both at cellular and network level, some aspects remain still unclear without the use of computer simulations. In this chapter, we use a bio-inspired network model made up of conductance-based neurons (see Section 2.1.4 or Compte et al (2003) for more details on the network), where short-term synaptic plasticity mechanisms (both facilitation and depression) have been added. In Benita et al (2012) the effects caused by short-term depression on this specific neuronal network have already been studied. Their results show that there exists a mutual interaction between synaptic depression and network activity. In this chapter, even though we reproduce the raster plots they obtain for depression, we aim to move a step forward by adding also the facilitation mechanism to the network. Moreover, we also aim to see, for both mechanisms, possible dynamics between the excitatory and the inhibitory populations of neurons by taking into account their firing rate dynamics. Finally, we also study the effects on the excitatory (AMPA, NMDA) and inhibitory (GABA) synaptic conductances caused by sweeping the levels of facilitation and depression, when spontaneous activity is only considered; that is, when the network is not perturbed by any kind of external stimulation. Besides, these goals, we also obtain "realistic" conductance traces from our simulations that become a excellent source of *in sillico* examples to test the methods developed in Chapter 5.

This chapter is structured as follows. In Section 4.1, we briefly explain the neuronal network and some neuronal coding tools that we use to obtain our results, presented in Section 4.2. In Subsection 4.2.1 we explain the results obtained when the short-term depression level is changing, whereas in Subsection 4.2.2 we depict the results obtained by changing the short-term facilitation level. Finally, in Section 4.3, we give some conclusions.

4.1   Models and data treatment

To develop this chapter, we use the bio-inspired network in Compte et al (2003), where a short-term plasticity mechanism has been added according to the description presented in Dayan and Abbott (2005). Briefly explained, the model is made up of a population of excitatory multi-compartment neurons and inhibitory single-compartment neurons. These neurons contain different membrane channels that are modelled according to the Hodgkin-Huxley formalism. In order to emulate the connectivity rule observed in visual cortex, neurons are supposed to be spatially arranged on a segment line. Moreover, the synaptic transmission has been mediated by excitatory AMPA and NMDA, and inhibitory GABA currents, under the presence of short-term depression and facilitation mechanisms.

When no short-term plasticity is added to the network, the activity of the network presents alternations of UP and DOWN states. The UP states are intervals of time where neurons are continuously firing. On the other hand, DOWN states are those intervals where all neurons are, in general, in a silent state (they do not spike); only a reduced number of neuron might sporadically fire, without altering the silent state of the rest of neurons in the network. To see more details about the network see Section 2.1.4.

Because of the big amount of neurons considered in the network, we use two different neural coding schemes to describe their activity. These schemes are the instantaneous firing rate (IFR), explained in Section 2.4.1.1, and the raster plot, explained in Section 2.4.1.2. Details about the numerical integration of the network are given in Section 2.4.2.

4.2 Results

In this section we present the computational results obtained by sweeping the depression and the facilitation levels of plasticity in the neuronal network described in Section 4.1. In Subsection 4.2.1 we depict the results by only changing the depression level, whereas in Subsection 4.2.2 we depict the results by only changing the facilitation level.

4.2.1 Effects of the short-term depression

By changing the depression level, a gradual change of the activity of the network is observed. As already shown in Benita et al (2012), raster plots (upper subpanels) in Figure 4.1 depict how the duration of the UP and DOWN states changes. As we decrease the depression factor, and so we increase the synaptic depression, the network response presents longer UP states until DOWN states are completely removed. There exists a specific value f_D^* close to 0.84 and 0.85 where neurons stop to present an UP/DOWN behaviour (observed for $f_D > f_D^*$) to present a tonic firing state (for $f_D < f_D^*$). Simulations presented in Figure 4.1 last 10 s; however, longer simulations (of 20 s) have been done to ensure, with more certainty, that a second UP state does not occur.

The f_D^* value may change depending on the intrinsic fluctuations of the neuron. In order to see their effects we have simulated the network several times, keeping the same f_D but using different random fluctuations. In all cases we have tested this value remains between 0.84 and 0.85

In order to move a step forward from results in Benita et al (2012) and see possible dynamic explanations, we plot the lower subpanels of Figure 4.1, which represent the IFR averaged over the excitatory population (red line) and over the inhibitory population (grey line). These plots show that the inhibitory activity is greater than the excitatory one. Moreover, the inhibitory population also presents longer activity since inhibitory neurons do spikes for a longer time period. In fact, the tails depicted at the end of the UP state in the raster plots correspond to inhibitory neurons. When neurons do not stop firing, i.e. when $f_D < f_D^*$ (see panels G-I), both the excitatory and inhibitory IFR present a damped oscillation around some fixed value, which is different for each f_D. This behaviour might be caused by the presence of an attracting focus, but the complexity of the model does not allow to ensure this point. This fact would also explain that, when this point is reached, then there is no possibility to generate a down state.

To gain insight in the joint dynamics, in Figure 4.2, we depict the dynamics of excitatory IFR versus the inhibitory IFR, where each panel corresponds to a specific depression level. In these plots, the mathematical mechanism generated to prevent neurons from firing can be intuited, as well as why a second UP state is generated. For values of f_D lower than $f_D^* \approx 0.85$, the trajectory goes from the initial condition to some fixed point, where the trajectory turns around before remaining there. This point acts as an attractor (seemingly, a focus) and the intrinsic fluctuations of the network are not able to eject the trajectory from this point. For this reason, a continuous UP state is presented.

When $f_D > f_D^*$, see panels A-F, the depression level is not enough to reach the attractor point and so, the activity of the network is driven close to another fixed point, the $O = (0,0)$. At this point there is no activity both for excitatory and inhibitory populations. Hence, a DOWN state occurs and it lasts the same time than the trajectory takes to leave the vicinity of O. When this happens, the trajectory makes a long excursion to come back
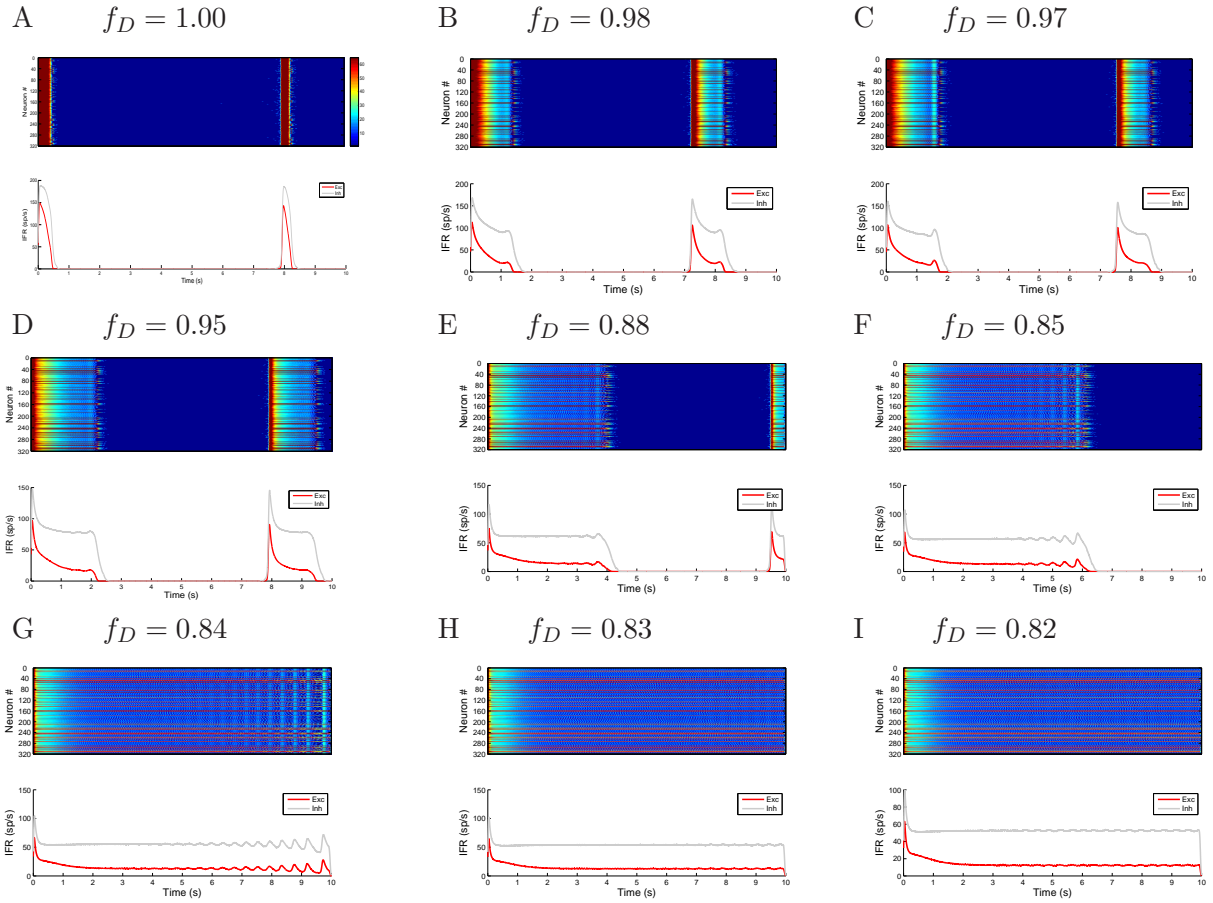
Figure 4.1: **Raster plot and instantaneous firing rate for different values of the depression factor f_D.** Upper plots in all panels represent, for all neurons in the network, the coloured raster plot where colours indicate the instantaneous firing rate (IFR), where as warmer is the colour as higher is the membrane potential. When colour is different from dark blue, means neurons are spiking (UP state), otherwise, they don't (DOWN state). Lower plots in all panels represent the instantaneous firing rate of the excitatory population (red line) and of the inhibitory population (grey line). The depression level $f_D = 0.85$ is the bifurcation value where the network switches from presenting UP and DOWN states to only present a continuous UP state.

again to the vicinity of O after some period. Therefore, when $f_D > f_D^*$ the dynamics seems to be close to a homoclinic orbit being O a saddle point.

Figure 4.3, Panel A, represents the duration of the UP (blue line) and the DOWN (red line) states. This plot shows how the UP states are longer when depression factor decreases, as it was reported in Benita et al (2012). However, for the duration of the DOWN state, even though it was reported to be decreasing in Benita et al (2012), in our case behaves at a nearly constant rate. From different traces of membrane potential extracted from different simulations maintaining the same f_D, we have seen that there are no substantial differences regarding the duration of the UP and the DOWN state among them, as we can see in Panel B for $f_D = 0.88$.

The dynamics of the model is given, in part, by the probability of neurotransmitter release, $P_{rel}(t)$. In Figure 4.4 we depict the first seconds of this function for two different levels of depression. These levels corresponds to $f_D = 0.5$, where network presents a tonic firing state, and $f_D = 0.95$, where network presents UP and DOWN states.
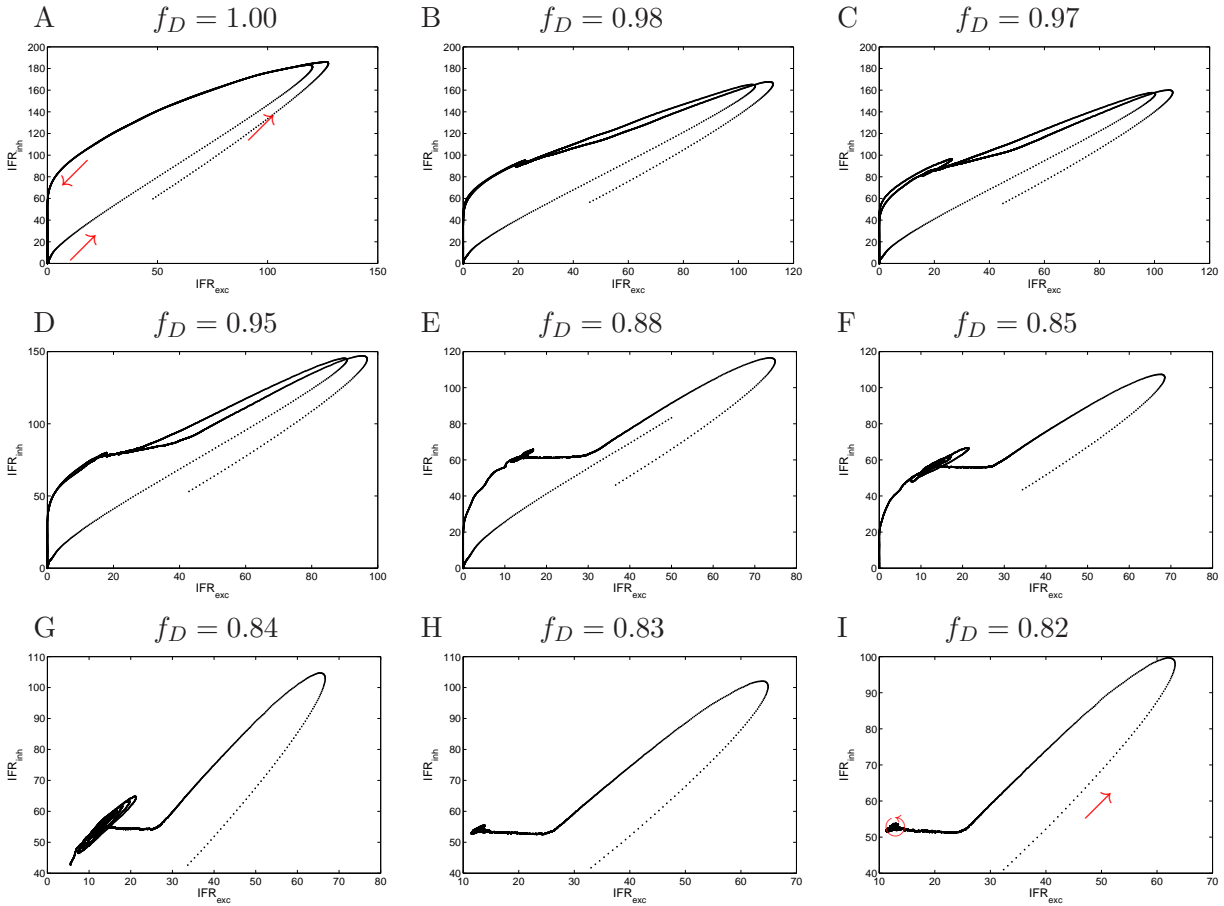
Figure 4.2: **Excitatory versus inhibitory instantaneous firing rate dynamics for different values of the depression factor** f_D**.** All panels depict a phase plot of the exictatory IFR versus the inhibitory IFR (measured in spikes/s) by sweeping the depression level. Red arrows in the first and last panels indicate the direction of the flow, which is akin in all panels.
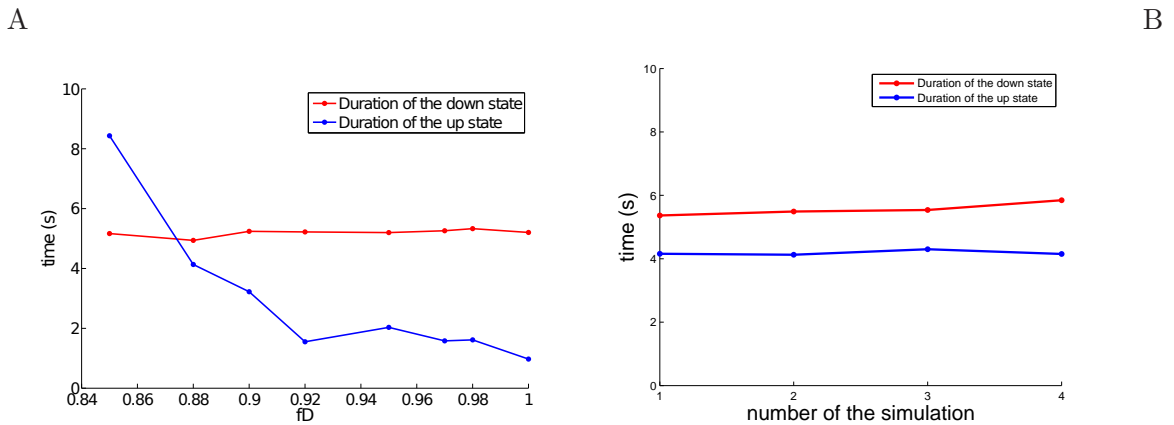

Figure 4.3: **Duration of the UP and the DOWN state for different values of the depression factor.** Panel A represents the time that the UP state (blue line) and the DOWN state (red line) for different values of f_D such that the network presents UP/DOWN state behaviour, that is $f_D > f_D^*$. Panel B depicts also the time that the UP state (blue line) and the DOWN state (red line) for different simulations of the model keeping $f_D = 0.88$.
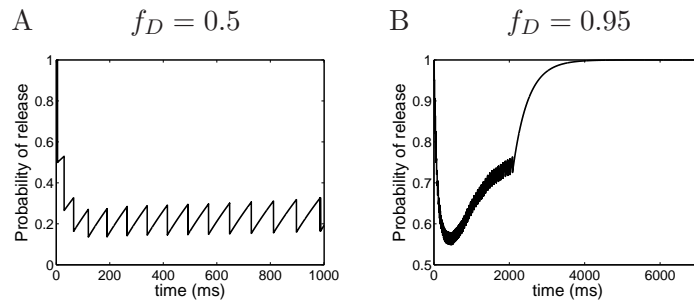
Figure 4.4: **A representation of the probability of release function for the depression case.** Panels show the time course of the probability of release for different levels of depression. Dynamics of the probability of release has been modelled according to Dayan and Abbott (2005) (see also Section 2.1.4).

4.2.1.1   Changes in synaptic conductances

For each neuron in the network, we extract the excitatory (AMPA plus NMDA) and the inhibitory (GABA) conductances. In Figure 4.5, we depict the first second of both the excitatory (panels A and C) and the inhibitory conductances (panels B and D) for an excitatory neuron (upper panels) and an inhibitory neuron (lower panels), where a higher activity on the excitatory conductance can be noticed. These traces correspond to the case $f_D = 0.8$, where the network presents a "continuous" firing, and each peak on the conductance trace corresponds to the time where the neuron is spiking. In Figure 4.6, we
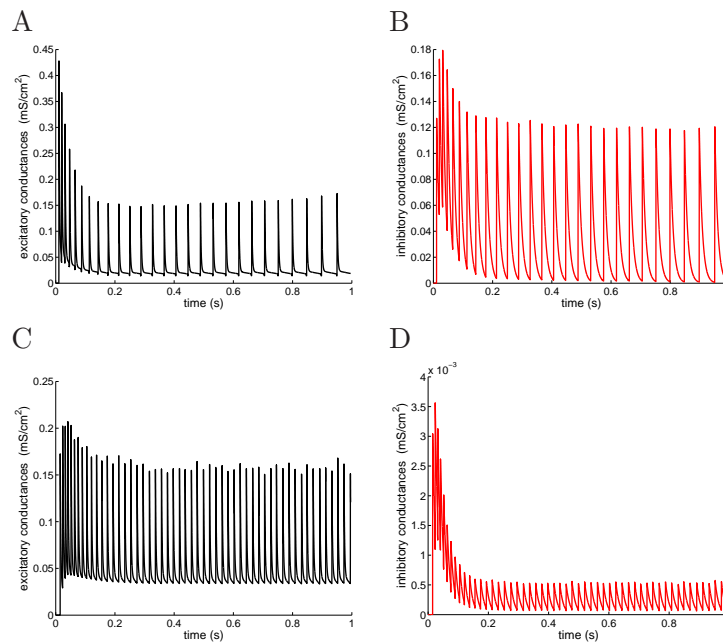

Figure 4.5: **Conductances of a single neuron for the depression factor $f_D = 0.80$.** Panels A and B depict the excitatory and the inhibitory conductances, respectively, for an excitatory cell when a level of depression $f_D = 0.80$ is applied to the network. Panels C and D depict also the excitatory and the inhibitory conductances, respectively, but for an inhibitory cell when a level of depression $f_D = 0.80$ is applied to the network.

depict the first 10 seconds also of both the excitatory (panels A and C) and the inhibitory

conductances (panels B and D) for an excitatory neuron (upper panels) and an inhibitory neuron (lower panels), but for a depression level of $f_D = 0.95$. In this Figure we also notice a higher activity on the excitatory conductance. The UP and DOWN states, that are presented in the network for this depression level, are also reflected on the conductance traces, which also present higher amount of conductances during the UP state than those observed during the DOWN state. This high activity corresponds to the black and red regions in the panels, where, if we do a zoom, we will see a similar pattern to the one observed in the corresponding panel in Figure 4.5.
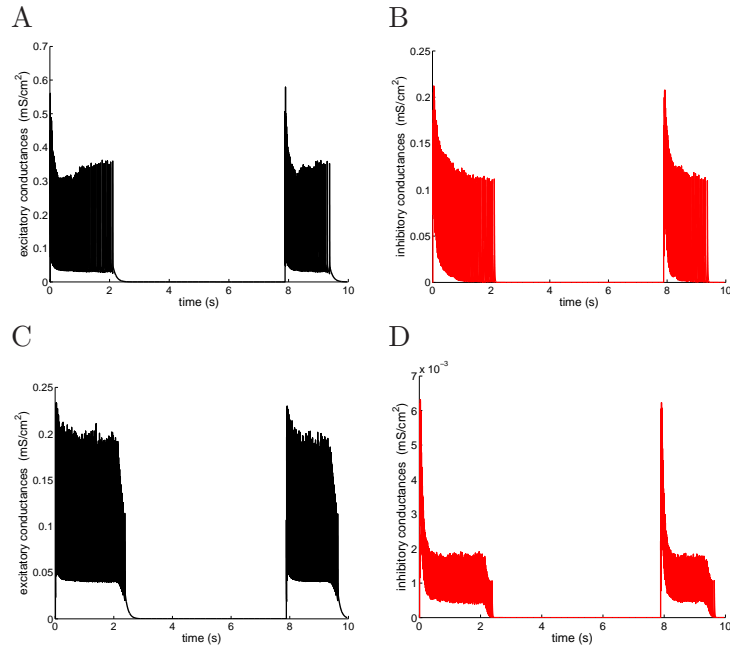

Figure 4.6: **Conductances of a single neuron for the depression factor** $f_D = 0.95$. Panels A and B depict the excitatory and the inhibitory conductances, respectively, for an excitatory cell when a level of depression $f_D = 0.95$ is applied to the network. Panels C and D depict also the excitatory and the inhibitory conductances, respectively, but for an inhibitory cell when a level of depression $f_D = 0.95$ is applied to the network.

To study the changes on the synaptic conductances under the depression effects, we only consider those cases where UP and DOWN states are generated. Then, in order to obtain a mean value of the conductances in the network per each depression level, we do the following steps:

1. We first average the conductances over time for each neuron, by considering the full second UP state.

2. After averaging over time, we average the result over all neurons obtaining a constant value for each f_D.

The data points we obtain after this averaging process, can be exponentially fitted, see Figure 4.7. The fits done for each type of conductances present a coefficient of determination R square, R^2, close to 1. In fact, they are $R^2 = 0.90$, $R^2 = 0.80$ and $R^2 = 0.93$ for the AMPA, GABA and NMDA conductances, respectively. Therefore, we can state that the averaged conductances change exponentially under the effects of the depression, being

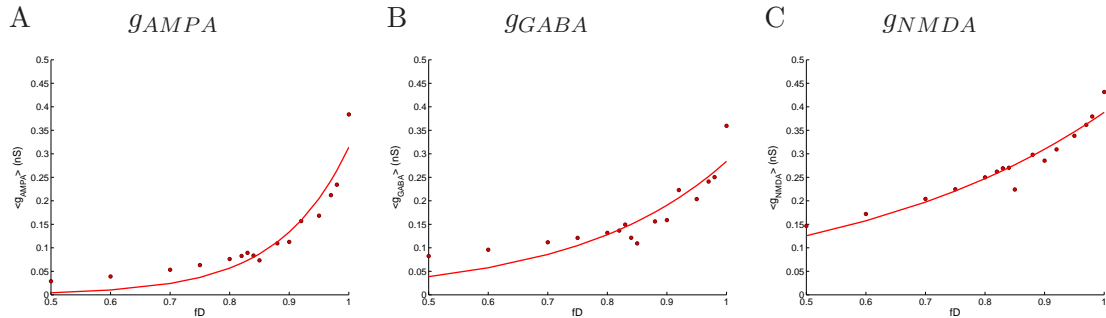bigger as smaller is the synaptic depression presented on the network (and so, the larger f_D).

Figure 4.7: **Averaged conductances for different values of the depression factor f_D.** Panel A depicts for the AMPA conductances changes whereas Panel B is devoted to the GABA conductances and Panel C to the NMDA conductances. The different dots depict the averaged conductance over neurons and over all the second UP state duration, obtained for different depression level. Red line shows the exponential fitting of those points.

4.2.2   Effects of the short-term facilitation

When facilitation level changes, behaviours from those observed in the depression arise, both in the membrane potentials and in the conductances. In this case, according to Dayan and Abbott (2005) (see also synaptic drive in Section 2.1.4), we changed the initial conditions of probability of release in the network to suppose the synapse to be weak; then by increasing the facilitation level, the synapse becomes stronger. For this purpose, the facilitation factor f_F moves from 0 to 1, being the case $f_F = 1$ equivalent to the case $f_D = 1$ of the previous subsection, where no depression was considered.

Upper subpanels in Figure 4.8 depict that, for low values of the facilitation factor f_F, the network presents a unique UP state at the beginning of the simulation. However, for higher values of f_F, and so when network is highly facilitated, it presents repetitive UP and DOWN states. Therefore, there also exists a specific value f_F^*, being close to 0.66, where network changes its behaviour. Even though longer simulations and more values of f_F have been considered in order to approximate f_F^*, in Figure 4.8 we only present some of them and in a time window of 10 s.

While f_F increases from 0 to f_F^*, in upper and lower panels A-E in Figure 4.8 one can appreciate that the activity inside the UP state also increases. In this case, some isolated neurons (around 4 or 5) sporadically fire during the DOWN state. However, these two increments of activity are not enough to excite the full neuronal network to generate a second UP state. On the other hand, when $f_F > f_F^*$, see panels F-I, more neurons are spiking after the first UP state, being the responsible of generating the second one.

From the excitatory and inhibitory IFRs a possible dynamics on the network is observed. In Figure 4.9, where both the excitatory and the inhibitory IFRs are plotted, one against the other, a similar pattern to the depression case is observed for values of $f_F > f_F^*$. In this case, also an homoclinic orbit seems to appear as a transition between UP and DOWN states. Moreover, for these f_F values, plots in Figure 4.9 depict a trajectory leaving from a vicinity of the origin $O = (0, 0)$ and coming back to it right after an excursion to higher IFR values. The dynamics is fast when we are far from O and, on the contrary, it is
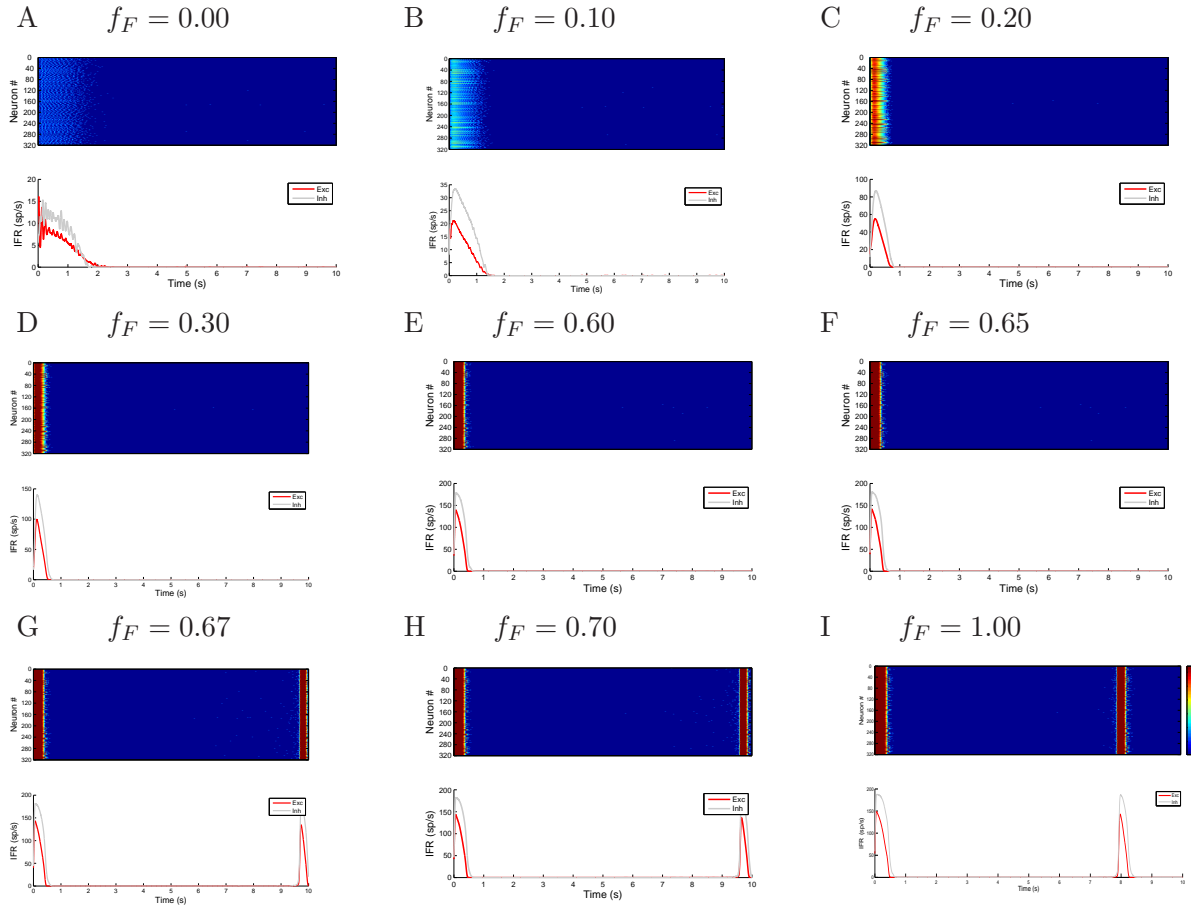
Figure 4.8: **Raster plot and instantaneous firing rate for different values of the facilitation factor** f_F**.** Upper subplots in all panels represent, for all neurons in the network, the coloured raster plot where colours indicate the instantaneous firing rate (IFR), where as warmer is the colour as higher is the membrane potential. A colour different from dark blue means neurons are spiking (UP state), otherwise, they do not (DOWN state). Lower subplots in all panels represent the instantaneous firing rate of the excitatory population (red line) and of the inhibitory population (grey line). The facilitation level $f_F = 0.66$ is the approximate bifurcation value where the network switches from presenting only one UP state to present repetitive UP and DOWN states.

slow when we are close to O, causing that the DOWN state duration is higher than the UP state, see Figure 4.10. When UP and DOWN states are generated, the trajectories performed for different f_F values also present similar patterns in magnitude. This fact implies that the firing rate presented in the UP states is similar for different facilitation levels.

On the other hand, when $f_F < f_F^*$, as we can see in Figure 4.9, the trajectory of excitatory IFR versus the inhibitory IFR ends to O, which acts as an attracting fixed point, from where the trajectory cannot scape, being the dynamics slow close to this point. Since trajectories are not jumped out of O, the network remains in a DOWN state. As we increase f_F, trajectories take larger values thus confirming the increment of activity that we were observing in the raster plots; but they still tend to the origin.

Observing the raster plots in Figure 4.8, one can already appreciate how the DOWN state is reduced by increasing the facilitation level. However, the UP state duration is not so
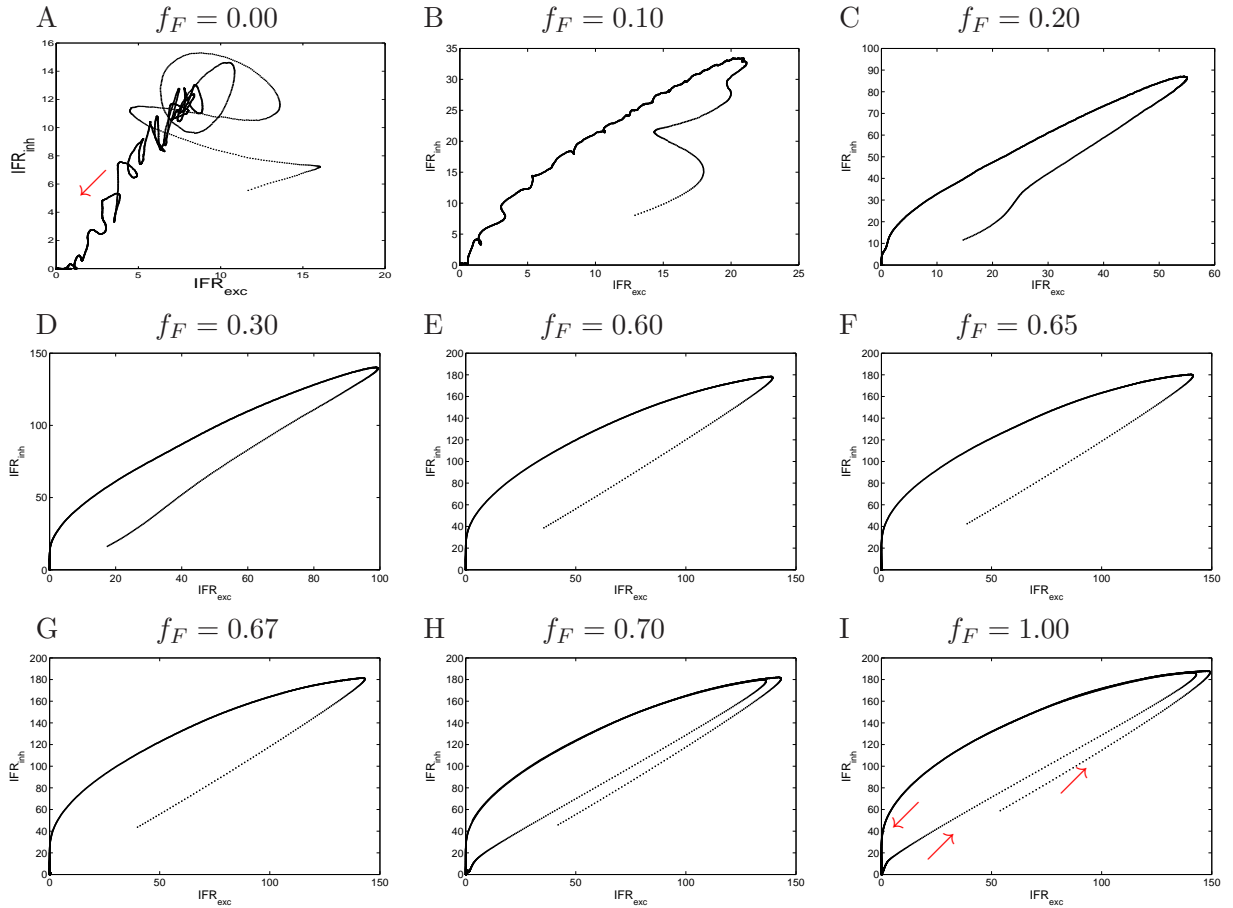
Figure 4.9: **Excitatory versus inhibitory instantaneous firing rate dynamics for different values of the depression factor f_F.** All panels depict a phase plot of the excitatory IFR versus the inhibitory IFR (measured in spikes/s) by sweeping the depression level. Red arrows in the first and last panels indicate the direction of the flow, which is akin in all panels.

clear. In Figure 4.10 we depict both UP and DOWN durations for those f_F values for which a second UP state is generated, that is $f_F > f_F^*$. Here, we can corroborate that the DOWN state is slightly shorter as f_F increase, while the duration of the UP state is almost constant when f_F changes.

In Figure 4.11, we depict the function in time of the probability of release, $P_{rel}(t)$, obtained after simulating the neuronal network for three different levels of facilitation: $f_F = 0.2$ and $f_F = 0.60$, where network presents a unique UP state, and $f_F = 0.7$, where network presents oscillatory UP and DOWN states. Comparing the dynamics of the $P_{rel}(t)$ with the corresponding raster plots in Figure 4.8, we can appreciate how both UP states and the probability of release coincide; that is, when the UP states begin, the P_{rel} increase, and when the UP state ends the P_{rel} have decreased to its initial condition. For the case $f_F = 0.20$, the $P_{rel}(t)$ only reaches the value 0.5, reason why the UP state shows less intra-activity (the IFR of each neuron is weaker than for the other cases). On the contrary, when $f_F = 0.60$, even though the network does not present a second UP state, the $P_{rel}(t)$ reaches higher values in magnitude (around 0.92), thus increasing the IFR of the neurons.
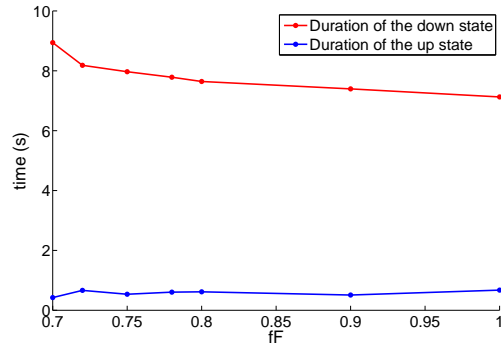
Figure 4.10: **Duration of the UP and the DOWN state for different values of the depression factor.** This plot represents the time that the UP state (blue line) and the DOWN state (red line) for different values of f_F such that the network presents UP/DOWN state behaviour, that is $f_F > f_F^*$.
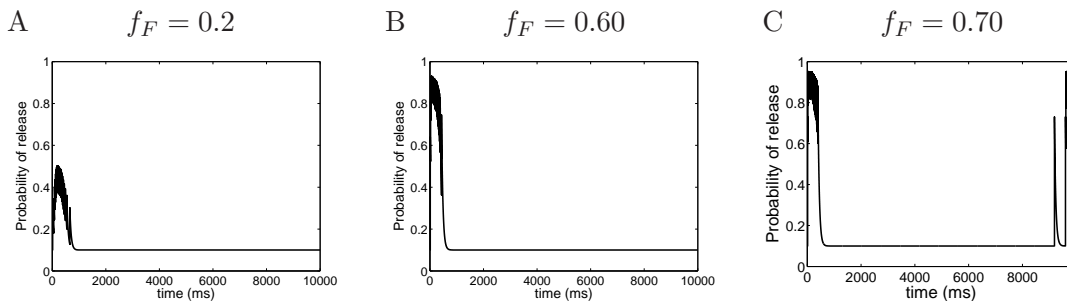

Figure 4.11: **A representation of the probability of release function for the facilitation case.** Panels show the time course of the probability of release for different levels of facilitation. Dynamics of the probability of release has been modelled according to Dayan and Abbott (2005) (see also Section 2.1.4).

4.2.2.1   Changes in synaptic conductances

To see changes on the synaptic conductances under the facilitation effects, we consider the average of the synaptic conductances over the duration of the UP state and over neurons, as we did for the depression case. However, in this case, we consider all facilitation levels since we always obtain at least one UP state. In the case such that only one UP state exists, we consider this one to average the conductances. Otherwise, we take the second UP state.

In this case, as we can see in Figure 4.12, a clear bimodal behaviour can be found for the facilitation case. Below the bifurcation point f_F^* (represented with a vertical line in the plots), conductances follow a parabolic shape; while above the threshold, the dynamics is irregular and far to be fitted. Below f_F^*, even though we have also tried to fit the dots using piecewise linear fittings and also exponential ones, the quadratic fittings provide the best results, presenting a coefficient of determination R square, R^2, close to 1 in all cases. They are $R^2 = 0.973$, $R^2 = 0.967$ and $R^2 = 0.974$ for the AMPA, GABA and NMDA conductances, respectively. Therefore, we can state that conductances are well fitted by a parabolic function, for those facilitation levels smaller than f_F^*. However, above f_F^* we do not observe a typeable behaviour, in fact the obtained averages are almost identical, except for a multiplicative factor.
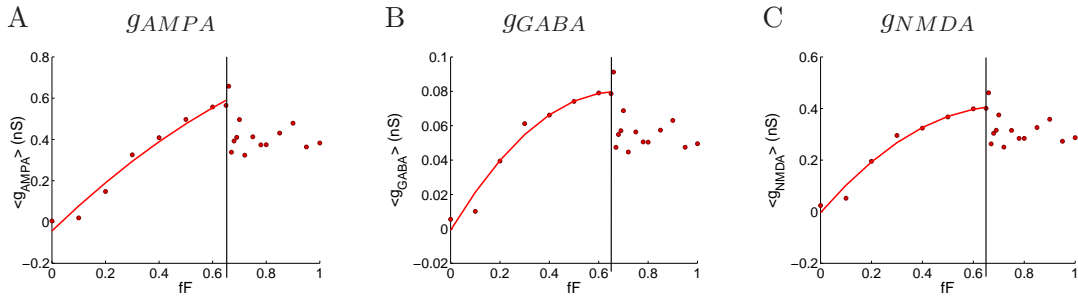
Figure 4.12: **Averaged conductances for different values of the depression factor f_F.** Panel A depicts for the AMPA conductances changes whereas Panel B is devoted to the GABA conductances and Panel C to the NMDA conductances. The different dots depict the averaged conductance over neurons and over all the second UP state duration, obtained for different depression level. Red line shows the quadratic fitting of those points and the vertical line is $f_F = f_F^*$.

4.3   Discussion

In this chapter we have considered a cortical network with slow oscillation and we have analysed the effects of both short-term depression and facilitation on the network activity and also on the conductances. We have seen that the presence of only short-term facilitation or depression can modulate the duration of the network UP states. By increasing the synaptic depression, network presents a smaller IFR but neurons are regularly spiking along the time. Repetitive simulations of the network, by a fixed depression level, have shown that intrinsic fluctuations of the neurons perturbs the bifurcation parameter f_D^* only slightly. Moreover, the duration of the UP and DOWN states do not present high variations from one simulation to the other.

Under short-term facilitation effects, when network is not facilitated, only one UP state with low IFR is presented. By increasing the facilitation factor, the IFR becomes higher and some neurons sporadically fire. Above some specific level, the probability of release reaches high values close to 1, causing that a higher number of sporadic cells fire, and so the network is able to recursively oscillate between UP and DOWN states.

Regarding the conductances, both mean excitatory and inhibitory synaptic conductances follow a nonlinear relationship under the effects of depression and facilitation. As the depression level decreases, the mean excitatory and inhibitory conductances increase exponentially. However, for the facilitation case, no global fitting can be provided since conductances presents a bimodal behaviour. Below the bifurcation point f_F^*, conductances follow a parabolic shape, while above the threshold, the dynamics is irregular and difficult to fit to any simple enough function.

Since a mean conductance could be fitted by an exponential function under the depression effects, one could think of a possible inverse method to predict changes on the conductances when depression on the network is changing.

These results are a first approach to study further the dynamics of the network. Computationally we have been able to detect some possible bifurcations, and how the single-cell slow-fast dynamics arises at the neuronal level. However, a deeper study needs to be developed in order to analytically corroborate the computational results. To do that, a rate model can be used (see future work regarding this chapter in Chapter 6). However, since in this thesis we are interested on estimating synaptic conductances, we think focus

on the possibility of extracting realistic conductance traces, which can also be used on the estimations in Section 5.2.

Chapter 5

Estimation of conductances in single point neurons

Unveiling the amount of information that a neuron is receiving from other neurons, and discerning between excitatory and inhibitory inputs, is a current challenge in neuroscience. In other words, we aim at estimating the time course of the synaptic conductances impinging on a neuron. From an experimental perspective, this becomes a difficult task due to the diversity of synaptic inputs and, mainly, the impossibility of recording conductances in a direct way. Therefore, inverse mathematical methods are compulsory to achieve this goal.

No completely effective solutions to this problem are yet available in the literature. In general, solutions provided by the literature depart from linear models (see, for instance, Borg-Graham et al (1998), Anderson et al (2000), Wehr and Zador (2003), Rudolph et al (2004), Pospischil et al (2009), Bédard et al (2011b), Berg and Ditlevsen (2013)). Noise has been taken into account through either stochastic linear processes (see Rudolph et al (2004), Pospischil et al (2009), Paninski et al (2012), and Berg and Ditlevsen (2013), among others) or sophisticated filtering techniques (Lankarany et al (2013b), Ditlevsen and Samson (2014), and Closas (2014), among others).

It is known that the use of linear models prevents from obtaining good estimations in spiking regimes (see Guillamon et al (2006)), so most of the above results are applied only to data coming from subthreshold activity. However, given that the basic reason for the misestimations is that some nonlinear terms are active, the problem could be spread also over non-spiking regimes as well due to the eventual activity of subthreshold ionic channels, widely described from the eighties after seminal works as Hotson and Prince (1980). This nonlinear subthreshold activity cannot be discarded, even in the most careful experimental results on conductance estimation obtained up-to-date, see for instance Figure 6 in Rudolph et al (2004), where this type of channels is explicitly considered. In that paper, Rudolph *et al.* already warned about errors caused in the estimations attributed to the activation of subthreshold voltage-dependent membrane conductances, but they concluded that these conductances did not seem to have strong effects on the estimates. Of course, pharmacological blocks can reduce the activity of some targeted channels, but still it is actually difficult to completely reduce the neuron's activity to a pure passive filter.

In Section 5.1.1, we aim at showing that misestimations induced by the presence of subthreshold-activated ionic currents are ubiquitous and independent on the mechanisms that activate these currents. For this purpose, firstly, we take a conductance-based com-

putational model of a spiking neuron with two significant types of subthreshold currents, a calcium-activated potassium afterhyperpolarizing current (AHP) and a low-threshold calcium current (LTS); secondly, to elude the possible contaminating effects (specially on the AHP currents) of the spiking activity, we take a conductance-based model of a non-spiking neuron which currents are a persistent sodium current (NaP) and an h-current. Both models are fed with realistic excitatory and inhibitory conductance traces obtained from an *in sillico* (noisy) network of visual cortex (see McLaughlin et al (2000) and Tao et al (2004)). The resulting voltage traces are then used to obtain estimated conductance courses by linear estimation methods. Finally, the input synaptic drive and the estimated conductance courses are compared in order to quantify and analyse the estimation errors due to the presence of the above mentioned subthreshold currents. We also study alternative procedures to estimate the conductances taking into account the nonlinear effects. On one hand, we explore the role of ionic channels time scales and, on the other hand, we propose a method based on a quadratization of the subthreshold dynamics.

However, the method does not incorporate noise and, moreover, it requires the use of voltage traces from two trials. In fact, variability across trials is an important source of errors in estimating synaptic conductances. Many existing methods require several recordings of the membrane potential, although some of the above mentioned contributions (Pospischil et al (2009), Bédard et al (2011b), Paninski et al (2012), Berg and Ditlevsen (2013), Lankarany et al (2013b), Ditlevsen and Samson (2014), Closas (2014), Yasar et al (2016)) apply to single voltage traces, thus avoiding this problem. They usually take advantage of the time constants and statistical inference tools. In Section 5.1.2, we will focus on two of them: the *oversampling method* (see Bédard et al (2011b)), based on a deterministic approach, and the method from Berg and Ditlevsen (2013) which will be referred heretofore as the *OU-based method*, being an stochastic version of the leaky integrate-and-fire (LIF) model combined with an Ornstein-Uhlenbeck process.

The obstructions above discussed strengthen the challenge of seeking for single-trial stochastic models incorporating nonlinear effects. In Section 5.1.2, we aim at extending the procedure to estimate synaptic conductances based on a quadratization of a stochastic model. Our approach is based on a combination of the results from Berg and Ditlevsen (2013) and the ones obtained in Section 5.1.1 in order to capture both subthreshold nonlinearities and noise in the experimental data. On one hand, from Section 5.1.1 we know that linear procedures may distort the estimation of conductances in the subthreshold regime when ionic currents are active, a problem that can be mitigated by using a (deterministic) quadratic model. On the other hand, the OU-based method presented in Berg and Ditlevsen (2013) is very effective in dealing with noise using single trial voltage traces. Thus, we attempt to improve the results given by the OU-based method (Berg and Ditlevsen (2013)) by adding a quadratic term to the underlying model; more specifically, by considering a stochastic version of the *quadratic integrate-and-fire* (QIF) model. We will call SQIF to this stochastic version. The QIF is characterized to approximate the subthreshold dynamics of the conductance-based models since it captures the $f - I$ curve accurately for a broad range of input currents. Moreover, under the presence of activated subthreshold currents, this quadratic approximation is more accurate than that obtained by the LIF model, see Ermentrout and Kopell (1986) and Fourcaud-Trocmé et al (2003).

Therefore, in Section 5.1.2, we present a new statistical model to estimate conductances and we apply it to both computational and experimental data. Computational data are obtained from three different neuron models using prescribed synaptic inputs. Experimental data are intracellular recordings in current-clamp mode of spinal motoneurons of red-eared turtles, and has been analyzed elsewhere (Berg et al, 2007; Jahn et al, 2011;

Berg and Ditlevsen, 2013). Given a membrane potential trace, we fit the data into the reference model (SQIF) and, finally, we estimate the time course of the conductances by means of an approximated maximum likelihood procedure. In the case of computational data, we can compare the estimated conductances with the prescribed ones to see the efficiency of the procedure.

Even though we provide two partial solutions for subthreshold regimes with active (non-linearly behaving) ionic currents, no solutions for spiking neurons have been yet proposed. In Section 5.2 we provide a first proof-of-concept to perform estimations of synaptic conductances during spiking activity. We approach this problem by considering the neuronal firing rate, f, as a function of the input current, I; i.e. the spike frequency f vs. the input strength current I function, the $f - I$ curve. We have chosen the McKean model, a simplified piecewise linear model of neuronal activity with regular firing, that can be derived from the FitzHugh-Nagumo model (see McKean (1970) and Coombes (2001)). The piecewise linearity of the vector field allows a very precise knowledge of the nonlinear $f - I$ curve by means of standard techniques of non-smooth dynamical systems. In the standard McKean model, we put special emphasis on the synaptic current, I_{syn}.

In this last section of the chapter, we aim at obtaining an approximation of the period given in a regular firing regime of the neuron model. Therefore, given this expression of the period, by knowing both the period and the current applied to the neuron, we solve an inverse problem to estimate the steady synaptic conductance of the cell's oscillatory activity. Finally, we extend the method to estimate the time course of the synaptic conductance.

Summing up, this chapter is divided in two parts containing three capital pieces of work of this thesis. In Section 5.1, we describe, on one hand, the misestimations of linear procedures when subthreshold ionic currents are active and, on the other hand, we develop two different procedures to estimate conductances: Subsection 5.1.1, where a quadratic deterministic model is presented, and Subsection 5.1.2 in which we present a quadratic stochastic model. Finally, Section 5.2 is devoted to estimate synaptic conductances in the spiking regime, where neuron presents an oscillatory behaviour. Finally, in Section 5.3 we discuss the results obtained.

5.1 Estimation in the silent state under presence of activated subthreshold ionic currents

This section is devoted to see the influence of ionic currents active in the non-spiking regime and provide new strategies to estimate conductances under these influences. Therefore, as we said in the introduction, in Section 5.1.1, we see how linear procedures may distort the estimation of conductances in the subthreshold regime when ionic currents are active. In this section we also provide a deterministic strategy to estimate conductances in this case based on a quadratic model. In Section 5.1.2 we provide an stochastic approach also based on a quadratic model, in order to take into account possible noise from experimental recordings.

5.1.1 Deterministic framework

In this subsection, we aim to see the effects that subthreshold activated ionic current cause on the linear estimation procedures established until now. Moreover we also provide

a deterministic solution to estimate conductances in this case.

In Subsection 5.1.1.1, we cite the different neuronal models we are considering in this section and some indications about the synaptic drive and other tools we are going to use. In Subsection 5.1.1.2 we describe the linear filtering method and we provide two alternative methods to estimate conductances in the subthreshold regime. Subsection 5.1.1.3 is devoted to the results which imply that caution has to be applied also in subthreshold regimes to ensure the absence of nonlinear behaviours. In particular, attention must be paid to check that Ca^{2+}-dependent K^+ currents and other ionic currents responsible for subthreshold oscillations are inactive before proceeding to linearly estimate the synaptic conductances from voltage traces. We also analyse how the alternative procedures improve the linear regression.

5.1.1.1   Models and data treatment

As we have mentioned in the introduction, in this section two different conductance-based models are considered: a first one where a subthreshold current and a hyperpolarized current coexist, that is the pyramidal model described in Section 2.1.2.1 with external current given in Section 2.2.1; and a second one with two currents that jointly induce subthreshold oscillations. That is, the reduced stellar model described in Section 2.1.2.2 with external current given in Section2.2.1. Details about the numerical integration of the models are given in Section 2.4.2.

For the pyramidal cell model, we construct an index to discern whether each subthreshold current is dominant over all the other ionic currents whereas, for the stellate cell model, we refer to the quadratization procedure described in Rotstein (2015) as a simplification of the model (see also the mode in Section 2.1.2.2 at the reduced model).

Index of dominance of subthreshold currents.   In order to have, for this first example, a clear description of the time intervals where the currents I_{AHP} and I_{LTS} prevail over the rest of the currents, we have defined an index $\chi(t)$ as

$$\chi(t) = \frac{-I_{AHP}(t) - I_{LTS}(t)}{\sqrt{I_{ion}(t)^2 + (I_{AHP}(t) + I_{LTS}(t))^2}}, \tag{5.1}$$

where $I_{ion}(t) = I_{Na}(t) + I_K(t) + I_{Ca}(t)$.

Note that, because of the respective reversal potentials, when the index $\chi(t)$ is greater than $\sqrt{2}/2$, $-I_{LTS}$, which is positive, is the dominant current whereas the index $\chi(t)$ being smaller than $-\sqrt{2}/2$ implied that the dominant current is $-I_{AHP}$, which is negative. Otherwise, the neuron is spiking and so the other ionic currents prevail over the sum of I_{LTS} and I_{AHP}. We also point out that the index is not defined when $I_{ion}(t)^2 + (I_{AHP}(t) + I_{LTS}(t))^2 = 0$; we have included a condition in the code so as to maintain the value of $\chi(t - \Delta t)$ when $I_{ion}(t)^2 + (I_{AHP}(t) + I_{LTS}(t))^2 < TOL$, with $TOL = 10^{-12}$. However, this only occurs transiently and does not affect any result in this paper.

Synaptic drive.   In this section we use prescribed synaptic conductances from an *in sillico* described in Section 2.2.2.3.

5.1.1.2 Estimation procedures

Linear estimation approach

As we mentioned in the Introduction, some experimental studies try to get rid of spikes and linearise the $I_{app} - V$ relationship by filtering the intracellular spiking voltage. Our aim is to mimic these standard experimental procedures and analyse their pitfalls. Thus, as in Guillamon et al (2006), we smooth the membrane potential traces $V(t)$ for a fixed I_{app} using a median filter and obtaining a new signal $v_{filt}(t; I_{app})$. In particular, for each point $p := (t, V(t))$ of the voltage trace, we compute the median of the values in window which includes $2N + 1$ points and is centered at p:

$$V_{filt}(t; I_{app}) = \text{median}_{j=-N}^{N} \{V(t + j\,h)\},$$

where h is the integration step (that is, $1/h$ is the sampling frequency in KHz). In our computations, we have taken $N = 10$. We have also explored the possibility that a repetitive application of the same filter could lead to a better smoothing and thus a better approximation using linear methods. However, we have proved that the median filter with an usual recording step does not improve beyond a second successive filtering. Therefore, after this filtering process we get $V_{filt}(t; I_{app})$ for any time value t and any applied current value I_{app}.

Then, for each t independently, we estimate the conductances on the basis of linear regression assuming that the solutions of the neuron model are close to the steady-state which implies that the activity of the ionic channels is not significant and, in addition, $\dot{V_{filt}} \approx 0$. We thus estimate the total synaptic conductance $g_{syn}(t)$ and the effective reversal potential $V_{eff}(t)$ through

$$V_{filt}(t; I_{app}) = V_{eff}(t) + \frac{I_{app}}{g_{syn}(t)}, \tag{5.2}$$

where $g_{syn}(t) = g_E(t) + g_I(t) + g_L$ and $V_{eff}(t) = (g_E(t)V_E + g_I(t)V_I + g_L V_L)/g_{syn}(t)$, by presenting M different values of I_{app} for each time t, where M (≥ 2) is the number of trials each of them with a different value of I_{app}.

Once we have estimated $g_{syn}(t)$ and $V_{eff}(t)$, using (5.2), we can estimate $g_E(t)$ and $g_I(t)$ assuming that we know the rest of parameters (namely, g_L, V_L, V_E and V_I) by solving, for each value of t, the linear system:

$$\begin{cases} g_E(t) + g_I(t) = g_{syn}(t) - g_L, \\ g_E(t)\,V_E + g_I(t)\,V_I = g_{syn}(t)\,V_{eff}(t) - g_L\,V_L. \end{cases} \tag{5.3}$$

Linearization of the subthreshold ionic currents approach

The linear estimation is based on the fact that the activity of the ionic channels is not significant, and so the ionic currents are null. However, these currents are activated on the subthreshold regime independently of the spikes. Its time scale changes according to the steady state value of the current and so, a better estimation could be done if we could assume that the ionic channels are in the steady state. Therefore, in the phase where the subthreshold currents are dominating and the spiking currents are negligible, the $I - v$ relationship would become

$$v(t; I_{app}) = V_{eff}(t) - \frac{I_{\infty}(t)}{g_{syn}(t)} + \frac{I_{app}}{g_{syn}(t)}, \tag{5.4}$$

where $I_\infty(t) := I_{ion,\infty}(V(t;I_{app}))$ and $I_{ion,\infty}(V)$ is the sum of the ionic currents at the steady state. Thus, obtaining a relationship $v = v(I_{app};V_{eff},g_{syn})$ from the implicit equation $v = V_{eff} - I_\infty(v)/g_{syn} + I_{app}/g_{syn}$, where V_{eff} and g_{syn} are thought of as parameters, would allow to have a general formula to estimate $V_{eff}(t)$ and $g_{syn}(t)$ for each t. Unfortunately, this is not easy to perform but, considering the pyramidal cell model described in Section 2.1.2.1 with external current given in Section 2.2.1, an interesting observation is that, in the phase where I_{LTS} is dominating ($v \in [-75, -60]\, mv$ approximately), the function

$$I_{LTS,\infty}(V) := g_{LTS}\, m_{LTS,\infty}(V)^3\, h_{LTS,\infty}(V)\,(V - V_{Ca})$$

can be very well fitted by a straight line. In other words, the range of voltage values where I_{LTS} activates and the other ionic currents are negligible coincides with a straight ramp of the bell-shaped $I_{LTS,\infty}$ function. This observation provides a new approach consisting of approximating $I_{LTS}(V) \approx \alpha_{LTS}\, V + \beta_{LTS}$, and then, for each t, applying the following steps:

1. Obtain the slope a and the intercept b from a linear regression of the set of points $\{(I_{app,j}, V(t;I_{app,j}))\}_{j=1}^M$.

2. Estimate $g_{syn}(t) = 1/a - \alpha_{LTS}$ and $V_{eff}(t) = (b + a\,\beta_{LTS})/(1 - a\,\alpha_{LTS})$.

3. Estimate $g_E(t)$ and $g_I(t)$ from equation (5.3).

Observe that taking $\alpha_{LTS} = \beta_{LTS} = 0$, we obtain again (5.2).

Quadratization approach

As we have mentioned in the description of the stellate model, in Section 2.1.2.2 with external current given in Section 2.2.1, when resonant and amplifying currents coexist, it has been proved (see Rotstein (2015)) that the system presents nonlinearities of quadratic type in the voltage response. In turn, it is possible to approximate the model by a minimal model with linear and quadratic terms; this process is also konwn as the quadratization of the original system. More precisely, the quadratization is given by the differential system (2.6). We reparameterize the system by the slow time $\tau = t\varepsilon$ thus obtaining

$$\varepsilon\, \frac{dV}{d\tau} = aV^2(\tau) - w(\tau) + I(\tau),$$

$$\frac{dw}{d\tau} = (\alpha V(\tau) - \lambda - w(\tau)).$$

$$(5.5)$$

Since the voltage is a fast variable of system (5.5) and the gating variable w is slow, the differential system (5.5) can be considered as a slow-fast system where the difference on the time scales of both variables is given by the parameter ε. When ε tends to zero, the associated system is known as the slow subsystem and contains the singular dynamics of the system (5.5). Fenichel's geometric theory (see Fenichel (1979)) ensures the persistence of the critical manifold of the slow subsystem when it is perturbed. Therefore, in order to make an estimation of the total current, one can assume the limiting case $\varepsilon = 0$ to obtain an approximated expression of the total current. In this case, the second equation of the system is a linear non-autonomous ordinary differential equation which can be solved as

$$w(\tau) = e^{-\tau}\left(w(\tau_0)e^{\tau_0} + \int_{t_0}^\tau (\alpha V(s) - \lambda)ds\right).$$

Moreover, from the first equation of the slow subsystem and the fact that $I(\tau) = I_{syn}(\tau) + I_{app}$, we can reconstruct the total input current from

$$I_{syn}(\tau) = -aV^2(\tau) + e^{-\tau}\left(w(\tau_0)e^{\tau_0} + \int_{t_0}^{\tau}(\alpha V(s) - \lambda)ds\right) - I_{app}. \qquad (5.6)$$

To extract the excitatory and the inhibitory conductances, we can take, for instance, two different injected currents, $I_{app,j}$, $j = 1, 2$, obtain the respective $I_{syn,j}(t)$, $j = 1, 2$, from (5.6), and finally solve

$$\begin{cases} I_{syn,1}(t) = -g_E(t)(V_1(t) - V_E) - g_I(t)(V_1(t) - V_I), \\ I_{syn,2}(t) = -g_E(t)(V_2(t) - V_E) - g_I(t)(V_2(t) - V_I). \end{cases} \qquad (5.7)$$

It is worth noting that in order to apply (5.6) one has to make a guess of the initial condition $w(\tau_0)$ which is not observable as it is $V(\tau_0)$. However, the method is robust enough to converge with a wide range of initial conditions.

5.1.1.3   Results

The study made in Guillamon et al (2006) showed the goodness of the linear estimation when the system is only driven by the synaptic activity, a regime where the equation (5.2) holds true. However, it was also shown that the estimations fail when the neuron is either spiking or near to spikes in which case the linear relation between the membrane potential V_{filt} and the applied current I_{app} is broken. Here, we explore the influence of subthreshold ionic activity in the estimation of synaptic conductances, a paradigm that was not taken into account in that previous work.

The way we proceed is, first, consider the pyramidal cell model described in Section 2.1.2.1 with external current given in Section 2.2.1 to study the possible errors caused by an afterhyperpolarization current, I_{AHP}, and a subthreshold-activated current, I_{LTS}, both together and separately. For this purpose and also to avoid the influence of the currents promoting spikes, we have introduced the χ index defined in (5.1) to discriminate the time intervals when either I_{AHP}, I_{LTS} or the spiking currents dominate (see also Figure 5.1). In the first two regimes we detect important relative errors in estimating the synaptic conductances. For the I_{LTS}-dominated regime, we have come up with an alternative way to improve the linear estimation based on the method explained in Subsection 5.1.1.2, *Linearization of the subthreshold ionic currents approach*. Even though this example already illustrates the misestimations in subthreshold regimes, it could be argued, in the case I_{AHP}-dominated regimes, that these misestimations are an artefact of the misestimations in the spiking regime. To enhance our warning message on subthreshold misestimations we have also considered a second model with no spiking mechanisms and two different subthreshold-activated currents, I_{NaP} and I_h, that is the reduced stellar model described in Section 2.1.2.2 with external current given in 2.2.1. Moreover, in this case we are able to provide an improvement of the linear estimation based on the quadratization explained in Subsection 5.1.1.2, *Quadratization approach*. Next, we develop both cases separately.

Misestimations in the pyramidal cell model with an AHP and an LTS currents

Let us consider the pyramidal model described in Section 2.1.2.1 with external current given in Section 2.2.1. For the sake of comparison, we perform the estimation both under

the presence of subthreshold-activated ionic channels (AHP and LTS) and without it. The case with both AHP and LTS off (already studied in Guillamon et al (2006)) is included for completeness and reference, but we are mainly interested in the experiment with either I_{AHP} or I_{LTS} on.

In Figure 5.1A, we show the total subthreshold current ($I_{AHP} + I_{LTS}$) versus the rest of ionic currents when no applied current was added to the neuron model, that is $I_{app} = 0$. It can be observed that in the time interval $(62, 100)\,ms$ the value of the subthreshold currents dominates over the sum of the other currents. More precisely, in the time interval $(77, 100)\,ms$, the sum of the rest of ionic currents almost vanishes and so the neuron has only subthreshold activity. These subthreshold-dominant time intervals can be better appreciated in Figure 5.1B, where the *ad hoc* index of dominance $\chi(t)$ (see equation (5.1)) is shown: index values below $-\sqrt{2}/2$ indicate dominance of AHP currents whereas index values above $\sqrt{2}/2$ indicate dominance of LTS currents. We recall that, for each time t, this index is a statistical measure calculated from the currents for all I_{app}. In Figure 5.1C subthreshold-dominant intervals are shaded over the membrane potential for $I_{app} = 0$.
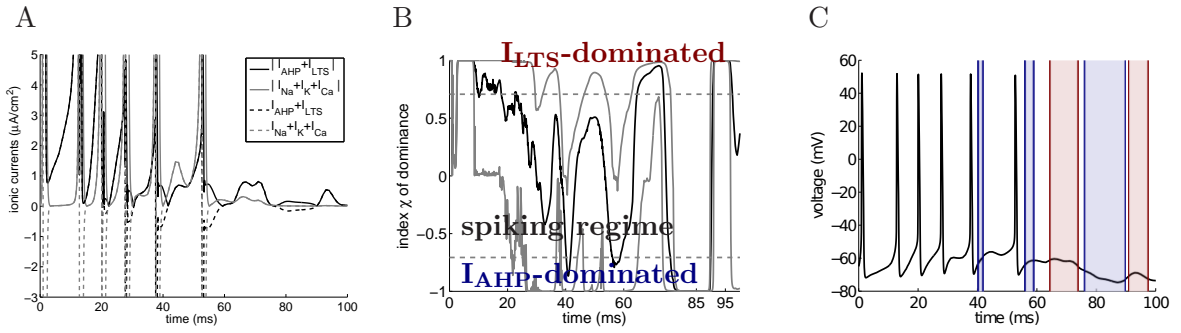
Figure 5.1: **Representation of the subthreshold-activated ionic currents.** In panel A, we compare the sum of the subthreshold currents, $-(I_{AHP} + I_{LTS})$ (black trace), with the sum of all other ionic currents, $I_{Ca} + I_{Na} + I_K$ (gray trace) with no applied current, that is $I_{app} = 0$. The solid trace represents, in each case, the absolute value of the sums, whereas the dotted traces represent the actual values. We have chopped off the graphs for the sake of clarity. Panel B shows the mean (solid trace, in black) and the minimum and maximum values (solid traces, in gray) of the index of dominance of subthreshold currents over the different values of I_{app}. The two horizontal dotted lines (in gray) are the limits between the spiking and the non-spiking regimes and define three zones: a I_{LTS}-dominated non-spiking regime (upper zone), a spiking regime (middle zone) and an I_{AHP}-dominated non-spiking regime (lower zone). In panel C, we show the I_{AHP}-dominated (bluish shadowed) and I_{LTS}-dominated (reddish shadowed) regimes obtained from panel B (mean across all applied currents) over the voltage course for $I_{app} = 0$.

The representation of index χ in Figure 5.1B is useful to select different situations of activation of subthreshold currents, see also Figure 5.1C. In particular, we analyse (see Figure 5.2): a case where the AHP current prevails over the LTS current (we choose $t = 85\,ms$, see Figure 5.1B-C), and a case where the dominating current is LTS (we choose $t = 95\,ms$, see Figure 5.1B-C). Note that in both cases the traces of the currents lie clearly under the threshold. We have applied the linear estimation procedure explained in Section 5.1.1.2, *Linear estimation approach*, both for I_{AHP}-dominance ($t = 85\,ms$) and I_{LTS}-dominance ($t = 95\,ms$).

When both I_{AHP} and I_{LTS} are inactivated, the estimation in the subthreshold regime is very accurate, as we predicted. Indeed, in Figure 5.2A, the actual and the estimated slopes (corresponding to the estimation of $1/g_{syn}$) and intercepts (corresponding to the estimation of V_{eff}) show a substantial agreement.
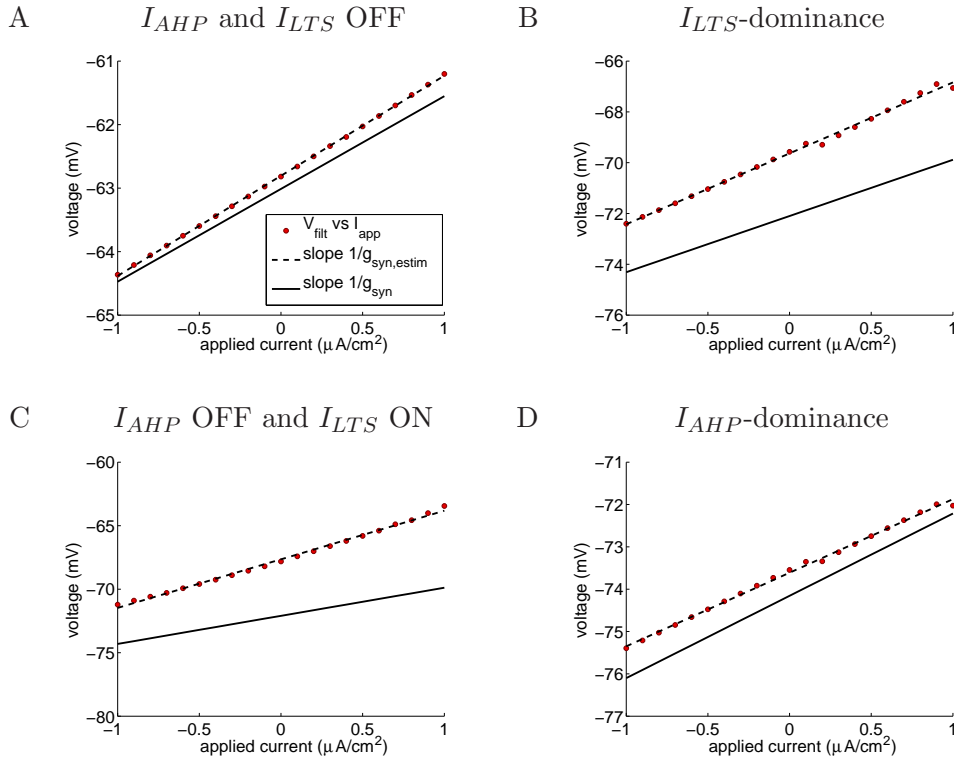
Figure 5.2: **Comparison of the actual and estimated parameters for the pyramidal cell model under different dominance regimes.** Panel A shows the estimation for time $t = 70\,ms$ (silent regime) when both subthreshold currents, I_{AHP} and I_{LTS}, are inactive. Panels B and D show the estimation for times $t = 95\,ms$ (I_{LTS}-dominated non-spiking regime) and $t = 85\,ms$ (I_{AHP}-dominated non-spiking regime), respectively, when both I_{AHP} and I_{LTS} are active. Panel C shows a case where I_{LTS} is activated but not the I_{AHP}. In all panels, the solid trace represents the theoretical regression line whereas the dotted trace is the straight line estimated from the data (red dots, which indicate the filtered membrane potential for different values of the applied current I_{app}). The relative errors in estimating g_{syn}, V_{eff}, g_E and g_I in panels B, C and D are quantified in rows 1, 2 and 3 of Table 5.1, respectively.

The most interesting differences arise when we estimate the conductances under the presence of either I_{AHP} or I_{LTS}, as shown in Figure 5.2B-C-D. Whereas both the slope ($1/g_{syn}$) and the intercept (V_{eff}) are well estimated with this kind of currents off (Figure 5.2A), the activation of any of them induces a mismatch between the theoretical $v - I_{app}$ line and the estimated one (see Figure 5.2B-C-D), where both the intercept and the slope are altered.

When the I_{AHP} dominates (see Figure 5.2D), this situation clearly leads to an overestimation of the total synaptic conductance because the slope ($1/g_{syn}$) is underestimated; the effective reversal potential (V_{eff}) is also overestimated. On the other hand, when the dominating current is I_{LTS} (see Figure 5.2B-C), the total synaptic conductance is underestimated whereas the effective reversal potential is overestimated. It is clear, then, that the solutions of the linear system (5.3) contain errors both in either V_{eff} and g_{syn}, thus indicating that the linear relationship hypothesis between v_{filt} and I_{app} can also be broken in (apparently) silent regimes. Interestingly, this effect was not detected when subthreshold currents are not considered (see Guillamon et al (2006)).

Using the estimations obtained from Figure 5.2 and applying the equations in (5.3), we can compute the relative errors in the estimation of synaptic conductances at critical time

instants both when the dominating current is I_{AHP} and I_{LTS}, see Table 5.1.

	relative error			
	V_{eff}	g_{syn}	g_E	g_I
$t = 95\,ms$ LTS dominates	3.42%	−20.76%	6.86%	−29.32%
$t = 95\,ms$ LTS ON AHP OFF	6.17%	−42.18%	−16.59%	−57.16%
$t = 85\,ms$ AHP dominates	0.74%	11.85%	44.51%	13.29%

Table 5.1: **Relative errors in the pyramidal cell model.** For three different situations, I_{LTS} dominance, I_{AHP} dominance and only I_{LTS} activated, we compute the relative error of the estimated effective reversal potential and the conductances with respect to the actual ones, that is $100(x_{estimated} - x_{actual})/|x_{actual}|\%$, where x stands for V_{eff}, g_{syn}, g_E and g_I. Rows 1, 2 and 3 correspond, respectively, to panels B, C and D of Figure 5.2. Moreover, row 1 corresponds to time $t = 95\,ms$ in the panels of Figure 5.3 and row 3 to time $t = 85\,ms$.

As explained above, in Figure 5.2 we have shown, for specific time values, how the activation of subthreshold ionic currents has an adverse effect on the estimations of synaptic conductances. However, these values constitute a too punctual examination of the problem; to show that these misestimations are maintained along a significative time interval, in Figure 5.3 we plot the actual conductances, the estimated ones and the relative errors for $t \in [77.35, 96.6]\,ms$: panels A and B refer to g_{syn} whereas panels C and D refer to g_E and g_I, respectively. From panels B-C in Figure 5.1, we can see that this interval contains both an I_{AHP}-dominated subinterval (below $t = 89.65\,ms$) and a I_{LTS}-dominated subinterval (above $t = 89.9\,ms$). We discriminate the analysis according to these subintervals in order to discern the contamination due to the presence of the afterhyperpolarizing current from the presence of the low-threshold current.

Estimation errors in the I_{AHP}-dominated time interval   The explanation for the influence of this kind of currents in the estimations can be found in the time scale of activation, namely the long-time scale of $[Ca^{2+}]$. It turns out that the I_{AHP} has a strong influence during around $55\,ms$ after the spike (since $\tau_{Ca} = 80\,ms$ and $[Ca^{2+}]$ has an exponential decay, see equation (2.4) in Appendix A). Then, it may happen that, for some I_{app}, the I_{AHP} current is still influencing while for other I_{app}, the I_{AHP} is negligible at this moment in time. This fact leads to a breaking of the linearity of the $I_{app} - V_{filt}$ relationship. Observe (see Figure 5.1A) that spiking regimes finish around $t = 53\,ms$ so that the I_{AHP}-dominance interval, $t \in [77.35, 89.65]\,ms$, is coherent with the time scale of this calcium-induced potassium channel.

For this time interval, we observe (see Table 5.2) an average error in the total synaptic conductance around $8.64 \pm 6.45\%$, that is somehow preserved for the inhibitory conductance ($10.12 \pm 9.07\%$) but a notable increase of the excitatory conductance error up to $27.82 \pm 35.14\%$. Our results confirm and quantify the discrepancies between the actual and estimated histograms of g_{AMPA} and g_{GABA} observed in Figure 6 of Rudolph et al (2004) under the presence of subthreshold-activated ionic channels. Our quantitative analysis
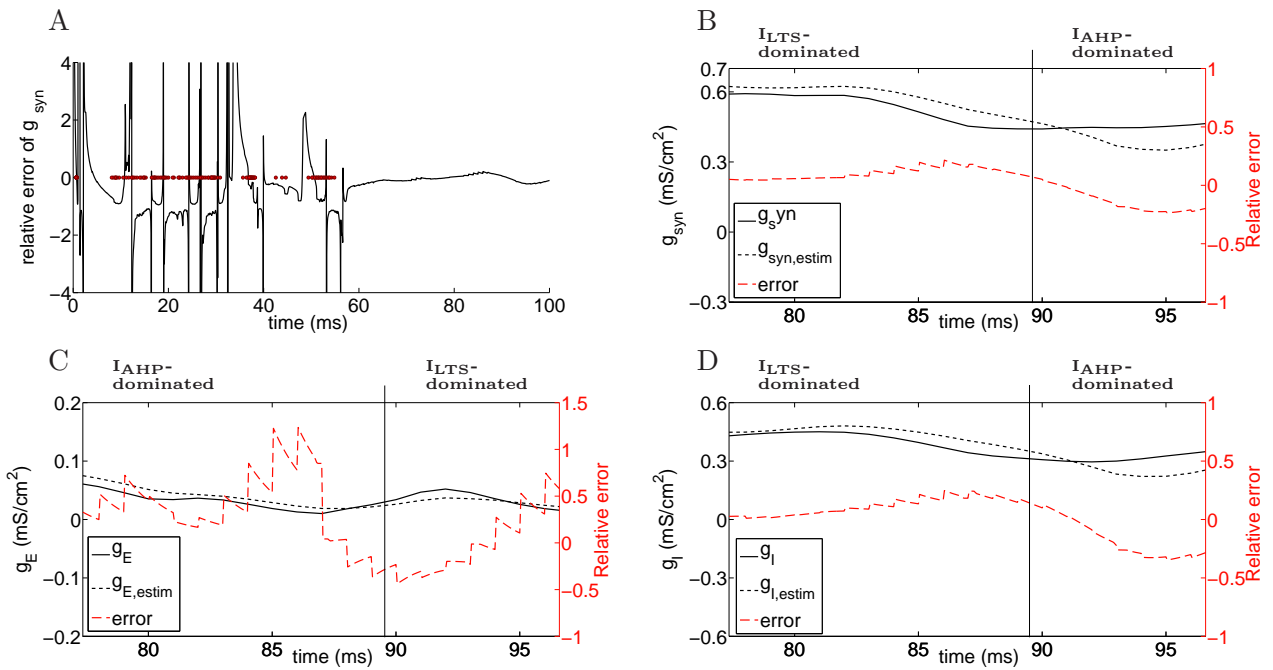
Figure 5.3: **Relative errors in the I_{AHP}-dominated and I_{LTS}-dominated phases.** Panel A shows the relative error of the synaptic conductance (solid trace) together with the spiking times (dots, in red) for each I_{app} value in $\{-1, -0.9, -0.8, \ldots, 0.8, 0.9, 1\}$ in order to show the influence of spikes in the misestimations. Panels B, C and D show the relative error (dashed red trace), the estimated value (dotted black trace) and the actual value (solid black trace) of the total, excitatory and inhibitory synaptic conductances, respectively, in the subthreshold regime. Vertical lines show the border between the I_{AHP}- and I_{LTS}-dominance phases, as in Figure 5.1C.

MEAN	I_{AHP}-dominated	I_{LTS}-dominated
g_{syn}	8.6%	-11.23%
g_E	27.82%	-2.85%
g_I	10.12%	-13.87%

STD	I_{AHP}-dominated	I_{LTS}-dominated
g_{syn}	6.45%	9.69%
g_E	35.14%	30.48%
g_I	9.07%	16.30%

Table 5.2: **Statistics of average relative errors for the pyramidal cell model.** Statistics of relative errors in the estimation of total, excitatory and inhibitory synaptic conductances. The rows show the averages along time intervals and are computed $100\,(x_{estimated} - x_{actual})/|x_{actual}|\%$, where x stands for g_{syn}, g_E and g_I, respectively. Left column: averages over the time interval $[77.35, 89.65]\,ms$, where I_{AHP} dominates; right column: averages over the time interval $[89.65, 96.6]\,ms$, where I_{LTS} dominates, see also Figure 5.3 for reference.

shows that these errors cannot be disregarded and that they can lead to wrong conclusions about the reconstruction of g_E and g_I temporal profiles.

Estimation errors in the I_{LTS}-dominated time interval   The I_{AHP} current needs spiking activity before being activated and it could be argued that the observed errors are due to this post-influence of the spiking misestimations rather than the presence of subthreshold ionic channels. To ensure that this is a pure subthreshold effect, we have chosen another type of subthreshold-activated channel, a low-threshold one which activates in a range of voltage values still far from the spiking threshold but sufficiently above the hyperpolarized state.

For this time interval, we observe an average error in the total synaptic conductance around $-11.23 \pm 9.69\%$, that become somehow steady for the inhibitory conductance ($-13.87 \pm 16.30\%$) and a low mean disperse estimation for the excitatory conductance ($-2.85 \pm 30.48\%$).

Considering the I_{AHP} current inactive, Figure 5.4 shows the actual and the estimated conductances when only the I_{LTS} current is active, that is $t \in [70, 100]$. In this plot we can appreciate the misestimations of the linear regression even in the subthreshold regime since, the dots of the scatter plot do not tend to align along the identity line.

Source of misestimations   We know by previous studies, see Guillamon et al (2006), that the mismatches of the estimation in the spiking regime come from the wrong assumption that the different ionic currents vanish. When either AHP or LTS currents are on, the errors in the estimation spread to the regimes where these currents are active since we can not suppose that they vanish. Therefore the linear regression (5.2) should be corrected as

$$V(t; I_{app}) = V_{eff}(t) - \frac{I_{AHP}(t) + I_{LTS}(t)}{g_{syn}(t)} + \frac{I_{app}}{g_{syn}(t)}. \tag{5.8}$$

If we examine the effect of the new term $I_{AHP}(t) + I_{LTS}(t)$ in equation (5.8) on the solution of the linear regression (5.3), we obtain that the solution is modified by adding an extra
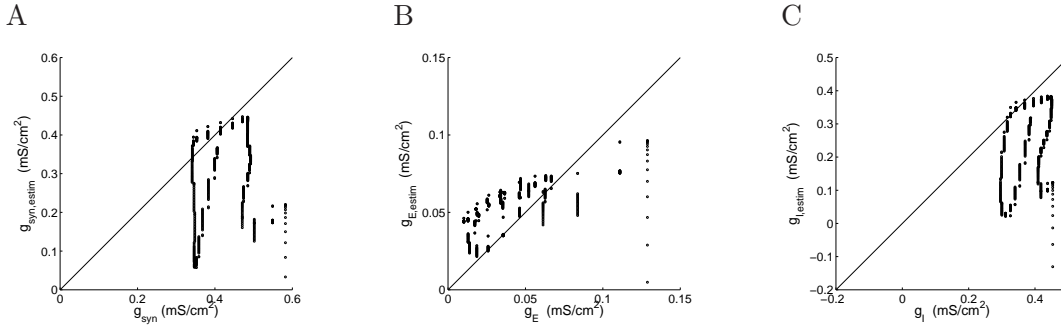
Figure 5.4: **Actual versus estimated conductances for the pyramidal cell model with only I_{LTS} active.** Panels A, B and C represent the scatter plot of the actual versus the estimated total, excitatory and inhibitory synaptic conductances, respectively, for a time interval where only the I_{LTS} current is active. The identity line has been added on the scatter plot as a reference to compare how the estimated conductances agree with the actual ones.

term depending on the subthreshold currents to the g_E and g_I expressions:

$$g_E = \frac{(g_{syn}-g_L)V_I - V_{eff}\,g_{syn} + g_L V_L}{V_I - V_E} - \frac{I_{AHP}+I_{LTS}}{V_I - V_E}$$

$$g_I = \frac{-(g_{syn}-g_L)V_E + V_{eff}\,g_{syn} - g_L V_L}{V_I - V_E} + \frac{I_{AHP}+I_{LTS}}{V_I - V_E}$$

(5.9)

The cause of the pitfalls of the estimation are thus due to ignore the $I_{AHP}(t) + I_{LTS}(t)$ term in the linear estimation procedure. Basically three different situations may arise: (a) if $I_{AHP} + I_{LTS}$ were constant with respect to I_{app}, then we would obtain a perfect fit and estimation of g_{syn}, whereas V_{eff} would be misestimated; (b) if $I_{AHP} + I_{LTS}$ were to vary linearly with respect to I_{app}, then the fit would remain perfect, but both g_{syn} and V_{eff} would be misestimated; (c) otherwise, neither the fit would be good and the estimations trustable.

In the first two cases ((a) and (b)) one could devise a way to foresee whether V_{eff} and g_{syn} are underestimated or overestimated. For instance, in the AHP-dominated regime, since $I_{AHP} + I_{LTS} < 0$ (see Figure 5.1B), the $(I_{app}, V(t; I_{app}))$ points obtained from the experiments would be distributed above the line corresponding to the ideal situation where no ionic currents are active. For case (a), this would lead to an overestimation of V_{eff} and, for case (b), to an overestimation of V_{eff} and an underestimation (resp., overestimation) of g_{syn} if the $(I_{AHP} + I_{LTS})$ versus I_{app} slope is positive (resp., negative). Unfortunately, the most common case is (c), in which the above predictions can be taken only as an orientation. Indeed, in Table 5.1 we can observe, for instance, underestimations of V_{eff} in the AHP-dominate regime. The same analysis can be applied to the estimations of g_E and g_I from g_{syn} and V_{eff} (see equation (5.9)), so we cannot assess a general relationship between AHP or LTS domination and the sign of the misestimations.

Linearization of the subthreshold ionic currents approach In the case of LTS, this current is activated on the subthreshold regime independently of the spikes. Its characteristic time scale τ_{LTS} changes according to the steady state value of the current which is given by equations (2.2 -2.3) with $w = h_{LTS}$.

As we have mentioned in Subsection 5.1.1.2 *Linearization of the subthreshold ionic currents*

approach, during the phase where I_{LTS} is dominating, the plot of the function

$$I_{LTS,\infty}(V) := g_{LTS}\, m_{LTS,\infty}(V)^3\, h_{LTS,\infty}(V)\,(V - V_{Ca})$$

is not far from linear. Then, $I_{LTS,\infty}(V)$ can be linearised for $v \approx [-75, -60]\, mV$ and the estimation described in Subsection 5.1.1.2, *Linearization of the subthreshold ionic currents approach*, can be done. However, this approach did not lead to good estimations either, the reason being the slow approach of the h_{LTS} variable to its steady state $h_{LTS,\infty}(V)$ (see Figure 5.5A). Anyway, we found interesting to show the slight improvement obtained following this approach. Just as a proof-of-concept, we tried with a 10-times smaller
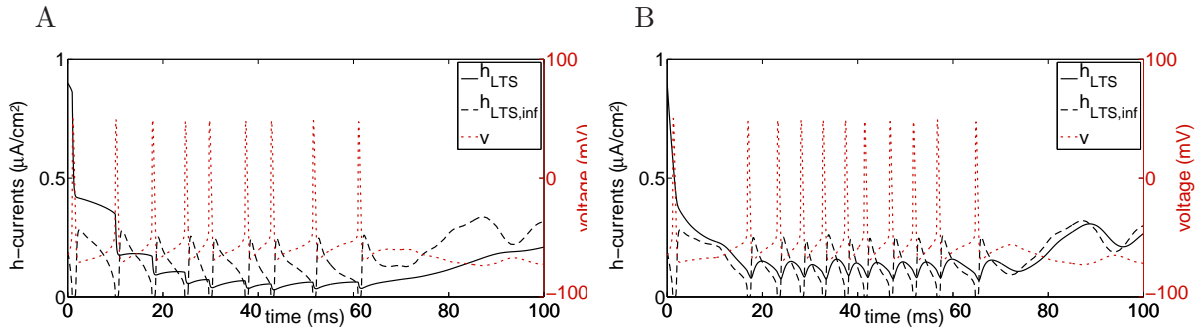

Figure 5.5: **Behaviour of h_{LTS} and $h_{LTS,\infty}(V)$** Both panels show the voltage of the neuron (dotted red trace) and the behaviour of h_{LTS} (solid black trace) and of $h_{LTS,\infty}(V)$ (dashed black trace) over time. In panel A we can see how h_{LTS} and $h_{LTS,\infty}(V)$ do not match when using the characteristic time scale of the system. Otherwise, in panel B, where the parameter τ_{LTS} has been fixed to be 4.5, we observe that h_{LTS} reaches $h_{LTS,\infty}(V)$ very quickly.

time constant, namely $\tau_{LTS} = 4.5\, ms$, in which case h_{LTS} catches $h_{LTS,\infty}(V)$ sufficiently fast to be close enough during the I_{LTS}-dominance phase (see Figure 5.5B). Thus we get that h_{LTS} closer to $h_{LTS,\infty}(V)$ in the interval in which $I_{LTS,\infty}(V)$ is linear and so $I_{LTS,\infty}(V) \approx I_{LTS}(m, h, V)$. Then, the procedure proposed at the end of Subsection 5.1.1.2, *Linearization of the subthreshold ionic currents approach*, can be applied to improve the linear estimation of the synaptic conductances. Obviously we are certainly loosing biophysical interest since this would be a valid approach only for putative "fast low-threshold" channels, which are seldomly reported in the literature, see Carbone et al (2006). In this case, as we can see in Figure 5.6, the agreement of the estimated data with the actual data presents an important improvement.

Misestimations in the stellate cell model with NaP- and h- currents

In the previous section we have seen how the subthreshold-activated currents lead the linear estimation to significant errors. Let us now consider the reduced stellate cell model, described in Section 2.1.2.2 with external current given in 2.2.1, to stress the misestimations of the linear regression under the presence of currents, which cause oscillatory activity in the subthreshold regime and nonlinear effects. Finally, we are presenting an improvement of the linear estimation to take into account this nonlinearities and the fact that the ionic currents may not reach the steady state, where the alternative presented in Subsection 5.1.1.3, paragraph *Linearization of the subthreshold ionic currents approach*, fails.

In contrast to the pyramidal cell model, the model we are currently considering has no presence of currents that lead the neuron to fire. For this reason, the goodness of the
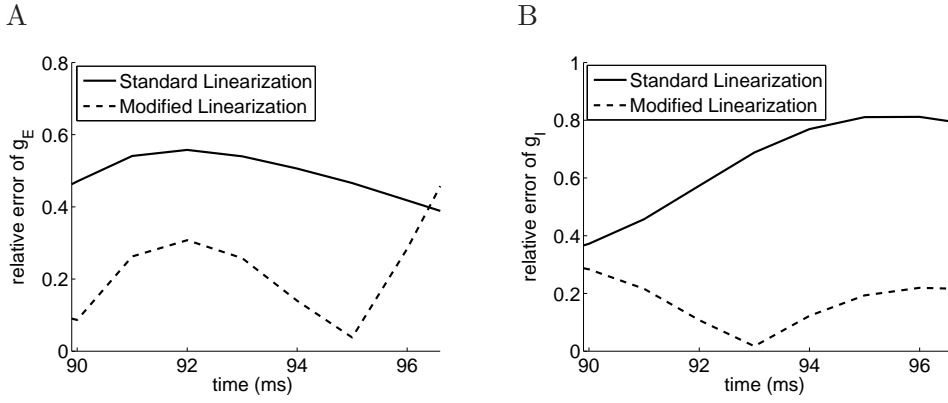
A

B

Figure 5.6: **Estimation of excitatory and inhibitory conductances using a rectified linear regression.** For fast low-threshold dynamics ($\tau_{LTS} = 4.5\,ms$), panels A and B show the relative errors of g_E and g_I, respectively, when the *standard* linear estimation (using (5.2) and (5.3)) has been used (solid trace) and when the estimation has been *modified* using the procedure proposed at the end of Subsection 5.1.1.2, *Linearization of the subthreshold ionic currents approach,* (dashed trace).

estimation can not be affected by the presence of spiking currents, but only for the sub-threshold ones. In order to proceed with the linear estimation, we check that, for values of $I_{app} \in [-4, -3]$, both subthreshold currents are active. Their magnitudes oscillate between 1 and 7 $\mu A/cm^2$ for the I_{NaP}, and with magnitude between 4 and 7 $\mu A/cm^2$ for the I_h (see Figure 5.7 for a representation of I_{NaP} and I_h when $I_{app} = -3.5$).
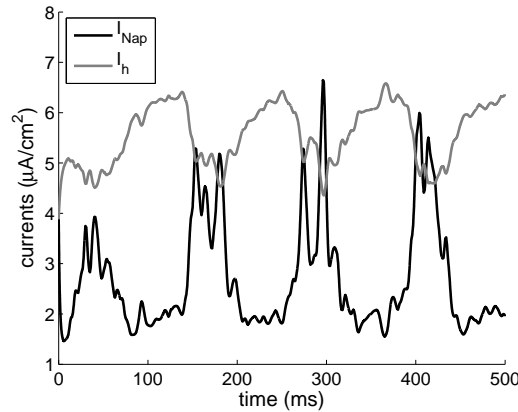

Figure 5.7: **Representation of the subthreshold-activated ionic currents in the stellate cell model.** Activity of the two active subthreshold currents in this model, the persistent sodium current (black trace) and the h-current (gray trace) for a central value of the set of applied currents used in the estimation, that is, $I_{app} = -3.5$.

Figure 5.8 shows the results of applying the standard linear estimation procedure defined by formulas (5.2) and (5.3). Upper panels show how the estimated synaptic conductances (either the total one or both excitatory and inhibitory) clearly diverge from the actual ones along time. Lower panels of Figure 5.8 contain the scatter plots of the set of paired points ($g_{actual}, g_{estimated}$) for the total, excitatory and inhibitory conductances. The arrangement of the points far from the identity line gives a clear evidence of the non-validity of the standard linear estimation procedure.
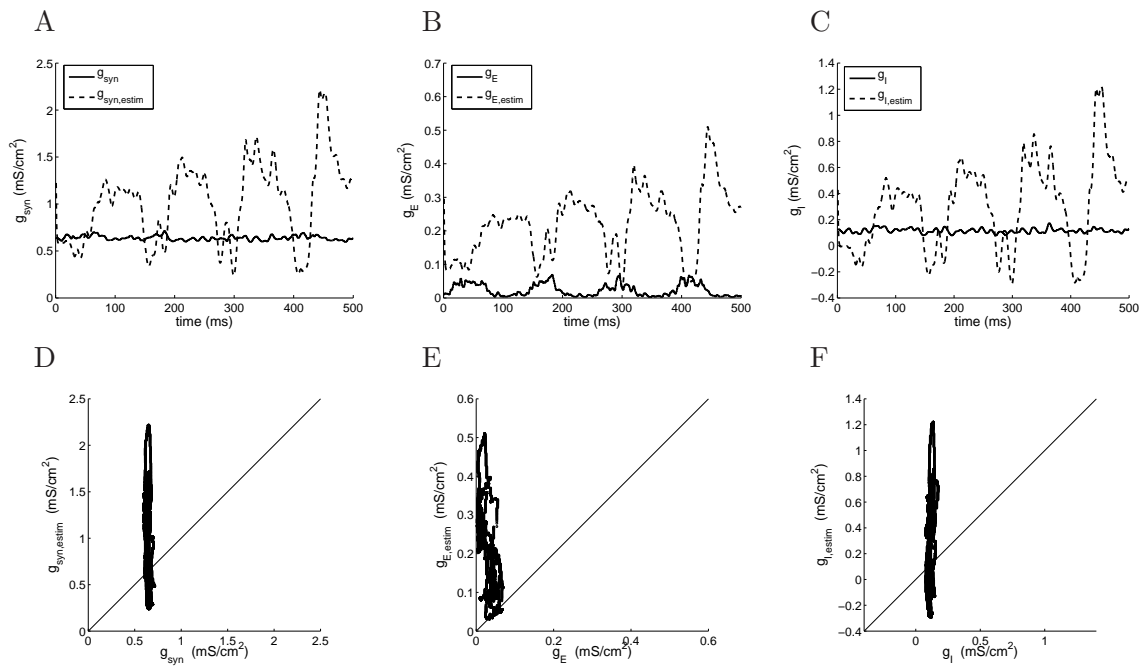
Figure 5.8: **Comparison of the actual and the linearly estimated conductances for the stellate cell model.** Upper panels show the actual time course (solid black traces) and the estimated time courses (dotted black traces) of the total (panel A), the excitatory (panel B), and the inhibitory (panel C) synaptic conductances when the linear estimation has been applied for 21 values of $I_{app} \in [-4, -3]$, equispaced. Low panels represent the scatter plot of the actual conductances versus the estimated. The plotted conductances are the synaptic one, the excitatory one, and the inhibitory one (from left to right). The identity line has been added on the scatter plot to compare how the estimated conductances disagree with the actual ones.

Finally, in Figure 5.9, we show the membrane potential computed by using the actual conductances together with the membrane potential obtained with the estimated conductances (the *reconstructed* voltage). Comparing the results obtained in this figure and the time course of the ionic currents (see Figure 5.7), we can see how the reconstructed voltage is worse when subthreshold currents present higher activity, as it is also noticeable for the synaptic conductances.
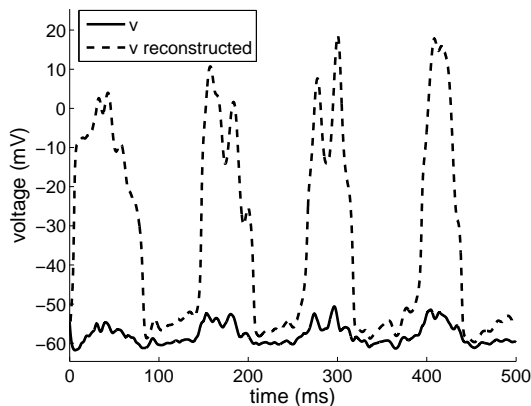

Figure 5.9: **Voltage dynamics generated by both the actual and the linearly estimated conductances in the stellate cell model.** Solid black trace represents the voltage obtained with the actual conductances while the dotted black trace represents the reconstructed voltage, obtained by plugging the estimated conductances into the model. The applied current considered in both cases is $I_{app} = -3.5$.

Summing up, te results shown for the stellate cell model up to this point, together with those obtained for the pyramidal cell model with I_{AHP} and I_{LTS} currents, clearly demonstrate that the standard linear estimation procedure turns out to be inappropriate as well in subthreshold regimes. For the pyramidal cell model, we have come up with a modified linear regression which mildly improved the estimations. For the stellate cell model, taking advantage of the *minimal model* reduction given in Rotstein (2015), we are able to propose a promising nonlinear estimation procedure, see Subsection 5.1.1.2, *Quadratization approach*, that improves the estimations by more than one order of magnitude.

Quadratization alternative   Following the procedure presented in Subsection 5.1.1.2 *Quadratization approach*, from the total synaptic current, we can discern between excitatory and inhibitory conductances using two trials corresponding to different applied currents. In this section we want to show the goodness of this new approach.

Having two different voltage traces for different applied currents, from equation (5.6) one can estimate the total synaptic current for each trial. In Figure 5.10A, we can appreciate how the estimated synaptic current fits to the actual one along time. The scatter plot presented in panel B illustrates how the estimated and the actual values are concentrated in the vicinity of the identity line, which means a good estimation of the synaptic current.

Using two different applied currents, say $I_{app,1}$ and $I_{app,2}$, and the corresponding voltage traces $V_1(t)$ and $V_2(t)$, we obtain $I_{syn,1}(t)$ and $I_{syn,2}(t)$, respectively, from equation (5.6), see also Figure 5.10. Then, using (5.7), we obtain an estimation of the time course of the excitatory and the inhibitory conductances which are shown and compared with the actual ones in Figure 5.11. In the upper panels of this figure, one can see how the actual and the
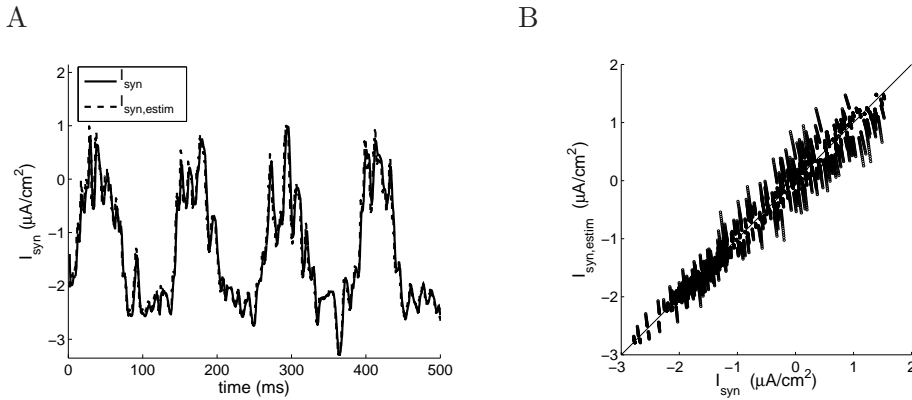
Figure 5.10: **Actual synaptic currents compared to those estimated through the quadratizaton procedure.** Panel A shows the time course of the actual synaptic current (solid black traces) and the estimated one (dotted black traces) when the quadratization approach has been applied for $I_{app} = -3.5$. Panel B represents the scatter plot of the actual synaptic current versus the estimated. The identity line has been added on the scatter plot to compare how the estimated values agree with the actual ones.

estimated traces fit better than in the linear regression case. Moreover, the estimation is better for the excitatory conductances than for the inhibitory ones, as it can also be seen in the lower panels, where the scatter plot presents higher concentration on the vicinity of the identity line for the g_E case. In Table 5.3, we give a complete quantitative description of the errors of the estimation both for the linearization and the quadratization procedures.

MEAN	Linearization	Quadratization
g_{syn}	61.73%	-0.46%
g_E	2335.03%	-4.92%
g_I	155.68%	-1.06%

STD	Linearization	Quadratization
g_{syn}	69.79%	4.35%
g_E	2507.84%	30.84%
g_I	287.09%	20.94%

Table 5.3: **Statistics of average relative errors for the stellate cell model.** Statistics of relative errors in the estimation of total, excitatory and inhibitory synaptic conductances. The rows show the averages along time intervals and are computed $100 \left(x_{estimated} - x_{actual} \right) / |x_{actual}|\%$, where x stands for g_{syn}, g_E and g_I, respectively. Left column: averages corresponding to the Linearization procedure; right column: averages corresponding to the Quadratization procedure.

Finally, to study the effect of the errors done in the estimation, we reconstruct the voltage traces of the neuronal model using the estimated conductances. As we can see in Figure 5.12, both the actual and the reconstructed voltages do not present big changes, contrary to the case when linear regression is applied.

These results imply that the quadratization approach is a better alternative to estimate conductances when nonlinear activity coming from subthreshold-activated ionic currents is present.
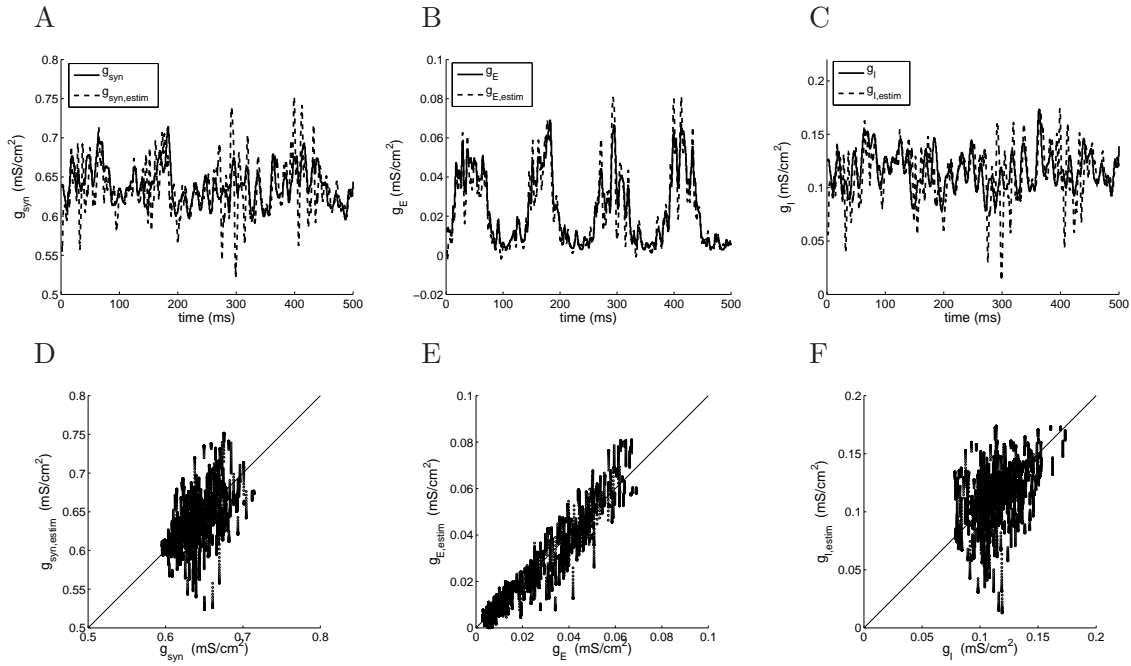
Figure 5.11: **Comparison of the actual and estimated conductances using the quadratization approach.** Upper panels show the actual time course (solid black traces) and the estimated time courses (dotted black traces) of the total (panel A), the excitatory (panel B), and the inhibitory (panel C) synaptic conductances when the quadratization approach is applied for $I_{app} = -4$ and $I_{app} = -3.5$. Low panels represent the scatter plot of the actual conductances versus the estimated ones, showing a good agreement.
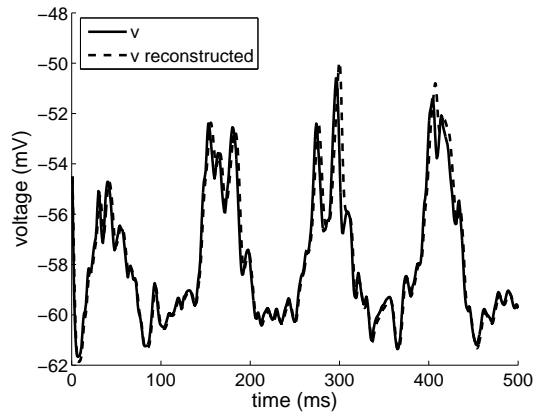

Figure 5.12: **Voltage dynamics generated by both the actual and the quadratically estimated conductances in the stellate cell model.** Solid black trace represents the voltage obtained with the actual conductances while the dotted black trace represents the reconstructed voltage, obtained by plugging the estimated conductances into the model. The applied current considered in both cases is $I_{app} = -3.5$.

5.1.2   Non-deterministic framework

After seen the errors in the subthreshold regime caused by the presence of nonlinear terms, and corroborate that quadratic approximations can be useful to reduce those errors, in this section we aim to introduce an stochastic quadratic model to estimate conductances

in this case. This procedure also takes into account possible noise from experimental data and only needs one trial to estimate conductances and discern between the excitatory and the inhibitory ones.

This section is structured in the following way: in Subsection 5.1.2.1, we indicate those models, data and mathematical tools we are using along the different subsections. In Subsection 5.1.2.2, we describe the estimation procedure we develop. In Section 5.1.2.3, we show the results obtained when the estimation procedure is applied to both the *in silico* and *in vivo* voltage traces. We also compare in Section **??** our estimations to those obtained by other existing methods based on single-trial recordings.

5.1.2.1   Models and data treatment

To generate membrane potential traces we use three different neuronal models that contain non-linear subthreshold activity, namely: (a) the QIF model with noise and the appropriate parameters to replicate the pyramidal model; and the Hodgkin-Huxley type models describing (b) a pyramidal neuron and (c) a stellate neuron. The pyramidal neuron model is endowed with a spiking mechanism generated by sodium, potassium and calcium currents, and two different types of subthreshold currents: a calcium-activated potassium afterhyperpolarizing current (AHP) and a low-threshold calcium current (LTS) (see model in Section 2.1.2.1 and external current in Section 2.2.1). The stellate neuron model is also endowed with a spiking mechanism generated by sodium and potassium, and two subthreshold currents, the persistent sodium (NaP) current and the h-current (see model in Section 2.1.2.2 and external current in Section 2.2.1).

Parameters choice. In the estimation procedure, we will be interested in two distinguished parameters: the largest input current such that the neuron does not present spikes, I_T, and its corresponding membrane potential, V_T. To determine the value of these parameters when dealing with the pyramidal and the stellate neuron models, we use the $V - I$ bifurcation diagram of both models obtained in the absence of noise and synaptic currents. Then, we assign to $(V_T, \ I_T)$ the bifurcation values corresponding to the spike initiation point. For the pyramidal neuron model we have obtained that $I_T = -1.359 \ \mu A/cm^2$ and $V_T = -74.27 \ mV$ whereas for the stellate neuron model we have obtained $I_T = -1.46 \ \mu A/cm^2$ and $V_T = -73.499 \ mV$.

Note that, since a noise may drive the voltage over the threshold for lower I values than I_T, the effective spike initiation point of the stochastic model will advance with respect to the deterministic one. In practice, we extract the *in sillico* data from stochastic models, and so we may expect the value of I_T to be lower than the one obtained from the bifurcation diagram.

This problem does not prevail in the *in vivo* data, where I_T is chosen, by applying different pulses to the neuron without synaptic inputs, as the minimum input current that induces spikes.

Synaptic drive. To computationally test our estimation procedure, we consider a trace of conductances that follows an Ornstein-Uhlenbeck (OU) process with a sinusoidal drift, which is described in Section 2.2.2.2.

Smoothing data Since some of the methods we will apply require smoothing of the signal, we consider the median filter for the smoothing step, which we following explain. Let L ms be the duration of the voltage traces, and let a time windows of length l ms, where $l \ll L$. Set the parameters $m = [l/\Delta]$ and $M = [L/\Delta]$. For simplicity and without loss of generality, we assume that l and L are multiples of Δ, and m and M are even (integers). Then, the median filter for the smoothing step consists in, for each point $p := (t, x_n)$ of an x signal, computing

$$\tilde{x}_n = \underset{n-m/2 \leq j \leq n+m/2}{\text{median}} \{x_j\}. \tag{5.10}$$

We chose this filter since it is often used by experimentalists to clip spikes, but any filter can be used. Unless otherwise stated we set $L = 5$ s and $l = 50$ ms in the simulations, to be consistent with the sliding window used for the estimation procedure.

Details about the numerical integration of the models are given in Section 5.1.2.1

Experimental data. As we have mentioned in the introduction, we test the estimation procedure presented in this subsection using experimental data from intracellular recordings in current-clamp mode of spinal motoneurons of red-eared turtles. Details about the experimental recordings are provided in Section 2.3.

5.1.2.2 Estimation procedure

To capture non-linearities in the subthreshold regime, we use the approximation given by the QIF model with noise, see model in Section 2.1.1.1 and external current in Section 2.2.1.

Consider the equation (2.1) written as the stochastic differential equation

$$dV = \left(aV^2 + bV + c\right) dt + \sigma dW_t \tag{5.11}$$

where

$$a = \frac{\alpha}{C},$$

$$b = \frac{1}{C} \left(-2\alpha V_T - g_E(t) - g_I(t)\right), \tag{5.12}$$

$$c = \frac{1}{C} \left(\alpha V_T^2 + g_E(t)V_E + g_I(t)V_I - I_T + I_{app}\right).$$

Notice that coefficients b and c are time dependent, whereas coefficient a is not. Therefore, to estimate a as a constant and the time course of b and c using only one voltage trace, we use a recursive method based in the maximum likelihood estimator (MLE).

We discretize the diffusion process in equation (5.11) as

$$V_{n+1} = V_n + (aV_n^2 + b_n V_n + c_n)\Delta + \sigma\sqrt{\Delta}\xi_{n+1},$$

where

$$b_n = \frac{1}{C} \left(-2\alpha V_T - g_{E,n} - g_{I,n}\right), c_n = \frac{1}{C} \left(\alpha V_T^2 + g_{E,n}V_E + g_{I,n}V_I - I_T + I_{app}\right), \tag{5.13}$$

$g_{E,n} = g_E(n\Delta)$, $g_{I,n} = g_I(n\Delta)$, $\Delta = t_{n+1} - t_n$ is the constant time step of the discretization, and ξ_{n+1} follows a Gaussian distribution with mean 0 and variance 1.

The discretized process follows (locally) a Gaussian distribution with mean $V_n + (aV_n^2 + b_n V_n + c_n)\Delta$ and variance $\sigma^2 \Delta$. Assuming the conductances to be approximately stationary for a time window $l\ ms$ implies that also the parameters b and c are constant in this window. Thus, in the considered sample window, we compute the estimator $\hat{\theta}$ by maximum likelihood (see B for more details). We distinguish two situations: (1) when $\theta = (a, b, c)^T$, i.e., both α and the conductances are unknown, in which case the MLE is given by equation (B.1); (2) when $\theta = (b, c)^T$, i.e., only the conductances are unknown, in which case the MLE is given by equation (B.2). Then, by moving the sample window, we obtain a discretized sequence for $\hat{\theta}(t)$, providing a discretized time course of $\hat{\alpha}(t)$, $\hat{g}_E(t)$ and $\hat{g}_I(t)$ through equations (5.12). The details of this procedure, which constitutes the basic step of our estimation algorithm, are next explained.

Consider the discretized voltage trace $\{V_n\}_{n=0}^M$ and let $\theta = (a, b, c)^T$ be the vector containing the unknown coefficients of the discretized diffusion process.

Algorithm 5.1. *Sliding MLE.*

1. *Set $n = m/2$.*

2. *While $n \leq M - m/2$, do:*

   (i) *estimate $\hat{\theta}_j$ by MLE from the subsequence $\{V_j\}_{j=n-m/2}^{n+m/2}$;*

   (ii) *set $n = n + 1$.*

3. *For each n from $m/2$ to $M - m/2$, use $\hat{\theta}_n$ and (5.13) to find $\hat{g}_{E,n}$ and $\hat{g}_{I,n}$ (if only the conductances are unknown), and $\hat{\alpha}_n = \hat{a}_n C$ (if also α is unknown).*

When α is assumed unknown, the Sliding MLE algorithm for $\theta = (a, b, c)^T$ estimates α as a non-constant value. To amend this disagreement with the model (where α is assumed to be constant), we suggest a recursive algorithm in which both α and the conductances are successively refined forcing α to be constant.

Algorithm 5.2. *Recursive estimation procedure.*

1. *Fix a tolerance TOL and a bound N_{max} for the maximum number of iterations.*

2. *Apply the sliding MLE algoritm for $\theta = (a, b, c)^T$ to find estimates $\hat{\alpha}_n$, $\hat{g}_{E,n}$ and $\hat{g}_{I,n}$.*

3. *Put $\hat{\alpha}^{(0)} = \frac{1}{M-m} \sum_{n=m/2}^{M-m/2} \alpha_n$ and estimate $\hat{g}_{E,n}^{(0)}$ and $\hat{g}_{I,n}^{(0)}$ using the Sliding MLE algorithm for $\theta = (b, c)^T$.*

4. *Fix the conductances at $\hat{g}_{E,n}^{(0)}$ and $\hat{g}_{I,n}^{(0)}$ and estimate $\hat{\alpha}^{(1)}$ by equation (B.3).*

5. *Set $i = 1$. While $|\hat{\alpha}_{i-1} - \hat{\alpha}_i| > TOL$ and $i < N_{max}$, do*

   (i) *Fix $\hat{\alpha} = \hat{\alpha}^{(i)}$ and estimate $\hat{g}_{E,n}^{(i)}$ and $\hat{g}_{I,n}^{(i)}$ by the sliding MLE algorithm for $\theta = (b, c)^T$;*

   (ii) *Fix $\hat{g}_{E,n}^{(i)}$ and $\hat{g}_{I,n}^{(i)}$ and estimate $\hat{\alpha}^{(i+1)}$ by equation (B.3);*

   (iii) *let $i = i + 1$.*

6. *If smoother results are wanted, then apply the median filter given in equation (5.10) (or any other filter) to the estimated traces.*

Note that since $g_E(t)$ and $g_I(t)$ depend linearly on α, it is sufficient to consider changes in α to stop the recursive process. If two consecutive estimated values of α are close, so are the corresponding estimated traces of $g_{E,n}$ and $g_{I,n}$. Moreover, when the recursive procedure is applied, the conductances during the first and the last $l/2$ ms are not estimated due to the sliding window.

5.1.2.3   Results

In this section, we present the results obtained using our QIF estimation procedure, which is described in Subsection 5.1.2.2. We apply the model to simulated (*in sillico*) and actual (*in vivo*) data. For the simulated data, three membrane potential traces are generated by different neural models: the QIF model, the pyramidal neuron model and the stellate neuron model, described in Chapter 2, using prescribed synaptic conductances described in Section 2.2.2.2. The actual data is extracted from a motor neuron as described in Section 2.3. Finally, the results obtained from the estimation procedure on the pyramidal neuron model as well as from experimental recordings, are compared to both the oversampling method and the OU-based method.

Results of the estimation in the QIF model.

Figure 5.13 shows the estimation results when the membrane potential is simulated from the QIF model (see model in Section 2.1.1.1 and external current in Section 2.2.1), setting $\alpha = 0.0067$. This value was estimated to $\hat{\alpha} = 0.0077$. Panel A depicts the true (dark blue curve) and the estimated (light blue curve) excitatory conductances, and panel B shows the true (dark magenta curve) and the estimated (light magenta curve) inhibitory conductances. The true excitatory trace is well approximated by the estimated trace, whereas the estimation of the inhibitory conductances only captures the overall shape and level, and is much more noisy. This is because the membrane potential is close to the inhibitory reversal potential, whereas it is far from the excitatory reversal potential, and thus, the synaptic drive is higher for excitation. This was also shown in Berg and Ditlevsen (2013), where analytic expressions for approximations of the variance of the estimators were derived from the Fisher Information matrix. Panels D and E show scatter plots of the true versus the estimated values (for excitation and inhibition, respectively), and higher concentration in the vicinity of the identity line (red line) indicate better estimation. Panel C shows the true membrane potential (dark curve) and the reconstructed voltage by using the estimated conductances (light curve). The reconstructed voltage reproduces the real one well; this is also corroborated in the scatter plot of the estimated versus true voltage (Panel F), where the points are concentrated in a small neighbourhood along the identity line.

Results of the estimation in the pyramidal neuron model.

Another computational neural model considered to estimate conductances is the pyramidal neuron model (see model in Section 2.1.2.1 and external current in Section 2.2.1. The results for this neuron model are in Figure 5.14. Panels are as in Figure 5.13. Both the excitatory and inhibitory conductances are well approximated; however, as in the QIF model, the estimation for the excitatory conductances is more accurate. It can be appreciated how well the reconstructed voltage matches the true voltage. The estimated
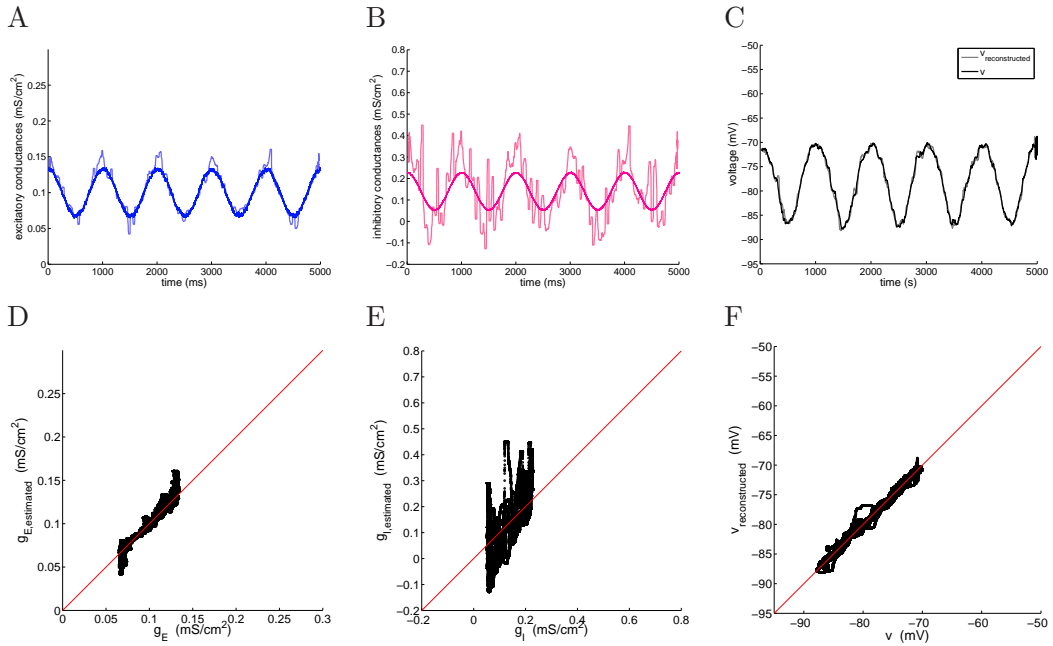
Figure 5.13: **Estimation of the conductances when data are generated by the QIF neuron model**. A: true (dark line) and estimated (light line) excitatory conductances. B: true (dark line) and estimated (light line) inhibitory conductances. C: simulated voltage using the true conductances (dark line) and the estimated conductances (light line). D: scatter plot of the estimated versus the true excitatory conductances. E: scatter plot of the estimated versus the true inhibitory conductances. F: scatter plot of the estimated versus the true voltage. The data have been obtained each $dt = 0.05\ ms$ and the MLE is applied with a $l = 50\ ms$ sliding window. The neuron parameters are: $C = 1\ \mu F/cm^2$ $g_L = 0.1\ \mu S/cm^2$, $V_L = -65\ mV$, $V_E = 0\ mV$, $V_I = -80\ mV$, $\alpha = 0.0067$, $V_T = -74.27\ mV$, $I_T = -1.359\ \mu A/cm^2$, and $I_{app} = -8.7\ \mu A/cm^2$.

value of α is 0.0067.

Surprisingly, the estimated values for this model are nearly as good as the original QIF model, and shows robustness of the method. It also indicates that a quadratic approximation seems to be sufficient to capture the nonlinearities caused by the ionic currents.

Results of the estimation in the stellate neuron model.

Finally, we also estimate the conductances using the complete version of the stellate model (see model in Section 2.1.2.2 and external current in Section 2.2.1). The results for this neuron model are depicted in Figure 5.15. Panels are as in Figure 5.13. Conclusions are similar to the conclusions for the pyramidal model. The estimated value of α is 0.0046. Again, the results indicate robustness of the estimation procedure.

Results of the estimation in experimental data

In Figure 5.16 we show the results obtained when the presented estimation procedure has been applied to the experimental data described in 2.3. The magenta line shows the estimated inhibitory conductances whereas the blue line shows the estimated excitatory
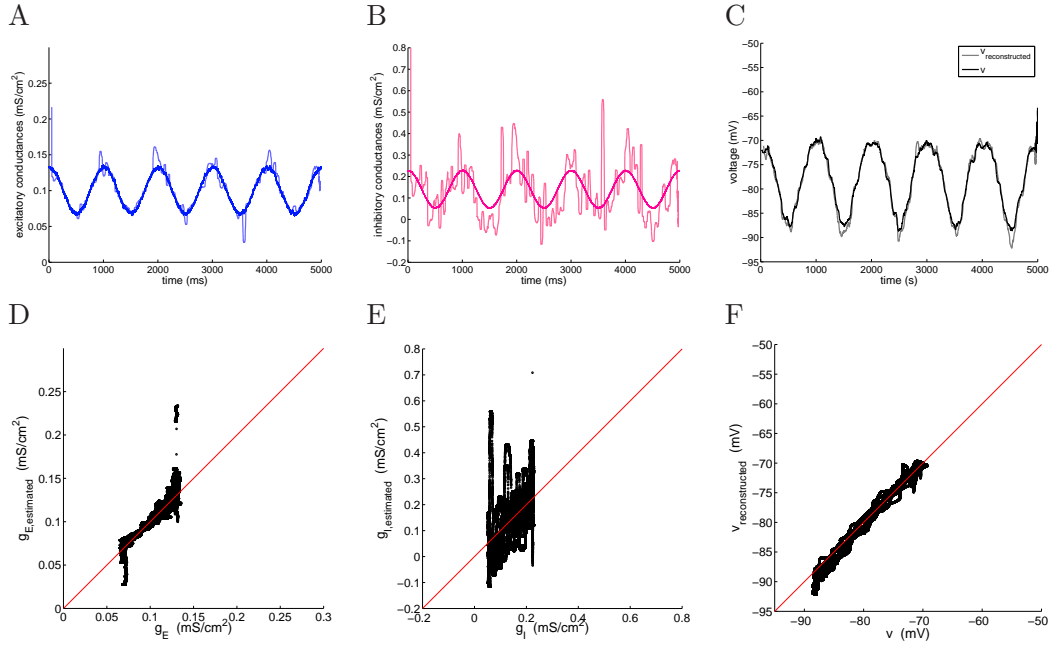
Figure 5.14: **Estimation of the conductances when data is generated by the pyramidal cell model**. A: true (dark line) and estimated (light line) excitatory conductances. B: true (dark line) and estimated (light line) inhibitory conductances. C: simulated voltage using the true conductances (dark line) and the estimated conductances (light line). D: scatter plot of the estimated versus the true excitatory conductances. E: scatter plot of the estimated versus the true inhibitory conductances. F: scatter plot of the estimated versus the true voltage. The data has been obtained each $dt = 0.05\ ms$ and the MLE sample window was $l = 50\ ms$. The neuron parameters are: $C = 1\ \mu F/cm^2$, $V_L = -65\ mV$, $V_E = 0\ mV$, $V_I = -80\ mV$, $g_L = 0.1\ \mu S/cm^2$, $V_T = -74.27\ mV$, $I_T = -1.359\ \mu A/cm^2$, and $I_{app} = -8.7\ \mu A/cm^2$.

conductances. Contrary to the *in sillico* data, in this case we have no information on the true input conductances, and so we cannot compare with it.

To further investigate the conclusions drawn from Figure 5.16, we compare them with the profile of the experimental voltage trace given in 5.17. One can see that both the conductance traces follow the shape of the membrane potential. Moreover, the QIF method provided an estimated value of the quadratic coefficient of $\alpha \approx 0.1094$. When reconstructing the membrane potential dynamics using the QIF model with the estimated conductances as synaptic input, Figure 5.17 shows a strong agreement with the true voltage trace; only a small underestimation can be identified on the scatter plot (Panel B) of the reconstructed versus the real membrane potential.

Comparison of our procedure with other existent methods

In this section we aim to compare the QIF method with other existent procedures that are also able to estimate conductances from a single trace. For this purpose we consider the stochastic approach presented in Berg and Ditlevsen (2013), which we will call OU method, and the oversampling method presented in Bédard et al (2011b), which is based on a deterministic model.
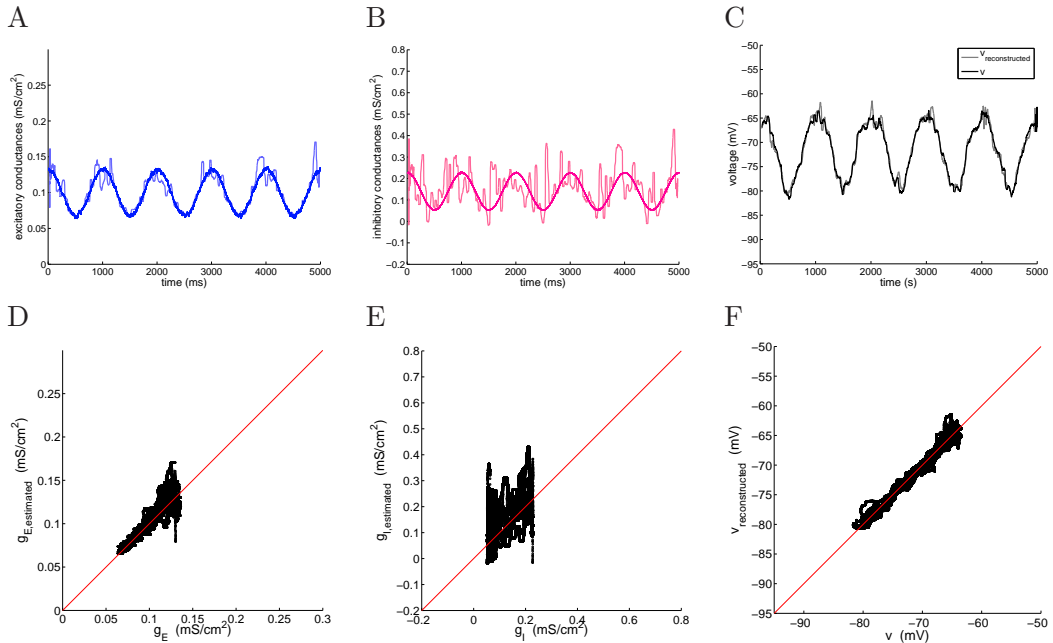
Figure 5.15: **Estimation of the conductances when data is generated by the stellate cell model**. A: true (dark line) and estimated (light line) excitatory conductances. B: true (dark line) and estimated (light line) inhibitory conductances. C: simulated voltage using the true conductances (dark line) and the estimated conductances (light line). D: scatter plot of the estimated versus the true excitatory conductances. E: scatter plot of the estimated versus the true inhibitory conductances. F: scatter plot of the estimated versus the true voltage. The data has been obtained each $dt = 0.05\ ms$ and the MLE sample window was $l = 50\ ms$. The neuron parameters are: $C = 1\ \mu F/cm^2$, $V_L = -65\ mV$, $V_E = 0\ mV$, $V_I = -80\ mV$, $g_L = 0.1\ \mu S/cm^2$, $V_T = -73.499\ mV$, $I_T = -1.46\ \mu A/cm^2$, and $I_{app} = -7.2\ \mu A/cm^2$.

The OU method is based on an stochastic version of the leaky integrate-and-fire that models the subthreshold activity by means of an Ornstein-Uhlenbeck process. This estimation procedure assumes, in a given time window, the membrane potential to be stationary. Then, using the maximum likelihood estimator within each window, the excitatory and inhibitory conductances are inferred, see Berg and Ditlevsen (2013) for more details on the method.

On the other hand, the oversampling method assumes the dynamics of the membrane potential to be free of noise and free of applied and ionic currents. It is based on the model $\dot{V} = g_\alpha(t)V + g_\beta(t)$, where g_α and g_β are called *preconductances* and they depend linearly on the conductances. The differential equations is discretized in such a way that the sampling frequency of the preconductances is half of that of V. Parameters g_α and g_β are computed and used to finally estimate both excitatory and inhibitory conductances. Along the process, two thresholds, κ_α and κ_β, need to be defined to avoid possible singularities, see Bédard et al (2011b) for more details on the method.

The codes of these procedures are published by the authors in a model database, so we use them to do the estimation. For the OU method we use the code from the database Berg (2013). In this method we need to fix the sample window, and after testing different values, we consider the one which provides better results. On the other hand, for the oversampling method, the code can be found in the database Bédard et al (2011a). In
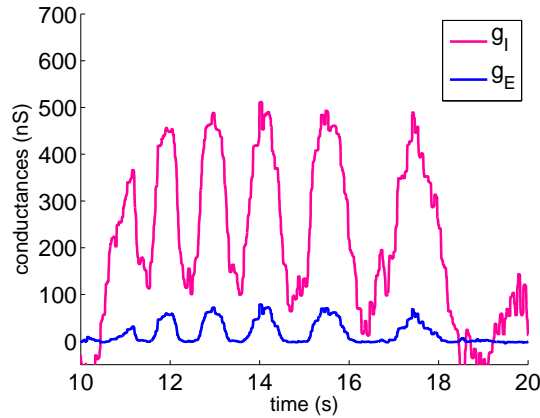
Figure 5.16: **Estimation of conductances for the experimental data**. This figure depicts the excitatory and inhibitory conductances obtained when the estimation procedure has been applied to the membrane potential obtained from *in vivo* experiment. The QIF method has been applied using a sliding window of $l = 50 \ ms$. The magenta line show the estimated inhibitory conductances, the blue line show the estimated excitatory conductances.
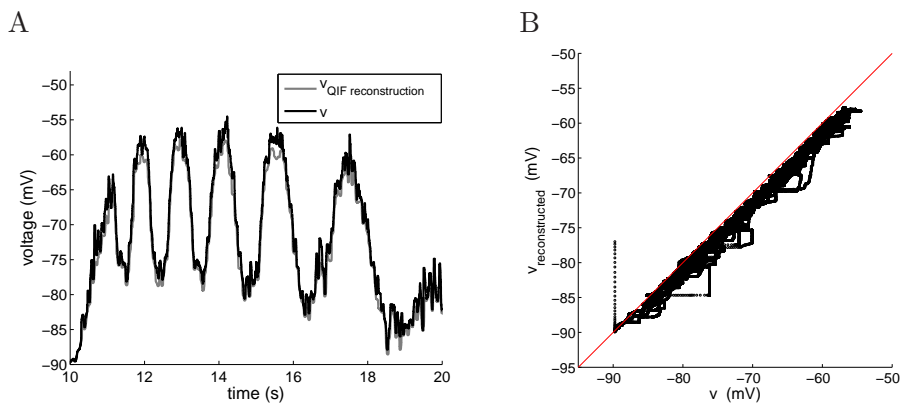

Figure 5.17: **Reconstruction of the *in vivo* membrane potential recordings for the QIF method.** Panel A shows the membrane potential extracted from *in vivo* experiments (black line) and reconstructed membrane potential obtained by using the estimated values of conductance traces and the estimated α parameter (gray line). Panel B shows the scatter plot of the reconstructed versus the true voltage.

this case, authors recommend that the limit values for the singularity points, that is κ_α and κ_β, should be close to 0.1 (see Bédard et al (2011b)). However, after estimating the conductances using different limit values, we have chosen those values which provide better results.

Both methods have been tested using the neuronal model in which each procedure is based, and the prescribed conductances given in 2.2.2.2. In order to test the code of the oversampling method, authors first oversample the membrane potential; that is, each two consecutive times, t_i and t_{i+1}, they split the interval $[t_i, t_{i+1}]$ into 3 subintervals by adding two extra points, $t_{i,1}$ and $t_{i,2}$, between the given ones, where they suppose that the conductance are stationary. Then, they use the prescribed conductance corresponding to t_i to compute the membrane potential at $t_{i,1}$ and $t_{i,2}$. Since for the computational data

we know the actual conductances, we can do the same procedure to corroborate that we use the code correctly.

Comparison with the OU method in computational data. In Figure 5.18 we compare the results obtained with our estimation procedure versus the OU method given in Berg and Ditlevsen (2013), using simulated data from the pyramidal cell model described in Section 2.1.2.1 with external current in 2.2.1. Panels A and B depict the time course
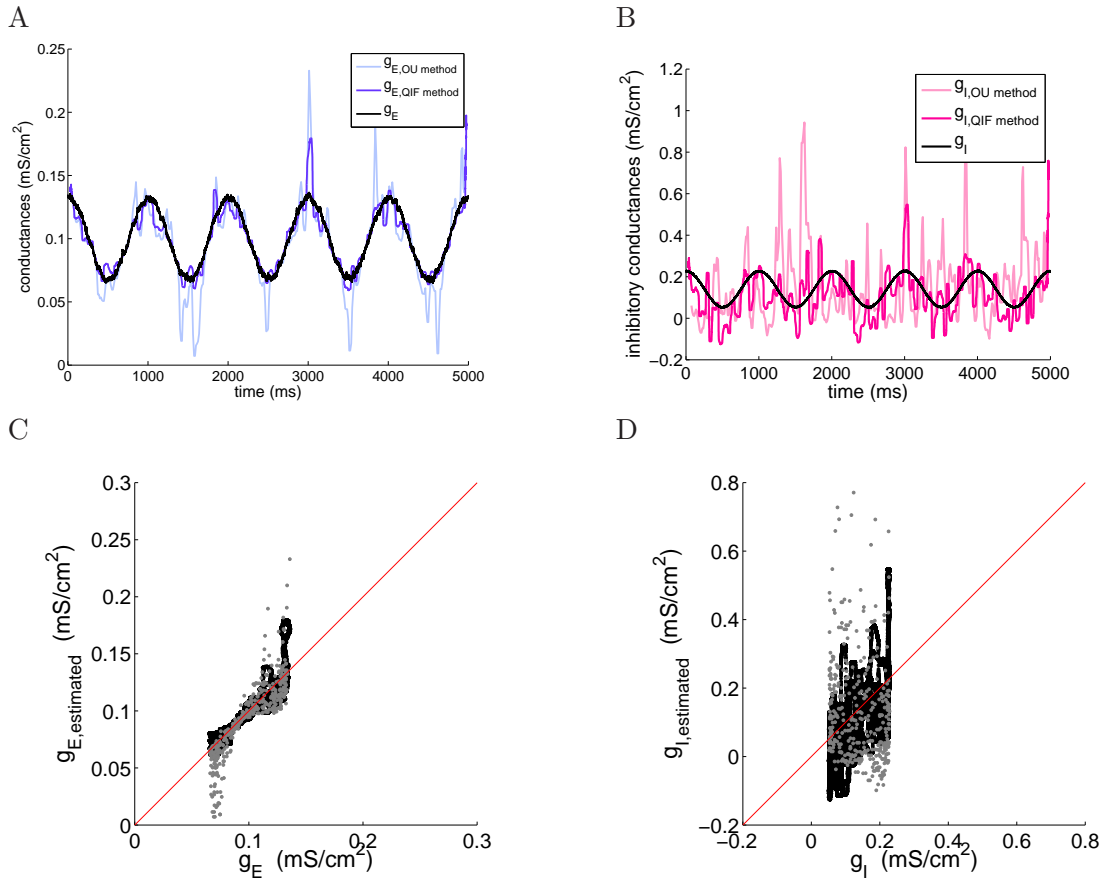

Figure 5.18: **Comparison between single-trial estimation procedures**. panels A and B show the prescribed and the estimated synaptic input generated from equation (2.7). Panel A refers to the excitatory conductance trace while Panel B refers to the inhibitory one. Data are generated by the pyramidal cell model described in Section 2.1.2.1. Panels C and D show the scatter plot of the estimated conductances versus the true ones, where Panel C refers to the excitatory conductances whereas Panel D refers to the inhibitory ones. The sample window considered in both methods is $l = 50\ ms$. The estimated conductances have been filtered, in both cases, by the median filter using a sample window of $50\ ms$.

of the conductances, showing the results of the estimation of the excitatory (panel A) and the inhibitory (panel B) conductances, for both methods. The black lines in both panels show the true values of the conductances (the prescribed synaptic input) whereas the dark coloured lines refer to the results of the QIF method and the light coloured lines represent the results of the OU method.

Panel A revels a slight improvement on the estimation of the excitatory conductances

when they are estimated by the QIF method instead of the OU method. Note that dark coloured line in Panel A seems to be closer to the black one than the light coloured line. However, the improvement obtained with the QIF method is higher when we are referring to the inhibitory conductances, where the OU method estimates the inhibitory conductance worse that the QIF method.

To better appreciate the improvements using the QIF method, we depict in panels C and D the scatter plot of the estimated conductances versus the prescribed ones. The black and grey dots represent the results of the QIF and the OU methods, respectively. Note that, even though a concentration of dots along to the identity line (red line) is observed in both cases, grey dots tend to be more dispersed than the black ones. Consequently, the QIF method is more precise than the OU method. This fact strengthens results obtained in Section 5.1.1, where we have seen that the presence of subthreshold ionic currents can cause misestimations when they are active coming from nonlinearities.

Comparison with the oversampling method in computational data.   In Figure 5.19 we depict the results of the oversampling method, also using simulated data from the pyramidal cell model described in Section 2.1.2.1 with external current in 2.2.1.

When using the oversampling method, two problems may arise. As we said above, the oversampling method is based on a linear method, which does not consider the applied current, besides not considering neither ionic currents nor noise. However, in the pyramidal cell model we consider a constant applied current, which allows us to avoid the neuron from firing. This problem can be solved by modifying, in an appropriate way, the code. However, another problem that might arise in this method is the need to oversample the data. Indeed, in *in vivo* experiments, since we do not know, a priori, which are the conductances, the data can not be forced to be oversampled.

In Figure 5.19 we present the results obtained both when the membrane potential is oversampled (panels A and B) and when it is not (panels C and D). Moreover, the first column (panels A and C) corresponds to the case where the applied current is not considered into the oversampling method whereas the second column (panels B and D) refers to the case where it is. In all cases, the estimated data does not follow the prescribed one, neither for the excitatory nor for the inhibitory conductances. These results imply that, even though we have chosen the best options for κ_α and κ_β, this method is not efficient to estimate conductances in those situations where noise and ionic currents (having influence in the subthreshold) are present (see also results in Section 5.1.1 for the ionic currents effects).

Comparison with both methods in experimental data.   Finally, we apply the three procedures we are comparing (that is the oversampling, the OU and the QIF methods) to estimate the conductances in the experimental data described in Section 2.3. Results are depicted in Figures 5.20 and 5.21.

In Figure 5.20 we plot the OU method (solid coloured lines) together with the QIF method (dashed coloured lines). Panel A shows the estimated excitatory conductances for the different methods, and Panel B shows the inhibitory conductances. The results of the oversampling method are presented in Figure 5.21, apart from the other traces of conductances because of the singularities it presents.

The results of the three different methods obtained in Figures 5.20 and 5.21 for the experimental data are very different. Only the excitatory conductances estimated with the OU
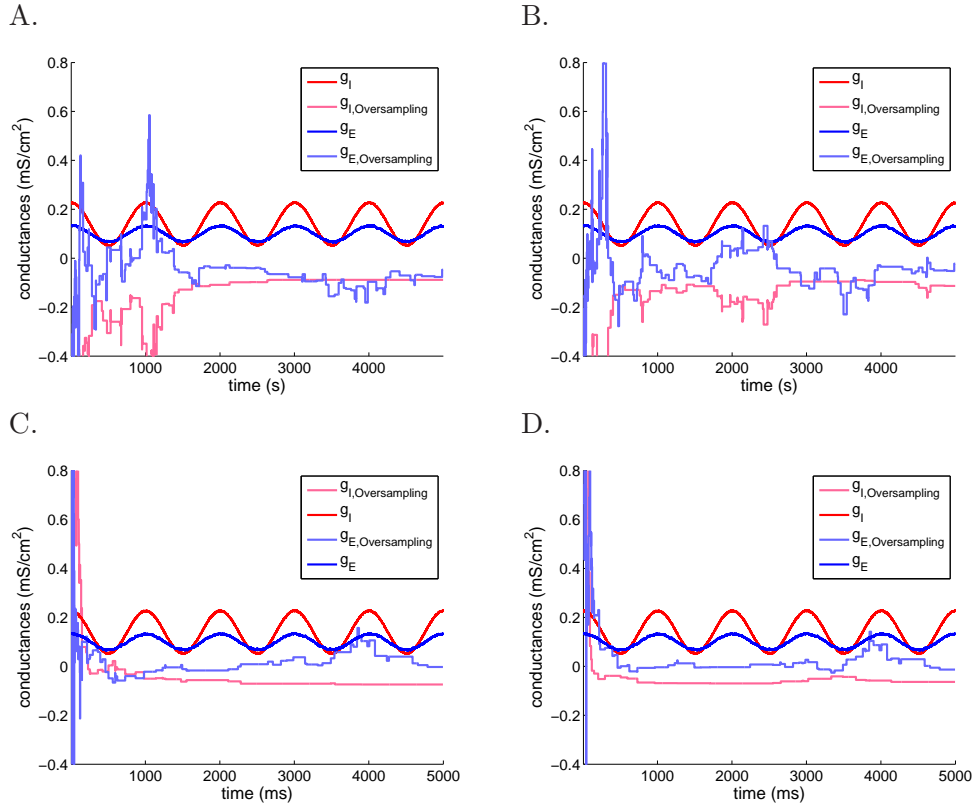
Figure 5.19: **Results of the oversampling method for the Pyramidal cell model**. Each panel shows the prescribed (dark traces) and the estimated (light traces) synaptic input generated from equation (2.7). The excitatory conductance traces correspond to the blue traces while the inhibitory ones correspond to the red traces. Data are generated by the pyramidal cell model described in Section 2.1.2.1 and the estimation of conductances have been done using the oversampling estimation procedure with the optimal values of κ_α and κ_β considered in the singularities removal procedure. In Panel A and B the membrane potential has been oversampled with $\kappa_\alpha = \kappa_\beta = 0.55$ and $\kappa_\alpha = \kappa_\beta = 0.6$, respectively. In Panel B, the data has not been oversampled and $\kappa_\alpha = \kappa_\beta = 0.5$ in both cases.

and our QIF method seem to follow a similar pattern, even though there is a relatively small vertical shift between the two. However, the oversampling method presents a similar pattern than the ones obtained in Bédard et al (2011b), Figure 2, where the results before apply the algorithm to suppress singular points are represented. However, our results are after this suppression. We have tried for different parameters of κ_α and κ_β in order to readjust them but without success. Therefore, it seems that this method is not able to handle this data to give plausible estimations.

Both the oversampling and the OU method assume a linear behaviour of the subthreshold activity. In Section 5.1.1, we have seen that under the presence of nonlinear effects caused by subthreshold ionic currents, these methods can lead to misestimations of the conductances. However, the $V - I$ curve obtained from experimental recordings (see Figure 2.8) is better fitted by a quadratic regression rather than a linear one, which indicates a quadratic behaviour, revealing the existence of such nonlinear subthreshold activity. Then, from these previous observations and because of the results obtained in the comparison of the OU and the QIF methods in the *in silico* case, if we add the fact that the inhibitory conductances trace obtained with the QIF method oscillates (see Figure 5.20.B) as the
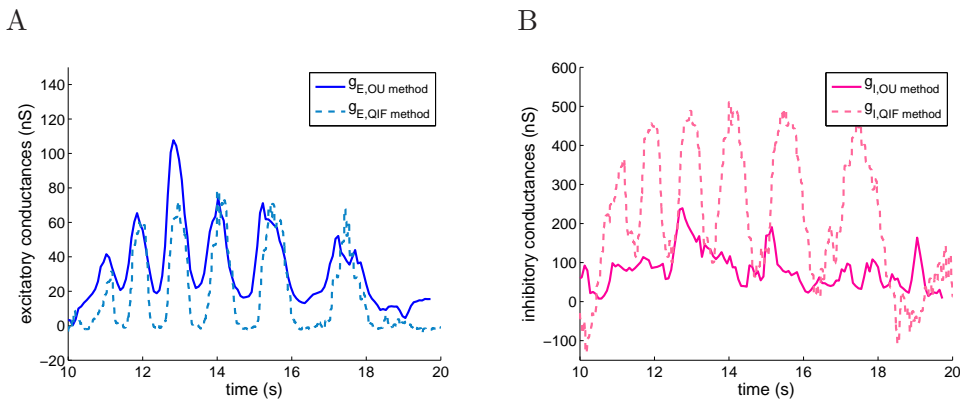
A

B

Figure 5.20: **Estimated conductances in experimental data obtained using the OU and the QIF methods**. This figure depicts the predicted estimated conductances of the experimental *in vivo* data described in Section 2.3, when both the OU (solid lines) and the QIF (dashed lines) methods have been used. For the OU method, the time window is considered to be $l = 300\ ms$. For the QIF method, it is fixed to be $l = 50\ ms$. Panel A depicts the results of the excitatory conductances whereas Panel B depicts the results of the inhibitory conductances.

A

B
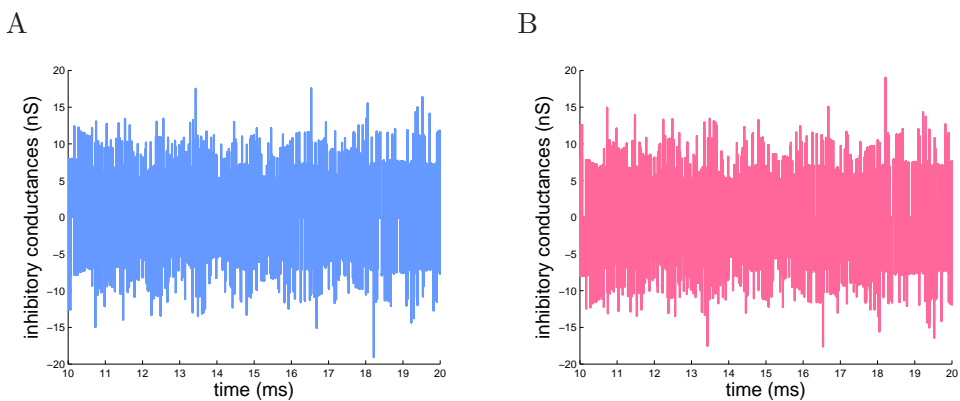
Figure 5.21: **Estimated conductances in experimental data obtained using the oversampling method**. Panel A depicts the result obtained for the excitatory conductances whereas Panel B are those obtained as inhibitory conductances. In the oversampling method, we set $\kappa_\alpha = \kappa_\beta = 0.1$

intracellular recorded membrane potential (see results in 5.1.2.3), we are in conditions to state that the results obtained with the QIF method are closer to the real ones than the others.

5.2 Estimation in the spiking regime

In previous sections, different estimation procedures has been obtained to estimate conductances in the subthreshold regime under the presence of nonlinear ionic currents. In this section we aim at giving a first proof-of-concept to tackle the estimation of the synaptic conductances in the spiking regime.

We tackle the problem by considering the McKean model, which is described in Section 2.1.3.1, with external current given in Section 2.2.1. This system is the simplified piecewise linear model of neuronal activity with regular firing given by

$$\begin{cases} C\dot{V} = f(V) - w - w_0 + I_{total}, \\ \dot{w} = V - \gamma w - V_0, \end{cases} \tag{5.14}$$

where $I_{total} = I - I_{syn}(V)$, $I_{syn}(V) = g_{syn}(V - V_{syn})$ and

$$f(V) = \begin{cases} -V & V < a/2, \\ V - a & a/2 \leq V \leq (1+a)/2, \\ 1 - V & V > (1+a)/2. \end{cases}$$

Notice that, in order to reduce the notation, in this section we denote I to the applied current and I_{total} to the external current.

Since we are interested in the synaptic conductances, in the standard McKean model we pay special attention to the synaptic current $I_{syn}(V)$. At a first instance, the synaptic conductance, g_{syn}, is considered to be constant, a fact that can be understood as the synaptic current $I_{syn}(V)$ being a representation of the mean field of the synaptic inputs. Other special parameter we need to take into account is the capacitance C. Since C is assumed to be small, the variables V and w evolve with very different velocities, and so system (5.14) can be considered a slow-fast dynamical system, where the variable V is the fast one whereas the variable w is the slow one.

As it has been reported in some previous studies, being two examples Abbott (1990) and Tonnelier and Gerstner (2003), system (5.14) presents different neuronal behaviours depending on the total amount of constant current that the neuron is receiving, $I_{total} = I$. In particular, authors show that there exist two boundary values I_1 and I_2 such that, if $I_{total} \leq I_1$, the system presents low activity and the membrane potential tends to a silent state, that is, variable V tends to an equilibrium state with low value. Moreover, when $I_1 < I_{total} < I_2$, the system exhibits a periodic orbit and so the neuron presents an oscillatory behaviour corresponding to a regular firing. Otherwise, if $I_{total} \geq I_2$, the neuron tends to a steady high activity, that is, the variable V tends to an equilibrium state with high value, corresponding to a nerve block. We remark that, in contrast with our model, in all these studies the total current, I_{total}, was considered constant. In this work, I_{total} is considered to have a linear dependence on the membrane potential since $I_{total} = I - I_{syn}(V) = I - g_{syn}(V - V_{syn})$.

Since we are interested in the estimation of conductance g_{syn} in spiking regimes, we will focus in the region of the parameter space where the model presents a unique periodic orbit crossing the two switching manifolds $V = a/2$ and $V = (1+a)/2$. Several approximations of the period T of the periodic orbit, exhibited by different versions of the McKean model, have been recently studied. In Coombes (2008), the period T is computed numerically for different constant inputs I_{total}. In other works, such as Abbott (1990), Coombes (2001), and Tonnelier (2003), the approximation of T has been carried out by considering the singular limit ($C = 0$) of the periodic orbit, consisting of segments of orbits from both subsystems, the slow and the fast one. The approximation is then obtained from the total amount of flight time on the slow manifold. We note that this value coincides with the constant term of the power series expansion in C of the period T. More recently, in Fernández-García et al (2015), the authors provide an approximate expression of the period T by taking advantage of the slow invariant manifolds for $0 < C \ll 1$. In this case, T is approximated by computing the flight time of the periodic orbit in each lateral regime, i.e. in $V < a/2$ and $V > (1+a)/2$, and supposing that the flight time in the central band,

i.e. in $a/2 < V < (1+a)/2$, is negligible. In this section, with the aim of improving the approximations done so far for T, we consider the central regime as non-negligible. We remark that this consideration will also allow us to improve the results obtained in the lateral regimes.

The new approximation of the period function, that we denote by $\hat{T}$, depends on the parameters of the model, and, in particular, on the synaptic conductance g_{syn} and the applied current I, i.e. $\hat{T}(g_{syn}, I)$. As we prove in this section, the dependence of $\hat{T}$ on the synaptic conductance, g_{syn}, is non-linear but turns out be monotonic for the range of input current values for which $\hat{T}$ has sense; that is, for the input currents that drive the neuron to regularly spiking. Hence, as a consequence of the monotonicity, by knowing $\hat{T}$ and the applied current I (i.e. knowing the $f - I$ curve), one would be able to compute g_{syn} by solving numerically a non-linear equation having a unique solution; and so, estimate the steady synaptic conductance of the neuron, which is the goal of this section.

We would like to note that, even though some studies consider the synaptic conductances as a constant input, in real experiments synaptic conductances change along time thus causing non-regular spiking. Indeed, we have a non-autonomous system which may have a very complicated dynamics. If the changes in conductances are relatively slow, then we may assume to be "riding" on a periodic orbit with a constant conductance during a certain time window. This fact suggests that each inter-spike interval (ISI), which corresponds to the time between two consecutive spikes, can be a good approximation of T for a specific constant value $\tilde{g}_{syn}$ provided that $g_{syn}(t)$ has a slow variation. Hence, for each ISI one can estimate a different steady conductance and so, obtain a time course estimation of $\tilde{g}_{syn}$, say $\hat{g}_{syn}(t)$.

The above explained procedure and the results obtained in this section are distributed in the following way. In Subsection 5.2.1, we present the model and revise the main features of its qualitative dynamics, namely the existence and character of equilibrium points, and the conditions on the parameters that ensure the existence of a unique periodic orbit. In Subsection 5.2.2, we present the expression $\hat{T}$ that we obtain as an approximation of the period T, and show that this approximation $\hat{T}$ is a monotonically decreasing function of the synaptic conductance g_{syn}. In Subsection 5.2.3, we deal with the estimation procedure, where we are able to infer, in Subsection 5.2.3.2, a steady synaptic conductance from the cell's oscillatory activity; and, in Subsection 5.2.3.1, we extend the results to a more realistic case, where we present a proof-of-concept to estimate the full time course of the conductances. Details about the numerical integration of the model are given in Section 2.4.4.

5.2.1 Qualitative analysis of the model

Let us consider the modified McKean model given by system (5.14). This system is a non-symmetric continuous piecewise linear system, and it is defined in three different regions, namely $\{(V, w) \in \mathbb{R}^2; V < a/2\}$, $\{(V, w) \in \mathbb{R}^2; \ a/2 \leq V \leq (1+a)/2\}$, and $\{(V, w) \in \mathbb{R}^2; V > (1+a)/2\}$. Observe that system (5.14) is not globally differentiable but piecewise differentiable. Moreover, since parameter C is assumed to be small, system (5.14) is endowed with a slow-fast dynamics, being the membrane potential, V, the fast variable, meanwhile the auxiliary variable, w, is the slow one. Notice that the dynamics of system (5.14) is parametrized by the slow time.

The function $f(V)$ depends piecewise linearly on the parameter V, with three different slopes according to the three different zones defined by the model. This fact causes that

the determinant and the trace of the model vary across the different regions. In the central region, the determinant is given by $d_M = (\gamma(g_{syn} - 1) + 1)/C$ whereas the trace is $t_M = -((g_{syn} - 1)/C + \gamma)$. In the lateral regions, the determinants and traces are $d_L = d_R = (\gamma(1 + g_{syn}) + 1)/C$ and $t_L = t_R = -((1 + g_{syn})/C + \gamma)$, respectively, where the subscript L stands for the left region and R for the right one. As a consequence, different equilibrium points can coexist on the model and they are located in different regions. These facts depend on the value of the external input I and the synaptic conductance g_{syn}, as it is illustrated in Figure 5.22, where I_1 and I_2 are defined as

$$
\begin{aligned}
I_1 &= \left(\frac{a}{2} - V_{syn}\right) g_{syn} + \frac{(\gamma + 1)a - 2v_0 + 2\gamma w_0}{2\gamma}, \\
I_2 &= \left(\frac{a+1}{2} - V_{syn}\right) g_{syn} + \frac{(\gamma + 1)a - 2v_0 + 2\gamma w_0 - \gamma + 1}{2\gamma}.
\end{aligned}
\tag{5.15}
$$

In fact, $I_j \equiv I_j(g_{syn}; V_{syn}, \gamma, a, v_0, w_0)$, $j = 1, 2$, but we will omit these dependencies to simplify the notation. We note that when $g_{syn} < 1 - 1/\gamma$, lines $I = I_1$ and $I = I_2$ corresponds to a subcritical saddle-node-like bifurcations, where two equilibrium points merge in one and disappears after they collide.
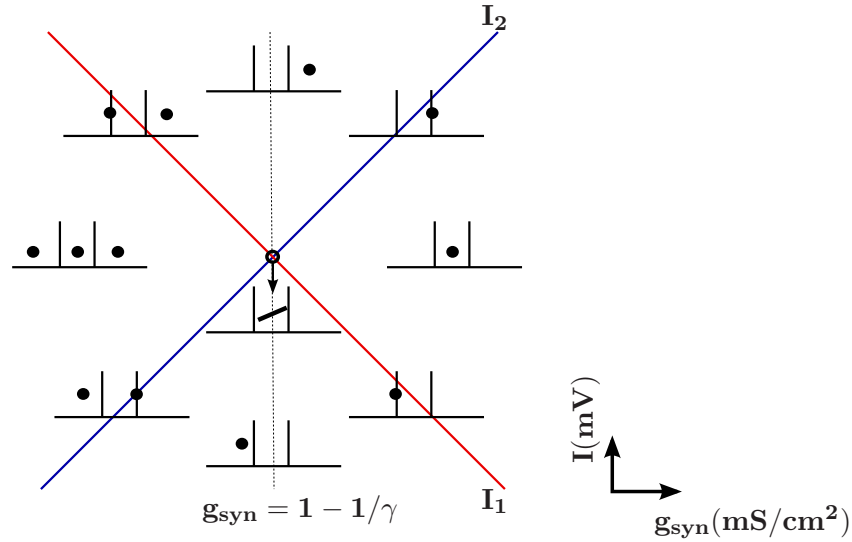

Figure 5.22: **Location of the equilibrium points**. According to expressions in (5.15), the solid blue line represents $I = I_2$ whereas the solid red line represents $I = I_1$. The dotted line is $g_{syn} = 1 - 1/\gamma$. Each box on the figure represents the three different regions of system (5.14) (left, central and right) separated by vertical segments. The dots are depicted on the box corresponding to the region where the equilibrium point exists. On the intercept of $I = I_1$ and $I = I_2$, the line in the central part of the corresponding box indicates that there exists a full segment of equilibrium points in such region, which corresponds to the central piece of the V-nullcline. The different locations and configurations of critical points follow from Proposition 5.1 and from the arguments used in its proof.

In the next proposition, we show necessary and sufficient conditions to ensure existence and uniqueness of an equilibrium point of system (5.14) located in the central region or on either of the two switching manifolds. We point out that, from the arguments used in the proof of this proposition, the rest of possible locations and configurations of critical points given in Figure 5.22 follows.

Proposition 5.1. *Let us consider system (5.14) satisfying that $g_{syn} > 1 - 1/\gamma$. Then, this system has a unique equilibrium point and it is located*

a) in the interior of the central region, if and only if $I_1 < I < I_2$;

  b) *on the switching manifold $V = a/2$, if and only if $I = I_1$;*

  c) *on the switching manifold $V = (1 + a)/2$, if and only if $I = I_2$.*

Proof. The equilibrium points of system (5.14) are given by the solutions of

$$- f(v) + (g_{syn} + \frac{1}{\gamma})V = \frac{v_0}{\gamma} - w_0 + g_{syn}V_{syn} + I \quad \text{and} \quad w = \frac{V - v_0}{\gamma} \tag{5.16}$$

where $f(V)$ takes its expression according to the corresponding region. Therefore, we proceed by considering each of the regions separately.

Let us first consider the left region. Since $f(V) = -V$, $g_{syn} \geq 0$ and $\gamma > 0$, the unique solution of system (5.16) is given by the point $\mathbf{p}_L = (V_L, w_L)$, where

$$V_L = \frac{\gamma(I - w_0 + g_{syn}V_{sys}) + v_0}{1 + \gamma(1 + g_{syn})} \quad \text{and} \quad w_L = \frac{I - w_0 + g_{syn}(V_{syn} - v_0) - v_0}{1 + \gamma(1 + g_{syn})}.$$

Therefore, by imposing that $V_L < a/2$, it follows that $\mathbf{p}_L$ is an equilibrium point in this region if and only if $I < I_1$

In the central region, where $f(V) = V - a$, the unique solution of system (5.16) is the point $\mathbf{p}_M = (V_M, w_M)$ given by

$$V_M = \frac{\gamma(I - w_0 + g_{syn}V_{syn} - a) + v_0}{1 - \gamma(1 - g_{syn})} \quad \text{and} \quad w_M = \frac{I - w_0 + g_{syn}(V_{syn} - v_0) + v_0 - a}{1 - \gamma(1 - g_{syn})}.$$

Hence, by forcing V_M to lie in the interval $(a/2, (a + 1)/2)$, it follows that $\mathbf{p}_M$ is an equilibrium point if and only if either of the pair of inequalities

$$g_{syn} > 1 - \frac{1}{\gamma} \quad \text{and} \quad I_1 \leq I \leq I_2; \quad \text{or} \quad g_{syn} < 1 - \frac{1}{\gamma} \quad \text{and} \quad I_2 \leq I \leq I_1,$$

are held. However, notice that the first component of the equilibrium point is exactly $V = a/2$ when $I = I_1$, and so the equilibrium point is located on the left switching manifold. Similarly, when $I = I_2$, the equilibrium point is located on the right switching manifold. Otherwise, i.e. when $I_1 < I < I_2$, the equilibrium point stays inside the central region.

We remark that in the case where $g_{syn} = 1 - 1/\gamma$, if $I = I_1 = I_2$ all points along the central part of the V-nullcline are equilibrium points. This fact is caused by the slopes of V and w nullclines being the same.

Finally, in the right region, i.e. when $f(V) = 1 - V$; the unique solution of system (5.16) is the point $\mathbf{p}_R = (V_R, w_R)$ given by

$$V_R = \frac{\gamma(I - w_0 + g_{syn}V_{syn} + 1) + v_0}{1 + \gamma(1 + g_{syn})} \quad \text{and} \quad w_R = \frac{I - w_0 + g_{syn}(V_{syn} - v_0) - v_0 + 1}{1 + \gamma(1 + g_{syn})}.$$

Since $g_{syn} \geq 0$ and $\gamma > 0$, by imposing that $V > (1 + a)/2$, an equilibrium point in this region exists if and only if $I > I_2$.

To sum up, if $0 < g_{syn} < 1 - 1/\gamma$, when $I < I_2$ or $I > I_1$ only an equilibrium point exists on the left and right regions, respectively. However, if $I_2 < I < I_1$, three equilibrium points coexist, one in each region. If $g_{syn} > 1 - 1/\gamma$, only one equilibrium point exists located in either the left, central or right region when $I < I_1$, $I_1 < I < I_2$ or $I > I_2$,

respectively. Otherwise, if $g_{syn} = 1 - 1/\gamma$ and $I = I_1 = I_2$, infinite equilibrium points coexist in the central region. A representation of these results are shown in Figure 5.22.

Hence, we only have an equilibrium point located in the central region when both conditions $g_{syn} > 1 - 1/\gamma$ and $I_1 < I < I_2$ hold, proving the proposition.   □

Remark 5.1. *By Proposition 5.1, when $g_{syn} > 1 - 1/\gamma$ and $I_1 < I < I_2$ system (5.14) has only one equilibrium point which lies in the central region. Let us call such point as $\mathbf{p}_M = (p_{V,M}, p_{w,M})$. When each linear system which is part of the vector field is considered to be defined on the full plane, thus two more zeros appear: one from the system described in the left zone, $\mathbf{p}_L = (p_{V,L}, p_{w,L})$, and another from the system in the right zone, $\mathbf{p}_R = (p_{V,R}, p_{w,R})$. Under these assumptions, these two points are located in the central region and, even thinking that they have influence on the global dynamics, they are not equilibrium points of system (5.14). These points are called virtual equilibrium points. Finally, note that when $I = I_1$ or $I = I_2$, $\mathbf{p}_M$ coincides with $\mathbf{p}_L$ or $\mathbf{p}_R$, respectively.*

The behaviour of the model is also governed by the eigenvalues associated to the system, which vary across the three different zones (left, central and right). In each region, there exist two different eigenvalues: one of $O(C)$, which is the responsible for the slow dynamics; and another one of $O(1)$, which is the responsible for the fast dynamics. These eigenvalues are given by

$$
\begin{aligned}
\lambda_{s,L} = \lambda_{s,R} &= -\frac{1}{2C}\left(1 + g_{syn} + C\gamma - \sqrt{(1 + g_{syn} - C\gamma)^2 - 4C}\right) \\
\lambda_{q,L} = \lambda_{q,R} &= -\frac{1}{2C}\left(1 + g_{syn} + C\gamma + \sqrt{(1 + g_{syn} - C\gamma)^2 - 4C}\right) \\
\lambda_{s,M} &= \frac{1}{2C}\left(1 - g_{syn} - C\gamma - \sqrt{(g_{syn} - 1 - C\gamma)^2 - 4C}\right) \\
\lambda_{q,M} &= \frac{1}{2C}\left(1 - g_{syn} - C\gamma + \sqrt{(g_{syn} - 1 - C\gamma)^2 - 4C}\right)
\end{aligned}
$$

where the subscripts L, R and M stand for the eigenvalues in the left, right, and central regimes, respectively; and the subscripts s and q denote the small and the big eigenvalue, respectively. These eigenvalues correspond to either focus or node equilibrium points, depending on the values of the parameters g_{syn}, γ and C. However, for sufficiently small values of C, one can guarantee that all equilibrium points are nodes since all the discriminants are positive when $C = 0$. In fact, all the equilibrium points are nodes if and only if $C \leq C^*$ where

$$
C^* = \min\left\{\frac{2 + \gamma(g_{syn} + 1) - 2\sqrt{1 + \gamma(g_{syn} + 1)}}{\gamma^2}, \frac{2 + \gamma(g_{syn} - 1) - 2\sqrt{1 + \gamma(g_{syn} - 1)}}{\gamma^2}\right\}.
$$

In this case, we call $\mathbf{v}_{ij} = (\lambda_{ij} + \gamma, 1)$ to the eigenvector associated to the eigenvalue λ_{ij}, where $i \in \{s, q\}$ and $j \in \{L, R, M\}$. Notice that the slow manifold of system (5.14) is piecewise defined, since it depends on the direction of the different eigenvectors. We refer each piece of the slow manifold as S_j where $j \in \{L, R, M\}$.

Since the piecewise differential system (5.14) is locally linear, it can be analytically solved at each region separately, being the local solutions

$$
\begin{cases}
V(t) = (\lambda_{s,i} + \gamma)K_{1,i}e^{\lambda_{s,i}t} + (\lambda_{q,i} + \gamma)K_{2,i}e^{\lambda_{q,i}t} + p_{V,i}, \\
w(t) = K_{1,i}e^{\lambda_{s,i}t} + K_{2,i}e^{\lambda_{q,i}t} + p_{w,i},
\end{cases}
\tag{5.17}
$$

where i represents either L, M or R depending on the region being left, central or right, respectively; and

$$
K_{1,i} = \frac{V(0) - p_{V,i} - (\lambda_{q,i} + \gamma)(w(0) - p_{w,i})}{\lambda_{s,i} - \lambda_{q,i}}, \qquad K_{2,i} = w(0) - K_{1,i} - p_{w,i}.
$$

Notice that equation (5.17) only represents a local expression of the solution of system (5.14). As long as the orbit, given by a fixed initial condition, remains in one region, this orbit is given by the expression of the solution of the system obtained in this particular region; however, if the orbit crosses to another region, the orbit is given by the corresponding expression obtained in this new region, which depends on the different eigenvalues and the initial conditions. Since the vector field defined by system (5.14) is globally non-linear, depending on the character of the equilibrium points and the eigenvalues, system (5.14) may exhibit limit cycles. In next proposition we give a sufficient condition so that system (5.14) can have a unique periodic orbit.

Proposition 5.2. *Consider the following assumptions*

$$g_{syn} > 1 - 1/\gamma, \ I_1 < I < I_2, \ |g_{syn} + C\gamma| < 1 \ and \ 0 < C \leq C^*.$$

Then:

a) *if $I_1 < I < I_2$, system (5.14) exhibits a unique limit cycle, this orbit crosses the two switching manifolds $V = a/2$ and $V = (a+1)/2$, and it is stable;*

b) *if $I = I_1$ or $I = I_2$, system (5.14) exhibits a homoclinic orbit to the equilibrium point $\mathbf{p}_M$, this orbit is stable from the exterior and delimits an open region which is foliated by homoclinic orbits to $\mathbf{p}_M$.*

Proof. Let us consider system (5.14) written in its Liénard form. To do that, we make the two different changes of variables. First, we switch to (V, u) through $w = C(u + \gamma V)$ and, second, we introduce (x, y) where $x = 4v - 2a - 1$ and $Cy = 4Cu + C\gamma(2a + 1) - 4I + 2a - 1$ (see Section 2 in Llibre et al (2013)). Then, moving the origin to the point $(0, ((2a + 1 - yV_{syn})g_{syn} + 4w_0)/C)$, the Liénard form of system (5.14) is given by

$$\begin{cases} \dot{x} = F(x) - y \\ \dot{y} = G(x) - \delta \end{cases}$$

where $\delta = -\frac{1}{C} \left(2a \left(\gamma + \gamma g_{syn} + 1 \right) - \gamma + \gamma g_{syn} + 1 - 4v_0 + 4\gamma \left(w_0 - I - g_{syn}V_{syn} \right) \right)$,

$$F(x) = \begin{cases} t_L(x + 1) - t_M & x < -1, \\ t_M x & -1 \leq x \leq 1, \\ t_R(x - 1) + t_M & x > 1, \end{cases} \quad \text{and} \quad G(x) = \begin{cases} d_L(x + 1) - d_M & x < -1, \\ d_M x & -1 \leq x \leq 1, \\ d_R(x - 1) + d_M & x > 1. \end{cases}$$

By Proposition 5.1, since $g_{syn} > 1 - 1/\gamma$ and $I_1 < I < I_2$, only one equilibrium point exists and it is located in the interior of the central region. Moreover, since $g_{syn} > 1 - 1/\gamma$ and $|g_{syn} + C\gamma| < 1$, the parameters of the functions $F(x)$ and $G(x)$ satisfy that $d_M > 0$, $-d_M < \delta < d_M$, $d_L, d_R \geq 0$, $t_L, t_R < 0$, and $t_M > 0$. Hence, the existence and uniqueness of a periodic orbit surrounding the equilibrium point is guaranteed by Theorem 1 in Llibre et al (2013), see also Theorem 1.2.

Finally, since $0 < C \leq C^*$ and $t_M > 0$, the equilibrium point is a repelling node. Consequently, the invariant lines defined by the eigenvectors force the periodic orbit to cross the three regions, which ends the proof of the statement (a).

In order to prove the statement (b), let us consider the case where $I = I_1$. Then, let $\mathbf{q}_L = (V_L, w_L)$ and $\mathbf{q}_R = (V_R, w_R)$ be the intersection points of the left and right pieces of the slow manifold with the vertical lines $V = a/2$ and $V = (1 + a)/2$, respectively; and let $\mathbf{q}_R^{**} = (V_R^{**}, w_R^{**})$ be the intersection point of the w-nullcline with the vertical line $V = (1 + a)/2$, see Figure 5.23.

In this case, the equilibrium point, $\mathbf{p}_M$ (that exists and it is unique from Proposition 5.1), coincides with the virtual equilibrium point $\mathbf{p}_L$ of the left region. Since it is contained in the intersection of S_L and S_M, which are respectively stable and unstable manifolds, the equilibrium point is a saddle node and $\mathbf{q}_L = \mathbf{p}_L$. Moreover, taking into account that $I = I_1$, it follows that

$$\mathbf{q}_L = \left(\frac{a}{2}, \frac{a - 2v_0}{2\gamma} \right), \quad \mathbf{q}_R = \left(\frac{1+a}{2}, p_{w,R} + \frac{1}{\lambda_{s,R} + \gamma} \left(\frac{1+a}{2} - p_{V,R} \right) \right), \text{ and}$$

$$\mathbf{q}_R^{**} = \left(\frac{1+a}{2}, \frac{1+a-2v_0}{2\gamma} \right).$$

Consider now the closed region delimited by the union of the line segments L_i, $i = 1 \ldots 5$, defined as follows:

i) L_1 denotes the line segment bounded by $\mathbf{q}_L$ and the intersection point of S_R with the line $w = w_L$, which we denote by $\mathbf{q}_{1,R}^*$;

ii) L_2 denotes the segment of S_R that is bounded by $\mathbf{q}_{1,R}^*$ and $\mathbf{q}_R$;

iii) L_3 denotes the vertical line segment bounded by $\mathbf{q}_R$ and $\mathbf{q}_R^{**}$;

iv) L_4 denotes the line segment bounded by $\mathbf{q}_R^{**}$ and the intersection point of S_L with the line $w = w_R^{**}$, which we denote by $\mathbf{q}_{1,L}^*$; and, finally,

v) L_5 denotes the segment of S_L that is bounded by $\mathbf{q}_{1,L}^*$ and $\mathbf{q}_L$.

Looking at the direction of the flow, one can see that the w-component of the flow in L_1 is given by $\dot{w} = V - a/2$, which is positive in the line segment under consideration, and so the flow positively crosses L_1. Similarly, the w-component of the flow on L_4 is given by $\dot{w} = V - (1+a)/2$, which is negative in the line segment under consideration, and so the flow positively crosses L_4. On another hand, segments L_2 and L_5 are contained in the pieces S_R and S_L of the slow manifold, respectively; this fact implies that both line segments are invariant under the flow. Finally, notice that the flow positively crosses the line $V = (1+a)/2$ if and only if $\dot{V} > 0$, and so

$$w|_{V=(1+a)/2} > 1 - \frac{1+a}{2} - w_0 + I - g_{syn} \left(\frac{1+a}{2} - V_{syn} \right).$$

Straightforward calculations show that, for a sufficiently small C, both w_R and w_R^{**} are greater that $w|_{V=(1+a)/2}$, and so the flow crosses the line segment L_3 positively, showing that the closed region obtained by these five segments is invariant under the flow of system (5.14); see Figure 5.23 (left) for a representation of both the invariant region and the direction of the flow. Therefore, by Poincaré-Bendixson Theorem (see for instance Perko (1982)) there exists a continuum of homoclinic orbits from the equilibrium point to itself, being the biggest homoclinic orbit stable.

Similar arguments can be applied to prove the result when $I = I_2$, where in this case $\mathbf{q}_R = \mathbf{p}_R$. In Figure 5.23 (right), we depict a representation of the invariant region and the directions of the flow in this case.
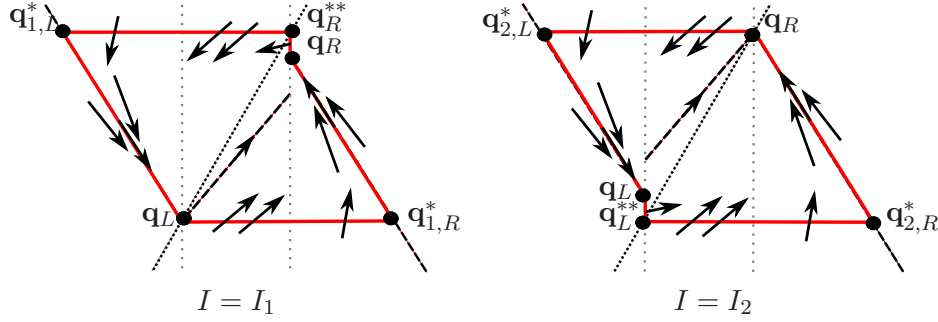
$\square$

Figure 5.23: **Invariant region and direction of the flow**. Representation of the invariant regions and the direction of the flow when $I = I_1$ (left) and $I = I_2$ (right). The dashed black lines represent the slow manifold whereas the dotted black line is the w-nullcline. Vertical dotted grey lines represent the two switching manifolds, $V = a/2$ (left line in each subplot) and $V = (1 + a)/2$ (right line in each subplot). The solid red line represents the boundary of each invariant region and the arrows give us information about the direction of the flow. See Proposition 5.2(b) for more details.

Corollary 5.1. *Under the suitable conditions*

$$g_{syn} > 1 - \gamma^{-1}, \qquad |g_{syn} + C\gamma| < 1, \quad \text{and} \quad 0 < C \leq C^*, \tag{H}$$

where C^* is a constant value, the previous three different neural behaviours persist (low-voltage steady state, regular firing and high-voltage steady-state).

In Figure 5.24, we represent the different phase portraits that we obtain when we change the value of the capacitance (when $C = 0$ and $0 < C \leq C^*$) and also the value of the applied current (when $I = I_1$, $I_1 < I < I_2$, and $I = I_2$). Notice that these configurations are obtained from Proposition 5.2.

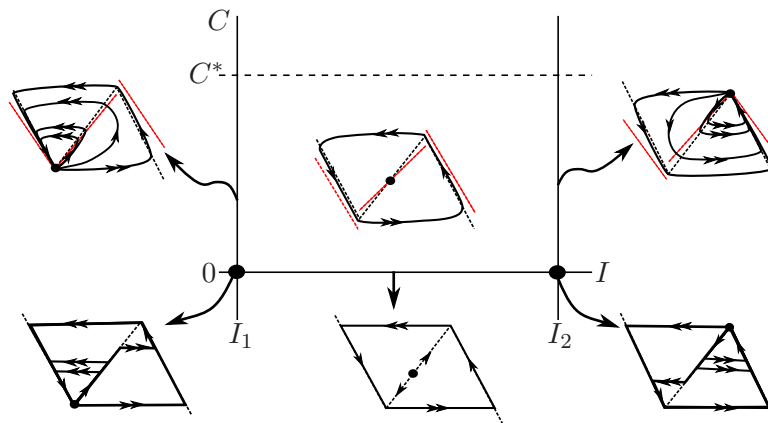Figure 5.24: **Bifurcation diagram**. Representation of the bifurcation diagram with the phase portraits of the periodic orbits for different values of C and I under conditions $g_{syn} > 1 - 1/\gamma$ and $|g_{syn} + C\gamma| < 1$. The phase portraits are obtained with the following parameter values: $a = 0.25$, $v_0 = 0$, $\gamma = 0.5$, $g_{syn} = 0.2$, $w_0 = 0$, and $V_{syn} = 1/4 + a/2$.

5.2.2   An approximation of the period of the periodic orbit

As we have mentioned in the Introduction, related works such as Tonnelier (2003) and Fernández-García et al (2015), among others, make approximations of the period T of a periodic orbit in a piecewise linear systems. In this section, we present a way to improve the approximations of T done so far and so an expression of it in our particular case (that is, $I_{syn}(V) \not\equiv 0$). This improvement is basically obtained by considering the flight time on the central region and using a better approximation of the flight time in the lateral regions.

From now on, let us assume that the hypothesis of Lemma 5.1 is satisfied and that $I_1 < I < I_2$. Hence, by Proposition 5.2(a), the considered model given by system (5.14) has a unique periodic orbit that intercepts the three different regions; and so, the period of the periodic orbit can be split into four parts: the first one (T_L) corresponds to the time that the orbit is contained in the left region; the second part ($T_{M,down}$) is the time taken by the orbit to cross the central zone from left to right following a counterclockwise movement; the third (T_R) is the sub-period that the orbit lies in the right region; and, finally, the last part ($T_{M,up}$) corresponds to the time taken by the orbit to cross the central part from right to left. The total period is then the sum of these four sub-periods and is analytically given in the following proposition.

Proposition 5.3. *Given system* (5.14) *under hypothesis of Lemma 5.1,*

a) *If $C = 0$, the period of the unique periodic orbit of the system is $T_0 = T_{0,L} + T_{0,R}$ such that*

$$T_{0,L} = B_0 \ \ln\left(\frac{\gamma(I - I_1)}{\gamma(I - I_1) + K_0}\right), \quad \text{and} \quad T_{0,R} = B_0 \ \ln\left(\frac{\gamma(I - I_2)}{\gamma(I - I_2) - K_0}\right)$$

where

$$B_0 = -\frac{1 + g_{syn}}{(1 + \gamma + \gamma g_{syn})} \ ; \qquad K_0 = \frac{(1 - g_{syn})(1 + \gamma + \gamma g_{syn})}{2(1 + g_{syn})}$$

b) *For a sufficiently small $C > 0$, the period of the unique periodic orbit of the system can be analytically approximated by*

$$\hat{T} = \frac{1}{\lambda_{s,L}} \ln\left(\left|\frac{\gamma(I - I_1)B_l}{\gamma(I - I_1)B_l - K_l}\right|\right) + \frac{1}{\lambda_{q,M}} \ln\left(\left|\frac{\gamma(I - I_2)B_m + K_m}{\gamma(I - I_2)B_m + K_{m,d}}\right|\right) +$$

$$\frac{1}{\lambda_{s,L}} \ln\left(\left|\frac{\gamma(I - I_2)B_l}{\gamma(I - I_2)B_l + K_l}\right|\right) + \frac{1}{\lambda_{q,M}} \ln\left(\left|\frac{\gamma(I - I_1)B_m + K_m}{\gamma(I - I_1)B_m + K_{m,u}}\right|\right),$$

where

$$B_l = \lambda_{q,L} - \lambda_{s,L},$$

$$B_m = (\gamma + \lambda_{q,M}) \left((g_{syn}\gamma + 1)(\lambda_{s,L} - \lambda_{s,M}) - \gamma(\lambda_{s,L} + \lambda_{s,M}) - 2\lambda_{s,L}\lambda_{s,M} \right),$$

$$K_l = \tfrac{1}{2}(\gamma + \lambda_{q,L})(g_{syn}\gamma + \gamma + 2\lambda_{s,L} + 1).$$

$$K_m = \tfrac{1}{2}(\gamma + \lambda_{s,M})(g_{syn}\gamma - \gamma + 1) \\ \left((g_{syn}\gamma + 1)(\lambda_{s,L} - \lambda_{q,M}) - \gamma(\lambda_{s,L} + \lambda_{q,M}) - 2\lambda_{s,L}\lambda_{q,M} \right),$$

$$K_{m,d} = \tfrac{1}{2}(\lambda_{q,M} - \lambda_{s,M}) \\ (\gamma + \lambda_{q,M})(g_{syn}\gamma - \gamma + 1)(g_{syn}\gamma + \gamma + 2\lambda_{s,L} + 1),$$

$$K_{m,u} = \tfrac{1}{2}(\gamma + \lambda_{q,M})(g_{syn}\gamma - \gamma + 1) \\ \left((g_{syn}\gamma + 1)(\lambda_{s,L} - \lambda_{s,M}) - \gamma(\lambda_{s,L} + \lambda_{s,M}) - 2\lambda_{s,L}\lambda_{s,M} \right),$$

Proof. Let us consider first the singular case when $C = 0$. Given the infinite velocity of system (5.14) in the central region, the central sub-periods can be taken as 0 so that the periodic orbit spends the whole period on the lateral slow manifolds. Then, the lateral sub-periods determine the period of the periodic orbit.

Since the left term of the first equation of system (5.14) is 0, V can be isolated and replaced in the second equation of system (5.14) obtaining the following non-autonomous linear ordinary differential equations

$$\begin{aligned} \dot{w} &= -(1+\gamma)w - w_0 - v_0 + I - I_{syn} && \text{if } v < a/2; \\ \dot{w} &= -(1+\gamma)w - w_0 - v_0 + I - I_{syn} + 1 && \text{if } v > (1+a)/2. \end{aligned} \tag{5.18}$$

Hence, from this system, the period orbit can be analytically solved by integrating the $\dot{w}$ equation at each lateral region separately. From the first differential equation in (5.18), which corresponds to the left region, integrating from $t = 0$ to $t = T_{0,L}$ we calculate the left sub-period $T_{0,L}$; and, from the second differential equation, which corresponds to the right region, integrating from $t = 0$ to $t = T_{0,R}$, we calculate the right sub-period $T_{0,R}$. Then, we obtain that

$$T_{0,L} = B_0 \, \ln\left(\frac{\gamma(I - I_1)}{\gamma(I - I_1) + K_0} \right), \quad \text{and} \quad T_{0,R} = B_0 \, \ln\left(\frac{\gamma(I - I_2)}{\gamma(I - I_2) - K_0} \right)$$

where

$$B_0 = \frac{1 + g_{syn}}{-(1 + \gamma + \gamma g_{syn})} \, ; \qquad K_0 = \frac{(1 - g_{syn})(1 + \gamma + \gamma g_{syn})}{2(1 + g_{syn})}.$$

Hence, the exact period when $C = 0$ is given by $T_0 = T_{0,L} + T_{0_R}$ which proves statement (a).

Consider now the perturbed case when $C > 0$. As we can see in Figure 5.24, in this situation the periodic orbit moves close to the lateral slow manifolds but does not lie on them. Therefore, techniques different from the ones used when $C = 0$ are required to find an approximated period. Since the period can be split into four parts, we need to approximate these four sub-periods separately. To simplify the notation, we denote the four approximations of the sub-periods as the actual ones, that is, T_L, $T_{M,down}$, T_R, and $T_{M,up}$.

Let us first approximate the central sub-periods. For this purpose, let $\mathbf{q}_L$ and $\mathbf{q}_R$ be again the intersection points of the left and right pieces of the slow manifold with the vertical

lines $V = a/2$ and $V = (1+a)/2$, respectively; and let $\mathbf{q}_{M,L}$ and $\mathbf{q}_{M,R}$ be the intersection points of the central slow manifold with $V = a/2$ and $V = (1+a)/2$, respectively (see Figure 5.25 for a representation of these points).
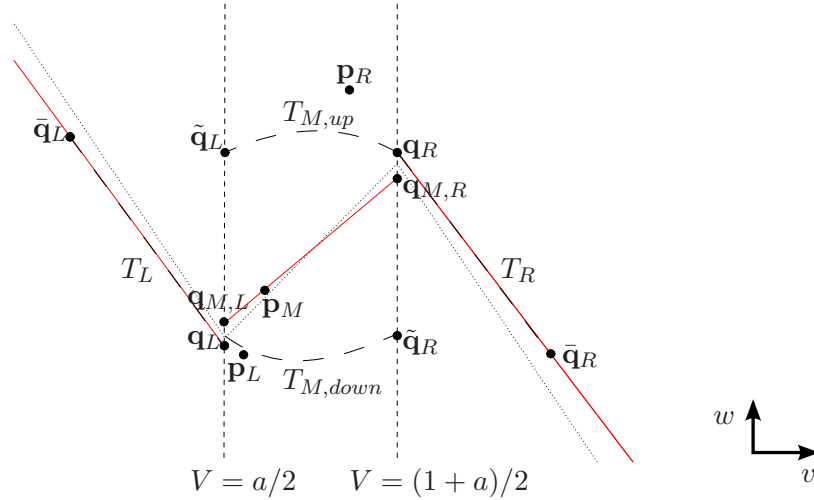

Figure 5.25: **Key points when $\mathbf{C} > \mathbf{0}$**. Representation of all the elements needed to find the expression of the period. The vertical dashed black lines represent the boundaries of the different regions and the rest of dashed black lines illustrate T_L, $T_{M,down}$, T_R and $T_{M,up}$. The dotted lines represent the slow manifold when $C = 0$ whereas the red lines represent the slow manifold when $C > 0$. See the proof of Proposition 5.3 for more details.

Since system (5.14) is a slow-fast piecewise linear system, the distance between $\mathbf{q}_L$ and $\mathbf{q}_{M,L}$ is of $O(C)$; and, the distance between $\mathbf{q}_R$ and $\mathbf{q}_{M,R}$ is also of $O(C)$ (see Fenichel (1979) and Jones (1995)). In fact, the periodic orbit follows the left slow manifold very close to it and crosses from the left region to the central one at some point between $\mathbf{q}_L$ and $\mathbf{q}_{M,L}$, exponentially close to $\mathbf{q}_L$. Similarly, the orbit moves very close to the right slow manifold and crosses from the right region to the central one at some point between $\mathbf{q}_R$ and $\mathbf{q}_{M,R}$, also exponentially close to $\mathbf{q}_R$ (see Figure 5.24). Hence, since C is close to 0, one can assume that the integral curve through $\mathbf{q}_L$, which is contained in the central region, will remain in a neighbourhood of the periodic orbit, and similarly for the integral curve through $\mathbf{q}_R$. Therefore, we consider $\mathbf{q}_L$ and $\mathbf{q}_R$ as an approximation of two points where the periodic orbit passes through.

Then, consider the central solution of the system, which is given in equation (5.17) when $i = M$, with $\mathbf{q}_L$ and $\mathbf{q}_R$ as initial conditions. In view of the fact that the eigenvalue $\lambda_{s,M}$ is approximately 0 for a sufficiently small C (since it is of order $O(C)$), one can suppose that $\lambda_{s,M} = 0$ and, consequently, find an expression of the sub-periods $T_{M,down}$ and $T_{M,up}$. Indeed, under the previous assumptions on the initial conditions, the sub-period $T_{M,down}$ corresponds to the piece of orbit that begins at $\mathbf{q}_L$ and ends on the boundary $v = (1+a)/2$; we call this point $\tilde{\mathbf{q}}_R$. By imposing that $V(t) = (1+a)/2$ and $\lambda_{s,i} = 0$ in the first expression of system (5.17) when $i = M$, the sub-period $T_{M,down}$ is the result of isolating the time t. That is,

$$T_{M,down} = \frac{1}{\lambda_{q,M}} \ln \left(\left| \frac{\gamma(I - I_2)B_m + K_m}{\gamma(I - I_2)B_m + K_{m,d}} \right| \right),$$

where

$B_m = (\gamma + \lambda_{q,M}) \left((g_{syn}\gamma + 1)(\lambda_{s,L} - \lambda_{s,M}) - \gamma(\lambda_{s,L} + \lambda_{s,M}) - 2\lambda_{s,L}\lambda_{s,M} \right),$
$K_m = \frac{1}{2}(\gamma + \lambda_{s,M})(g_{syn}\gamma - \gamma + 1) \left((g_{syn}\gamma + 1)(\lambda_{s,L} - \lambda_{q,M}) - \gamma(\lambda_{s,L} + \lambda_{q,M}) - 2\lambda_{s,L}\lambda_{q,M} \right),$
$K_{m,d} = \frac{1}{2}(\lambda_{q,M} - \lambda_{s,M})(\gamma + \lambda_{q,M})(g_{syn}\gamma - \gamma + 1)(g_{syn}\gamma + \gamma + 2\lambda_{s,L} + 1).$

Similarly, the sub-period $T_{M,up}$ corresponds to the piece of orbit that begins at $\mathbf{q}_R$ and ends on the boundary $V = a/2$; we call this point $\tilde{\mathbf{q}}_L$. Therefore, following the same procedure as for $T_{M,down}$, we obtain that

$$T_{M,up} = \frac{1}{\lambda_{q,M}} \ln \left(\left| \frac{\gamma(I - I_1)B_m + K_m}{\gamma(I - I_1)B_m + K_{m,u}} \right| \right),$$

where B_m and K_m are described as in $T_{M,down}$, and

$$K_{m,u} = \tfrac{1}{2}(\gamma + \lambda_{q,M})(g_{syn}\gamma - \gamma + 1)\left((g_{syn}\gamma + 1)(\lambda_{s,L} - \lambda_{s,M}) - \gamma(\lambda_{s,L} + \lambda_{s,M}) - 2\lambda_{s,L}\lambda_{s,M}\right).$$

Notice that both points $\tilde{\mathbf{q}}_R$ and $\tilde{\mathbf{q}}_L$ can be analytically computed using the second equation in system (5.17), since $T_{M,down}$ and $T_{M,up}$ are known, and the component V of $\tilde{\mathbf{q}}_R$ and $\tilde{\mathbf{q}}_L$ is $V = (1+a)/2$ and $V = a/2$, respectively. Then, the approximated period on the lateral regions will be the necessary time to travel from $\tilde{\mathbf{q}}_L$ to $\mathbf{q}_L$ for the left sub-period T_L, and the necessary time to travel from $\tilde{\mathbf{q}}_R$ to $\mathbf{q}_R$ for the right sub-period T_R.

To compute the approximated period on the lateral regions let us consider $\bar{\mathbf{q}}_L$ and $\bar{\mathbf{q}}_R$ be the points that result from projecting $\tilde{\mathbf{q}}_L$ and $\tilde{\mathbf{q}}_R$ along the direction of the fast eigenvector on the slow manifold defined on the left and the right regions, respectively (see Figure 5.25 for a representation of these two points). See 1.2 for more details about this procedure.

Considering the coordinate system centered to the virtual equilibrium point $\mathbf{p}_L$ and generated by the left eigenvectors $\mathbf{v}_{s,L}$ and $\mathbf{v}_{q,L}$, the approximation of the left sub-period, T_L, can be computed as

$$T_L = \frac{1}{2\lambda_{s,L}} \ln \frac{\|\bar{\mathbf{q}}_L - \mathbf{p}_L\|^2}{\|\mathbf{q}_L - \mathbf{p}_L\|^2}.$$

Similarly, considering the coordinate system centered on the virtual equilibrium point $\mathbf{p}_R$ and generated by the right eigenvectors $\mathbf{v}_{s,R}$ and $\mathbf{v}_{q,R}$, the approximation of the right sub-period, T_R, can be computed as

$$T_R = \frac{1}{2\lambda_{s,L}} \ln \frac{\|\bar{\mathbf{q}}_R - \mathbf{p}_R\|^2}{\|\mathbf{q}_R - \mathbf{p}_R\|^2}.$$

Notice that the two former expressions can be written, in terms of the system parameters as

$$T_L = \frac{1}{\lambda_{s,L}} \ln \left(\left| \frac{\gamma(I - I_1)B_L}{\gamma(I - I_1)B_L - K_L} \right| \right), \qquad T_R = \frac{1}{\lambda_{s,L}} \ln \left(\left| \frac{\gamma(I - I_2)B_L}{\gamma(I - I_2)B_L + K_L} \right| \right)$$

where

$$B_L = \lambda_{q,L} - \lambda_{s,L}$$
$$K_L = \tfrac{1}{2}(\gamma + \lambda_{q,L})(g_{syn}\gamma + \gamma + 2\lambda_{s,L} + 1)$$

Therefore, an expression to approximate the period of the periodic orbit in system (5.14) is $\hat{T} = T_L + T_{M,down} + T_R + T_{M,up}$, thus proving statement (b).   □

Remark 5.2. *When C tends to 0, $T_L \longrightarrow T_{0,L}$, $T_{M,down} \longrightarrow 0$, $T_R \longrightarrow T_{0,R}$, and $T_{M,up} \longrightarrow 0$. Therefore, $\hat{T} \longrightarrow T_0$. Moreover, both for $C = 0$ and $C > 0$, the left sub-period tends to infinity when I tends to I_1. This limit agrees with the fact that, when $I = I_1$, the equilibrium point lies on the intersection of the central slow manifold with the vertical line $v = a/2$; therefore, the orbit reaches the equilibrium point and spends infinite time to escape. Similar arguments explain why the right sub-period tends to infinity when I tends to I_2.*

Remark 5.3. *Notice that, B_l, B_m, K_l, K_m, $K_{m,d}$, and $K_{m,u}$ in the expression $\hat{T}$ of Proposition 5.3, have a non-linear dependence on g_{syn}. Moreover, fixing all parameters in the model but keeping the synaptic conductance, g_{syn}, the applied current, I, and the capacitance of the neuron, C, as variable, then the approximated period can be written as the function*

$$\hat{T}(C, I, g_{syn}) = T_L(C, I, g_{syn}) + T_{M,down}(C, I, g_{syn}) + T_R(C, I, g_{syn}) + T_{M,up}(C, I, g_{syn}).$$

5.2.2.1 Goodness of the approximated period function

As we have mentioned in the proof of Proposition 5.3, only two assumptions have been supposed in order to approximate the period, which are the two initial conditions where the periodic orbit passes through. We suppose that these points are $\mathbf{q}_L$ and $\mathbf{q}_R$, while the real ones are exponentially close to them.

To see the global effect that these assumptions cause, and so the goodness of fit, in Figure 5.26, we show the relative error of the approximated period function $\hat{T}(C, I, g_{syn})$, first, keeping constant de parameter g_{syn} (panel A); second, keeping constant de capacitance C (panel B); and, finally, keeping constant de applied current I (panel C). The relative errors have been plotted, in all panels, considering the numerical solution of the period, which has been computed using the Newton-Raphson method in each region separately, as well as the actual one (see Appendix C.1 for details on the routine). In panel A we can see how the relative error in the proposed approximation function depends more significantly on the capacitance C than on the applied current I. Moreover, this panel reveals relative errors around $O(C/10)$. On the other hand, in panel B, one can see that, when parameter I varies, for a fixed value of g_{syn}, the error is not qualitatively altered, but for larger values of g_{syn}, the relative error significantly increases being, at most, $O(C)$; see also panel C, where we can better appreciate the errors in g_{syn} as C changes.

Observe that even though $\hat{T}(C, I, g_{syn})$ is defined for all values of C, g_{syn} and I, computing $\hat{T}$ makes sense only under the hypothesis of Lemma 5.1, that is, when I lies in (I_1, I_2) and $g_{syn} \in (1 - 1/\gamma, 1 - C\gamma)$. Figure 5.27 shows the shape of the approximated period function $\hat{T}(C, I, g_{syn})$ in the corresponding domain. As we have mentioned in Remark 5.2, the period substantially increases when I is close to I_2 and I_1, tending to infinity. Moreover, the V-shape of the function $\hat{T}(C, I, g_{syn})$ is given by the linear dependence that I_1 and I_2 have on g_{syn}. That is, as we increase the value of g_{syn}, the value of I_1 is greater whereas the value of I_2 is smaller; consequently, the window where I can move decreases and causes the V-shaped profile. Remarkably, in Figure 5.27 we can also see that $\hat{T}(C, I, g_{syn})$ seems to be monotonically decreasing with respect to g_{syn}. This fact gives us the opportunity to apply the implicit function theorem and so, for a given value, T^*, of the period, there exists a unique value g_{syn}^* such that $\hat{T}(C, I, g_{syn}^*) = T^*$. Even though we would like to analytically proof the monotonicity of $\hat{T}$, because of the multitude of parameters in the model, we have not been able to show it. However, some relevant properties of the shape of T, and also some computational evidences, have been obtained on the way. Next we state all of them.

Evidences of the monotonicity of $\hat{T}$. Under the hypothesis of Lemma 5.1, we had seen some evidences of fact that the approximated period function $\hat{T}(C, I, g_{syn})$ is monotonically decreasing with respect to the synaptic conductance parameter, g_{syn}.

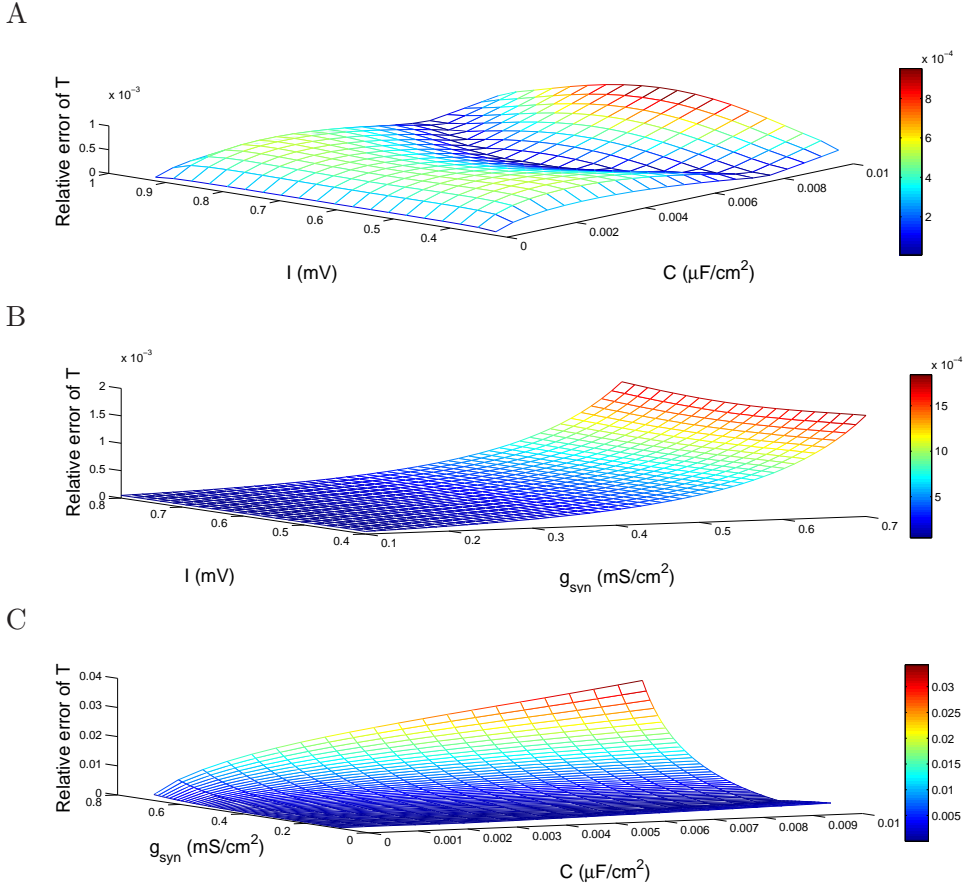Note that, at each region of the McKean model, see equation (5.14), the Poincaré return

A

B

C

Figure 5.26: **Goodness of fit of the periodic function** $\hat{T}(C, I, g_{syn})$. Panel A shows the relative error of the period for a fixed synaptic conductance $g_{syn} = 0.2$, panel B shows the relative error of the period when the capacitance is fixed as $C = 1e-4$, and panel C shows the relative error of the period when the applied current is fixed as $I = (I_1^0 + I_2^0)/2$ such that I_1^0 and I_2^0 are, respectively, the value of I_1 and I_2 corresponding to $g_{syn} = 0$. The relative error of the numerical value obtained using the Newton-Raphson method with respect to the approximated one using the expression in Proposition 5.3. The rest of parameters of the model are fixed as $a = 0.25$, $v_0 = 0$, $w_0 = 0$, $\gamma = 0.5$, and $V_{syn} = 0.25 + a/2$.

map is an analytical function in terms of C. Consequently, its composition is also an analytical function. Therefore, to prove the monotonicity of $\hat{T}(C, I, g_{syn})$, it is enough to prove the monotonicity in the limiting case $C = 0$. For this reason, let us consider the limit of $\hat{T}(C, I, g_{syn})$ when C tends to 0, which is given by $T_0 = T_{0,L} + T_{0,R}$, as described in Proposition 5.3(a) under the hypothesis of Lemma 5.1 with $C = 0$.

Note that T_0 is a function of g_{syn} and it can be rewritten as $T_0(g_{syn}) = B_0(g_{syn})f(g_{syn})$ where

$$f(g_{syn}) = \ln\left(\frac{\gamma(I - I_1)}{\gamma(I - I_1) + K_0}\right) + \ln\left(\frac{\gamma(I - I_2)}{\gamma(I - I_2) - K_0}\right).$$

Therefore, to prove that $T_0(g_{syn})$ is monotone, we need to see that the difference $T_0(g_{syn}) - T_0(g_{gsyn} + t)$, for all $t \in (0, 1 - g_{syn})$, is always either negative or positive. That is, we need to evaluate the sign of

$$B_0(g_{syn})f(g_{syn}) - B_0(g_{gsyn} + t)f(g_{gsyn} + t), \quad t \in (0, 1 - g_{syn}).$$
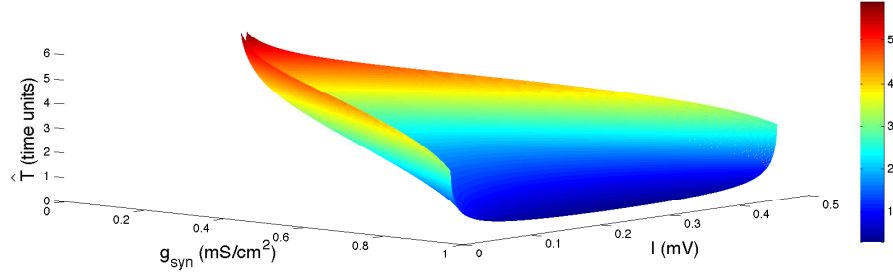
Figure 5.27: **Shape of the $\hat{T}(C, I, g_{syn})$ function**. This figure shows the shape of the approximated period $\hat{T}$ versus the applied current I and the synaptic current g_{syn}. The capacitance has been fixed as $C = 1e - 4$. The rest of parameters of the model are fixed as $a = 0.25$, $v_0 = 0$, $w_0 = 0$, $\gamma = 0.5$, and $V_{syn} = 0.25 + a/2$.

Another way to prove the monotonicity is also by seeing that the derivative of $T_0(g_{syn})$, with respect to g_{syn}, is always negative. That is,

$$\dot{T}(g_{syn}) = \dot{B}_0(g_{syn})f(g_{syn}) + B_0\dot{f}(g_{syn}) < 0$$

where the dot stands for the derivative respect to g_{syn}.

From Proposition 5.3(a), $B_0(g_{syn})$ is a strictly negative function and its derivative, $\dot{B}_0(g_{syn}) = -1/(1+\gamma+\gamma g_{syn})$, is also strictly negative. Consequently, $B_0(g_{syn})$ is a strictly decreasing function and so,

$$B_0(g_{gsyn} + t) < B_0(g_{gsyn}), \quad t \in (0, 1 - g_{syn}). \tag{5.19}$$

Moreover, the second derivative of $B_0(g_{syn})$ is always positive.

On the other hand, $K_0(g_{syn})$ is a positive function whereas its derivative with respect to g_{syn},

$$\dot{K}_0(g_{syn}) = -\frac{(1 + g_{syn})^2 \gamma + 2}{2(1 + g_{syn})^2},$$

is strictly negative. Therefore, $K_0(g_{syn})$ is a strictly decreasing function. Moreover, the second derivative of $K_0(g_{syn})$ is always positive.

Since $I \in (I_1, I_2)$, $f(g_{syn})$ results to be a negative function. In fact, since the arguments of the logarithms in both added terms in function $f(g_{syn})$ are smaller than 1, $f(g_{syn})$ is a negative function. By computing the derivative of $f(g_{syn})$, we get

$$\dot{f}(g_{syn}) = \frac{-\gamma\left(\frac{a}{2} - V_{syn}\right)K_0 - \gamma\left(I - I_1\right)\dot{K}_0}{(\gamma(I - I_1) + K_0)\,\gamma(I - I_1)} + \frac{-\gamma\left(\frac{a+1}{2} - V_{syn}\right)K_0 + \gamma\left(I - I_2\right)\dot{K}_0}{(\gamma(I - I_2) - K_0)\,\gamma(I - I_2)}.$$

Using the above considerations on the sign of B_0, K_0 and their derivatives together with the inequalities $a/2 - V_{syn} < 0$, $(a+1)/2 - V_{syn} < 0$, $\dot{f}(g_{syn})$ results to be strictly positive. Therefore, $f(g_{syn})$ is an strictly increasing function and so

$$f(g_{syn}) < f(g_{syn} + t), \quad t \in (0, 1 - g_{syn}).$$

However, all these properties on $B_0(g_{syn})$ and $f(g_{syn})$ (neither the ones on K_0), are not enough to show that, for all g_{syn} and $t \in (0, 1 - g_{syn})$ neither

$$B_0(g_{syn})f(g_{syn}) - B_0(g_{syn} + t)f(g_{syn} + t) \leq 0,$$

nor

$$\dot{B}_0(g_{syn})f(g_{syn}) + B_0\dot{f}(g_{syn}) \leq 0,$$

hold; and so to prove the monotonicity of $T_0(g_{syn})$. There is always a positive function added to a negative one. Hence, we need to know which one is higher for all g_{syn} values. However, the logarithm function complicates this calculus, since it cannot be easily fitted by a useful function working for all possible I_{app}.

For the chosen physiological parameter, in Figure 5.28 we represent the function $\hat{T}(g_{syn})$ (Panel A), the derivative $\dot{\hat{T}}(g_{syn})$ (Panel B) and the second derivative $\ddot{\hat{T}}(g_{syn})$ (Panel C), each of them for different values of applied current. Note that, from Panel B, all the applied currents considered show that $\dot{\hat{T}}(g_{syn}) < 0$. Therefore, at least for these values of I_{app}, $\hat{T}(g_{syn})$ is monotonically decreasing with respect to g_{syn}. On the other hand, the second derivative depicts a change in sign (see Panel C) for some I_{app}, thus showing the existence of an inflection point in $\hat{T}(g_{syn})$ of second order.

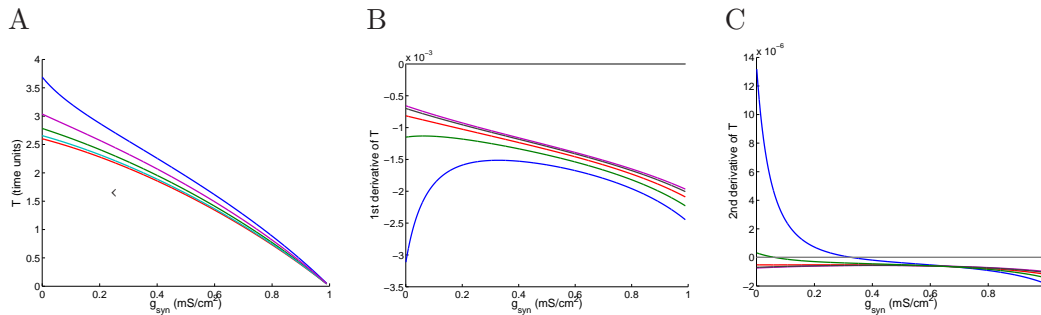

Figure 5.28: **Monotonicity of $\hat{T}(C, I, g_{syn})$ function respect to g_{syn}.** This figure shows different plots representing the approximated period $\hat{T}$ and its derivatives versus the synaptic current g_{syn} for different values of applied current. Panel A represents $\hat{T}(g_{syn})$ (coloured lines). In Panel B we depict the first derivative $d\hat{T}/dg_{syn}$ (coloured lines) and the line $d\hat{T}/dg_{syn} = 0$ (gray line). In Panel C, both the second derivative $d^2\hat{T}/dg_{syn}^2$ (coloured lines) and the line $d^2\hat{T}/dg_{syn}^2 = 0$ (gray line) are represented. The different coloured lines, in all panels, stand for different applied currents such that each color corresponds to a specific value of applied currents, which is $I_{app} \in [0.4,\ 0.5,\ 0.6,\ 0.7,\ 0.8]$. The rest of parameters of the model are fixed as $C = 1e-4$, $a = 0.25$, $v_0 = 0$, $w_0 = 0$, $\gamma = 0.5$, and $V_{syn} = 0.25 + a/2$.

Therefore, we have given computational evidences of the monotonicity of the approximated function of the period with respect to g_{syn}.

5.2.3   Estimation of the synaptic conductance

In this section we present a method to estimate the steady synaptic conductance from the cell's oscillatory activity. That is, knowing the frequency of the spikes for a fixed and constant injected current, we want to estimate the constant synaptic current that the neuron is receiving. The procedure has been then extended to estimate the time-course of the non-steady synaptic currents.

5.2.3.1   Estimation of a steady synaptic conductance

In Section 5.2.2, we have presented an analytical function $\hat{T}(C, I, g_{syn})$, which has a non-linear dependence on g_{syn}, to approximate the period of the periodic orbit of system (5.14). However, by the monotonicity of $\hat{T}(C, I, g_{syn})$ with respect to g_{syn} when $I_1 < I < I_2$, there exists a one-to-one correspondence between $\hat{T}$ and g_{syn}. Therefore, applying a specific applied current, I^*, one can experimentally approximate the corresponding actual period T^* of the membrane potential V. In other words, knowing the rest of parameters of the model, there exists a unique possible synaptic conductance g_{syn} that can be estimated by solving the implicit equation

$$\hat{T}(C^*, I^*, g_{syn}) = T^*. \tag{5.20}$$

To solve equation (5.20), one has to take into account that the logarithmic part of the analytical expression $\hat{T}$ contains an absolute function and, since I_1 and I_2 depend on g_{syn}, we could get up to three possible g_{syn} solutions for a fixed I. Fortunately, this dependence is linear and so only one of the three possible solutions for g_{syn} satisfies that $I_1 < I < I_2$. Then, (5.20) has to be solved with the additional condition

$$g_{syn} > \max\left(0, \bar{I}_1, \bar{I}_2\right), \tag{5.21}$$

where

$$\bar{I}_1 = \frac{2\gamma I - (\gamma + 1)a + 2v_0 - 2\gamma w_0}{2\gamma(\frac{a}{2} - V_{syn})} \quad and \quad \bar{I}_2 = \frac{2\gamma I - (\gamma + 1)a + 2v_0 - 2\gamma w_0 - \gamma + 1}{2\gamma(\frac{a+1}{2} - V_{syn})}.$$

When we apply the estimation procedure (5.20-5.21) to obtain the estimated synaptic conductance, $\hat{g}_{syn}$, we identify two main sources of error: an error coming from the numerical method used to solve the implicit equation and another error coming from the approximation of the period function, which is at most $O(C)$ (see Section 5.2.2.1). To visualize the impact of both error sources and so to test the goodness of the estimation procedure, we show the relative error of the estimated synaptic conductance $\hat{g}_{syn}$ with respect to the actual value of g_{syn}, both using different values of applied currents (see Figure 5.29(A)), and using different values of the membrane capacitance (see Figure 5.29(B)). In these plots we estimate different values of the synaptic conductance (from 0.1 to 0.3, equally spaced), each one represented by a different colour trace.

In Figure 5.29(A) we can see how the estimation of the conductance improves when the applied current is close to I_1 and I_2. The error takes the maximum at $I = (I_1 + I_2)/2$. On the other hand, in Figure 5.29(B) we also observe that the relative error is smaller when the membrane capacitance, C, is smaller; being this error $O(C)$. Therefore, we can conclude that the best estimation is done for small values of C and also for values of I close to I_1 or I_2. In Figure 5.29(C) we can better appreciate how the error increases for large values of C and for values of I far from I_1 and I_2. This panel presents the goodness of fit of the synaptic conductance when both parameters C and I change, where the relative error is considered in absolute value.

5.2.3.2   Generalization for non-constant conductance traces: inter-spike estimation.

In this section, we implement the previous methodology in order to estimate conductance traces that vary along time, that is, when $g_{syn} = g_{syn}(t)$. Strictly speaking this leads to
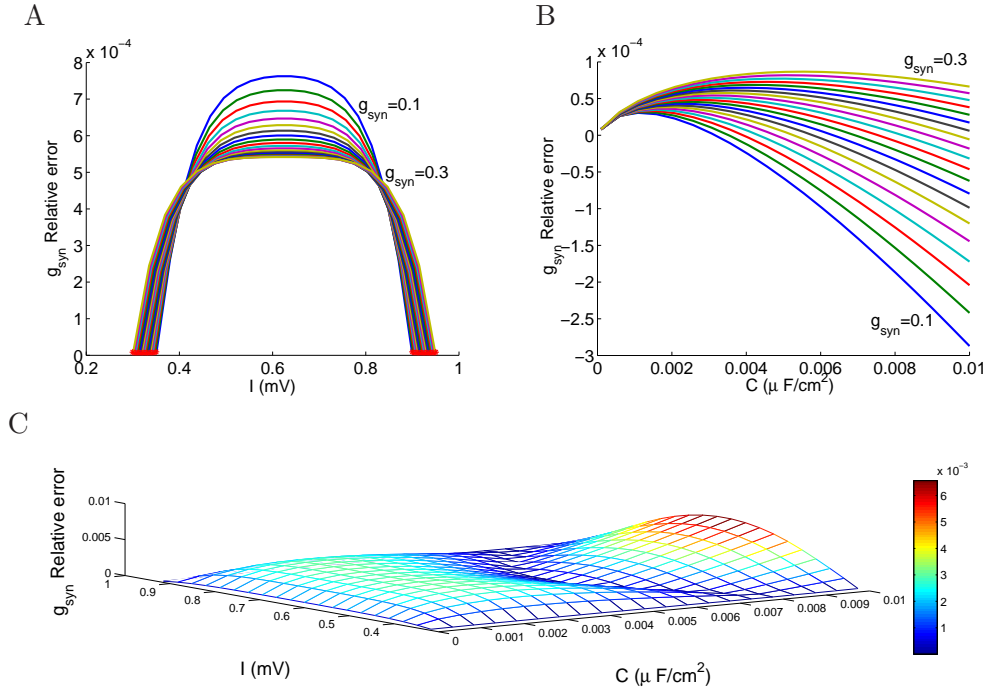
A

B

C

Figure 5.29: **Goodness of fit of the steady synaptic conductance parameter**. Panels A and B show the relative error caused when we estimate the synaptic conductance. The different traces correspond to different values of g_{syn} equally spaced from 0.1 to 0.3. Panel A represents the relative error versus the applied current for a fixed value of $C = 10^{-4}$, whereas panel B represents the relative error versus the membrane capacitance for a fixed value of $I = I_1 + 10^{-3}$. Red points in panel A represent the values of I_1 (left points) and I_2 (right points) for each g_{syn}. Panel C shows the relative error in absolute value for varying values of the membrane capacitance, C, and the applied current, I, being the actual synaptic conductance $g_{syn} = 0.2$. The rest of parameters are fixed as $a = 0.25$, $v_0 = 0$, $w_0 = 0$, $\gamma = 0.5$, and $V_{syn} = 0.25 + a/2$.

a non-autonomous differential system, and the system may not have a periodic orbit as for constant g_{syn}. However, for slow changes in the synaptic conductance, we may assume that the flow of the system stays close to a periodic orbit between two consecutive spikes. Given an inter-spike interval $[t^*, t^* + \tau]$, we propose to apply the associated procedure (5.20-5.21), that is, solving $\hat{T}(g_{syn}) = \tau$ to obtain an estimated $\hat{g}_{syn}$ on $[t^*, t^* + \tau]$. We summarize this idea in the following procedure:

Procedure 5.1. *Consider a voltage trace* $\{v(t), t \in [0, T_{max}]\}$ *obtained from the neuron model* (5.14) *under an (unknown) synaptic input* $\{g_{syn}(t), t \in [0, T_{max}]\}$ *and a specific applied current* I^* *leading together to a spiking activity. We assume that* $V(t)$ *reaches* $N + 1$ *peaks (maxima of the trace) and call* $\{T^{(k)}\}_{k=1}^N$ *the corresponding* N *inter-spike intervals. Then, the time-course of the synaptic conductance* $g_{syn}(t)$ *can be estimated by following the next steps:*

1. *For each* $T^{(k)}$, $k = 1, \ldots, N$, *solve* (5.20-5.21) *to estimate the corresponding synaptic conductance value,* $g_{syn}^{(k)}$.

2. *Assign at* $g_{syn}^{(k)}$ *the time* $t^{(k)}$ *corresponding to the* $(k + 1)$-*th peak to obtain a set of points* $\mathcal{P} := \{(t^{(k)}, g_{syn}^{(k)})\}_{k=1}^N$ *which are finally interpolated to obtain the full time-course of* $g_{syn}(t)$.

    3. Interpolate the set $\mathcal{P}$ (we use the cubic spline method) and call $\hat{g}_{syn}(t)$ the result of this interpolation, which will be the estimated conductance trace.

Figure 5.30 shows some test conductance traces which have been created in order to obtain scenarios with different spiking intensities. The first two rows present conductance traces with low frequency oscillations: the first one presents high amplitude oscillations ($g_{syn}(t) = 0.2\sin(2\pi t/10) + 0.2$), and the second one combines small with big oscillations ($g_{syn}(t) = 0.2\sin(2\pi t/30) + 0.2/5\sin(2\pi t/5) + 0.2$). In both cases we obtain a good estimation of the conductances, according to the high concentration of points on the vicinity of the identity line in the scatter plots, see panels in the second column. The reconstruction of membrane potential obtained using the estimated conductance trace $\hat{g}_{syn}(t)$ as synaptic input show an excellent agreement with the original membrane potential trace, see panels in the last column.
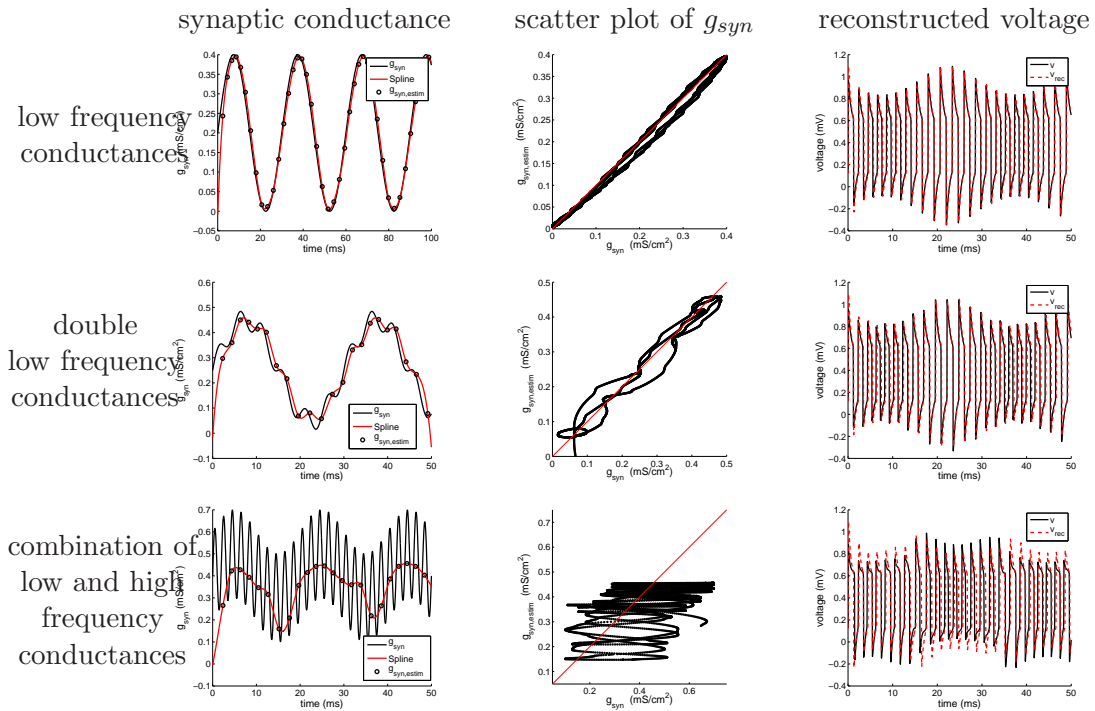

Figure 5.30: **Goodness of fit of the synaptic conductance time-course for different functions of g_{syn}**. The first column shows the estimated values of the discretization of g_{syn} (black dots) and the cubic spline interpolation of them (red solid line). The black line corresponds to the actual value of the synaptic conductance at each time. The second column represents the scatter plot of the real versus the estimated synaptic conductance after the interpolation. The red line is the identity line as a reference to observe the goodness of the estimation. The third column shows a comparison of the voltages computed using the actual conductances (solid black trace) and the estimated conductances (dotted red trace). Parameters are $a = 0.25$, $v_0 = 0$, $\gamma = 0.5$, $w_0 = 0$, $V_{syn} = 0.25 + a/2$, $C = 0.001 \ \mu F/cm^2$, $I = 0.625 \ \mu A/cm^2$, $g_{syn}(t_0) = 0.6278$.

In the last row of Figure 5.30, we consider a new conductance's trace where both frequency and amplitude of the small oscillations have been changed respect to the results in the second row ($g_{syn}(t) = 0.1\sin(2\pi t/20) + 2 \cdot 0.1\sin(2\pi t/2) + 0.4$). In the left panel we can see that the estimated conductances do not match with the real ones, where the fast oscillations have not been captured. However, on the reconstruction of the membrane

potential (see right panel on the last row), the frequency is captured, the amplitude of the spikes is not, and a small delay is presented.

From Figure 5.30, we can conclude that for a small changes in time of the synaptic conductance, the purposed method can estimated the time-course of the synaptic conductances with small errors, reproducing the same membrane potential. However, if the changes are abrupt then the method estimates a mean time-course synaptic conductance, which almost reproduce the membrane potential.
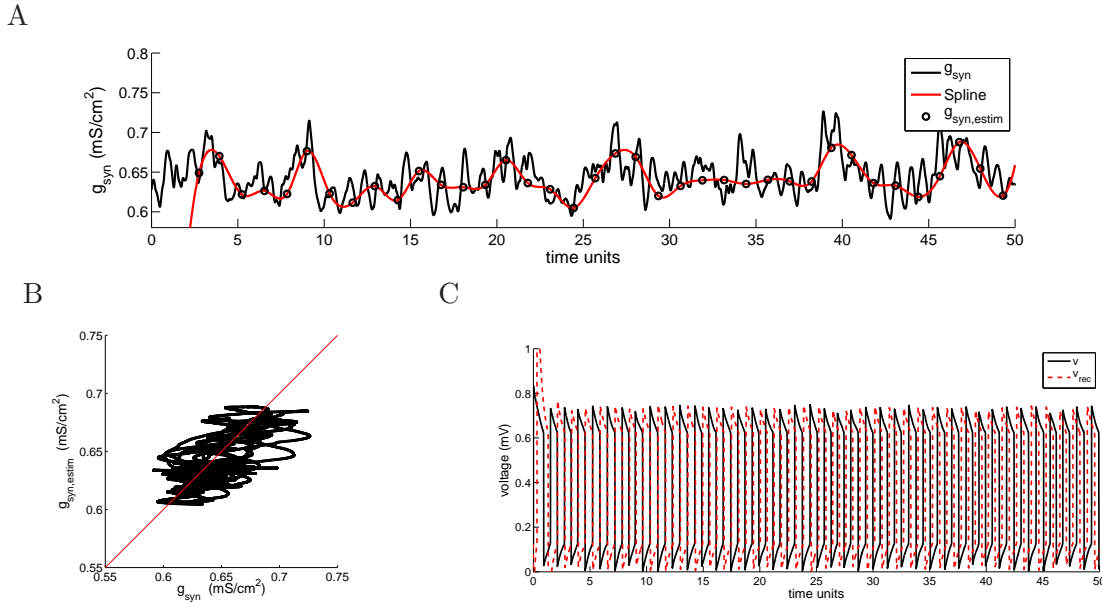

Figure 5.31: **Goodness of fit of the synaptic conductance time-course in Section 2.2.2.3, when we consider the inter-spike interval as the current period**. Panel A shows the estimated values of the discretization of g_{syn} (black dots) and the cubic spline interpolation of them (red solid line). The black line corresponds to the real value of the synaptic conductance at each time. Panel B represents the scatter plot of the real versus the estimated synaptic conductance after the interpolation. The red line in Panel B is the identity line as a reference to observe the goodness of the estimation. Panel C shows a comparison of the voltages computed using the real conductances (solid black trace) and the estimated conductances (dotted red trace). Parameters are $a = 0.25$, $v_0 = 0$, $\gamma = 0.5$, $w_0 = 0$, $V_{syn} = 0.25 + a/2$, $C = 0.001\ \mu F/cm^2$, $I = 0.625\ \mu A/cm^2$, $g_{syn}(t_0) = 0.6278$.

To test the estimation of the conductances' course in a more realistic case, in Figure 5.31, we use 1 ms conductance traces obtained from a computational network that models layer $4C\alpha$ of primary visual cortex (see Tao et al (2004) and McLaughlin et al (2000)). Panel A shows how the estimated conductances follow the trace of the actual ones but, as we can also see in Figure 5.30, the high oscillations are not well captured. We can corroborate this fact in panel B, where we show that the actual and the estimated conductances are poorly correlated (the coefficient of correlation is approximated 0.12). However, in order to display the effects of the misestimations, in panel C we compared the voltage computed using the actual conductance traces and the estimated ones (after interpolation). One can appreciate a small time shift of order 0.1 ms that remains almost constant along the time sequence.

5.2.3.3   Generalization for non-constant conductance traces: estimation based on the sub-periods

In the previous section we have seen that for highly varying conductances, we cannot obtain good estimations. This misestimations are partly caused by the fact that we are assuming the conductances to be stationary in a quite long time window. To reduce the errors and to better capture the oscillations of the synaptic conductances, in this section we present a more accurate way to estimate $g_{syn}(t)$ by taking into account the approximated expression of each sub-period separately, that is, the time spent in each region.

In the proof of Proposition 5.3(b), we found an approximated expression of each lateral and central sub-periods separately for a given periodic orbit. We denoted these sub-periods as T_L, $T_{M,upp}$, $T_{M,down}$, T_R. Similarly, for any monodromic trajectory of system (5.14), not necessarily periodic, we can split the trajectories in pieces lying only on one region. We denote by τ_ξ as the time spent in region ξ to go from $V_{\xi,1}$ to $V_{\xi,2}$, where ξ stands for L, $M, down$, M, up or R, and the crossing points $V_{L,1} = V_{L,2} = v_{M,down,1} = V_{M,upp,2} = a/2$, $V_{R,1} = V_{R,2} = v_{M,down,2} = V_{M,upp,1} = (1+a)/2$. We understand that regions M, up and $M, down$ are both the central region. With this notation, we present a refined version of the estimation procedure given in Procedure 5.1.

Procedure 5.2. *Consider a voltage trace $\{V(t), t \in [0, T_{max}]\}$ obtained from the neuron model (5.14) under an (unknown) synaptic input $\{g_{syn}(t), t \in [0, T_{max}]\}$ and a specific applied current I^* leading together to a spiking activity. We assume that the voltage trace describes N oscillations in the time interval $[0, T_{max}]$. Then, the time course of the synaptic conductance $g_{syn}(t)$ can be estimated by following the next steps:*

1. *Define $\{\tau_\xi^{(k)}\}_{k=1}^N$ as the time spent to go from $V = V_{\xi,1}$ to $V = V_{\xi,2}$ in the k-th oscillation, where ξ stands for L, M,down, M,upp or R.*

2. *For each $k = 1, \ldots, N$ and $\xi \in \{L; M,down; M,up; R\}$, solve (5.20-5.21) to estimate the time-course with $T^* = \tau_\xi^{(k)}$, and call the solution $\hat{g}_{syn}^{\xi,k}$. Define the set $\mathcal{P} = \left\{ \left(t^{\xi,k}, \hat{g}_{syn}^{\xi,k} \right) ; \xi \in \{L; M,down; M,up; R\}, \ k = 1, \ldots, N \right\}$, where $t^{\xi,k}$ is the time when the k-th oscillation crosses $V = V_{\xi,2}$.*

3. *Interpolate the set $\mathcal{P}$ and call $\hat{g}_{syn}(t)$ the result of this interpolation.*

Using Procedure 5.2 we can extract a more accurate discretization of the conductance traces, as we can see in Figure 5.32 and 5.33. If we compare the results from the ones obtained by using Procedure 5.1, see Figures 5.32(A) and 5.31(A), respectively, we can appreciate an improvement of the estimation when using Procedure 5.1. This improvement is more evident when conductances change abruptly; in this case, using Procedure 5.2 we can capture more oscillations.

Even though these figures present only slight changes on the scatter plots, see Figures 5.32(B) and 5.31(B), and the reconstructed voltage (panels C), in the sinusoidal trace case, which has been created to obtain low and high frequency conductances, a considerable improvement on the estimation and also in the reconstructed voltage has been obtained. Comparing Figure 5.33 to Figure 5.30 (last row), we observe how all the oscillations of $g_{syn}(t)$ are captured with frequency and amplitude; only a small delay in time exists without causing errors on the reconstructed voltage, which matches with the actual one.
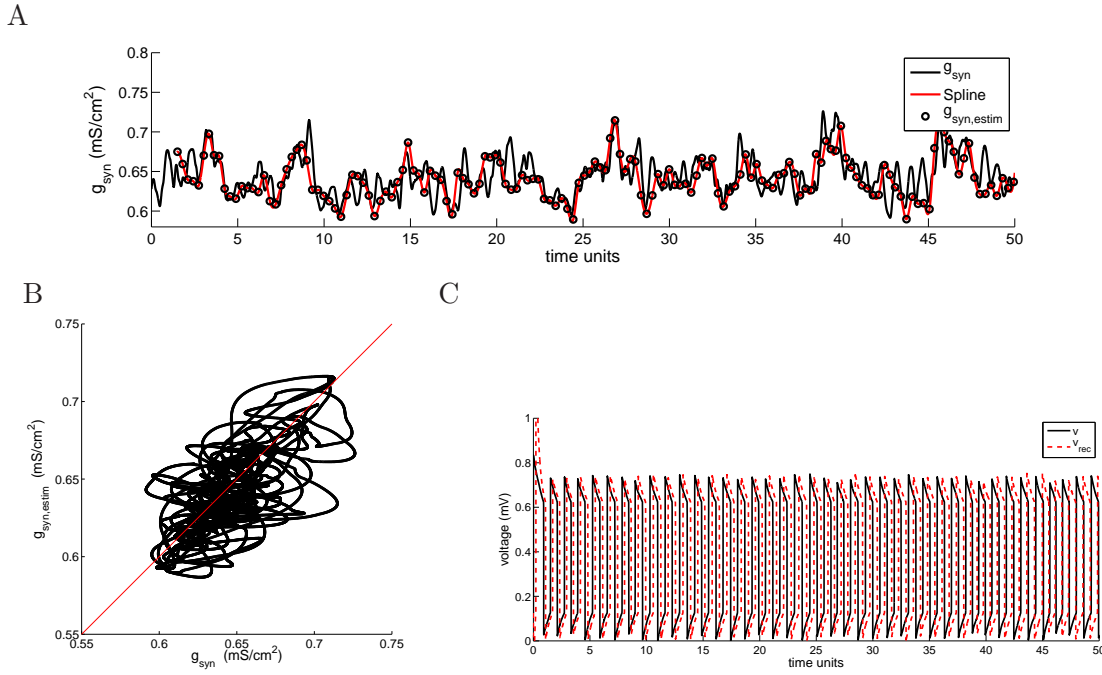
A

B   C

Figure 5.32: **Goodness of fit of the synaptic conductance time-course in Section 2.2.2.3, when we consider the sub-periods separately**. Panel A shows the cubic spline interpolation of the estimated values of the discretization of $g_{syn}(t)$ (red solid line) and the actual value of the synaptic conductance (black solid line). Panel B represents the scatter plot of the actual versus the estimated synaptic conductance after the interpolation. The red line in Panel B is the identity line as a reference to observe the goodness of the estimation. Panel C shows a comparison of the voltages computed using the actual conductances (solid black trace) and the estimated ones (dotted red trace). The other parameter values are $a = 0.25$, $v_0 = 0$, $\gamma = 0.5$, $w_0 = 0$, $V_{syn} = 0.25 + a/2$, $C = 0.001\ \mu F/cm^2$, $I = 0.625\ \mu A/cm^2$, $g_{syn}(t_0) = 0.6278$.

Finally, we apply the Method 5.2 to the synaptic conductances extracted from the *in sillico* network described in Section 2.1.4. We consider the total amount of synaptic input that an excitatory neuron is receiving when the level of depression of the network is $f_D = 0.8$. The results are depicted in Figure 5.34. As we can see in Panel A, the estimated synaptic conductances (red line) almost follow the shape of the actual ones (black line). However, the abrupt increment presented on the actual conductances is slightly anticipated by the estimation, which also causes an anticipation when the voltage is reconstructed (see Panel C). Moreover, during the decreasing part, the estimated conductance trace shows small down peaks along the curve, returning to the original curve. This behaviour occurs because the approximated lateral periods, obtained by the approximated period function $\hat{T}$, last slightly shorter than the real ones. These misestimations cause a delay in the reconstructed voltage in Panel C.

All the above effects are also shown in Panel B, where the estimated conductances are plotted versus the actual ones. Almost all the obtained dots lie on the vicinity of the identity line, showing good approximations. The rest of the dots, which are slightly further from the identity line, correspond to the estimated values on the abrupt increment.
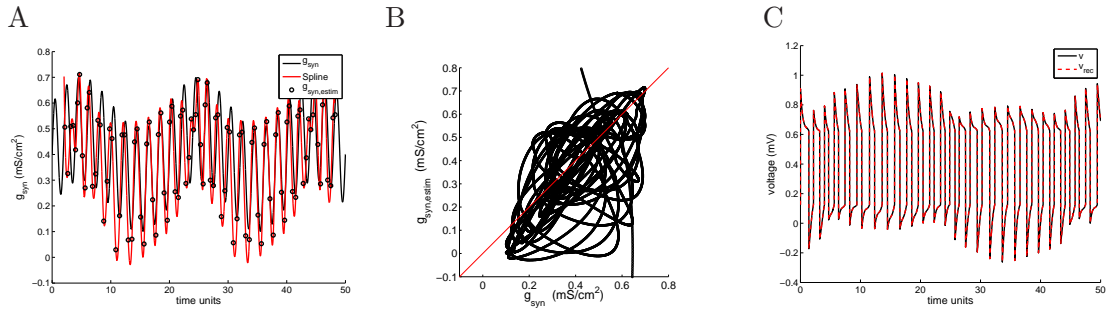
Figure 5.33: **Goodness of fit of the synaptic conductance time-course for the combination of low and high frequency conductances**. Panel A shows the estimated values of the discretization of g_{syn} (black dots) and the cubic spline interpolation of them (red solid line). The black line corresponds to the actual value of the synaptic conductance at each time. Panel B represents the scatter plot of the actual versus the estimated synaptic conductance after the interpolation. The red line is the identity line as a reference to observe the goodness of the estimation. Panel C shows a comparison of the voltages computed using the actual conductances (solid black trace) and the estimated ones (dotted red trace). The other parameter values are $a = 0.25$, $v_0 = 0$, $\gamma = 0.5$, $w_0 = 0$, $V_{syn} = 0.25 + a/2$, $C = 0.001\ \mu F/cm^2$, $I = 0.625\ \mu A/cm^2$, $g_{syn}(t_0) = 0.6278$.

Figure 5.34: **Goodness of fit of the synaptic conductance time-course obtained by the network in Section 2.1.4, when we consider the sub-periods separately**. Panel A shows the cubic spline interpolation of the estimated values of the discretization of $g_{syn}(t)$ (red solid line) and the actual value of the synaptic conductance (black solid line). Panel B represents the scatter plot of the actual versus the estimated synaptic conductance after the interpolation. The red line in Panel B is the identity line as a reference to observe the goodness of the estimation. Panel C shows a comparison of the voltages computed using the actual conductances (solid black trace) and the estimated ones (dotted red trace). The other parameter values are $a = 0.25$, $v_0 = 0$, $\gamma = 0.5$, $w_0 = 0$, $V_{syn} = 0.25 + a/2$, $C = 0.001\ \mu F/cm^2$, $I = 0.625\ \mu A/cm^2$, $g_{syn}(t_0) = 0.2055$.

5.3   Discussion

It is well-known that linear estimations of synaptic conductances are not trustable when data is extracted intracellularly from spiking activity of neurons, see Guillamon et al (2006). Data from experimental studies in the current literature are generally treated taking this cautious message into account but the probable presence of subthreshold-activated

currents confounding the impact of presynaptic activity is yet generally neglected.

Our study in Subsection 5.1.1 entails that estimation of synaptic conductances in the presence of subthreshold-activated currents, even obtained from periods of apparently silent activity, may not be accurate. We have explored this feature using first a computational model with either afterhyperpolarizing or low-threshold activated currents and both sources of subthreshold activity lead to similar conclusions.

To strengthen the message, a second model has been taken into account, consisting of two different activated-subthreshold currents, a resonant one (I_h) and a persistent one (I_{NaP}). In the first computational model, the pyramidal model described in Section 2.1.2.1 with external current given in Section 2.2.1, we have been able to isolate periods of activity where either AHP or LTS currents dominate. In the first case, the long-time scale of $[Ca^{2+}]$ provides an AHP-dominated time window ($55\,ms$ approximately) after the spiking activity in which linear estimations of synaptic conductances fail. One might argue that, since AHP is only present after spiking activity, this failure is a natural extension of bad estimations in spiking regimes rather than an effect of subthreshold activity. To rule out this interpretation, we have been considered both examining the periods where LTS currents dominate, which have no dependence on previous spiking activity, and the second model, the stellate model described in Section 2.1.2.2, with no mechanisms for spiking, and external current given in Section 2.2.1. In both cases we observed similar misestimations, being the main explanation is the loss of linearity in the $I - V$ relationship. Thus, we conclude that it is an ubiquitous feature in subthreshold-activated currents. Therefore, our findings add a new warning message for the treatment of data obtained from intracellular recordings and the conclusions that can be drawn from them, specially those concerning the balance between excitation and inhibition.

Unfortunately, the use of linear estimation methods to extract synaptic conductance time courses has been profusely used in experimental studies (for brief illustrations see Anderson et al (2000), Wehr and Zador (2003) and Bennett et al (2013)) and important conclusions about brain's functionality have been drawn from the excitatory-inhibitory separation of these time courses. Our results imply, at least, that caution has to be applied in trusting this type of results and, probably, a revision of functionality conclusions obtained from experimental data should be conducted.

Therefore, we would like to emphasize our message that, in the estimation of conductance in subthreshold regimes, one should also rule out the presence of ionic currents before proceeding with linear estimations methods.

In Subsection 5.1.1 we have also considered possible improvements to get more accurate estimations of the synaptic conductances. In particular, with the quadratization approach described in Subsection 5.1.1.2, we provide a strategy based on a quadratization of the neuronal model presented in Rotstein (2015). We think that this finding suggests experimental outcomes. Apart from the obvious alternative of a pharmacological block of all possible subthreshold-activated channels, which indeed could lead to a *too passive* integrator, we propose a fitting of the data to a quadratic model that could account for channels whose underlying dynamics is similar to that of the stellate cell model presented in this chapter.

This quadratization approach still allows for further improvements. This procedure requires to extract two different voltage traces from the neuron, if one wants to discern between excitatory and inhibitory conductances. This fact can cause misestimations given by the variability across trials. Moreover, other misestimations can be given by the noise com-

ing from the recordings, which are not considered. In Subsection 5.1.2, we have presented a new strategy to estimate conductances in the subthreshold regime, taking into account these two possible sources of misestimations. This procedure is based on a second order approximation to the model taking into account noise coming from the data. Moreover, only one trace is needed to discern between excitatory and inhibitory conductances.

This stochastic strategy has been applied to both computational and *in vivo* data. Moreover, we have compared this estimation procedure with other existent procedures that are also able to estimate conductances from a single trace. For this purpose, we have chosen a representative deterministic model, the oversampling method (see Bédard et al (2011b),) and a stochastic procedure similar to the one proposed here (see Berg and Ditlevsen (2013)). In general, the results obtained from the comparison of the three methods underpin the necessity of nonlinear strategies to estimate conductances also in the subthreshold regime, showing improved results when quadratic terms are considered on the estimation procedure.

Finally, in Section 5.2, we have presented a proof-of-concept that non-linear estimation methods can be implemented in order to estimate synaptic conductances in spiking regimes. The method relies on the knowledge of the $f - I$ curve. Two different versions of a procedure have been performed in order to estimate conductances: one that only allows to estimate them when they change slowly over time; and second, another procedure which allows the estimation even when the conductances change fast. The results obtained show good estimations of the conductances.

The estimation procedure during spiking regimes also allows for further improvements. The presence of noise on the recordings causes changes on the current boundary conditions, that is I_1 and I_2, which expressions in $\hat{T}(C, I, g_{syn})$ might change (see Lee DeVille et al (2005)).

Other directions to estimate conductances in spiking regimes may be considered. For instance, one could take advantage of recent papers dealing with the study of firing-rate responses (mainly in IF-like models) as a function of the input current, $I(t)$ (see, for instance, Granados and Krupa (2015)). In this case, one could include the synaptic activity into the firing-rate response function, and see whether the synaptic current can be extracted from the recorded firing-rate.

To sum up, we have seen that caution needs to be considered under the presence of subthreshold activated ionic currents. For this purpose, we have first presented a deterministic quadratic approach to estimate conductances. This procedure, has been then improved to take into account noise and the variability across trials. Finally, a proof-of-concept is also given as a first approach to estimate conductances in the spiking regime.

Despite of the improvements given by these estimation procedures, we have considered single-compartment neuron models, thus assuming that the voltage does not vary from the dendrite, where the signal is received by the neuron, to the soma, where we are focusing on. One could also add other misestimation sources such as those emanated from the dendro-somatic interaction (see for instance Cox (2004)), which we left as future work (see Chapter 6).

Chapter 6

Conclusions and future work

As we have seen in the Introduction, inverse methods are required to estimate conductances, and so to unveil the connectivity in the brain. In this thesis we have dealt with the problem of estimation of conductances from different mathematical theories, combining dynamical systems and stochastic techniques. These multiple approaches have provided us different tools that can be applied to slow-fast, piecewise linear and stochastic differential systems.

Chapters 3 and 4 are bridge-chapters in the thesis. Chapter 3 was a training opportunity to learn about geometric singular perturbation theory in piecewise linear differential systems. Moreover, at the same time, we found some good results that are useful to understand some dynamics happening in the smooth framework and that are complicated to prove in this case. An example of it is the canard phenomenon. Although the model we have been studying in Chapter 3 is rather general, it only considers a one-dimensional fast variable. Therefore, an improvement of this theory could be to generalize the model to a q-dimensional fast variable. Because of the properties of matrices we have used to prove the different theorems, we have the intuition that similar results can be easily obtained when the fast variable is described by $f(\mathbf{u}, \mathbf{v}, \varepsilon) = B_1 \mathbf{u} + B_2 \mathbf{v}$, where B_1 and B_2 are $s \times s$ and $q \times q$ real matrix, respectively, having the property that B_2 can be different in each region, but all of them need to be invertible. By considering higher dimensions of the fast variable, we could reproduce other neuronal behaviours such as bursting.

To combine the knowledge acquired about stochastic methods and the slow-fast dynamics, next step is to consider stochastic slow-fast systems. In Berglund and Gentz (2008), Chapter 3 *Stochastic dynamics bifurcation and excitability*, the authors discuss different methods that allow to describe quantitatively the effect of noise on slow-fast systems, by presenting a similar result to the Fenichel's theorem (see Fenichel (1979)) for the stochastic version. They explain which dynamics is conserved when system is perturbed by noise and which one is not. The study is done near stable equilibrium branches and in the vicinity of bifurcation points. Hence, by adding noise to the system presented in Chapter 3 (or similar), this theory could be used to see whether the canard explosion phenomenon persists.

Chapter 4 has been useful to learn about brain connectivity since we have implemented a complex neuronal network. By using this network, the effects of the depression and facilitation have been observed both in the neuronal response (the membrane potential of different neurons) and in the synaptic conductances. We have seen that these two plasticity mechanisms cause a different influence on the network, which changes behaviour accord-

ing to the depression and facilitation level. Synaptic conductances also present specific changes under the short-term plasticity mechanisms, which can lead to a possible procedure to predict conductances when the full network is subjected to those mechanisms. In addition, we have also obtained synaptic conductance traces in different plasticity regimes. In this chapter, only a computational study has been developed, which needs to be corroborated analytically. However, due to the huge amount of variables that the network contains, we need to reduce the number of equations or consider a rate model describing the considered network. Therefore, next step would be to implement a rate model, and adjust its parameters in such a way that it could reproduce the IFR dynamics of this network. In this case, we could then use the rate model to understand the bifurcations observed in the simulations in this chapter.

Even though we have only studied the depression and the facilitation mechanisms separately, as we have mentioned in the introduction of the Chapter 4, these mechanisms can be given simultaneously. Therefore, next step is to investigate how the coexistence of these two short-term plasticity mechanisms influences the dynamics of the synaptic conductances. Moreover, results have been obtained by considering the spontaneous activity of the network (without applying any kind of electrical stimulation). Then, another step is to reproduce the results performed by taking into account stimulus-evoked activity, i.e., when different patterns of electrical stimulation are delivered to one or few neurons of the network, discerning or not between excitatory and inhibitory sub-populations. These patterns can be considered of low-frequency or high-frequency. Moreover, these last results could be supported performing *in vitro* experiments of neuronal networks coupled to Micro-Electrode Arrays (MEAs) in collaboration with Prof. Paolo Massobrio at the NBT lab. They perform experiments using the High-density MEAs, which allow to simultaneously record the electrophysiological activity of neuronal populations from 4096 microelectrodes and, at the same time, to deliver electrical stimulation.

Chapter 5 brings together the main results of this thesis, which respond to the three questions mentioned in the Introduction, and give the title to the thesis. As we have said in the Introduction, research on the topic of estimation of conductances is well aware about the misestimations caused in the spiking regime. However, in Section 5.1.1, a new warning is addressed about the estimations done in the subthreshold regime. We have shown that, under subthreshold activated ionic currents, linear estimation methods can substantially misestimate the conductances. Therefore, caution needs to be extended also in the subthreshold regime if neuron contains ionic channels opened. This fact responds the first question we made: *Are those misestimations on the spiking regime also presented in the subthreshold regime under the presence of subthreshold-activated ionic currents?* Yes, they are.

To overcome this problem, and so to give answer to the second question, which refers to the challenge of providing new estimation strategies, in Section 5.1.1 we have also presented a new estimation procedure based on a quadratic approximation of the dynamics. This strategy consists of an adjustment of the data to a deterministic quadratic model from where we extract the synaptic conductances. If two trails are provided, then we are able to discern between excitatory and inhibitory conductances. Results of this estimation procedure show a considerable improvement on the estimation when it is compared with the usual linear procedures. Moreover, when the quadratization is considered, errors caused in the estimation are not significant (see Figures 5.8 and 5.9).

Even though the quadratic approach, presented in Section 5.1.1, allows good estimations, the procedure requires two trails in order to discern between excitatory and inhibitory conductances, which can lead to some possible errors on the estimation because of the

difficulty of having the same input synaptic conductances in different trials. Moreover, noise presented in experimental data can also alter the results of the estimation. To overcome these two possible sources of misestimations, in Section 5.1.2 we have developed an stochastic approach to estimate conductances. In this new strategy we also do second order approximations of nonliner models to capture the nonlinearities caused by subthreshold activated currents adding a Gaussian noise term. Then, we have used a slight version of the maximum likelihood estimator to unveil the synaptic conductances, discerning between excitatory and inhibitory conductances and using a single trial. This estimation procedure shows good results when it is applied to *in sillico* data. This method has been compared with other existent estimation procedures that require single trials to estimate the excitatory and the inhibitory conductances, namely the oversampling method from Bédard et al (2011b), and the OU method from Berg and Ditlevsen (2013). The *in sillico* results obtained with the stochastic quadratization exhibit a significant improvement with respect to the others (see Figures 5.20A and **??**). The method has been also applied to *in vivo* recordings, which $V - I$ curve is better fitted by a quadratic function than by a linear one. Even though actual conductances are unknown, the pattern estimated with the stochastic quadratization is more coherent that those obtained with the other linear procedures (see Figure 5.20B).

Hence, in Section 5.1 we provide two useful strategies to solve the estimation problem when ionic currents are active in the subthreshold, causing nonlinearities in the $V - I$ curve.

Even though we partially solved part of the estimation errors that linear methods provide in the subthreshold regime, other sources of misestimations could be taken into account, specially those originated from the dendro-somatic interaction (see Cox (2004)). As we have mentioned in Section 1.1, the input current coming from other cells is mainly received by the neuron in the dendrites. Then, this information flows to the soma where it can be recorded using different recording techniques. The flux coming from the dendrites to the soma is given by a partial differential equation (cable theory); we are aware of estimation techniques that have been developed in the area of image processing and could be used also in our problem, see Isakov (2006) and Aubert and Kornprobst (2006) among others.

Therefore, using some of these techniques, one could recover the synaptic current lost from the dendrite to the soma, where conductances can be estimated using one of our estimation procedures. Combining both methods, conductances in the dendrites might be estimated.

In order to answer the third equation, *can we also provide a first strategy to estimate conductances in those regimes where the target neuron presents an oscillatory behaviour?*, in Section 5.2 we have presented a procedure which shows good results both when synaptic current is constant (in its steady state) and when it slowly changes in time. Results indicate that new strategies can be obtained in this direction in order to successfully estimate conductances in the spiking regime, where no estimation procedures have been previously considered. The model considered in the estimation procedure, from where the periodic approximation is extracted, considers that the conductance is a constant parameter. An improvement to generalize the procedure is adding a third differential equation in the model in order to describe the dynamics of the conductances. Although we have to assume that conductances follow a pattern, they are usually supposed to follow an OU-process which could be a good candidate, as it is done in Rudolph et al (2004).

Despite of the variety of estimation procedures we have proposed in this thesis, the problem of conductances' estimation we think is a very difficult challenge to solve. From our point

of view, a multidisciplinary attack, including different areas of mathematics, is necessary. For this reason, in this thesis, we have approached the problem from different techniques in such a way that all the work done has a research goal, but also part of training purpose. In our opinion, it is good that a researcher in mathematical and computational neuroscience possesses an intense background in some mathematical areas, so we have emphasized in dynamical systems. However, it is also important to be aware of the benefits of using other mathematical approaches and computational tools. This is why we have introduced some research on stochastic processes and we have also used different computational methods along the thesis. Finally, a knowledge about neuroscience, both at cellular level and network level, is also fundamental, reason why we have also included the Chapter 4 about neuronal networks.

Appendix A

Matrix properties

Lemma A.1. *Given a block matrix or partitioned matrix*

$$X = \begin{pmatrix} A & B \\ C & D \end{pmatrix}$$

such that the block D is an invertible matrix, then $\det(X) = \det(D) \cdot \det(A - BD^{-1}C)$.

Proof. Since D is invertible, X can be factorized as

$$X = \begin{pmatrix} I & B \\ 0 & D \end{pmatrix} \cdot \begin{pmatrix} A - BD^{-1}C & 0 \\ D^{-1}C & I \end{pmatrix}.$$

Then, the lemma follows by noting that the determinant of both factors are $\det(D)$ and $\det(A - BD^{-1}C)$, respectively. $\square$

Lemma A.2. *Given two matrices A and X, the following statements hold.*

a) $\det(A + \varepsilon X) = \det(A) + O(\varepsilon)$.

b) If there exists a subscript i such that the i-th column of X is identically zero and the i-th column of A is of order one in ε, then $\det(A + \varepsilon X) = \det(A) + O\left(\varepsilon^2\right)$.

Proof. Let A_i and X_i be the i-th columns of the matrices A and X, respectively. By multilinearity, the determinant $\det(A + \varepsilon X)$ can be recast as

$$\det(A + \varepsilon X) = \det(A) + \varepsilon \left(\det(X_1, A_2 + \varepsilon X_2, \dots, A_n + \varepsilon X_n) \right.$$

$$+ \sum_{k=2}^{n-1} \det(A_1, \dots, A_{k-1}, X_k, A_{k+1} + \varepsilon X_{k+1}, \dots, A_n + \varepsilon X_n)$$

$$\left. + \det(A_1, \dots, A_{n-1}, X_n) \right),$$

which proves statement (a).

Without lost of generality, we assume that the i-th column in statement (b) is the last one. Therefore, from the above expression of $\det(A + \varepsilon X)$ it follows that, considering the term multiplied by ε, the determinant $\det(A_1, \dots, A_{n-1}, X_n)$ is zero whereas the rest of terms are order one in ε. This implies the proof of statement (b). $\square$

Lemma A.3. *Given $\lambda, \varepsilon \in \mathbb{R}$ with $\lambda \neq 0$, and an $s \times s$ matrix A, the following statements hold.*

a) *The determinant of the matrix $\varepsilon A - \lambda I$ can be expressed as*

$$\det(\varepsilon A - \lambda I) = (-\lambda)^s \left(1 - \mathrm{tr}(A)\frac{\varepsilon}{\lambda} + \frac{\mathrm{tr}(A)^2 - \mathrm{tr}(A^2)}{2}\left(\frac{\varepsilon}{\lambda}\right)^2 + \ldots + \det(A)\left(\frac{\varepsilon}{\lambda}\right)^s\right).$$

b) *For $|\varepsilon|$ small enough, the matrix $\varepsilon A - \lambda I$ is regular and*

$$(\varepsilon A - \lambda I)^{-1} = -\frac{1}{\lambda}\sum_{k=0}^{\infty}\left(\frac{\varepsilon A}{\lambda}\right)^k.$$

Moreover, let a_{ij} and z_{ij} be the (i,j)-th element of matrices A and $(\varepsilon A - \lambda I)^{-1}$, respectively. Then,

b.1) *the element z_{ij} satisfies*

$$z_{ij} = \begin{cases} -\dfrac{1}{\lambda}\left(1 + \dfrac{\varepsilon}{\lambda}a_{ii} + \left(\dfrac{\varepsilon}{\lambda}\right)^2 \sum_{k=1}^{s} a_{ik}a_{ki} + O(\varepsilon^3)\right) & \text{if } \ i = j, \\[4mm] -\dfrac{1}{\lambda}\left(\dfrac{\varepsilon}{\lambda}a_{ij} + \left(\dfrac{\varepsilon}{\lambda}\right)^2 \sum_{k=1}^{s} a_{ik}a_{kj} + O(\varepsilon^3)\right) & \text{if } \ i \neq j, \end{cases}$$

b.2) *and, when $a_{1j} = 0$ for all $j \in \{2, \ldots, s\}$,*

$$z_{11} = -\frac{1}{\lambda}\left(1 + \sum_{k=1}^{\infty}\left(\frac{\varepsilon a_{11}}{\lambda}\right)^k\right) \quad \text{and} \quad z_{1j} = 0 \text{ for } j \in \{2, \ldots, s\}.$$

Proof. The determinant $\det(\varepsilon A - \lambda I)$ is the characteristic polynomial of matrix εA evaluated at λ. Therefore, statement (a) follows by computing the coefficients of this polynomial by using the Newton's identities, see Kalman (2000).

The regularity of matrix $\varepsilon A - \lambda I$, for ε small enough, is a direct consequence of statement (a). On the other hand, since

$$(\varepsilon A - \lambda I)\left(I + \sum_{k=1}^{m}\left(\frac{\varepsilon A}{\lambda}\right)^k\right) = -\lambda I + \frac{(\varepsilon A)^{m+1}}{\lambda^m} = -\lambda\left(I + \left(\frac{\varepsilon A}{\lambda}\right)^{m+1}\right),$$

for every $m \geq 1$, we conclude that the series $I + \sum_{k=1}^{m}\left(\frac{\varepsilon A}{\lambda}\right)^k$ converges uniformly to $-\lambda(\varepsilon A - \lambda I)^{-1}$, for ε small enough.

Developing the three first terms of this series we obtain the expression of z_{ij} appearing in (b.1). Suppose now that $a_{1j} = 0$ for all $j \in \{2, \ldots, s\}$, that is $\mathbf{e}_1^T A = a_{11}\mathbf{e}_1^T$. Then $\mathbf{e}_1^T A^k = a_{11}^k \mathbf{e}_1^T$ for $k \geq 1$ and therefore

$$\mathbf{e}_1^T(\varepsilon A - \lambda I)^{-1} = -\frac{1}{\lambda}\sum_{k=0}^{\infty}\left(\frac{\varepsilon}{\lambda}\right)^k \mathbf{e}_1^T A^k = -\frac{1}{\lambda}\sum_{k=0}^{\infty}\left(\frac{\varepsilon a_{11}}{\lambda}\right)^k \mathbf{e}_1^T,$$

which proves statement (b.2). $\qquad\qquad\qquad\qquad\qquad\qquad\qquad\qquad\qquad\qquad\qquad\square$

Lemma A.4. *Given a matrix B and vectors $\mathbf{p}$ and $\mathbf{c}$ such that*

$$B = \begin{pmatrix} \varepsilon A & \varepsilon\mathbf{a} \\ \mathbf{e}_1^T & d \end{pmatrix}, \qquad \mathbf{p} = \begin{pmatrix} \mathbf{u} \\ 0 \end{pmatrix} \quad and \quad \mathbf{c} = \begin{pmatrix} \varepsilon\mathbf{b} \\ 0 \end{pmatrix}$$

where A is an $s \times s$ real matrix, $\mathbf{a}$, $\mathbf{b}$ and $\mathbf{u}$ are vectors in $\mathbb{R}^s$, $\mathbf{e}_1$ is the first element of the canonical base of $\mathbb{R}^s$ and d is a real constant. Therefore,

a) Assuming that $\mathbf{e}_1^T \mathbf{u} = 0$, then

$$B\,(B\mathbf{p} + \mathbf{c}) = \begin{pmatrix} \varepsilon^2 A\,(A\mathbf{u} + \mathbf{b}) \\ \varepsilon \mathbf{e}_1^T\,(A\mathbf{u} + \mathbf{b}) \end{pmatrix}.$$

b) For a given $k \geq 2$ and, assuming that $\mathbf{e}_1^T \mathbf{u} = 0$ and $\mathbf{e}_1^T A^l\,(A\mathbf{u} + \mathbf{b}) = 0$ for all $l = 0, \dots, k - 2$, then

$$B^k\,(B\mathbf{p} + \mathbf{c}) = \begin{pmatrix} \varepsilon^{k+1} A^k\,(A\mathbf{u} + \mathbf{b}) \\ \varepsilon^k \mathbf{e}_1^T A^{k-1}\,(A\mathbf{u} + \mathbf{b}) \end{pmatrix}.$$

Proof. The proof of statement (a) follows by straightforward computations.

To prove statement (b) we use a mathematical induction on the parameter k. Let $k = 2$ and assume $\mathbf{e}_1^T \mathbf{u} = 0$ and $\mathbf{e}_1^T\,(A\mathbf{u} + \mathbf{b}) = 0$. Then, using the expression in statement (a), we obtain that

$$B^2\,(B\mathbf{p} + \mathbf{c}) = \begin{pmatrix} \varepsilon A & \varepsilon\mathbf{a} \\ \mathbf{e}_1^T & d \end{pmatrix} \begin{pmatrix} \varepsilon^2 A\,(A\mathbf{u} + \mathbf{b}) \\ 0 \end{pmatrix} = \begin{pmatrix} \varepsilon^3 A^2\,(A\mathbf{u} + \mathbf{b}) \\ \varepsilon^2 \mathbf{e}_1^T A\,(A\mathbf{u} + \mathbf{b}) \end{pmatrix}.$$

Finally, assuming that $\mathbf{e}_1^T \mathbf{u} = 0$ and $\mathbf{e}_1^T A^l\,(A\mathbf{u} + \mathbf{b}) = 0$ for all $l = 0, \dots, k - 2$ and, supposing that expression in statement (b) holds for $k - 1$, we obtain

$$B^k\,(B\mathbf{p} + \mathbf{c}) = \begin{pmatrix} \varepsilon A & \varepsilon\mathbf{a} \\ \mathbf{e}_1^T & d \end{pmatrix} \begin{pmatrix} \varepsilon^k A^{k-1}\,(A\mathbf{u} + \mathbf{b}) \\ 0 \end{pmatrix} = \begin{pmatrix} \varepsilon^{k+1} A^k\,(A\mathbf{u} + \mathbf{b}) \\ \varepsilon^k \mathbf{e}_1^T A^{k-1}\,(A\mathbf{u} + \mathbf{b}) \end{pmatrix}.$$

$\square$

150

Appendix B

Maximum likelihood method

The Euler discretization of equation (5.11) is locally assumed to follow a Gaussian distribution with mean and variance $V_n + (aV_n^2 + bV_n + c)\Delta$ and $\sigma^2\Delta$, respectively. Hence, the probability density function is given by

$$p(V_n|V_{n-1}) = \frac{1}{\sqrt{2\pi\sigma^2\Delta}} \exp\left\{ -\frac{\left(V_n - V_{n-1} - (aV_{n-1}^2 + bV_{n-1} + c)\Delta\right)^2}{2\sigma^2\Delta} \right\},$$

and consequently, the log-likelihood of the diffusion processes is

$$\log \mathcal{L}(\theta) = \sum_{n=1}^{M} \left[\log\left(\frac{1}{\sqrt{2\pi\sigma^2\Delta}} \right) - \frac{\left(V_n - V_{n-1} - (aV_{n-1}^2 + bV_{n-1} + c)\Delta\right)^2}{2\sigma^2\Delta} \right]$$

such that θ is the vector of unknown parameters of the stochastic equation.

In the estimation procedure, we consider different cases of unknown parameters: the case when both α and the conductances are unknown, and so $\theta = (a, b, c)^T$; the case when only the conductances are supposed unknown, and so $\theta = (b, c)^T$ since $a = \alpha/C$ is considered to be known; and finally, the case when the only unknown parameter is α. Notice that in this last case, since g_E and g_I are known, b and c only depend on α/C, which is considered to be a; hence, b and c can be rewritten in terms of a and so $\theta = (a)$. Next we compute the maximum of the log-likelihood in each situation.

- When $\theta = (a, b, c)^T$, the maximum of the log-likelihood function is computed by solving the system given by

$$\left\{ \frac{d\log \mathcal{L}(\theta)}{da} = 0, \quad \frac{d\log \mathcal{L}(\theta)}{db} = 0, \quad \frac{d\log \mathcal{L}(\theta)}{dc} = 0 \right\}.$$

The solutions of this system, which are in turn the estimation of parameters a, b and c, must satisfy the following linear system:

$$\begin{pmatrix} \sum_{n=1}^{M} V_{n-1}^4 \Delta & \sum_{n=1}^{M} V_{n-1}^3 \Delta & \sum_{n=1}^{M} V_{n-1}^2 \Delta \\ \sum_{n=1}^{M} V_{n-1}^3 \Delta & \sum_{n=1}^{M} V_{n-1}^2 \Delta & \sum_{n=1}^{M} V_{n-1} \Delta \\ \sum_{n=1}^{M} V_{n-1}^2 \Delta & \sum_{n=1}^{M} V_{n-1} \Delta & \sum_{n=1}^{M} \Delta \end{pmatrix} \cdot \begin{pmatrix} a \\ b \\ c \end{pmatrix} = \begin{pmatrix} \sum_{n=1}^{M} (V_n V_{n-1}^2 - V_{n-1}^3) \\ \sum_{n=1}^{M} (V_n V_{n-1} - V_{n-1}^2) \\ \sum_{n=1}^{M} (V_n - V_{n-1}) \end{pmatrix}.$$

$$(\text{B.1})$$

- When $\theta = (b, c)^T$ the maximum of the log-likelihood function is computed by solving the system given by

$$\left\{ \frac{d \log \mathcal{L}(\theta)}{db} = 0, \quad \frac{d \log \mathcal{L}(\theta)}{dc} = 0 \right\},$$

to obtain an estimation of parameters b and c as solutions of the linear system

$$\begin{pmatrix} \sum\limits_{n=1}^{M} V_{n-1}^2 \Delta & \sum\limits_{n=1}^{M} V_{n-1} \Delta \\ \sum\limits_{n=1}^{M} V_{n-1} \Delta & \sum\limits_{n=1}^{M} \Delta \end{pmatrix} \cdot \begin{pmatrix} b \\ c \end{pmatrix} = \begin{pmatrix} \sum\limits_{n=1}^{M} (V_n V_{n-1} - V_{n-1}^2) - a \sum\limits_{n=1}^{M} V_{n-1}^3 \Delta \\ \sum\limits_{n=1}^{M} (V_n - V_{n-1}) - a \sum\limits_{n=1}^{M} V_{n-1}^2 \Delta \end{pmatrix} \tag{B.2}$$

- Finally, when $\theta = (a)$, the maximum of the log-likelihood is computed by solving the equation

$$\frac{d \log \mathcal{L}(\theta)}{da} = 0.$$

Since parameters b and c depend also on $a = \alpha/C$, we need to take into account that b and c are functions of a when we are deriving the log-likelihood respect to a. Then, the maximum of the log-likelihood is given by

$$\sum_{n=1}^{M} (V_{n-1}^2 - 2V_T V_{n-1} + V_T^2)^2 \Delta \, a = \sum_{n=1}^{M} (V_n - V_{n-1} - \beta_t V_{n-1} \Delta - \lambda_t \Delta)(V_{n-1}^2 - 2V_T V_{n-1} + V_T^2) \tag{B.3}$$

where

$$\beta_t = (-g_{E,n} - g_{I,n})/C, \quad \text{and} \quad \lambda_t = (g_{E,n} v_E + g_{I,n} v_I - I_T + I_{app})/C$$

Appendix C

Routines for the estimation procedures in the McKean model

C.1 Routine to compute the numerical period

Consider the solution (5.17) of the model given by the piecewise differential system (5.14).

a) Let $x_0 = (\frac{a}{2}, w_0) = \mathbf{q}_L$, $\bar{T}_0 = 0$ be the initial condition.

1. Let x_0 be the initial condition and compute $T_{M,down}$ as a zero of the equation $v(t) - \frac{1+a}{2}$. Then, knowing $t = T_{M,down}$, we can compute $w_1 = w(T_{M,down})$, and so we obtain a new point $x_1 = (\frac{1+a}{2}, w_1)$.

2. Let x_1 be the initial condition and compute T_R as a zero of the equation $v(t) - \frac{1+a}{2}$. Then, knowing $t = T_R$, we can compute $w_2 = w(T_R)$, and so we obtain a new point $x_2 = (\frac{1+a}{2}, w_2)$.

3. Let x_2 be the initial condition and compute $T_{M,up}$ as a zero of the equation $v(t) - \frac{a}{2}$. Then, knowing $t = T_{M,up}$, we can compute $w_3 = w(T_{M,up})$, and so we obtain a new point $x_3 = (\frac{1+a}{2}, w_3)$.

4. Let x_3 be the initial condition and compute T_L as a zero of the equation $v(t) - \frac{a}{2}$. Then, knowing $t = T_L$, we can compute $w_4 = w(T_L)$, and so we obtain a new point $x_4 = (\frac{a}{2}, w_4)$.

5. Compute $\bar{T} = T_L + T_{M,down} + T_R + T_{M,up}$

b) If $|w_0 - w_4| <$tolerance or $|\bar{T}_0 - \bar{T}| <$tolerance, DONE: the numerical period is $\bar{T}$. Otherwise, let $x_0 = x_4$, $\bar{T}_0 = \bar{T}$, and repeat steps 1-5.

The considered numerical method to find the zero of the function has been both the Newton method and the Bisection method, obtaining the same results. Moreover, we have considered a tolerance $1e - 11$ for the period of each regime (steps 1-4) and a tolerance $1e - 10$ for the step b).

C.2 Routine to estimate the steady synaptic conductance

Given a neuron that can be modelled by system (5.14), suppose known all its parameters except the synaptic conductance. Then, for an applied current I, one can compute the

period T of the *volatge*. Then,

a) Using a numerical method to solve implicit equations, such as the Bisection method or the Newton method, solve the equation $\hat{T}(C, I, g_{syn}) = T^*$ to compute g_{syn}. Then, for each solution found,

  1. If $g_{syn} > \max\left(0, \bar{I}_1, \bar{I}_2\right)$ such that

$$\bar{I}_1 = \frac{2\gamma I - (\gamma + 1)a + 2v_0 - 2\gamma w_0}{2\gamma(\frac{a}{2} - V_{syn})} \quad and$$

$$\bar{I}_2 = \frac{2\gamma I - (\gamma + 1)a + 2v_0 - 2\gamma w_0 - \gamma + 1}{2\gamma(\frac{a+1}{2} - V_{syn})}$$

  then, we accept the value of g_{syn} as the correct one.

  2. Otherwise, we need to find another solution of the implicit equation.

Bibliography

(2015) Divisive gain modulation of motoneurons by inhibition optimizes muscular control. J Neurosci 35:3711–3723

Abbott L (1990) A network of oscillators. Journal of Physics A: Mathematical and General 23(16):3835

Abbott LF, Regehr WG (2004) Synaptic computation. Nature 431:796–803, doi:10.1038/nature03010

Akman O, Broomhead D, Abadi R, Clement R (2005) Eye movement instabilities and nystagmus can be predicted by a nonlinear dynamics model of the saccadic system. Journal of Mathematical Biology 51(6):661–694

Anderson JS, Carandini M, Ferster D (2000) Orientation tuning of input conductance, excitation, and inhibition in cat primary visual cortex. Journal of neurophysiology 84(2):909–926, URL http://jn.physiology.org/content/84/2/909.abstract

Arima N, Okazaki H, Nakano H (1997) A generation mechanism of canards in a piecewise linear system. IEICE Transactions on Fundamentals of Electronics, Communications and Computer Sciences 80(3):447–453

Aubert G, Kornprobst P (2006) Mathematical Problems in Image Processing: Partial Differential Equations and the Calculus of Variations (Applied Mathematical Sciences). Springer-Verlag New York, Inc., Secaucus, NJ, USA

Baron M (2013) Probability and Statistics for Computer Scientists, Second Edition, 2nd edn. Chapman & Hall/CRC

Bédard C, Béhuret S, Deleuze C, Bal T, Destexhe A (2011a) https://senselab.med.yale.edu/modeldb/showmodel.cshtml?model=145803&file=%5cextraction-demo%5creadme.pdf

Bédard C, Béhuret S, Deleuze C, Bal T, Destexhe A (2011b) Oversampling method to extract excitatory and inhibitory conductances from single-trial membrane potential recordings. Journal of neuroscience methods doi:10.1016/j.jneumeth.2011.09.010, URL http://dx.doi.org/10.1016/j.jneumeth.2011.09.010

Benita J, Guillamon A, Deco G, Sánchez-Vives M (2012) Synaptic depression and slow oscillatory activity in a biophysical network model of the cerebral cortex. Frontiers in computational neuroscience 6(64):1–17, doi:10.3389/fncom.2012.00064

Bennett C, Arroyo S, Hestrin S (2013) Subthreshold mechanisms underlying state-dependent modulation of visual responses. Neuron 80(2):350 – 357, doi:http://dx.doi.org/10.1016/j.neuron.2013.08.007, URL http://www.sciencedirect.com/science/article/pii/S0896627313007186

Benoît E (1996) Asymptotic expansions of canards with poles. application to the stationary
unidimensional schrödinger equation. Bulletin of the Belgian Mathematical Society -
Simon Stevin pp 71–90, URL `http://eudml.org/doc/119561`

Benoît E, Callot J, Diener F, Diener M (1981) Chasse au ca-
nard (première partie). Collectanea Mathematica 31:37 – 119, URL
`http://www.raco.cat/index.php/CollectaneaMathematica/article/view/57730`

Berg RW (2013) www.mathworks.com/matlabcentral/fileexchange/41774-
synapticconductance

Berg RW, Ditlevsen S (2013) Synaptic inhibition and excitation estimated via the time
constant of membrane potential fluctuations. Journal of Neurophysiology 110(4):1021–
1034, doi:10.1152/jn.00006.2013

Berg RW, Alaburda A, Hounsgaard J (2007) Balanced inhibition and excita-
tion drive spike activity in spinal half-centers. SCIENCE 315(5810):390–393,
doi:10.1126/science.1134960

Berglund N, Gentz B (2008) Stochastic dynamic bifurcations and excitability. In: Stochas-
tic methods in Neuroscience, pp 64–93

Bologna LL, Pasquale V, Garofalo M, Gandolfo M, Baljon PL, Maccione
A, Martinoia S, Chiappalone M (2010) Investigating neuronal activity by
{SPYCODE} multi-channel data analyzer. Neural Networks 23(6):685 – 697,
doi:http://dx.doi.org/10.1016/j.neunet.2010.05.002, analysis and Modeling of Massively
Parallel Neural Signals

Borg-Graham L, Monier C, Frégnac Y (1998) Visual input evokes transient and
strong shunting inhibition in visual cortical neurons. Nature 393(6683):369–373,
doi:10.1038/30735, URL `http://dx.doi.org/10.1038/30735`

Brette R, Gerstner W (2005) Adaptive exponential integrate-and-fire model as an ef-
fective description of neuronal activity. Journal of Neurophysiology 94(5):3637–3642,
doi:10.1152/jn.00686.2005, URL `http://jn.physiology.org/content/94/5/3637`

Brøns M, Krupa M, Wechselberger M (2006) Mixed Mode Oscillations due to the General-
ized Canard Phenomenon, American Mathematical Society, pp 39–64. Fields Insititute
Communications

Brøns M, Desroches M, Krupa M (2013) Mixed-mode oscillations due to a sin-
gular Hopf bifurcation in a forest pest model. Rapport de recherche, URL
`http://hal.inria.fr/hal-00924098`

Brunel N, van Rossum M (2007) Lapicque's 1907 paper: from frogs to integrate-
and-fire. Biological Cybernetics 97(5-6):337–339, doi:10.1007/s00422-007-0190-0, URL
`http://dx.doi.org/10.1007/s00422-007-0190-0`

Burnham KP, Anderson DR (2002) Model selection and multimodel inference: A practical
information-theoretic approach. Springer

Buzsáki G, Draguhn A (2004) Neuronal oscillations in cortical networks. Sci-
ence (New York, NY) 304(5679):1926–1929, doi:10.1126/science.1099745, URL
`http://dx.doi.org/10.1126/science.1099745`

Buzzi C, De Carvalho T, Teixeira M (2012) On 3-parameter families of piecewise smooth
vector fields in the plane. SIAM Journal on Applied Dynamical Systems 11(4):1402–1424

Ramon y Cajal S (1894) The croonian lecture: La fine struc-
ture des centres nerveux. Proceedings of the Royal Society
of London 55(331-335):444–468, doi:10.1098/rspl.1894.0063, URL
`http://rspl.royalsocietypublishing.org/content/55/331-335/444.short`

Carbone E, Marcantoni A, Giancippoli A, Guido D, Carabelli V (2006) T-
type channels-secretion coupling: evidence for a fast low-threshold exocy-
tosis. Pflügers Archiv 453(3):373–383, doi:10.1007/s00424-006-0100-7, URL
`http://dx.doi.org/10.1007/s00424-006-0100-7`

Chen Z (2003) Bayesian Filtering: From Kalman Filters to Par-
ticle Filters, and Beyond. Tech. rep., McMaster University, URL
`http://soma.crl.mcmaster.ca/~{}zhechen/ieee_bayes.ps`

Closas P (2014) Sequential estimation of neural models by bayesian filtering. diploma
thesis, FME-Univ. Politènica de Catalunya

Compte A, Sánchez-Vives MV, McCormick DA, Wang XJ (2003) Cellular and network
mechanisms of slow oscillatory activity (. Journal of Neurophysiology 89(5):2707–2725,
doi:10.1152/jn.00845.2002, URL `http://jn.physiology.org/content/89/5/2707`

Coombes S (2001) Phase locking in networks of synaptically cou-
pled mckean relaxation oscillators. Physica D: Nonlinear Phenomena
160(3–4):173 – 188, doi:http://dx.doi.org/10.1016/S0167-2789(01)00352-9, URL
`http://www.sciencedirect.com/science/article/pii/S0167278901003529`

Coombes S (2008) Neuronal networks with gap junctions: A study of piecewise linear
planar neuron models. SIAM Journal on Applied Dynamical Systems 7(3):1101–1129,
doi:10.1137/070707579, URL `http://dx.doi.org/10.1137/070707579`

Coombes S, Thul R, Wedgwood K (2012) Nonsmooth dynamics in spik-
ing neuron models. Physica D: Nonlinear Phenomena 241(22):2042
– 2057, doi:http://dx.doi.org/10.1016/j.physd.2011.05.012, URL
`http://www.sciencedirect.com/science/article/pii/S0167278911001217`, dy-
namics and Bifurcations of Nonsmooth Systems

Cox SJ (2004) Estimating the location and time course of synaptic input from multi-site
potential recordings. J of Computational Neuroscience 17:225–243

Dayan P, Abbott LF (2005) Theoretical neuroscience: computational
and mathematical modeling of neural systems. MIT Press, URL
`http://www.worldcat.org/isbn/9780262041997`

Desroches M, Jeffrey MR (2011) Canards and curvature: nons-
mooth approximation by pinching. Nonlinearity 24(5):1655, URL
`http://stacks.iop.org/0951-7715/24/i=5/a=014`

Desroches M, Krauskopf B, HM O (2010) Numerical continuation of ca-
nard orbits in slow-fast dynamical systems. Nonlinearity 23(3):739, URL
`http://stacks.iop.org/0951-7715/23/i=3/a=017`

Desroches M, Guckenheimer J, Krauskopf B, Kuehn C, Osinga H, Wechselberger M
(2012) Mixed-mode oscillations with multiple time scales. SIAM Review 54(2):211–288,
doi:10.1137/100791233, URL `http://epubs.siam.org/doi/abs/10.1137/100791233`

Desroches M, Freire E, Hogan SJ, Ponce E, Thota P (2013) Canards in piecewise-linear systems: explosions and super-explosions. Proceedings of the Royal Society A: Mathematical, Physical and Engineering Science 469(2154), doi:10.1098/rspa.2012.0603, URL http://rspa.royalsocietypublishing.org/content/469/2154/20120603.abstract

Desroches M, Guillamon A, Ponce E, Prohens R, Rodrigues S, Teruel A (2016a) Canards, folded nodes and mixed-mode oscillations in piecewise-linear slow-fast systems, URL https://hal.inria.fr/hal-01243289, sIAM Review, in press

Desroches M, Guillamon A, Ponce E, Prohens R, Rodrigues S, Teruel AE (2016b) Canards, folded nodes and mixed-mode oscillations in piecewise-linear slow-fast systems. SIAM Review (to be published)

Destexhe A, Babloyantz A, Sejnowski T (1993) Ionic mechanisms for intrinsic slow oscillations in thalamic relay neurons. Biophysical Journal 65:1538–1552, URL http://www.ncbi.nlm.nih.gov/pmc/articles/PMC1225880/

Destexhe A, Rudolph M, Paré D (2003) The high-conductance state of neocortical neurons in vivo. Nature Reviews Neuroscience 4(9):739–751, doi:10.1038/nrn1198, URL http://dx.doi.org/10.1038/nrn1198

Di Bernardo M (2008) Piecewise-smooth dynamical systems : theory and applications. Applied mathematical sciences, Springer, London, URL http://opac.inria.fr/record=b1122347

Dickson CT, Magistretti J, Shalinsky MH, Fransén E, Hasselmo ME, Alonso A (2000) Properties and role of I(h) in the pacing of subthreshold oscillations in entorhinal cortex layer II neurons. Journal of neurophysiology 83(5):2562–2579, URL http://view.ncbi.nlm.nih.gov/pubmed/10805658

Diesmann M, Gewaltig MO, Aertsen A (1999) Stable propagation of synchronous spiking in cortical neural networks. Nature 402:529–533

Ditlevsen S, Samson A (2013) Stochastic Biomathematical Models: with Applications to Neuronal Modeling, Springer Berlin Heidelberg, Berlin, Heidelberg, chap Introduction to Stochastic Models in Biology, pp 3–35. doi:10.1007/978-3-642-32157-3_1, URL http://dx.doi.org/10.1007/978-3-642-32157-3_1

Ditlevsen S, Samson A (2014) Estimation in the partially observed stochastic morris-lecar neuronal model with particle filter and stochastic approximation methods. Ann Appl Stat 8(2):674–702, doi:10.1214/14-AOAS729, URL http://dx.doi.org/10.1214/14-AOAS729

Doi S, Kumagai S (2004) Complicated slow oscillations with simple switching dynamics in piecewise linear neuronal model. In: Circuits and Systems, 2004. MWSCAS '04. The 2004 47th Midwest Symposium on, vol 2, pp II–609 – II–612 vol.2, doi:10.1109/MWSCAS.2004.1354232

Dumortier F, Roussarie R (1996) Canard Cycles and Center Manifolds. No. núm. 577 in American Mathematical Society: Memoirs of the American Mathematical Society, American Mathematical Soc., URL https://books.google.es/books?id=olPBm-cFx_MC

Eckhaus W (1983) Asymptotic Analysis II —: Surveys and New Trends, Springer Berlin Heidelberg, Berlin, Heidelberg, chap Relaxation oscillations including a standard chase on French ducks, pp 449–494. doi:10.1007/BFb0062381, URL http://dx.doi.org/10.1007/BFb0062381

Ermentrout B, Terman DH (2010) Mathematical foundations of neuroscience. Interdisciplinary applied mathematics, Springer, New York, Dordrecht, Heidelberg, URL `http://opac.inria.fr/record=b1130863`

Ermentrout GB, Kopell N (1986) Parabolic bursting in an excitable system coupled with a slow oscillation. SIAM J Appl Math 46(2):233–253, doi:10.1137/0146017, URL `http://dx.doi.org/10.1137/0146017`

Eytan D, Marom S (2006) Dynamics and effective topology underlying synchronization in networks of cortical neurons. The Journal of neuroscience : the official journal of the Society for Neuroscience 26(33):8465–8476, doi:10.1523/jneurosci.1627, URL `http://dx.doi.org/10.1523/jneurosci.1627`

Fenichel N (1979) Geometric singular perturbation theory for ordinary differential equations. Journal of Differential Equations 31(1):53–98

Fernández-García S, Desroches M, Krupa M, Clément F (2015) A multiple time scale coupling of piecewise linear oscillators. application to a neuroendocrine system. SIAM Journal on Applied Dynamical Systems 14(2):643–673, doi:10.1137/140984464, URL `http://dx.doi.org/10.1137/140984464`

Filippov AF (1988) Differential Equations with Discontinuous Righthand Sides: Control Systems, 1st edn. Springer

FitzHugh R (1961) Impulses and Physiological States in Theoretical Models of Nerve Membrane. Biophysical Journal 1:445–466, doi:10.1016/S0006-3495(61)86902-6

Fourcaud-Trocmé N, Hansel D, van Vreeswijk C, Brunel N (2003) How spike generation mechanisms determine the neuronal response to fluctuating inputs. J Neurosci 23(37):11,628–11,640, URL `http://www.jneurosci.org/cgi/content/abstract/23/37/11628`

Granados A, Krupa M (2015) Firing-rate, symbolic dynamics and frequency dependence in periodically driven spiking models: a piecewise-smooth approach. Nonlinearity 28(5):1163, URL `http://stacks.iop.org/0951-7715/28/i=5/a=1163`

Guillamon A, McLaughlin DW, Rinzel J (2006) Estimation of synaptic conductances. Journal of Physiology-Paris 100(1-3):31–42, doi:10.1016/j.jphysparis.2006.09.010, URL `http://dx.doi.org/10.1016/j.jphysparis.2006.09.010`

Hirsch JA, Alonso JM, Reid CR, Martinez LM (1998) Synaptic Integration in Striate Cortical Simple Cells. Journal of Neuroscience 18(22):9517–9528, URL `http://www.jneurosci.org/cgi/content/abstract/18/22/9517`

Hodgkin AL, Huxley AF (1952) A quantitative description of membrane current and its application to conduction and excitation in nerve. The Journal of Physiology 117(4):500–544, doi:10.1113/jphysiol.1952.sp004764, URL `http://dx.doi.org/10.1113/jphysiol.1952.sp004764`

Hotson JR, Prince DA (1980) A calcium-activated hyperpolarization follows repetitive firing in hippocampal neurons. J Neurophysiology 43(2):409–419, URL `http://jn.physiology.org/content/43/2/409.full`

Iacus SM (2008) Simulation and Inference for Stochastic Differential Equations: With R Examples (Springer Series in Statistics), 1st edn. Springer Publishing Company, Incorporated

Isakov V (2006) Inverse problems for partial differential equations, Applied Mathematical Sciences, vol 127, 2nd edn. Springer, New York, URL `MR2193218.pdf`

Itoh M, Tomiyasu R (1990) Experimental study of the missing solutions canards. IEICE Transactions on Fundamentals of Electronics, Communications and Computer Sciences 73(6):848–854

Izhikevich EM (2007) Dynamical systems in neuroscience: the geometry of excitability and bursting. Computational Neuroscience, MIT Press, Cambridge, MA

Jacquemard A, Teixeira M, Tonon D (2013) Stability conditions in piece-wise smooth dynamical systems at a two-fold singularity. Journal of Dynamical and Control Systems 19(1):47–67, doi:10.1007/s10883-013-9164-9, URL `http://dx.doi.org/10.1007/s10883-013-9164-9`

Jahn P, Berg RW, Hounsgaard J, Ditlevsen S (2011) Motoneuron membrane potentials follow a time inhomogeneous jump diffusion process. JOURNAL OF COMPUTATIONAL NEUROSCIENCE 31(3):563–579, doi:10.1007/s10827-011-0326-z

Jeffrey M, Colombo A (2009) The two-fold singularity of discontinuous vector fields. SIAM Journal on Applied Dynamical Systems 8(2):624–640, doi:10.1137/08073113X, URL `http://epubs.siam.org/doi/abs/10.1137/08073113X`

Jimenez ND, Mihalas S, Brown R, Niebur E, Rubin J (2013) Locally contractive dynamics in generalized integrate-and-fire neurons. SIAM J Applied Dynamical Systems 12(3):1474–1514, URL `http://dblp.uni-trier.de/db/journals/siamads/siamads12.html#JimenezMBNR13`

Jones C (1995) Geometric singular perturbation theory. In: Dynamical systems, Springer, pp 44–118

Kalman D (2000) A Matrix Proof of Newton's Identities. Mathematics Magazine 73(4), doi:10.2307/2690982, URL `http://dx.doi.org/10.2307/2690982`

Kandel ER, Schwartz JH, Jessell TM, Mack S (eds) (2013) Principles of neural science. McGraw-Hill Medical, New York, Chicago, San Francisco, URL `http://opac.inria.fr/record=b1135227`

Khorasani K (1986) On linearization of nonlinear singularly perturbed systems. IEEE Trans Aut Control AC-31:256

Khorasani K (1989) A slow manifold approach to linear equivalents of nonlinear singularly perturbed systems. Automatica 25(2):301–306, doi:http://dx.doi.org/10.1016/0005-1098(89)90085-X, URL `http://www.sciencedirect.com/science/article/pii/000510988990085X`

Kobayashi R, Tsubo Y, Lansky P, Shinomoto S (2011) Estimating time-varying input signals and ion channel states from a single voltage trace of a neuron. Advances in Neural Information Processing Systems (NIPS) 24:217–225

Kokotović P, Khalil HK, O'Reilly J (1999) Singular Perturbation Methods in Control. Analysis and Design. Classics in Applied Mathematics, SIAM, Philadelphia, PA

Komuro M, Saito T (1991) Lost solution in a piecewise linear system. IEICE Transactions on Fundamentals of Electronics, Communications and Computer Sciences 74(11):3625–3627

Krupa M, Szmolyan P (2001) Extending Geometric Singular Perturbation Theory to Non-hyperbolic Points—Fold and Canard Points in Two Dimensions. SIAM Journal on Mathematical Analysis 33(2):286–314

Krupa M, Popović N, Kopell N, Rotstein HG (2008) Mixed-mode oscillations in a three time-scale model for the dopaminergic neuron. Chaos (Woodbury, NY) 18(1), doi:10.1063/1.2779859, URL http://dx.doi.org/10.1063/1.2779859

Kuehn C (2015) Multiple Time Scale Dynamics, vol. 191 edn. Applied Mathematical Sciences, Springer, URL http://link.springer.com/book/10.1007%2F978-3-319-12316-5

Lankarany M, Zhu WP, Swamy M, Toyoizumi T (2013a) Blind deconvolution of hodgkin-huxley neuronal model. In: Engineering in Medicine and Biology Society (EMBC), 2013 35th Annual International Conference of the IEEE, pp 3941–3944, doi:10.1109/EMBC.2013.6610407

Lankarany M, Zhu WP, Swamy MNS, Toyoizumi T (2013b) Inferring trial-to-trial excitatory and inhibitory synaptic inputs from membrane potential using Gaussian mixture Kalman filtering. Frontiers in Computational Neuroscience 7, doi:10.3389/fncom.2013.00109, URL http://dx.doi.org/10.3389/fncom.2013.00109

Lee DeVille R, Vanden-Eijnden E, Muratov C (2005) Two distinct mechanisms of coherence in randomly perturbed dynamical systems. Physical Review E 72(3), doi:10.1103/PhysRevE.72.031105

Llibre J, Teruel AE (2004) Existence of poincaré maps in piecewise linear differential systems in $\mathbb{R}^n$. International Journal of Bifurcation and Chaos 14(08):2843–2851, doi:10.1142/S0218127404010874, URL http://www.worldscientific.com/doi/abs/10.1142/S0218127404010874

Llibre J, Teruel AE (2013) Introduction to the qualitative theory of differential systems: planar, symmetric and continuous piecewise linear systems. Springer Science & Business Media

Llibre J, Nuñez E, Teruel AE (2002) Limit cycles for planar piecewise linear differential systems via first integrals. Qual Theory Dyn Syst 3(1):29–58

Llibre J, Ordóñez M, Ponce E (2013) On the existence and uniqueness of limit cycles in planar continuous piecewise linear systems without symmetry. Nonlinear Analysis: Real World Applications 14(5):2002 – 2012, doi:http://dx.doi.org/10.1016/j.nonrwa.2013.02.004, URL http://www.sciencedirect.com/science/article/pii/S1468121813000199

Lombardi F, Herrmann HJ, Perrone-Capano C, Plenz D, de Arcangelis L (2012) Balance between excitation and inhibition controls the temporal organization of neuronal avalanches. Phys Rev Lett 108:228,703, doi:10.1103/PhysRevLett.108.228703, URL http://link.aps.org/doi/10.1103/PhysRevLett.108.228703

Marguet SL, Harris KD (2011) State-dependent representation of amplitude-modulated noise stimuli in rat auditory cortex. The Journal of neuroscience : the official journal of the Society for Neuroscience 31(17):6414–6420, doi:10.1523/jneurosci.5773-10.2011, URL http://dx.doi.org/10.1523/jneurosci.5773-10.2011

Massobrio P, Baljon PL, Maccione A, Chiappalone M, Martinoia S (2007) Activity modulation elicited by electrical stimulation in networks of dissociated cortical neurons. In: Engineering in Medicine and Biology Society, 2007. EMBS 2007. 29th Annual International Conference of the IEEE, pp 3008–3011, doi:10.1109/IEMBS.2007.4352962

Matzinger E (2006) Asymptotic behaviour of solutions near a turning point: The example of the brusselator equation. Journal of Differential Equations 220(2):478 – 510, doi:http://dx.doi.org/10.1016/j.jde.2005.06.028, URL http://www.sciencedirect.com/science/article/pii/S0022039605002159

McKean HP (1970) Nagumo's equation. Advances in Math 4:209–223

McLaughlin D, Shapley R, Shelley M, Wielaard DJ (2000) A neuronal network model of macaque primary visual cortex (V1): orientation selectivity and dynamics in the input layer 4Calpha. Proceedings of the National Academy of Sciences of the United States of America 97(14):8087–8092, doi:10.1073/pnas.110135097, URL http://dx.doi.org/10.1073/pnas.110135097

Molleman A (2003) Patch Clamping: An Introductory Guide to Patch Clamp Electrophysiology. Wiley InterScience electronic collection, Wiley, URL https://books.google.es/books?id=JBY9NUsq2DkC

Monier C, Fournier J, Fregnac Y (2008) In vitro and in vivo measures of evoked excitatory and inhibitory conductance dynamics in sensory cortices. Journal of Neuroscience Methods 169(2):323–365, doi:10.1016/j.jneumeth.2007.11.008, URL http://dx.doi.org/10.1016/j.jneumeth.2007.11.008

Nagumo J, Arimoto S, Yoshizawa S (1962) An active pulse transmission line simulating nerve axon. Proceedings of the IRE 50(10):2061–2070, doi:10.1109/JRPROC.1962.288235

Nakano H, Honda H, Okazaki H (2005) Canards in a slow-fast continuous piecewise linear vector field. In: Circuits and Systems, 2005. ISCAS 2005. IEEE International Symposium on, pp 3757–3760 Vol. 4, doi:10.1109/ISCAS.2005.1465447

Paninski L, Vidne M, DePasquale B, Ferreira DG (2012) Inferring synaptic inputs given a noisy voltage trace via sequential monte carlo methods. Journal of Computational Neuroscience 33(1):1–19, URL http://link.springer.com/article/10.1007/s10827-011-0371-7

Parga N, Abbott LF (2007) Network model of spontaneous activity exhibiting synchronous transitions between up and down states. Frontiers in Neuroscience 1(4), doi:10.3389/neuro.01.1.1.004.2007, URL http://www.frontiersin.org/neuroscience/10.3389/neuro.01.1.1.004.2007/abstract

van Pelt J, Wolters PS, Corner MA, Rutten WLC, Ramakers GJA (2004) Long-term characterization of firing dynamics of spontaneous bursts in cultured neural networks. IEEE Trans Biomed Engineering 51:2051–2062

Perko L (1982) Dynamical systems. Springer

Petersen PC, Vestergaard M, Jensen KH, Berg RW (2014) Premotor spinal network with balanced excitation and inhibition during motor patterns has high resilience to structural division. The Journal of neuroscience : the official journal of the Society for Neuroscience 34(8):2774–2784, doi:10.1523/jneurosci.3349-13.2014, URL http://dx.doi.org/10.1523/jneurosci.3349-13.2014

Pokrovskii A, Rachinskii D, Sobolev V, Zhezherun A (2011) Topological degree in analysis of canard-type trajectories in 3-d systems. Applicable Analysis 90(7):1123–1139, doi:10.1080/00036811.2010.511193, URL `http://www.tandfonline.com/doi/abs/10.1080/00036811.2010.511193`

Pospischil M, Piwkowska Z, Bal T, Destexhe A (2009) Extracting synaptic conductances from single membrane potential traces. Neuroscience (158):545–552

Prohens R, Teruel AE (2013) Canard trajectories in 3d piecewise linear systems. Discrete Contin Dyn Syst 33(10):4595–4611, doi:10.3934/dcds.2013.33.4595

Prohens R, Teruel A, Vich C (2016) Slow–fast n-dimensional piecewise linear differential systems. Journal of Differential Equations 260(2):1865 – 1892, doi:http://dx.doi.org/10.1016/j.jde.2015.09.046, URL `http://www.sciencedirect.com/science/article/pii/S0022039615005203`

Reig R, Gallego R, Nowak L, Sanchez-Vives M (2006) Impact of cortical network activity on short-term synaptic depression. Cerebral Cortex 16(5):688–95, doi:10.1093/cercor/bhj014

Renart A, de la Rocha J, Bartho P, Hollender L, Parga N, Reyes A, Harris KD (2010) The Asynchronous State in Cortical Circuits. Science 327(5965):587–590, doi:10.1126/science.1179850, URL `http://dx.doi.org/10.1126/science.1179850`

Rotstein H (2015) Subthreshold amplitude and phase resonance in models of quadratic type: Nonlinear effects generated by the interplay of resonant and amplifying currents. Journal of Computational Neuroscience 38(2):325–354, doi:10.1007/s10827-014-0544-2, URL `http://dx.doi.org/10.1007/s10827-014-0544-2`

Rotstein H, Oppermann T, White J, Kopell N (2006) The dynamic structure underlying subthreshold oscillatory activity and the onset of spikes in a model of medial entorhinal cortex stellate cells. Journal of Computational Neuroscience 21(3):271–292, doi:10.1007/s10827-006-8096-8, URL `http://dx.doi.org/10.1007/s10827-006-8096-8`

Rotstein HG, Coombes S, Gheorghe AM (2012) Canard-like explosion of limit cycles in two-dimensional piecewise-linear models of fitzhugh-nagumo type. SIAM J Applied Dynamical Systems 11(1):135–180, URL `http://dblp.uni-trier.de/db/journals/siamads/siamads11.html#RotsteinCG12`

Rubin JE, Terman D (2000) Geometric singular perturbation analysis of neuronal dynamics. In: in Handbook of Dynamical Systems, North-Holland, pp 93–146

Rudolph M, Piwkowska Z, Badoual M, Bal T, Destexhe A (2004) A method to estimate synaptic conductances from membrane potential fluctuations. Journal of Neurophysiology 91(6):2884–2896, doi:10.1152/jn.01223.2003, URL `http://jn.physiology.org/content/91/6/2884.full`

Stevens CF, Wang Y (1995) Facilitation and depression at single central synapses. Neuron 14(4):795 – 802, doi:http://dx.doi.org/10.1016/0896-6273(95)90223-6, URL `http://www.sciencedirect.com/science/article/pii/0896627395902236`

Szmolyan P, Wechselberger M (2001) Canards in {R3}. Journal of Differential Equations 177(2):419 – 453, doi:http://dx.doi.org/10.1006/jdeq.2001.4001, URL `http://www.sciencedirect.com/science/article/pii/S002203960194001X`

Tao L, Shelley M, McLaughlin D, Shapley R (2004) An egalitarian network model for the emergence of simple and complex cells in visual cortex. Proceedings of the National Academy of Sciences of the United States of America 101(1):366–371, doi:10.1073/pnas.2036460100, URL http://dx.doi.org/10.1073/pnas.2036460100

Tonnelier A (2003) The mckean's caricature of the fitzhugh–nagumo model i. the space-clamped system. SIAM Journal on Applied Mathematics 63(2):459–484, doi:10.1137/S0036139901393500, URL http://dx.doi.org/10.1137/S0036139901393500

Tonnelier A, Gerstner W (2003) Piecewise linear differential equations and integrate-and-fire neurons : insights from two-dimensional membrane models. Phys Rev E 67(2):21,908, doi:10.1103/PhysRevE.67.021908, article

Vich C (2012) Analytical and numerical methods for estimating conductances in neurons. Master's thesis, Universitat Politècnica de Catalunya

Vich C, Guillamon A (2015a) Dissecting estimation of conductances in subthreshold regimes. Journal of Computational Neuroscience pp 1–17, doi:10.1007/s10827-015-0576-2, URL http://dx.doi.org/10.1007/s10827-015-0576-2

Vich C, Guillamon A (2015b) Estimation of conductance in a conductance-based model of quadratic type. URL http://senselab.med.yale.edu/ModelDb/ShowModel.cshtml?model=184141

Wagenaar DA, Madhavan R, Pine J, Potter SM (2005) Controlling bursting in cortical cultures with closed-loop multi-electrode stimulation. The Journal of neuroscience 25(3):680–688

Wang XJ (1998) Calcium coding and adaptive temporal computation in cortical pyramidal neurons. J Neurophysiol 79(3):1549–1566, URL http://view.ncbi.nlm.nih.gov/pubmed/9497431

Wang XJ, Buzsáki G (1996) Gamma oscillation by synaptic inhibition in a hippocampal interneuronal network model. The Journal of neuroscience : the official journal of the Society for Neuroscience 16(20):6402–6413, URL http://www.jneurosci.org/cgi/content/abstract/16/20/6402

Wechselberger M (2012) À propos de canards (apropos canards). Transactions of the American Mathematical Society 364(6):3289–3309

Wechselberger M, Weckesser W (2009a) Bifurcations of mixed-mode oscillations in a stellate cell model. Physica D: Nonlinear Phenomena 238(16):1598 – 1614, doi:http://dx.doi.org/10.1016/j.physd.2009.04.017, URL http://www.sciencedirect.com/science/article/pii/S0167278909001444

Wechselberger M, Weckesser W (2009b) Homoclinic clusters and chaos associated with a folded node in a stellate cell model. Disc Cont Dyn Sys 2(4):1598 – 1614, doi:http://dx.doi.org/10.3934/dcdss.2009.2.829

Wehr M, Zador AM (2003) Balanced inhibition underlies tuning and sharpens spike timing in auditory cortex. Nature 426(6965):442–446, doi:10.1038/nature02116, URL http://dx.doi.org/10.1038/nature02116

Wilkinson DJ (2006) Stochastic Modelling for Systems Biology (Chapman & Hall/CRC Mathematical & Computational Biology), 1st edn. Chapman and Hall/CRC, URL http://www.amazon.com/exec/obidos/redirect?tag=citeulike07-20&path=ASIN/1584885408

Yasar TB, Wright NC, Wessel R (2016) Inferring presynaptic population spiking from single-trial membrane potential recordings. Journal of Neuroscience Methods 259:13 – 21, doi:http://dx.doi.org/10.1016/j.jneumeth.2015.11.019, URL http://www.sciencedirect.com/science/article/pii/S0165027015004215

Zucker R, Regehr W (2002) Short-term synaptic plasticity. Annu Rev Physiol 64(1):355–405